Three-Dimensional Nano-Heterojunctions for Photo- and Chemical Sensing

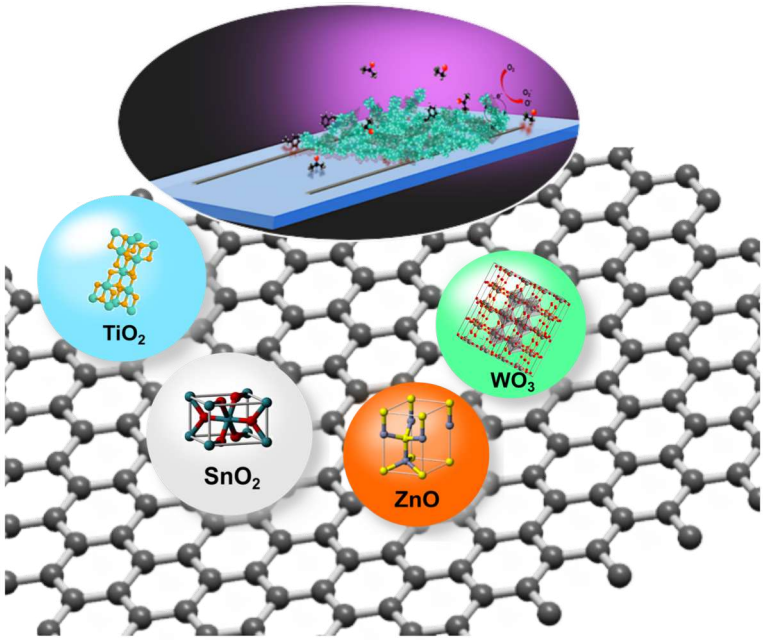

"If you can dream it, you can do it"

— Walt Disney

Cover design: "From graphene-metal oxide nano-heterojunctions to UV light-aided VOCs sensitive and selective thin films"

Three-Dimensional Nano-Heterojunctions for Photo- and Chemical Sensing
PhD Thesis

Università degli Studi di Milano, Dipartimento di Chimica

UNIVERSITÀ DEGLI STUDI DI MILANO
FACOLTÀ DI SCIENZE E TECNOLOGIE
DIPARTIMENTO DI CHIMICA

PhD COURSE IN INDUSTRIAL CHEMISTRY – XXXII CYCLE

THREE-DIMENSIONAL NANO-HETEROJUNCTIONS FOR PHOTO- AND CHEMICAL SENSING

CHIM/02

PhD Candidate
Eleonora PARGOLETTI

Supervisor: Prof. Giuseppe CAPPELLETTI
PhD School Coordinator: Prof. Dominique ROBERTO

Academic Year 2018/2019

This work was entirely supported by Università degli Studi di Milano (UNIMI) and through the Erasmus Mundus (Action 2 Strand 2) NANOPHI project, coordinated by Prof. Costantino De Angelis (University of Brescia) for the six-month period at the Nanotechnology Research Laboratory of Prof. Antonio Tricoli (The Australian National University, ANU).

To all the people who somehow helped me,
were close to me,
cared about me,
and fortunately, still do.
This is for You

Contents

Abstract

Abstract

The sensorial perception of the surroundings is critically related to the development of animal and human life. Human smell, or more generally, gas detection is a complex experience that subtly influences our decisions and actions. However, the human olfactory system is limited to a qualitative detection of few gases. Besides, the industrial development in the last decades, together with the drastic improvement of life quality and mobility, has increased the needs for quantitative detection of different analytes.

Online analysis of gas mixtures is fundamental in many research fields and, nowadays, the attention has been particularly focused on their analytical detection for diagnostic purposes. Specifically, the rapid development of smart wearable electronic devices is driving the engineering of novel miniaturized sensing materials that can rapidly respond to very small changes in the concentration of biomarkers at room temperature. In particular, sensitivity, low operating temperature, response/recovery times and selectivity are the main parameters to consider in order to prepare optimal sensing devices. Hence, carbon-based nanomaterials offer numerous attractive properties such as low resistivity, good mechanical robustness and integration potential, but lack a strong detection for the measurement of chemical molecules or photons. On the other hand, chemiresistors based on Metal Oxide Semiconductors (MOS) have been widely exploited, even if they still show several drawbacks especially connected to the high operating temperatures and scarce selectivity.

Thus, the focus of the present PhD research project was the synthesis of three-dimensional nanostructured architectures comprising of optimally integrated Graphene Oxide (GO) – n-type MOS heterojunctions for the photo-assisted low temperature sensing of Volatile Organic Compounds (VOCs, *i.e.* ethanol, acetone, toluene and ethylbenzene). Specifically, different transition metal oxides (ZnO, SnO_2, WO_3, TiO_2 or a solid solution of SnO_2-TiO_2) have been deeply investigated in order to prepare few micrometers porous films with promising chemoresistive properties. Moreover, while MOS is usually responsible for the gas detection at high operating temperatures, the addition of graphene oxide plays the pivotal role of enhancing the sensitivity, especially at room temperature, by exploiting the UV light. These layouts have been also demonstrated to provide excellent response to UV irradiations showcasing their applicability as visible-blind photodetectors. Furthermore, the effect of low and high GO content has been evidenced, emphasizing the different result when combined to ZnO or SnO_2 matrix. Notably, in the case of tin dioxide, great GO content allows to obtain both a response at RT and an increased selectivity towards bigger and non-polar molecules, as ethylbenzene. Whereas, small amounts of GO lead to a higher selectivity to polar molecules as ethanol, opening up new horizons for the preparation of well-performing low ppb sensing

materials. In addition, SnO_2 matrix seems to have higher sensing features than zin oxide material, in terms of either signal intensity or sensitivity. Therefore, preliminary studies, aimed at further improving the selectivity, were carried out by fabricating ternary compounds composed by SnO_2-TiO_2 solid solution and GO: a smooth selectivity towards large and non-polar molecules (such as toluene) was noticed.

Parallelly, the physico-chemical properties of chemoresistors strongly influence their sensing behavior: adopting WO_3 as a case study, the synthetic strategy was modified by finely tuning the tungsten precursors and the structure directing agents. Notably, it was noticed that the crystallite diameters, the surface area and the pores volume/shape drastically affect the sensing performances, in terms of either the signal intensity or the response/recovery times. Concurrently, a computational study and *in situ* XANES measurements (at the European Synchrotron Radiation Facility, ESRF in Grenoble) on acetone detection by tungsten trioxide were conducted to further corroborate the sensing mechanism. Finally, an extension of this mechanism to MOS-GO composites was hypothesized in which the formation of p(GO) – n(MOS) junctions clearly enhances the sensing behavior.

In conclusion, we believe that the findings obtained with this doctoral project can provide guidelines for the future engineering of hybrid carbon-metal oxide devices for application extending from optoelectronics to chemical sensing and electrocatalysis.

La percezione sensoriale dell'ambiente circostante è strettamente correlata allo sviluppo della vita animale e umana; in particolare, il rilevamento di gas è un'esperienza sensoriale complessa che influenza le nostre decisioni e azioni. Tuttavia, il sistema olfattivo umano è limitato ad una rilevazione qualitativa di pochi gas. Inoltre, lo sviluppo industriale negli ultimi decenni, insieme al drastico miglioramento della qualità della vita e della mobilità, ha aumentato le esigenze di rilevazione quantitativa di diversi analiti.

L'analisi di miscele di gas *online* è fondamentale in molti campi di ricerca e, al giorno d'oggi, l'attenzione è rivolta al rilevamento analitico a fini diagnostici. In particolare, il crescente sviluppo di dispositivi innovativi ha portato all'ottenimento di nuovi sensori miniaturizzati, capaci di sentire basse concentrazioni di differenti biomarker, con veloci tempi di risposta a temperatura ambiente. Nello specifico, i principali parametri da considerare per la fabbricazione di dispositivi ottimali sono i seguenti: sensibilità, basse temperature di lavoro, tempi di risposta/recupero e selettività. A tal proposito, i nanomateriali a base di carbonio, nonostante mostrino numerose proprietà come una bassa resistività e buona resistenza meccanica, non possiedono buone capacità di rilevazione e trasduzione nei confronti di molecole o fotoni. D'altra parte, i chemoresistori a base di Semiconduttori di Ossidi Metallici (MOS) nonostante siano ampiamente utilizzati, presentano ancora numerosi inconvenienti, in particolare legati alle alte temperature operative e alla scarsa selettività.

Lo scopo del presente progetto di dottorato è, quindi, la sintesi di nanostrutture tridimensionali, caratterizzate da eterogiunzioni perfettamente integrate di Ossido di Grafene (GO) e MOS (di tipo n) per il rilevamento a bassa temperatura e sotto irraggiamento UV di Composti Organici Volatili (VOC come ad esempio etanolo, acetone, toluene ed etilbenzene). Nello specifico, sono stati investigati diversi ossidi di metalli di transizione (ZnO, SnO_2, WO_3, TiO_2 o una soluzione solida di SnO_2-TiO_2) al fine di preparare film porosi e micrometrici (alcuni micron) aventi promettenti proprietà chemoresistive. Inoltre, mentre il semiconduttore a base ossidica è di solito responsabile del rilevamento di gas ad alte temperature, l'ossido di grafene svolge il ruolo fondamentale di migliorare la sensibilità e soprattutto la detection a bassa temperatura, anche grazie alla presenza della luce UV. I materiali così ottenuti, avendo un'eccellente risposta alle radiazioni ultraviolette, risultano essere anche ottimi fotorilevatori. Successivamente, è stato studiato l'effetto della quantità di GO sulle performance dei semiconduttori, specialmente in presenza di una matrice di ZnO o di SnO_2. Nel caso del biossido di stagno, infatti, un alto contenuto di GO consente di ottenere sia una risposta a temperatura ambiente, che una maggiore selettività verso molecole più grandi e non polari, come l'etilbenzene. Al contrario, basse quantità di GO aumentano la selettività verso molecole

polari come l'etanolo, aprendo di fatto nuovi orizzonti alla sintesi e all'ingegnerizzazione di nuovi materiali, in grado di rilevare concentrazioni di VOC dell'ordine dei ppb. In aggiunta, la matrice di SnO_2 porta a performance migliori rispetto a quelle ottenute con l'ossido di zinco, sia in termini di intensità del segnale che di sensibilità. Quindi, studi preliminari, volti a migliorare ulteriormente la selettività, sono stati condotti preparando composti ternari formati da una soluzione solida SnO_2-TiO_2 e GO: in questo caso è stata osservata una maggiore selettività per le molecole grandi e non polari, come il toluene.

Inoltre, è noto che le proprietà chimico-fisiche dei chemoresistori influenzano fortemente le loro caratteristiche di detection. Quindi, parallelamente al precedente studio, l'attenzione è stata focalizzata sulla sintesi *ad hoc* di ossido di tungsteno adottando diversi precursori e agenti strutturanti. In particolare, si è osservato che il diametro dei cristalliti, l'area superficiale e il volume/forma dei pori sono i principali parametri alla base delle performance sensoristiche in termini di intensità del segnale e tempi di risposta/recupero. Allo stesso tempo, calcoli computazionali e misurazioni XANES *in situ* presso il sincrotrone (ESRF) di Grenoble sono stati effettuati al fine di confermare/ipotizzare il meccanismo di sensing. Particolare attenzione è stata, poi, rivolta ai sistemi misti MOS-GO, dove la formazione di giunzioni p (GO) – n (MOS) amplifica e migliora il segnale.

In conclusione, i risultati ottenuti con questo progetto di dottorato possono essere considerati delle linee guida per l'ingegnerizzazione di nuovi dispositivi ibridi a base di materiali carboniosi e ossidi di metallo, per applicazioni che vanno dall'optoelettronica al campo sensoristico e a quello dell'elettrocatalisi.

Acknowledgements

It's been almost three years since I started my Doctorate and, now, at the very last days, I can look back to see what I've done. I cannot deny PhD life is difficult, here and there characterized by stressful situations and moments of despair…

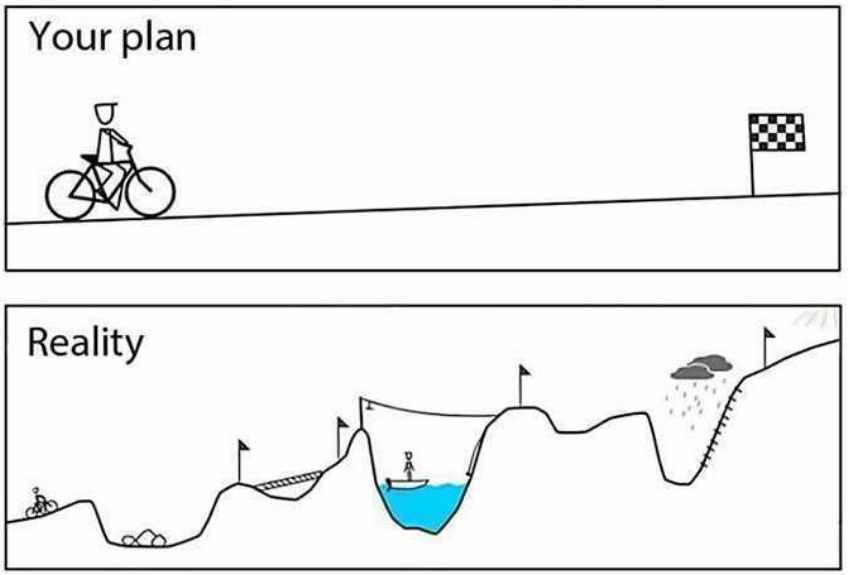

…but these three years have also signified much more. They have been plenty of instructive and motivating discussions, fruitful ideas even on topics less related to the scientific field, particularly thanks to the people I've met during this period. Hence, with a little bit of meditation and love, I'll try to express my sincere gratitude to whom has helped me and encouraged me to do always my best.

The first person I'd like to acknowledge and deeply thank is my supervisor, Prof. Giuseppe Cappelletti. There have been lots of ups and downs in this three-year experience, but you have always kept pushing me, you have always had constructive advices (not only related to science), critical evaluations, and innumerable helpful suggestions. I know I'm "a little bit" a pain in the neck, so thank you for your constant helpfulness, for always being keen on answering to my questions, thank you for your huge patience and your understanding. I hope to have been a positive spin, after all!

Of course, this work would not be so satisfactory and rewarding without the scientific contribution of some people I've met during this period. First of all, Prof. Antonio Tricoli and all the guys of the Nanotechnology Research Laboratory group, who I've had the luck to know in the six months spent at the Australian National University. My deepest thank to you, guys! Your constant kindness and hospitality made me feel at home. Thanks to Zelio Fusco, Dr. Habiba Hossain, Dr. Iolanda Di Bernardo, Dr. Hongjun Chen, Thanh Tran-Phu and Dr. Josh Lipton-Duffin (of Queensland University of

Technology in Brisbane) who somehow helped me with some physico-chemical characterizations and sensing measurements.

Dr. Mariangela Longhi (UNIMI), Prof. Gian Luca Chiarello (UNIMI), Prof. Marco Derudi (POLIMI), Prof. Giuseppina Cerrato (UNITO) and Dr. Vittoria Guglielmi (UNIMI) are gratefully acknowledged for BET analyses, synchrotron experiments, engineering of the sensing set-up, TEM and Raman measurements, respectively. Prof. Claudia Bianchi (UNIMI) is deeply acknowledged for XPS analyses. A grateful acknowledgement goes also to Prof. Luigi Falciola and Dr. Valentina Pifferi (ELAN group at UNIMI) for their suggestions and helpful discussions concerning the electrochemical tests. Dr. Davide Ceresoli, Dr. Mario Trioni, Dr. Fausto Cargnoni and Dr. Raffaella Soavi (ISTM-CNR in Milan) are deeply thanked for the computational study on acetone sensing by WO_3 material. For the thermogravimetric analyses, I'd like to acknowledge the Regione Lombardia - Fondazione Cariplo joint SmartMatLab project (Fondazione Cariplo 2013-1766 project).

For this work, I'd also like to express my deepest appreciation to all the Bachelor and Master students who somehow have helped me and, so, contributed to the success of this project. And, of course, to all the guys I've had the fortune to meet and know during this period.

I hope to have acknowledged all the people that made this research work better, giving me advice and assistance at times when my capabilities were not enough. However, in these three years I've had the pleasure to meet people who have also contributed to my personal growth. For this reason, I'd like to deeply thank Anna with whom I shared the best and worst instants of our PhD life. Thank you for your suggestions, light moments (sometimes based on alcoholic drinks, of course!) and important advices. "Corza e Foraggio, we're doing it!".

Special thanks I'd like to give to my friends, with particular regards to those who have known me for a long time. It does not matter how often we see each other, as long as we can count on each other. Thanks for always being there whenever I need.

Hoping not to have forgotten someone, the most important acknowledgement and appreciation go to my family, for the unconditioned support throughout all my life. I know, I wouldn't have achieved this goal without you. I admit being (sometimes?) a difficult person, so simply thank you for your constant encouragement, patience and infinite endurance.

Eleonora

Chapter 1

Introduction

Reproduced with permission[1], Copyright 2017, *Wiley-VCH*.

"Think, believe, dream and dare"

— Walt Disney

1.1. Gas sensors applications

A sensor can be defined as a device able to convert a target chemical or physical variation into an easily processable signal. The sensing element has to fulfill two different tasks: first, it has to interact with the target gas through various mechanisms, like surface adsorption, charge transfer or ionic exchange (*receptor* task); then, this interaction has to be transformed into a signal, as a change in the electrical conductivity or in optical transmission (*transducer* task). There is a variety of sensing devices that rely on different chemical or physical phenomena. Specifically, the analyte can be detected through changes in electrical properties (conductivity,[2–4] impedance,[5] capacitance[6,7]), optical properties (refractive index[8]) or other physical features (thermal conductivity[6,9,10], acoustic waves propagation[6,9,10]).

Besides, the latest achievements in wearable and portable electronics/optoelectronics are driving the demand for miniaturized sensor materials capable of detecting a wide variety of signals ranging from UV light exposure to biomarkers[6,11,12]. The challenges and potential of these few-millimetres in size devices are: (*i*) the implementation in on-chip electronic systems with ultra-low power consumption; (*ii*) the replacement of the traditional expensive and time-consuming analytical instrumentations; (*iii*) the engineering of next-generation wireless sensors[1]. Moreover, the monitoring of gaseous components in real matrices is of particular practical importance with applications extending from environmental protection[13,14], medical diagnostics[1,15,16], industrial manufacturing[17,18], agriculture (*e.g.* biohazards, fruit ripening)[18], and safety (*e.g.* explosive detection). As concern the diseases diagnosis, human breath is mainly composed by N_2, O_2, CO_2, H_2O, and inert gases. The remaining small fraction consists of more than 1000 different Volatile Organic Compounds (VOCs) with concentrations in the range from parts-per-million (ppm) to parts-per-trillion (ppt)[19–21]. Compounds with relatively high concentrations in the exhaled breath comprise ammonia (median concentration: 833 ppb), acetone (477 ppb), isoprene (106 ppb), methanol (461 ppb), ethanol (112 ppb), propanol (18 ppb) and acetaldehyde (22 ppb)[22]. Alongside, it is well known that many diseases are accompanied by characteristic odours. Hence, their recognition can provide diagnostic clues, guide the laboratory evaluation, and affect the choice of immediate therapy. For instance, the correlation between the VOCs concentration and the occurrence of certain

disease has been evaluated as follows: *i*) higher concentrations of ethane and pentane are connected to inflammatory diseases[23,24]; *ii*) acetone has been associated to dextrose metabolism and diabetes[25]; *iii*) elevated concentration of exhaled sulphur-containing compounds is a probe of liver failure and allograft rejection[26]; *iv*) atopic asthma and lung inflammation increase the concentration of exhaled NO/NO_2[27,28]. Particularly, the nature, origin, emission, and related biochemical pathways of some VOCs/inorganic species, as primary and secondary alcohols, aldehydes/branched aldehydes, ketones, esters, nitriles and aromatic compounds, in volatolomics, have been recently reviewed thoroughly (see Table 1.1)[4,29–36].

Biomarker	Purpose	Levels	Sensor technology	Ref.
Acetone	Hyperglycemia diabetes type 1	30 ppb > 1800 ppb	Si-doped WO_3 nanoparticle films	[29,37]
Ammonia	Liver failure	50 ppb	Chemoresistive nano-MOx	[30]
Ammonia	Liver failure	10 ppb	p-n oxide semiconductor heterostructures	[31]
2-Butanone	Helicobacter pylori	500 ppb	Chemoresistive graphene-ZnO	[32]
Ethanol/Toluene	Alcohol/cigarette consumption	0.1 ng	GC-MS	[33]
H_2S NO	Asthma Lung injury	534 ppt 206 ppt	Chemoresistive	[4]
Menthone, C_8H_8, $C_9H_{18}O$	Amount of cigarettes smoked	≈ ppt	Atmospheric pressure chemical ionization	[34]
2-EH, $C_7H_{14}O$, $C_{10}H_{20}O$, $C_{16}H_{34}$	Ovarian cancer	400 ppb	Chemoresistive flexible nanoparticle-based sensor array	[35]
Trimethylamine	Chronic kidney disease	1.76 ppb	GC-MS	[36]

Table 1.1. *List of some common volatile biomarkers and sensor technologies. Adapted with permission[1], Copyright 2017, Wiley-VCH.*

Specifically, as claimed in Table 1.1, acetone is related to type 1 diabetes[38] since its concentration increases from a value in the range 300-900 ppb in healthy people to more than 1800 ppb in diabetics' breath. Similarly, ethylbenzene, already widely studied for environmental pollution as BTEX (Benzene Toluene Ethylbenzene Xylene) compounds, has been recently recognized as one of the potential biomarkers for lung cancer detection (0.04 ppb

in healthy humans *vs* 0.11 ppb in ill patients)[10,22,39]. Alongside, the detection of ethanol gaseous molecules (< 100 ppm) can be useful for food quality monitoring in fermentation industries and in several medical applications[40]. Therefore, an early and accurate diagnosis of a specific disease plays a decisive role for its effective treatment. In this context, there is a great demand for Point-of-Care testing (PoC) devices[41,42], which ensure the quality and performance requirements of *in vitro* diagnostics, performed in a short period by non-experts[43]. This will also pave the way for novel home health monitoring systems and add valuable information for personalized medicine.

However, notwithstanding volatile organic compound analysis from human breath is the least invasive and instinctive method of medical diagnostics, high sensitivity and selectivity, fast response to the analyte, low cross sensitivity to humidity (due to the water vapor present in the breath), small size and simplicity, low production and maintenance costs are nowadays challenging issues. Nevertheless, the development of novel solid-state sensors for the selective detection of ultra-low concentrations of specific gas molecules is becoming increasingly more feasible, due to the recent progress in nanofabrication approaches, which are capable of providing atomic-level control of the surface composition in high surface-area/porosity detectors[2,44]. In particular, the sensing mechanism of semiconductor chemoresistive sensors has been recently summarized: the conductivity of a nanostructured sensor film changes significantly as a function of the concentration of reducing/oxidizing gases and their reactivity with the semiconductor surface. This technology enables the particle-per-billion detection of important VOCs such as acetone[44,45] and ethanol[46], by a simple and highly miniaturizable resistance measurement. Hence, miniaturized chemoresistive gas nanodetectors, made of nanostructured Metal Oxides Semiconductors (MOS), can be a promising alternative to the traditional and more sophisticated analytical techniques (such as PTR-MS or gas chromatography)[47]. Acting as the key part of the gas sensors, MOS nanomaterials should be rationally designed in an appropriate way. Commonly, the design of sensing materials is based on prior knowledge, which avoids time-consuming synthesis, testing or numerous candidates. However, this design method requires more detailed knowledge about how the intrinsic properties of sensing materials are associated with their performance characteristics, such as the magnitude of response to analytes and interferences, resistance to poisoning, optimum operation temperature, the response/recovery rate, and long-term stability[48,49]. Unfortunately, the gaining of this knowledge often needs extensive experimental and simulation data. Furthermore, the design of sensing materials becomes more and more difficult as a result of the increase in synthesis methods, the complex interactions between functionality and composition, and the strict end-use conditions of the sensing materials. In these cases, the design of effective sensing materials is a great challenge because it requires a

large number of experiments and identification, which could provide tremendous impetus for the development of combinatorial and high-throughput screening methods.

For instance, sensor arrays of SnO_2 have been optimized to detect acetone and tested to discriminate diabetic from non-diabetic volunteers[50]. Nanosized γ-Fe_2O_3 sensors can also selectively detect 1 ppm of acetone in the background of human breath[51]. Epitaxially oriented polycrystalline WO_3-based thin films are highly sensitive to nitrogen dioxide and acetone[16,52]. In 2010, Righettoni *et al.*[44] reported the synthesis of a highly selective nanostructured material for acetone sensing, the major breath marker for diabetes. Films of Si-doped WO_3 nanoparticles were deposited by flame synthesis on a simple interdigitated electrode layout (see Figure 1.1a), capable of chemoresistive measurement down to 20 ppb of acetone at 90% relative humidity[1]. The potential of this compact sensor layout for online measurement of acetone was thereafter confirmed in real human breath, by comparison with proton transfer reaction mass spectrometry (PTR-MS), showing excellent accuracy (Figure 1.1b)[1,44].

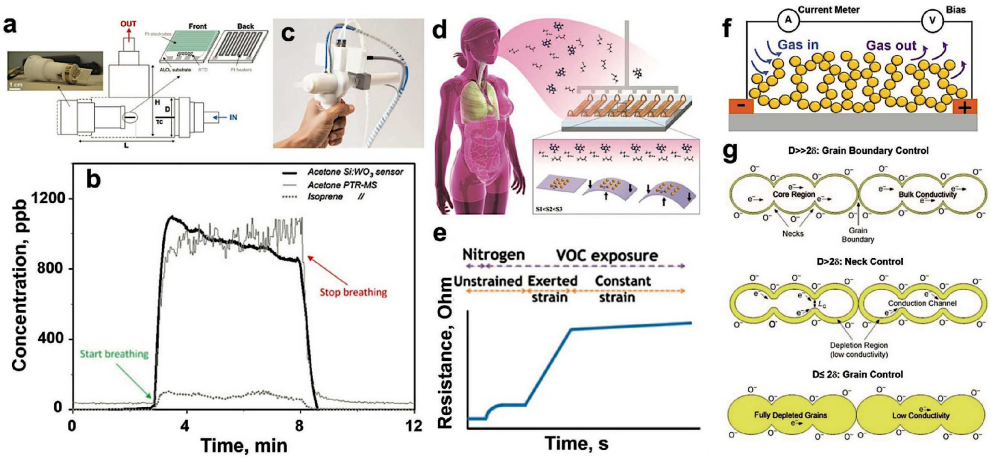

Figure 1.1. *(a) Schematic and prototype of a compact chemoresistive breath acetone sensing device, for diabetes diagnostics, showing (b) excellent accuracy with PTR-MS measurements and (c) integration in a hand-held device. (d) Scheme and (e) characterization of a flexible gold nanoparticle sensor array for accurate detection of ovarian carcinoma from breath analysis. (f,g) Example of operation principle and sensing mechanism of chemoresistive sensors. Reproduced with permission*[1]*, Copyright 2017, Wiley-VCH.*

A fully hand-held version of this technology for direct measurement of breath acetone has been recently presented (Figure 1.1c). Further miniaturization of this type of chemoresistive sensor is possible, enabling devices as small as few millimetres in size. Several research groups are developing carefully engineered sensing nanostructures for selective and room temperature detection of important VOCs[53–55]. Moreover, it is reported that light activation of the sensing nanomaterials may further help in decreasing the operative temperature and

increasing the selectivity[56–58]. Besides, the development of flexible and stretchable sensing materials has recently shown some potentialities so that the selectivity of these nanostructured sensors can be increased (Figures 1.1d,e)[1]. The mechanism underneath the chemoresistive sensing behavior can be schematically represented by Figures 1.1f and g. Usually, a constant voltage is applied between two interdigitated electrodes connected through a nanostructured semiconductor layer, such as a film of oxide nanoparticles. The latter is commonly kept at a constant temperature and engineered to promote the reduction or oxidation of the target analyte. These redox reactions change the concentration of surface charges on the nanostructured film, thus modifying the material conductivity and increasing or decreasing the current, that flows between the two electrodes[3]. If the size of the nanostructures is comparable to the Debye's length of the semiconductor, the change of conductivity affects the whole material and, thus, it can result in several orders of magnitude strong current rise or decay (redox reactions), already at analyte concentrations of few ppm[3].

Notably, although chemoresistive gas sensors synthesized by aerosol routes are sensitive to many gases and VOCs, to date, they do not reach the required low concentration sensitivities for an application such as breath analysis for medical diagnostics. Moreover, the poor selectivity, scarce life-time and usually high operating temperatures[12] represent the major shortcomings of this type of detection. As previously touched on, among the most performing metal oxides, ZnO, SnO_2 and WO_3 nanoparticles have been successfully used to sense some VOCs, as ethanol and acetone, down to ppb level[13,18,44,59–61]. Specifically, in order to overcome their main drawbacks (*i.e.* large power consumption, scarce selectivity[47,62], high operating temperatures[63]), co-synthesis of metal oxides with other oxides/non-metal elements[58,64], their doping with metal nanoparticles (such as Pt or Ag)[65] or, even, their coupling with graphene-based materials[6,66] can be valuable alternatives. Particularly, graphene possesses several optimal properties such as thermo-electric conduction and mechanical strength, resulting in an enhancement of the final sensing response[10,67,68]. In this context, reduced graphene oxide (rGO) has been widely investigated and offers great potentialities for the gas sensing. On the contrary, pure graphene oxide (GO) has not been so studied due to its less defective structure and to the many functional groups on its surface if compared to rGO[69–71]. However, these functionalities can be the anchor points for the controlled chemical growth of metal oxide nanoparticles, thus giving rise to composite materials. Notably, there is still a lack of literature concerning the chemical growth of metal oxide nanoparticles on GO. Specifically, the available literature[11,46,72] reports data about mechanically mixed or impregnated MOS-GO compounds. For instance, Vessalli *et al.*[46] described ZnO nanorods, with controlled size and morphology, grown through a wet deposition on gold interdigitated electrodes, previously covered with graphene oxide. Besides,

Wang *et al.*[72] reported ZnO/GO nanocomposites by impregnation of GO with zinc oxide nanosheets. Furthermore, Zhang *et al.* stated that sensors based on ZnO/graphene hybrid materials can exhibit remarkably enhanced response towards acetone with respect to the pristine metal oxide[73]. Kalidoss *et al.* investigated a ternary composite based on GO, SnO_2 and TiO_2 and they have demonstrated that this sensor can be a good candidate for the highly selective detection of acetone gas in breath of diabetes mellitus patients, at operating temperature of ca 200 °C[74].

In conclusion, to the author's best knowledge, the interests in the study of nanomaterials have escalated in the recent decades, whereas their application in the gas sensing field (also towards their further production on industrial scale) is still in its infancy[6,12]. Continued progress in graphene-based composite gas sensors will overcome the current challenges, get through the close siege and lead to a class of gas sensors with superior sensitivity, excellent selectivity, reduced size and extended lifetimes for a wide range of applications[12]. However, there are several drawbacks to phase out, such as *i*) the quantification and control of the humidity influence on sensors performances[6], *ii*) the ability to sense non-polar and large molecules (in particular VOCs, such as acetone, ethanol, acetaldehyde, formaldehyde *etc*.)[6], *iii*) the improvement of gas selectivity[12], and *iv*) the enhancing of sensing performances at room temperature[7,75], especially in real matrices.

1.2. The aim of the PhD Thesis

The present PhD Thesis work is focused on the development of metal oxide semiconductor-based chemoresistors for the sensing of some volatile organic compounds, either small and polar (ethanol, acetone) or big and non-polar ones (toluene and ethylbenzene). The main goal is the synthesis of composite materials, in which well-integrated graphene oxide sheets into MOS matrix (such as ZnO, SnO_2, TiO_2) could enhance both their chemical and photo-sensing.

Specifically, graphene oxide synthesis (*i.e.* the well-known modified Hummers method) is tailored in order to tune the physico-chemical properties of the final powders. Then, the most suitable experimental conditions are adopted for the preparation of GO to be used in the following functionalization with MOS nanoparticles. Notably, different MOS-GO ratios are investigated, aiming at delineating the most performing materials in terms of sensitivity, low operating temperature (exploiting the UV light), response/recovery times and selectivity. In particular, zinc oxide, tin dioxide, titanium dioxide and a solid solution of SnO_2-TiO_2 are chosen as chemoresistive materials. All the samples are finely characterized on physico-chemical-electrochemical points of view, trying to connect the as-obtained results with the observed sensing behavior. Besides, a very easy and cheap spraying method is adopted for powders deposition on interdigitated electrodes, giving rise to very homogeneous and highly porous (> 90%) films.

Furthermore, to stress the importance of the synthetic route in tailoring the powders features, a detailed study on pure WO_3 semiconductor preparation methods is conducted. Besides, due to its large use as chemoresistor, tungsten trioxide is also adopted for further computational investigations, which resulted fundamental for a deeper comprehension of the sensing mechanism. The theoretical outcomes are also corroborated by *in situ* XANES experimental tests, alongside with acetone sensing measurements by pure WO_3, at the European Synchrotron Radiation Facility, in Grenoble.

Finally, the improved MOS sensing performances, achieved by the addition of GO, is believed to be due to the formation of p-n nano-heterojunctions between p-type GO and n-type metal oxides. In order to confirm this hypothesis, optoelectronic and electrochemical properties of the composites are examined thoroughly. Finally, starting from the mechanism already reported in the literature, an extension of it is proposed herein, which contemplates the UV-aided low operating temperature conditions.

References

[1] A. Tricoli, N. Nasiri, S. De, *Adv. Funct. Mater.* **2017**, *27*, 1605271.

[2] C. O. Blattmann, A. T. Güntner, S. E. Pratsinis, *ACS Appl. Mater. Interfaces* **2017**, *9*, 23926.

[3] A. Tricoli, M. Righettoni, A. Teleki, *Angew. Chemie Int. Ed.* **2010**, *49*, 7632.

[4] H. G. Moon, Y. Jung, S. D. Han, Y.-S. Shim, B. Shin, T. Lee, J.-S. Kim, S. Lee, S. C. Jun, H.-H. Park, C. Kim, C.-Y. Kang, *ACS Appl. Mater. Interfaces* **2016**, *8*, 20969.

[5] S. H. Lee, J. Yang, Y. J. Han, M. Cho, Y. Lee, *Sensors Actuators B Chem.* **2015**, *218*, 137.

[6] S. Gupta Chatterjee, S. Chatterjee, A. K. Ray, A. K. Chakraborty, *Sensors Actuators B Chem.* **2015**, *221*, 1170.

[7] J. Zhang, X. Liu, G. Neri, N. Pinna, *Adv. Mater.* **2016**, *28*, 795.

[8] Z. Fusco, M. Rahmani, R. Bo, R. Verre, N. Motta, M. Käll, D. Neshev, A. Tricoli, *Adv. Mater.* **2018**, *30*, 1.

[9] A. O. Simm, S. Ward-Jones, C. E. Banks, R. G. Compton, *Anal. Sci.* **2005**, *21*, 667.

[10] K. M. Tripathi, T. Kim, D. Losic, T. T. Tung, *Carbon N. Y.* **2016**, *110*, 97.

[11] U. Latif, F. Dickert, *Sensors* **2015**, *15*, 30504.

[12] T. Wang, D. Huang, Z. Yang, S. Xu, G. He, *Nano-Micro Lett.* **2016**, *8*, 95.

[13] W. Li, X. Wu, N. Han, J. Chen, X. Qian, Y. Deng, W. Tang, Y. Chen, *Sensors Actuators B Chem.* **2016**, *225*, 158.

[14] V. K. Tomer, S. Devi, R. Malik, S. P. Nehra, S. Duhan, *Sensors Actuators B Chem.* **2016**, *229*, 321.

[15] J.-H. Kim, S. S. Kim, *ACS Appl. Mater. Interfaces* **2015**, *7*, 17199.

[16] L. Wang, A. Teleki, S. E. Pratsinis, P. I. Gouma, *Chem. Mater.* **2008**, *20*, 4794.

[17] D. Chen, Y. J. Yuan, S. Member, **2015**, *15*, 6749.

[18] Z. Song, Z. Wei, B. Wang, Z. Luo, S. Xu, W. Zhang, H. Yu, M. Li, Z. Huang, J. Zang, F. Yi, H. Liu, *Chem. Mater.* **2016,** *28*, 1205.

[19] R. Mukhopadhyay, *Anal. Chem.* **2004**, *76*, 273A.

[20] W. Cao, *Clin. Chem.* **2006**, *52*, 800.

[21] M. Phillips, J. Herrera, S. Krishnan, M. Zain, J. Greenberg, R. N. Cataneo, *J. Chromatogr. B. Biomed. Sci. Appl.* **1999**, *729*, 75.

[22] B. Buszewski, M. Kęsy, T. Ligor, A. Amann, *Biomed. Chromatogr.* **2007**, *21*, 553.

[23] C. O. Olopade, M. Zakkar, W. I. Swedler, I. Rubinstein, *Chest* **1997**, *111*, 862.

[24] P. Paredi, S. A. Kharitonov, D. Leak, S. Ward, D. Cramer, P. J. Barnes, *Am. J. Respir. Crit. Care Med.* **2000**, *162*, 369.

[25] M. J. Sulway, J. M. Malins, *Lancet* **1970**, *296*, 736.

[26] O. Lawal, W. M. Ahmed, T. M. E. Nijsen, R. Goodacre, S. J. Fowler, *Metabolomics* **2017**, *13*, 110.

[27] S. A. Kharitonov, P. J. Barnes, *Biomarkers Biochem. Indic. Expo. response, susceptibility to Chem.* **2002**, *7*, 1.

[28] D. Biagini, T. Lomonaco, S. Ghimenti, F. G. Bellagambi, M. Onor, M. C. Scali, V. Barletta, M. Marzilli, P. Salvo, M. G. Trivella, R. Fuoco, F. Di Francesco, *J. Breath Res.* **2017**, *11*, 047110.

[29] M. Righettoni, A. Tricoli, *J. Breath Res.* **2011**, *5*, 037109.

[30] F. Xie, H. Lu, D. Chen, X. Ji, F. Yan, R. Zhang, Y. Zheng, L. Li, J. Zhou, *IEEE Sens. J.* **2012**, *12*, 2086.

[31] C. Sun, P. K. Dutta, *Sensors Actuators B Chem.* **2016**, *226*, 156.

[32] Y.-C. Weng, Y.-H. Yang, I.-T. Lu, Detection of 2-Butanone for the Diagnosis of Helicobacter Pylori Using Graphene and ZnO Nanorod Electrodes. *J. Nanosci. Nanotechnol.* **2016,** *16*, 7077–7084.

[33] Y.-K. Cheng, C.-H. Lin, T. Kaneta, T. Imasaka, *J. Chromatogr. A* **2010**, *1217*, 5274.

[34] L. M. Heaney, D. M. Ruszkiewicz, K. L. Arthur, A. Hadjithekli, C. Aldcroft, M. R. Lindley, C. P. Thomas, M. A. Turner, J. C. Reynolds, *Bioanalysis* **2016**, *8*, 1325.

[35] N. Kahn, O. Lavie, M. Paz, Y. Segev, H. Haick, *Nano Lett.* **2015**, *15*, 7023.

[36] B. Grabowska-Polanowska, J. Faber, M. Skowron, P. Miarka, A. Pietrzycka, I. Sliwka, A. Amann, *J. Chromatogr. A* **2013**, *1301*, 179.

[37] M. Righettoni, A. Tricoli, S. Gass, A. Schmid, A. Amann, S. E. Pratsinis, *Anal. Chim. Acta* **2012**, *738*, 69.

[38] M. Righettoni, A. Tricoli, S. E. Pratsinis, *Chem. Mater.* **2010**, *22*, 3152.

[39] G. J. Zhang, X. X. Guo, S. L. Wang, X. L. Wang, Y. P. Zhou, H. Xu, *J. Chromatogr. B Anal. Technol. Biomed. Life Sci.* **2014**, *969*, 128.

[40] A. Naskar, M. Narjinary, S. Kundu, *J. Electron. Mater.* **2017**, *46*, 478.

[41] S. K. Vashist, P. B. Luppa, L. Y. Yeo, A. Ozcan, J. H. T. Luong, *Trends Biotechnol.* **2015**, *33*, 692.

[42] G. Gauglitz, *Annu. Rev. Anal. Chem.* **2014**, *7*, 297.

[43] P. B. Luppa, A. Bietenbeck, C. Beaudoin, A. Giannetti, *Biotechnol. Adv.* **2016**, *34*, 139.

[44] M. Righettoni, A. Tricoli, S. E. Pratsinis, *Anal. Chem.* **2010**, *82*, 3581.

[45] M. Righettoni, A. Tricoli, S. E. Pratsinis, *Chim. Int. J. Chem.* **2011**, *65*, 105.

[46] B. A. Vessalli, C. A. Zito, T. M. Perfecto, D. P. Volanti, T. Mazon, *J. Alloys Compd.* **2017**, *696*, 996.

[47] A. M. K. Janghorban, B. H. G. Neri, *J. Nanoparticle Res.* **2015**, *17*, 1.

[48] G. Soliveri, V. Pifferi, G. Panzarasa, S. Ardizzone, G. Cappelletti, D. Meroni, K.

Sparnacci, L. Falciola, *Analyst* **2015**, *140*, 1486.

[49] A. T. E. Vilian, S. M. Chen, Y. T. Hung, M. A. Ali, F. M. A. Al-Hemaid, *Anal. Methods* **2014**, *6*, 6504.

[50] S. Karthikeyan, R. Boopathy, G. Sekaran, *J. Colloid Interface Sci.* **2015**, *448*, 163.

[51] N. T. A. Thu, N. D. Cuong, L. C. Nguyen, D. Q. Khieu, P. C. Nam, N. Van Toan, C. M. Hung, N. Van Hieu, *Sensors Actuators B Chem.* **2018**, *255*, 3275.

[52] L. Saadi, C. Lambert-Mauriat, V. Oison, H. Ouali, R. Hayn, *Appl. Surf. Sci.* **2014**, *293*, 76.

[53] Z. Wang, Y. Zhang, S. Liu, T. Zhang, *Sensors Actuators B Chem.* **2016**, *222*, 893.

[54] Z. Gao, Z. Lou, S. Chen, L. Li, K. Jiang, Z. Fu, W. Han, G. Shen, *Nano Res.* **2018**, *11*, 511.

[55] A. P. Sharma, P. Dhakal, D. K. Pradhan, M. K. Behera, B. Xiao, M. Bahoura, *AIP Adv.* **2018**, *8*, 095219.

[56] L. Zhu, W. Zeng, *Sensors Actuators A Phys.* **2017**, *267*, 242.

[57] Z. Q. Zheng, J. D. Yao, B. Wang, G. W. Yang, *Sci. Rep.* **2015**, *5*, 1.

[58] S.-P. Chang, K.-Y. Chen, *ISRN Nanotechnol.* **2012**, *2012*, 1.

[59] Y. Xu, P. Liu, D. Sun, Y. Sun, G. Zhang, D. Gao, *Mater. Lett.* **2015**, *161*, 495.

[60] W. Li, S. Ma, Y. Li, G. Yang, Y. Mao, J. Luo, D. Gengzang, X. Xu, S. Yan, *Sensors Actuators B Chem.* **2015**, *211*, 392.

[61] Y. He, P. Tang, J. Li, J. Zhang, F. Fan, D. Li, *Mater. Lett.* **2016**, *165*, 50.

[62] H. J. Kim, J. H. Lee, *Sensors Actuators, B Chem.* **2014**, *192*, 607.

[63] W. Wang, Y. Tian, X. Wang, H. He, Y. Xu, C. He, X. Li, *J. Mater. Sci.* **2013**, *48*, 3232.

[64] P. Zhang, G. Pan, B. Zhang, J. Zhen, Y. Sun, *Mater. Res.* **2014**, *17*, 817.

[65] M. Righettoni, A. Amann, S. E. Pratsinis, *Mater. Today* **2015**, *18*, 163.

[66] F. Meng, Z. Guo, X. Huang, *Trends Anal. Chem.* **2015**, *68*, 37.

[67] H. W. Kim, Y. J. Kwon, A. Mirzaei, S. Y. Kang, M. S. Choi, J. H. Bang, S. S. Kim, *Sensors Actuators, B Chem.* **2017**, *249*, 590.

[68] S. S. Varghese, S. H. Varghese, S. Swaminathan, K. K. Singh, V. Mittal, **2015**, *4*, 651.

[69] S. Pei, J. Zhao, J. Du, W. Ren, H. M. Cheng, *Carbon N. Y.* **2010**, *48*, 4466.

[70] H. Moussa, E. Girot, K. Mozet, H. Alem, G. Medjahdi, R. Schneider, *Appl. Catal. B Environ.* **2016**, *185*, 11.

[71] E. Pargoletti, A. Tricoli, V. Pifferi, S. Orsini, M. Longhi, V. Guglielmi, G. Cerrato, L. Falciola, M. Derudi, G. Cappelletti, *Appl. Surf. Sci.* **2019,** *483*, 1081.

[72] P. Wang, D. Wang, M. Zhang, Y. Zhu, Y. Xu, X. Ma, X. Wang, *Sensors Actuators B Chem.* **2016**, *230*, 477.

[73] H. Zhang, Y. Cen, Y. Du, S. Ruan, *Sensors (Switzerland)* **2016**, *16*, 1.

[74] R. Kalidoss, S. Umapathy, Y. Sivalingam, *Appl. Surf. Sci.* **2018**, *449*, 677.

[75] D. Acharyya, P. Bhattacharyya, S. Member, **2016**, *37*, 656.

Chapter 2

Overview on photo- and chemical sensing

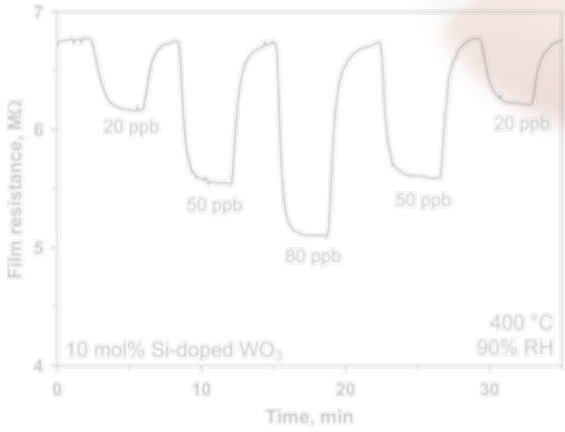

"I am not what happened to me,
I am what I choose to become"

— Nelson Mandela

2.1. General outlines

2.1.1. A hint on visible-blind UV photodetectors

Ultraviolet photodetectors have gained extensive attention in recent years thanks to their broad applications including flame monitoring, missile-plume detection and space communication[4–6]. All these research fields require a very high degree of sensitivity with great signal-to-noise ratio and very rapid responses[7]. Therefore, the ideal UV photodetector should show high responsivity, detectivity and quantum efficiency alongside with a good photocurrent linearity as a function of the incident optical power, a low noise level, high selectivity to UV light and a fast response kinetic[8]. Indeed, the latter is particularly important for real-time signal processing, as in optical communications[9].

In this context, one of the most exploited and outperforming photodetector materials is silicon, showcasing very quick responses on the one hand, and some intrinsic limitations, including either poor visible and infrared radiations selectivity or its degradation tendency under UV light, on the other[10]. Hence, as alternative materials, wide band-gap (E_g > 3.3 eV)[7] semiconductors have been deeply investigated, especially for electronic and optoelectronic devices[7], owing to their superior temperature, chemical stability and visible light transparency. This class includes gallium nitride (GaN)[11], tin dioxide (SnO_2)[12,13], titanium dioxide (TiO_2)[7], silicon carbide (SiC)[14], and zinc oxide (ZnO)[5,15,16]. Notwithstanding the aforementioned advantageous features, these semiconductors display some drawbacks, mainly related to their inferior carrier diffusion lengths, internal quantum efficiency and electron/hole recombination kinetics with respect to silicon, thus leading to poorer micro-macroscale performances[7]. Therefore, in order to overcome these weaknesses, semiconductors nano-structuring has been proved to be a powerful strategy, resulting in superior ultraviolet-responsive photodetectors[9].

Notably, quantum dots (QDs), nanowires[17], nanorods[15], core/shell structures[12], and heterostructures[18] are believed to be the future building blocks of visible-blind UV photodetectors. Indeed, low-dimensional nanostructures (*e.g.* 1D, 2D or 3D layouts) usually

show higher responsivity and photoconductivity than thin-films and bulky materials, thanks to both the very high surface-to-volume ratio and the nanoscale carriers transport kinetics[7,9]. Particularly, the large surface-to-volume ratio significantly increases the number of surface trap states that can prolong the photocarrier lifetime by delaying the electron-hole recombination process[7].

There are plenty of methods to produce nanostructured UV photodetecting materials, such as flame spray pyrolysis[9], sol-gel route[19] and magnetron sputtering[20]. A critical aspect remains the accurate control of the hierarchical network from the atomistic scale to the microscopic final device. For instance, ZnO nanowires are usually reported to achieve responsivity and detectivity orders of magnitude higher than ZnO compact thin films[21]. Similarly, ultraporous nanoparticle networks have shown thousand folds higher photo-to-dark current ratios than denser ZnO nanoparticle layers, thus resulting in among the highest detectivity, already reported for such materials[7,9].

2.1.2. Tips about gas sensors

Parallelly to the previous topic, in today's world, the demand for developing simple and reliable gas sensors is huge[22–24]. Indeed, the monitoring of gaseous components in real matrices is of great practical importance in many fields, such as in environmental protection (in particular in indoor or closed ambient)[25,26], medical diagnosis[27], industrial manufacture (*e.g.* in automotive industry)[28,29], agriculture[29], and so on. As widely reported in the literature, typical compounds to be monitored include toxic, flammable and combustible gases[22], as well as Volatile Organic Compounds (VOCs)[25]. In particular, one of the most recent applications of gas sensors is the diagnosis of diseases by detecting biomarkers in the exhaled humans breath, which contains a certain number of VOCs, known to have strong correlations with specific diseases[27]. This non-invasive diagnostic technique has advantages over other commonly used methods, such as tomography or endoscopy[27]. Moreover, the detection of gas molecules such as NO, NO_2, NH_3, CO, *etc*.[22] is necessary in environmental monitoring, due to their toxicity and associated risk to the ecosystem, in particular in industrialized countries. Many detection techniques, such as gas chromatography or mass spectroscopy, can be used to monitor the aforementioned gases. However, these traditional techniques are either expensive or time-consuming because of the large equipment and complicated method necessary for the sample preparation[30].

Hence, various materials, covering from Metal Oxide Semiconductors (MOS)[22,29,31] to conducting polymers[32], have been investigated to assemble sensing devices that exploit the different materials properties (*e.g.* optical, calorimetric and acoustic sensing)[22]. Indeed,

according to the diverse types of reaction with the external atmosphere, gas sensors can be classified into chemoresistors, silicon-based Field-Effect Transistors (FET), Capacitance Sensors (CS), Surface Work Function (SWF) change transistors, Surface Acoustic Wave (SAW) change transistors, Optical Fibre Sensors (OFS), and so on[24]. Among them, chemoresistors are the most widely used for practical applications, because of their long-history research, simple structures, convenience to implement and relatively low cost[24]. Nevertheless, there are several limitations of the already commercialized gas sensors: *i*) they are too expensive, *ii*) sensitivity in ppb level is rare, *iii*) selectivity is poor, *iv*) life-time is limited, *v*) repeatability is scarce, *vi*) miniaturization is difficult and *vii*) power consumption is very high, since they usually operate at high temperatures[22]. As a suitable alternative, nanomaterials-based gas sensors have gained significant attention, due to their electrical, optical and thermal properties combined with high surface-to-volume ratio, short response and recovery times, high sensitivity, selectivity, reversibility and stability. Actually, the higher the detection area of the nanomaterials, the greater the adsorption of the gas species, thus leading to an increase of the sensing performances. Up to now, cheap and fast nanomaterials-based gas microsensors have been developed and they are already present on the market (Figure 2.1). However, they suffer from problems associated with long term stability and limited measurement accuracy[24].

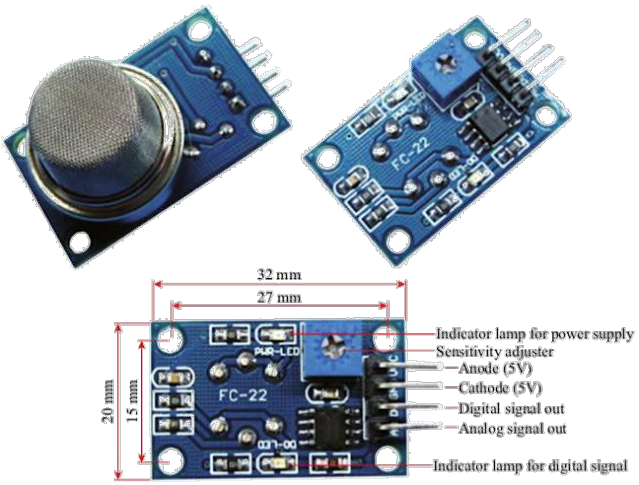

Figure 2.1. *SnO_2–based gas sensor for CO detection, product model: MQ-9. Reproduced with permission[24], Copyright 2015, Tao Wang, Da Huang, Zhi Yang et al., Springer.*

In order to try to overcome the aforementioned drawbacks, graphene and its derivatives like Pristine Graphene (PG), Graphene Oxide (GO) and reduced Graphene Oxide (rGO) have been recently reported to enhance the sensing properties[22,33,34]. Notably, they display several optimal properties, such as high mechanical strength, good thermal stability, ballistic

conductivity, high carrier mobility at room temperature, low electrical noise thanks to the unique 2D honeycomb lattice, as well as large surface area[22,24]. Moreover, 2D materials can screen charge fluctuations (*i.e.* very little signal disturbance) better than one-dimensional ones, like Carbon Nanotubes (CNTs)[24]. Graphene has been also considered as a promising gas sensing material, owing to its electronic properties which are strongly affected by the adsorption of gas molecules. Indeed, according to its discoverers, "graphene has the ultimate sensitivity because in principle it cannot be beaten – you cannot get more sensitive than a single molecule"[22]. Furthermore, it exhibits potential advantages such as low cost, high surface-to-volume ratio and ease of processing[22,24]. The first graphene-based gas sensor was reported in 2007 by Novosëlov's group[35], who showed that the absorbed gas molecules change the local carrier concentration in graphene, resulting in resistance changes. These gas-induced variations can be different in magnitudes according to the target gases, and the sign of the change can indicate whether the gas is an electron acceptor (*e.g.* NO_2, H_2O, iodine, *etc.*) or an electron donor (*e.g.* NH_3, CO, ethanol, *etc.*). Moreover, the interactions between graphene sheets and the adsorbates could vary from weak Van der Waals to strong covalent bonds. Thus, all these interactions change the electronic structure of graphene, which can be readily monitored by suitable electronic methods. However, there are several problems related to the use of this material: *i*) it is not producible in large scale, *ii*) pristine graphene has no functional groups (required for gas/vapour adsorption) and *iii*) it has no band-gap. Therefore, to enhance the sensing performances, doping agents, hybridization, functionalization, *etc.* have been carried out. In this context, Graphene Oxide (GO) and reduced Graphene Oxide (rGO, a form of graphene produced by chemical reduction of graphene oxide), which contain many functional groups and defects, offer a great potential as they are easy and cheap to produce in large scale (around 300 €/kg)[36]. Furthermore, they can be readily functionalized, and the band-gap created and tuned. Researchers have further explored chemical or physical functionalization of graphene with nanomaterials and, in particular, with metal oxides[22,24,37].

On the other hand, as outlined previously, metal oxide nanoparticles (*e.g.* ZnO[25,38,39], SnO_2[27,29,40], WO_3[26], and Cu_2O[22]) have been extensively explored for gas sensing. Nevertheless, these sensors have the disadvantage of high operating temperature, resulting in high power consumption, which in turn adversely affects the long-term stability. Hence, for instance, hybrid-nanostructures composed by graphene-based materials and metal oxides could be particularly interesting, because they may also exhibit additional synergistic properties that are desirable and advantageous for gas sensor applications. One of the major advantages of such composite sensors lies in the exploitation of graphene near-metallic conductivity with a possible inherent-amplified sensing configuration, especially at room temperature when blended with metal oxides, thus enhancing both sensitivity and selectivity.

In addition, while bare graphene, GO and rGO exhibit a p(hole)-dominant conducting properties[41,42], in moisture environments due to the adsorbed water and oxygen molecules, hence decoration of these materials with an n-type metal oxide can lead to the formation of a p–n heterojunction, therefore resulting in performances far better than those of the individual materials[22].

Moreover, the unique heterojunction structure fabricated from several metal oxide materials exhibited outstanding gas sensing properties. For instance, nano-gas sensors composed by p–n heterojunctions can largely overcome the shortcomings of high resistance, high working temperatures and long response/recovery times[43,44]. In a typical p–n junction structure, the conduction and valence bands usually bend and the Fermi levels are equalized forming a depletion layer, which directly influence the conductivity and the acceleration of response and recovery times[44]. In recent years, several studies concerning the formation of binary MOS have been conducted. Notably, Tomer *et al.*[26] reported the successful fabrication of mesoporous WO_3–SnO_2 nanocomposite with superior sensing properties towards Volatile Organic Amines (VOA). Besides, Duhan *et al.*[45] investigated the TiO_2/SnO_2 heterojunction, eventually modified by silver nanoparticles, that shows excellent ethanol response down to 1 ppm. Indeed, due to the higher Fermi level of TiO_2 with respect to SnO_2, they stated the electrons are transferred from titanium to tin dioxide by band bending, thus creating a potential barrier between the heterojunctions. This potential barrier causes a hindrance in the electron transfer through the nanostructures and the electrons present on the sensor surface are more prone to react with the oxygen species present in the atmosphere, increasing the sensor response[45].

Recent studies have also highlighted a new insight into the role played by noble metals nanoparticles (*e.g.* Au[22,46], Ag[47–50] and Pt[27,46]), which are attached to the metal oxide surfaces using various methods, such as Chemical Vapour Deposition (CVD)[46], wet-chemical reduction[47] and γ-ray radiolysis[50]. Indeed, their presence seems to improve the gas sensing performances, both at common high operating temperatures (around 150-300 °C, which are necessary to accelerate either the gas adsorption-desorption kinetics or the carrier mobility) and at less usual room temperature[33,51]. Actually, it is reported that catalytic noble metals nanoparticles can either facilitate the dissociation of gas molecules into more reactive species, thereby enhancing the gas sensitivity, or increase the electronic conductivity thus improving the sensing performances[47].

2.2. Visible-blind UV photodetectors: features and critical aspects

2.2.1. Photodetectors materials and their architecture

A plethora of wide band-gap semiconductors have been explored as promising materials for photodetection applications (Table 2.1), such as chemical and environmental analyses, optical communications, and so on[9,14,52–71]. In this section, several semiconducting materials will be briefly itemized, including ZnO, SnO_2 and TiO_2, along with their architectural networks.

Firstly, low-dimensional materials are reported to have the highest photodetector performances; hence, 0D, 1D and 2D nanostructures have been deeply investigated to this end[7,16,66]. Regarding zero-dimensional materials, Quantum Dots (QDs) have been studied since 1980s, when Ekimov and his co-workers noticed unusual optical spectra from samples of glass containing CdS or CdSe. However, it took more than a decade for the fabrication of QDs colloids, with size-tunable band-edge absorption and emission (Figure 2.2a)[7]. Indeed, QDs are 2-10 nm semiconducting nanocrystals, whose size, energy levels and emission color can be precisely controlled.

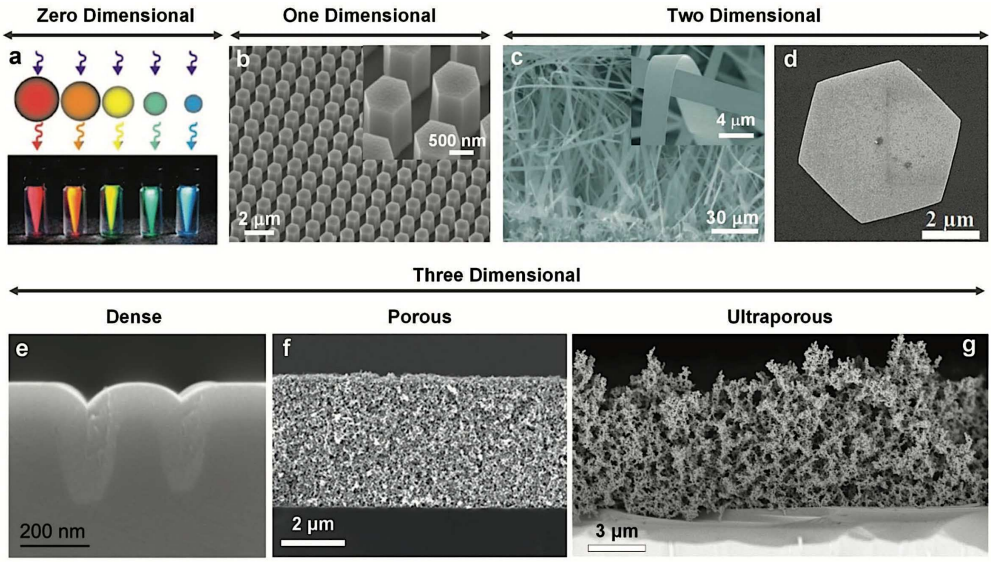

Figure 2.2. *(a) Differently sized colloidal quantum dots, when irradiated with UV light, emit different color light due to quantum-confinement effect. SEM images of (b) regularly patterned hydrothermal ZnO nanorods; (c) belt-like structure by vapor–liquid–solid (VLS) process; and (d) ZnO nanodisk fabricated by drop-casting procedure. Cross-sectional SEM images of (e) dense TiO_2 structure grown using atomic layer deposition technique; (f) porous TiO_2 film prepared by spin-coating; and (g) ultraporous nanoparticles network made by flame spray pyrolysis. Reprinted with permission[7], Copyright 2019, American Chemical Society.*

Owing to their reduced size, they behave differently from bulk solids, as a result of the quantum-confinement effects that impart them unique properties. Specifically, QDs size affects the allowed quantum states for electrons and holes, which in turn determine the energies and therefore the colors of the emitted photons[7].

1D-nanomaterials comprise nanowires and nanorods. The main difference between the two lies in the length-to-diameter ratio. Notably, the former generally have tens of nanometers diameters, with unconfined length scale: they are reported to possess ratios up to 1000. On the contrary, nanorods possess ratios below 10. Similarly, they have diameters between 1 and 500 nm (see Figure 2.2b). Moreover, thanks to their nanoscale dimensions in the radial direction, both nanowires and nanorods show confinement effects, bestowing them novel and promising physical features with respect to bulky compounds. Indeed, because of either their large surface-to-volume ratio or the Debye length comparable to their small size[7], 1D nanonetworks are considered among the likely building blocks for photodetecting applications[7]. The key aspect regarding their fabrication lies in the growth step that has to be controlled at the atomic scale level, in order to define the correct final nanomaterial size. For this purpose, many synthetic approaches have been studied and developed, which include vapor–liquid–solid (VLS) process (Figure 2.2c), chemical vapor deposition (CVD), wet synthesis, and so on[7].

Nevertheless, both QDs and 1D-nanomaterials have some limitations. Particularly, for the former, the electrical performances are limited by the scattering due to the very high number of grain boundaries. In contrast, the surface of one-dimensional compounds is not completely covered, thus lowering their photodetection features[7]. Hence, ultrathin 2D structures can represent an optimal alternative, satisfying the requirements for optimal photodetectors. For instance, ZnO nanodisks, displayed in Figure 2.2d, are reported to show efficient charges separation thanks to the reduction of the disadvantageous grain boundary effects, alongside with an enhanced carriers transportation[7].

2.2.1.1. *SiC photodetectors*

Silicon carbide (SiC), with its wide band-gap value (ca. 2.2-3.0 eV) is one of the most used materials for photodetectors. Indeed, devices made of SiC show large gains, high signal-to-noise ratios, visible-blind responses and an outstanding long-term stability even under high-intensity UV irradiations and high operating temperatures[7]. However, its main drawback is related to the quite high current response time (> 15 s), which limits their applicability in real time signal processing applications[7]. Nanostructured SiC has been reported to possess superior properties with respect to bulk SiC, for applications in light-emitting diodes and UV photodetectors.

Photodetector	Bias	Dark-current	Photocurrent	I_{photo}/I_{dark}	Light intensity	Rise time	Decay time	Responsivity	Detectivity (Jones)	Ref.
ZnO ultraporous nanoparticle networks	0.2 mV	1.32 pA	440 nA	3.3×10^5	86 μW cm^{-2}	≈250 s	≈150 s	14 mA W^{-1}	1.45×10^{15}	[9]
	1 V	24 pA	205 μA	8.6×10^6				6.8 A W^{-1}	3.2×10^{12}	
Hydrogenated ZnO nanoflakes	0 V		1 μA	1000	3000 μW cm^{-2}	23 ms	26 ms	2.65 mA W^{-1}	5.25×10^{10}	[62]
ZnO/SpiroMeOTAD heterojunction	0 V	≈2.5 nA	≈57.5 nA	≈23	1000 μW cm^{-2}	160 ms	200 ms	0.8 mA W^{-1}	4.2×10^9	[65]
Al doped ZnO nanorod arrays	0 V	≈72 μA	≈75 μA	≈1.04	3200 μW cm^{-2}	3.2 s	3.84 s	22.5 mA W^{-1}		[66]
ZnO nanowire/CuSCN	0 V		51 μA cm^{-2}		10^5 μW cm^{-2}			20 mA W^{-1}		[67]
ZnO nanowire/SiO_2	5 V	≈100 μA	≈400 μA	4	1.4 × 10^4 μW cm^{-2}	0.59 s	6.2 s	500 mA W^{-1}		[68]
ZnO@CdS core-shell nanorod arrays	0 V	1.3 nA	3.65 μA	2800	1 mW cm^{-2}	20 ms	40 ms			[69]
ZnO nanorods with Cu nanowire electrodes	-2 V	18.4 μA	669 μA	36.36	400 μW cm^{-2}	0.7 s	1.9 s			[70]
Graphdiyne:ZnO nanocomposites	1 V	1 pA	2 μA	2×10^6	400 μW cm^{-2}	6.1 s	2.1 s	1260 A W^{-1}		[71]
p-Si/n-ZnO heterojunction	-2 V	3 μA	95.8 μA	31.93	3700 μW cm^{-2}	19 μs	22 μs	13 mA W^{-1}	1.4×10^9	[52]
Type-II ZnO/ZnS core shell nanowire arrays	1.5 V	12 μA	51 μA	4.25	1320 μW cm^{-2}			≈65 mA W^{-1}		[53]
ZnO/CdO heterojunction nanofiber arrays	1 V	≈0.2 pA	≈120 nA	6×10^5	6540 μW cm^{-2}			≈1 A W^{-1}		[54]
3C-SiC/ZnO nanowire	2 V	0.68 nA	127.7 nA	187.8	2.6 μW cm^{-2}	40 ms	60 ms	4.8 × 10^5 A W^{-1}		[55]
Nanocave ZnO thin film	1 V	≈0.3 nA	≈1 μA	≈3.3 × 10^5		24 s	15 s			[56]
TiO_2 nanorod arrays	0 V	≈20 nA	≈5 μA	250	1.25 mW cm^{-2}	0.15 s	0.05 s	0.025 A W^{-1}		[57]
TiO_2 nanotube array/monolayer graphene film Schottky junction	-5 V	≈20 μA	150 μA	7.5	100 μW cm^{-2}			15 A W^{-1}		[58]
TiO_2 nanowires	5 V	30 pA	1.62 nA	54	0.54 mW cm^{-2}			6.85 × 10^{-2} mA W^{-1}		[59]
SnO_2 2D (nanonet) film	1 V	89.9 μA	375.2 μA	4.17	0.91 mW cm^{-2}			≈0.07 mA W^{-1}		[60]
SiC thin film	5 V	0.12 μA	45 μA	375	2 mW cm^{-2}	18 s		0.15 A W^{-1}		[14]
Ga_2O_3/SiC thin film	-8 V	1.4 μA	92.81 μA	63.3	70 μW cm^{-2}	8 s	17 s	0.18 A W^{-1}		[61]
GaN nanowires	1 V	43 μA	128 μA	3	0.2 mW cm^{-2}			25 A W^{-1}		[63]
AlGaN (MSM)	10 V	1 fA	10 nA	>10^6	87.4 μW cm^{-2}			0.14 A W^{-1}		[64]

Table 2.1. *Figures of merit of some state-of-the-art low operation voltage photodetectors. Adapted with permission*[9]*, Copyright 2017, American Chemical Society.*

2.2.1.2. *TiO_2 photodetectors*

It is a well-known fact that titanium dioxide is a particularly suitable UV photodetector[7,72], thanks to its transparency, appropriate band gap (3.2 eV for anatase and 3.0 eV for rutile[7,73]), high refractive index[74], and low costs. A recent study reported the fabrication of assembled 1D TiO_2 nanostructure that can be transferred onto different substrates, such as fluorine-doped tin oxide (FTO), Ti foil or flexible polyethylene terephthalate (PET), according to the final application[7]. Nevertheless, notwithstanding a very good sensitivity of these transferable TiO_2 nanorod cloths (TNRCs), they exhibited a low responsivity of about 0.015 A W^{-1}, under light power illumination of 1.25 mW cm^{-2} and a bias of -1 V. Besides, in another study, Zou et al.[7,10] reported a high-performing UV-sensitive photodetectors made of pure electrochemical anodized TiO_2 nanotube arrays, showing fast responses with rise and decay times of only 0.5 and 0.7 s, respectively (Table 2.1). A high responsivity of 13 A W^{-1} was also found under 1.06 mW cm^{-2} UV illumination (λ = 312 nm), at 2.5 V bias. It was hypothesized this high responsivity mainly derives from the internal gain, as a consequence of both oxygen desorption from nanotubes large surfaces and the reduction of the Schottky barrier at TiO_2/Ag contact, upon UV illumination.

2.2.1.3. *SnO_2 photodetectors*

Among the most investigated semiconductors, tin dioxide has been deeply explored due to its wide band-gap (around 3.6 eV), high transparency to visible light and, in addition, its electrical conductivity that is strongly dependent from its surface properties: indeed, surface molecular adsorption/desorption can influence the band modulation and space-charge layer, thus making SnO_2 a very promising and, then, widely exploited gas sensing material[7]. As reviewed by Nasiri *et al.*[7], since tin dioxide with hierarchical structure can possess remarkable high active surface area, 1D nanostructures (*e.g.* nanowires, nanorods, *etc.*) has been largely adopted. For instance, a 2D SnO_2 monolayer nanofilm (Table 2.1), fabricated using an oil–water interfacial self-assembly method, showed a significantly high photocurrent of about 375 µA at 320 nm, with a positive bias of 1 V[60]. On the other hand, the device exhibited low photo-to-dark current ratio of only 4, probably due to a significantly higher dark-current (90 µA)[60]. This high dark current is ascribable to the great number of nanoparticles close one to each other in the 2D SnO_2 monolayer film, which results in higher electrical conductivity. Therefore, the low photo-to-dark current ratio can be attributed to the poor light penetration into the film, limiting the photo-excitation to the very top film layers[7,60]. In a different approach, Lan *et al.*[75] proposed a high-performance UV photodetector combining the SnO_2 semiconductor

with three-dimensional Graphene Nanowalls (GNWs). The as-prepared nanocomposite films show strong absorption in the wide UV region, owing to the presence of the 3D-GNWs network that efficiently suppresses the recombination of the photo-induced electron-hole pairs. This results in a great enhancement of GNWs/SnO_2 photoresponse compared to pure SnO_2 one. Notably, the responsivity of GNWs/SnO_2 photodetector is reported to be 8.6 mA W^{-1} (light power density of 32 mW cm^{-2}) at a bias voltage of 1 V, which is around 8 times higher than that of the reported pristine tin dioxide[75].

2.2.1.4. *ZnO photodetectors*

After SiC, one of the most exploited materials for photodetector applications is ZnO[7,9]. Indeed, with its wide bandgap (ca. 3.37 eV[9,76]) and great exciton binding energy (around 60 meV[7]), zinc oxide represents a very promising candidate for electronic applications, such as surface acoustic wave devices or electrochemical gas sensors[7]. Nasiri *et al.*[7] reported a comparison among different ZnO nanostructured morphologies (*e.g.* single nanowires, nanostructured, and nanowire films), highlighting the responsivity behavior as a function of the dark current values. Notably, for all the different morphologies, the higher responsivity usually results from a higher dark current. Surprisingly, single nanowire devices obtained the highest UV photoresponsivity at considerably low dark currents and this fact may be attributed to the effective surface area considered for the device responsivity. For a single nanowire device, the cross-sectional area is usually considered as effective surface area in responsivity measurements, while the entire outer area of the nanowire is exposed to UV light and may contribute to light absorption[7]. Recently, Chen *et al.*[17] have demonstrated the incorporation of low-dimensional carbon material into ZnO nanowires effectively enhances the separation efficiency of photo-generated electron-hole pairs, providing efficient carrier transport pathways. They stated rGO/ZnO-based photodetector has high photoresponsivity (~16 A W^{-1}), high on/off current ratio (2.81×10^4) and great specific detectivity (1.14×10^{14} Jones), under low UV irradiation (< 10 μW cm^{-2}) and at 1.0 V bias. Moreover, uniform and oriented GO/ZnO nanorods have been obtained thanks to the presence of GO that influences the growth process of ZnO nanorods, giving rise to less light scattering and thereby stronger absorption and enhanced photocurrent. Therefore, when the growth time is 1 h, the optimum photocurrent of GO/ZnO nanorods is about 10 times than pure ZnO nanorods, whereas the detectivity reaches 7.17×10^{11} cm $Hz^{1/2}$ W^{-1}[21]. Very recently, Bo *et al.*[9] proposed a novel hierarchical morphology of zinc oxide nanoparticles made by Flame Spray Pyrolysis (FSP, see Figs. 2.3a,b). This UV photodetector resulted in excellent selectivity, low dark current (nA), and high photocurrent (mA) to low light intensities (ca. 80 μW cm^{-2}).

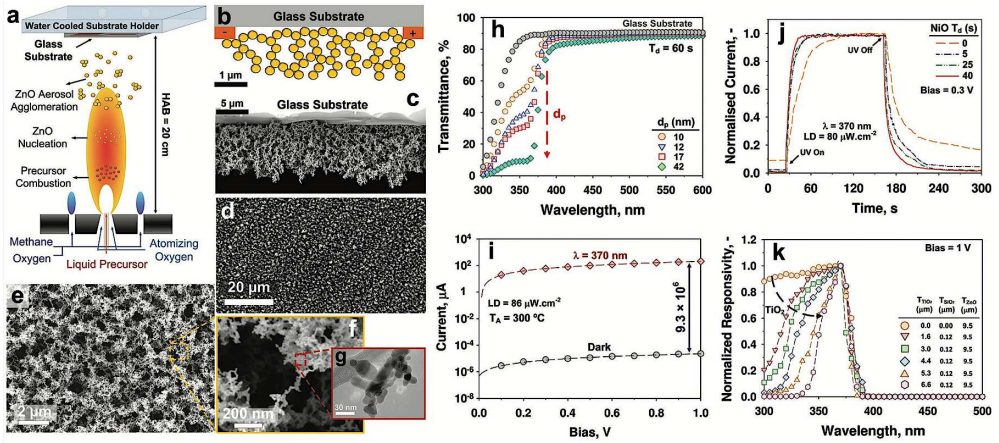

Figure 2.3. *(a) Flame spray pyrolysis set-up and (b) schematics of aerosol self-assembly of (c–g) ZnO ultraporous nanostructured films. (h) Optical transmittance of films with different particle sizes (10−42 nm) fabricated on glass substrates at the same deposition time (60 s). (i) I–V plot of the device after annealing at the optimal temperature of 300 °C. (j) Comparison of the normalized photocurrent dynamics between pure ZnO and NiO/ZnO networks as a function of the NiO sputtering time at 0.3 V. (k) Normalized responsivity signals of the IMONN devices as a function of TiO_2 film thickness. Reprinted with permission*[7]*, Copyright 2019, American Chemical Society.*

The authors demonstrated a rapid, one-pot self-assembly synthesis of transparent ultraporous nanostructured devices composed of crystalline ZnO nanoparticles (Figs. 2.3c–f), resulting in an absorption of more than 80% of the incoming UV light and transmission of more than 90% of the visible light (Fig. 2.3h)[77]. The photo-to-dark current ratio is the highest so far reported at this light intensity (9.3×10^6; Figure 2.3i); whereas, the response dynamics of the fabricated devices is in the range of 100–200 s due to either its ultrahigh porosity or the adsorption and desorption of O_2 trapping states[9]. To overcome this drawback, a 3D coating of a 98% porous film of n-type ZnO nanoparticles has been coupled with p-type NiO nanoclusters, thus forming a nano-heterojunction[78]. Therefore, the formation of p-n type domains enables the rapid separation of the photogenerated electron–hole pairs, largely decreasing the photocurrent rise and decay times (Fig. 2.3j). The NiO coating also increases the overall photodetector properties, such as the responsivities of more than 12 A W^{-1} and ultra-high detectivities of up to 3×10^{12} Jones, at a bias of 1 V and light density of 80 µW cm^{-2}[78]. In another approach, the device layout relied on the 3D integration of ultraporous functional layers of ZnO, SiO_2 and TiO_2 nanoparticles[7]. A band-selective photoresponse was obtained by exploiting the transmittance window between the indirect band-gap of TiO_2 and the sharp-edge of the direct band-gap of ZnO. As a result, these ultraporous Integrated Metal-Oxide Nanoparticle Networks (IMONNs) can efficiently block UVB radiation while transmitting a significant fraction of UVA (Fig. 2.3k)[7]. Hence, these tunable nano-architectures are

compatible with micromachining technologies and they can provide a flexible solution for the engineering of wearable band-selective photodetectors.

2.2.2. Photodetection mechanism

The photoresponse of wide band-gap semiconductors has been reported to be significantly influenced by numerous factors, including the defects concentration, grain size and crystallographic orientation[7]. The proposed mechanism underneath the photodetection process is visually represented in Figure 2.4.

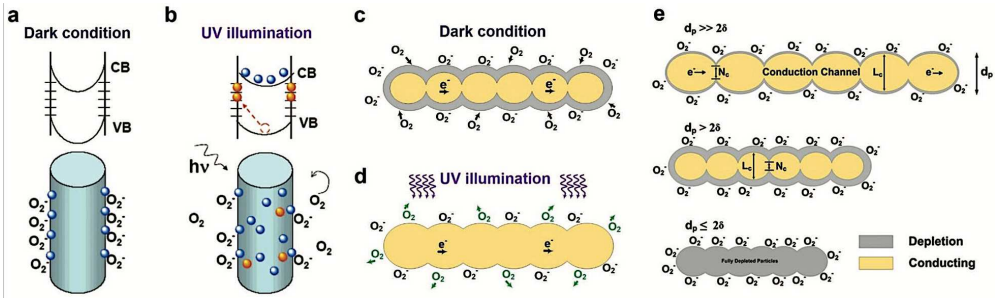

Figure 2.4. *Schematics of (a,b) nanowire- and (c,d) nanoparticle-network photoconductors both under (a,c) dark and (b,d) UV conditions. (e) Photodetection mechanisms expected depending on the ratio between particles diameter (d_p) and the Debye length (δ). Reprinted with permission[7], Copyright 2019, American Chemical Society.*

Considering zinc oxide semiconductor, the very high performances are attributed to oxygen holes-trap states on the material surface, which adsorb atmospheric oxygen molecules provoking a decrease of the electrons density in the n-type semiconductor (Figs. 2.4a,c). The formation of this oxygen-containing species causes the formation of an electron depleted region, very close to the surface, with a consequent band bending that decreases remarkably the device conductance[79]. Notably, the surface band bending induces the generation of an internal electric field, which physically separates the electron and holes, thus slowing down their recombination and prolonging their life-time. This effect is particularly notable in nanocrystalline materials, whose surface area is large and the depletion region is delocalized on the entire film[7]. Upon illumination with photon energy higher or equal to the semiconductor band-gap, electron–hole pairs are photo-generated (Figs. 2.4b,d). For an n-type semiconductor, the electrons in the valence band (VB) are excited to the conduction band (CB) with simultaneous generation of the same number of holes in the VB. The holes that migrate to the surface along the potential gradient produced by band bending can either neutralize the negatively charged adsorbed oxygen ions or get trapped at the semiconductor surface[7]. This leads to an increased number of free carriers and a reduction of the width of the depletion

layer, as shown in Figure 2.4d. Conversely, when the UV illumination is switched off, the photo-accumulated holes recombine with the unpaired electrons, resulting in the gradual readsorption of oxygen molecules with a concomitant current decay.

Moreover, it has been widely stated that photocurrent results depend strongly on the ratio between the Debye length (δ) and the grain particles size (d_p)[7,9,79] (see Figure 2.4e). If d_p is larger than twice the Debye length, then a light-unresponsive conduction channel is formed. This leads to relatively high dark-currents and the UV light does not help so much increase the photocurrent values, it only results in the modulation of the conduction channel width. On the contrary, by decreasing the particles size, higher photoresponses can be achieved, since light-sensitive domains start contributing to the total film conductivity. Hence, two different situations can occur: *i*) $d_p >> 2\delta$, the sensing mechanism is controlled by electron transport at the grain boundary; and *ii*) $d_p > 2\delta$, a significant portion of the bulk participate to light sensing, increasing the photocurrents. In contrast, if $d_p \leq 2\delta$, the whole particle is electron depleted (Figure 2.4e), and this fact leads to highly resistive films with very low dark currents. Therefore, for these ultrafine nanostructures, a conduction channel is created, increasing the electrical conductivity of the entire film alongside with a photocurrent enhancement[7,9,79].

2.2.3. Possible outlooks

The outstanding breakthroughs in wide band-gap semiconductors fabrication have been reached through the development of nanostructured (especially 0D, 1D and 2D) materials that have opened up the way for the development of low-cost UV photodetectors. Indeed, these new devices can operate in severe atmospheres, showing very promising results. Among the widely studied semiconductors, zinc oxide seems to be the material with the highest potentialities, owing to its easiness of fabrication, high transmittance for visible light, and low-cost. However, one of the major issues to solve is still the slowness of the responses. Hence, the current research is focusing the attention on the combination of the aforementioned wide band-gap semiconductors with other materials (such as graphene), in order to achieve superior electrical conduction properties and, eventually, form nano-heterojunctions that could enhance and speed-up the final photoresponses.

2.3. Chemoresistors for gas sensing: a detailed review

As so far stated, the metal oxides-based gas sensors are currently constituting one of the most investigated type of sensing devices[79,80]. Indeed, thanks to their low cost, flexibility in production, simplicity of use, large number of detectable gases/possible application fields, they have attracted great research attention, not only in the scientific world. However, there is still some room for improvement, especially regarding the development of smart ready-to-use devices, showing both high sensitivity and selectivity towards a specific target molecule.

2.3.1. Proposed detection mechanisms in chemoresistors

The knowledge of the mechanism underneath the sensing behavior is mandatory to outline the optimal features a material should possess, that can guarantee a very high sensing response. Besides, understanding the working principles is pivotal to pave the way for the development of novel semiconductors films, with improved sensing capabilities.

Firstly, the class of semiconductor materials has to be divided into two main groups: *p-type* (*e.g.* CuO, In_2O_3) semiconductors, in which holes (h^+) are the majority carriers; and *n-type* (SnO_2, ZnO, WO_3, TiO_2) ones where, conversely, electrons (e^-) are the main charge carriers. For instance, concerning the latter, the conductivity is increased upon contact with a reducing analyte and, *vice versa*, it is decreased with an oxidizing one[79].

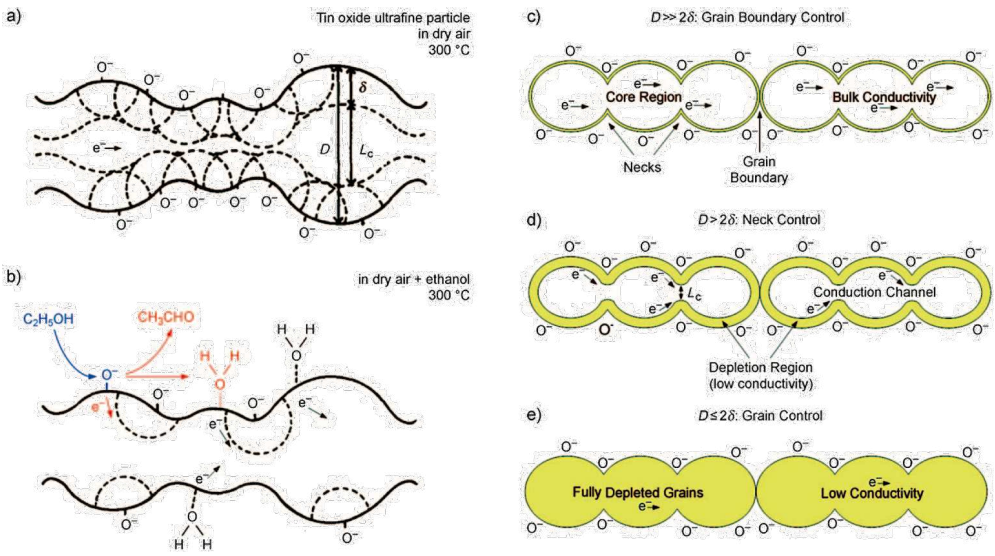

Figure 2.5. *Schematic model of oxygen ionosorption on tin dioxide surface in (a) pure dry air and (b) in presence of ethanol, as the target analyte. (c–e) Similar mechanism already reported for photodetectors (see 2.2.2. Paragraph) Reproduced with permission[79], Copyright 2010, Wiley-VCH.*

Hence, since the present research Thesis will be focused on n-type MOS, only hypotheses about the sensing mechanism by n-type materials will be discussed in the following. Notably, the mechanism previously mentioned for photodetectors lay the groundwork for the MOS gas sensing behavior, as clearly displayed in Figure 2.5. Herein, tin dioxide compound was chosen as representative n-type MOS. According to Tricoli *et al.*[79], two general approaches can be described: *i*) the *oxygen-vacancy* model (reduction–reoxidation mechanism) and *ii*) the *ionosorption* model. However, authors underline that neither the former nor the latter can describe all the experimental observations[79].

As the name implies, the oxygen-vacancy model contemplates the partial reduction and reoxidation of the MOS surface. Specifically, considering an n-type semiconductor, which is rich in oxygen vacancies acting as electron donors, its partial reduction, by interacting with a reducing analyte (*e.g.* ethanol), causes the formation of other oxygen vacancies and consequently an injection of electrons in the MOS CB, thereby increasing the conductivity. Once the analyte is oxidized, it leaves the semiconductor surface, thus reoxidizing it if oxygen, that fills the vacancies, is present in the atmosphere over the material surface. The following reactions (considering, for simplicity, CO as the reducing gas) summarize the previous discussion:

(2.3.1.a) $CO_{(g)} + O_o^X \rightleftharpoons CO_{2(g)} + v_o^X$

(2.3.1.b) $v_o^X \rightleftharpoons v_o^\bullet + e^-$

(2.3.1.c) $2v_o^\bullet + O_{2(g)} + 2e^- \rightleftharpoons 2O_o^X$

where v_o^X is neutral oxygen vacancy, $v_o^\bullet$ is single ionized oxygen vacancy and O_o^X is neutral lattice oxygen[79]. An opposite mechanism is, then, believed in the case of oxidizing analytes, such as NO_x. However, the vacancies diffusion in the MOS bulk is strongly affected by either the material itself or the operating temperature.

In the ionosorption model (Figures 2.5c–e), instead, the sensing mechanism is subdivided into two functions: the reception and the transduction one[79,81]. This mechanism is quite close to the one already reported (Figure 2.4) for photodection processes. As shown in Figure 2a, the adsorbed oxygen species can be considered as free oxygen ions electrostatically stabilized on the MOS surface. The first step implies a physisorption mechanism that turns into ionosorption upon electrons transfer from the semiconductor to the oxygen species themselves. Hence, several negatively charged species are formed, such as O_2^-, O^- and O^{2-}. Zheng *et al.*[82] reported that, in general, below 150 °C the O_2^- molecular form dominates; whereas, above this temperature, the other two atomic species prevail[83]. The chemisorption of these oxygen-containing ions causes the formation of a depleted region, characterized by

reduced electron mobility near the oxide surface (Figure 2.5a). Hence, in the presence of a reducing gas (Figure 2.5b), the oxygen ions concentration on MOS surface is decreased, due to the reaction with the target analyte and, thus, the generated electrons are released back to the semiconductor surface. The following reaction, relative to ethanol molecules, sum up the mechanism just described:

(2.3.1.d) $C_2H_5OH_{(g)} + O_{ad}^- \rightleftharpoons CH_3CHO_{(g)} + H_2O(g) + e^-$

Notably, here the first step of the ethanol oxidation process has been reported. Generally, it is believed the complete reaction to carbon dioxide can occur[84]. As previously highlighted, in the case of oxidizing analytes the concentration of ionosorbed oxygen is increased, therefore recording a reduction of the final conductivity. Besides, as mentioned in 2.2.2. Paragraph ("Photodetection mechanism"), the mechanism controlling both the conductivity change and its magnitude is mainly controlled by the ratio between the grain size (d_p or D, in Figs. 2.5c–e) and the Debye length (δ)[7,79,81]. Three different situations can occur: *i*) if D >> 2δ, the depletion of the surface between the grain boundaries controls the conductivity variation. In this case low sensitivity is expected, since a small part of the semiconductor is affected by interaction with the analyte. *ii*) If D > 2δ, a conduction channel with high conductivity exists but its width (L_c, in Figure 2.5d) is controlled by the surface concentration of oxygen ions (neck control), leading to moderate sensitivities. *iii*) If D ≤ 2δ, the whole grain is depleted and changes in the surface oxygen concentration affects the whole semiconductor (grain control), resulting in an enhancement of the final sensitivity.

2.3.1.1. *The role of light activation*

Owing to the recent development of wearable gas sensors, especially for health monitoring, the necessity of fabricating flexible, transparent and, above all, RT working devices is a current issue. Hence, along with the MOS surface modification with doping agents or their coupling with other materials, light activation can represent an optimal alternative to thermal one[85]. Huang *et al.*[20] have recently reported UV-enhanced ethanol sensing properties of RF magnetron sputtered zinc oxide film in terms of high sensitivity, excellent selectivity, rapid response/recovery and low detection limit (down to 0.1 ppm, see Fig. 2.6).

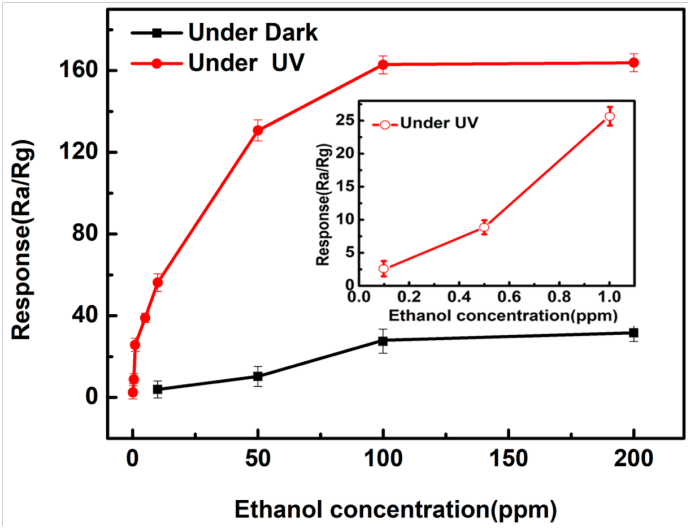

Figure 2.6. *Ethanol sensing by RF magnetron sputtered ZnO films in dark conditions (black series) and upon UV irradiation (red series). Reproduced with permission*[20]*, Copyright 2017, MDPI (open access).*

According to literature data[82,86], the light-controlling sensing mechanism can be described as follows, starting from the aforementioned ionosorption model. When MOS nanoparticles are exposed to air (in the dark), the adsorbed oxygen molecules withdraw electrons from the conduction band, thus forming O_2^- species. This leads to a low-conductivity depletion region on the surface and to narrow the MOS conduction channel. Due to the large adsorption energy, the oxygen ions (O_2^-) are thermally stable and difficult to be removed from the metal oxide surface, at room temperature. In this way, the gas sensing response is very scarce (Fig. 2.6, black data). When the device is irradiated with an appropriate wavelength, the photo-induced electron-hole pairs will be generated, due to the greater photon energy with respect to the MOS band gap. Then, some of the photo-generated holes will desorb the adsorbed oxygen ions, according to the following reactions:

(2.3.1.1.a) $O_2^- + h^+ \rightarrow O_2$

resulting in either a reduction of the depletion layer width or in the subsequent increase of the free carriers concentration. This provokes a drastic rise in photocurrents. Besides, the ambient oxygen molecules, reacting with the photo-generated electrons, give rise to new photo-induced chemisorbed oxygen molecules, following the reaction:

(2.3.1.1.b) $O_2 + e^-_{(hv).} \rightarrow O_2^-{}_{(hv)}$

These photo-generated oxygen ions are reported to be weakly bound to MOS surface, thus being easily removed[82]. Hence, upon exposure to ethanol gas, these additional adsorbed oxygen molecules will react with ethanol ones:

(2.3.1.1.c) $C_2H_5OH + 3O_2^-{}_{(hv)} \rightarrow 2CO_2 + 3H_2O + 3e^-$

This reaction releases electrons back to the conduction band of MOS, decreasing the surface depletion layer width and, then, increasing the electrical conductivity of the device. As the carrier density under UV light is greater than that in the dark, a larger amount of photo-induced highly reactive oxygen ions is registered, which are responsible for the room-temperature gas sensing.

2.3.2. Influence of both MOS features and their synthesis on gas sensing

As it has just been touched on, when a reducing gas like CO or H_2 comes across the sensor surface (Fig. 2.7), it changes the density of the ionosorbed oxygen species, which in turn varies the device conductivity. As a consequence, this sensing mechanism is strictly connected to the MOS features, such as the crystallites size, the nanoparticles morphology, MOS film thickness and porosity, surface properties, and so on.

In Figure 2.7, the pivotal characteristics which influence the sensing performances are schematically displayed. Once again, the fundamental role played by the grain size (D) is underlined in Figure 2.7a: if $D \leq 2\delta$, an improvement of the sensor performances is recorded. Since SnO_2 has a Debye length of about 3 nm[87–89], increasing too much the crystallite size has a damaging effect towards the sensing of the reducing species. Furthermore, as it will be deeply described in the following, in order to enhance the response intensity, the doping/decoration of MOS with non-metal or metal nanoparticles, along with their coupling with other MOS can be a key answer. Indeed, as shown in Figure 2.7b, by increasing the Si-content in SnO_2 or WO_3 lattice, a specific and different response can be obtained. Parallelly, a major parameter to consider is the operating temperature (OT). Generally, the usual OT for MOS-gas sensors is from 200 to 500 °C[3,90,91]. Notably, in order to avoid changes in the material itself, MOS should work at temperatures low enough to prevent significant bulk modifications, and high enough to guarantee the occurrence of gas reactions, within a reasonable response time. Hence, the efficacy of the catalytic reactions is strongly influenced by the OT (Fig. 2.7c,d). Indeed, as reported in Figures 2.7c,d, the maximum catalytic activity corresponds to the maximum sensor response, at different temperatures depending on the tailored Pd-doped MOS: specifically, a shift towards lower operating temperatures is obtained together with an increase in the sensor response at a suitable additive content.

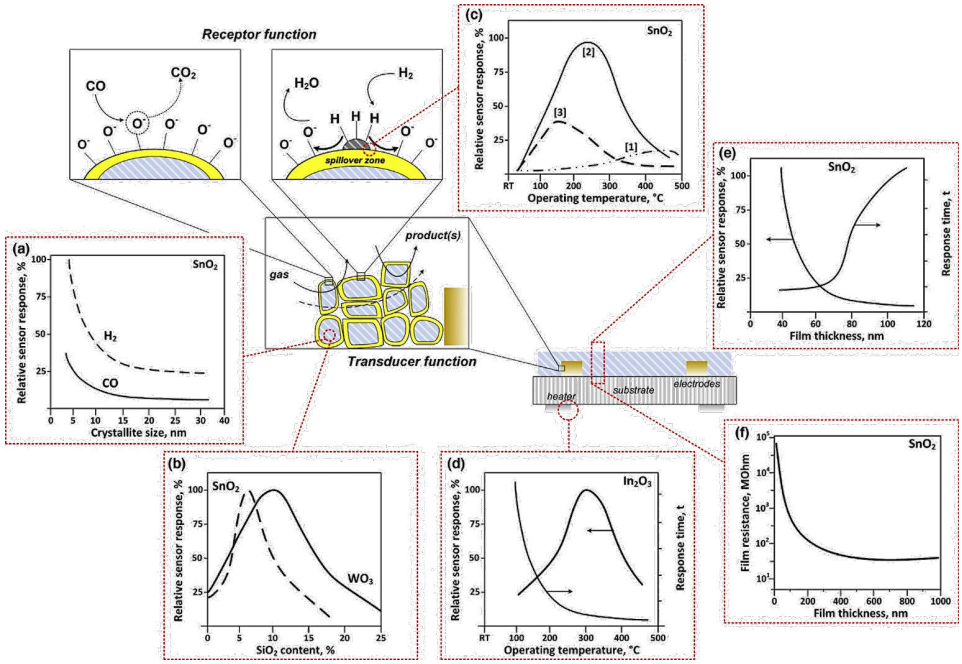

Figure 2.7. *Schematics of receptor and transducer functions relative to MOS ionosorption mechanism. Indexing of the most fundamental parameters influencing sensor performances: (a) SnO_2 response as a function of crystallites size; (b) comparison between SnO_2 and WO_3 responses by varying the Si-content; (c) influence of Pd nanoparticles (at 0 [1], 0.12 [2] and 1.10 [3] %wt) on SnO_2 gas sensor response; (d) effect of the operating temperature on In_2O_3 sensor performance and on its response time. Influence of SnO_2 film thickness on both (e) intensity and response time; and (f) SnO_2 film resistance. Reproduced with permission*[81]*, Copyright 2015, Elsevier.*

Besides, an excessive Pd loading increase leads to a reduction in the sensor response attributed to a catalytic conversion without electron transfer[81]. In addition, another parameter influencing the sensing behavior is the MOS film thickness. Figures 2.7e and f display the SnO_2 sensor response with the rising of the layer thickness. Notably, by reducing it from 600 to 50 nm, a five-time higher response was obtained: this is ascribable to a deeper penetration of the analyte into the sensing film[81]. However, as reported in Figure 2.7f, if the layer is too thin, its resistance increases dramatically. Hence, the optimization of all these parameters is essential to enhance the sensing devices performances, overcoming the current issues, such as the high operating temperatures, the scarce selectivity and the influence of interfering species, such as the atmospheric humidity (see in the following).

2.3.2.1. *MOS morphology and films features*

As well as for photodetectors, the performances of gas sensing materials are strictly connected to their structural/morphological/surface properties. Moreover, the

aforementioned mechanism, based on chemi- and physisorbed oxygen species (*i.e.* ionosorption model), implies a very large active surface area of the material. In this scenario, nanomaterials can certainly improve the sensitivity[81]. Besides, during MOS synthesis, either the size or the morphology can be tuned in order to fabricate spherical particles, rods or wires, showing peculiar features. Indeed, spheres have lower surface-to-volume (SV) ratio with respect to 1D or 2D geometries, as rods and plates respectively. Hence, many efforts have been made to tailor the nanoparticles synthesis in order to increase their surface-to-volume ratio[81]. 1D nanostructures have high surface-to-volume ratio along with unique electro-conductive properties. Depending on the aspect ratio, they can be divided into: nanorods, nanotubes, nanobelts, and nanowires/nanofibers[81]. Notably, a major advantage of nanobelts is their lack of crystallographic defects due to their rectangular shape, promoting ideal sensing[81]. Figure 2.8 shows the response of WO_3 nanoparticles towards H_2S, in comparison with 2D platelet-like and 1D wire-particles, respectively[81]. By keeping constant the operating temperature, the response intensity obtained with WO_3 nanowires is definitely higher than the nanoplatelets and nanoparticles ones. This increase is believed to be due to the greater surface-to-volume ratio of nanowires, which favors a larger adsorption of the analyte gas molecules. Furthermore, decreasing the aspect ratio while maintaining rectangular cross-section leads to 2D structures, like nanoplatelets. For instance, gas sensors made of ZnO nanosheets of about 10–20 nm thickness detect selectively acetone and gasoline at 360 and 180 °C, respectively[81].

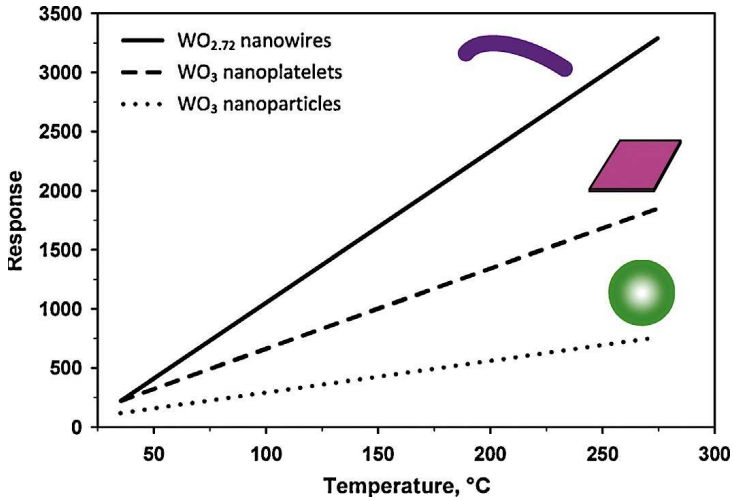

Figure 2.8. *Comparison of WO_3 sensor response to 1000 ppm of H_2S for different nanostructures, as a function of temperature. Reproduced with permission[81], Copyright 2015, Elsevier.*

Besides, thin-walled WO_3 hemitubes, fabricated through a polymeric fiber template-based synthesis, exhibit very high H_2S selectivity, at high (85%) relative humidity mandatory for

breath analysis applications[81]. Recent efforts have been made to prepare films of hollow multi-layered porous spheres, that can maximize the mass transfer throughout the bulk, preserving a high SV ratio[81]. Li *et al*.[39] reported enhanced results relative to the ethanol sensing by a novel hollow ZnO-SnO_2 structure. Particularly, this core-shell layout improves the response intensity and shortens the response/recovery times. Recently, even more complex structures have been prepared to obtain high-performing sensors such as urchin, flowers and cubes[92].

Regardless of the mechanism underneath materials sensing behavior, the interaction between MOS surface and the reducing/oxidizing analyte strictly depends on the film morphology. According to Tricoli *et al*.[79], sensing films can be subdivided into *dense* (compact) and *porous* ones. Notably, for the former, the gas interactions take place only at the geometric MOS surface, without being able to penetrate inside the material layer. Conversely, in porous films, the gaseous molecules can go through, interacting with the single grains. However, this distinction is too simplistic to describe all the feasible morphologies; indeed, several synthetic methodologies can produce films with a certain degree of porosity, without achieving a complete homogeneity in terms of crystal properties throughout the entire film. Thus, either dense or porous regions can co-exist in the same sample. Hence, a new class of MOS film has been introduced, *i.e.* the *particulate* sensing films, which is obtained by depositing solid nanoparticles, under moderate sintering temperatures. Going in detail, dense layers are not so used in gas sensing applications, since the number of active sites, available for the interaction with the gaseous analytes, are scarce. On the contrary, porous films are the most common for gas sensing. They can be fabricated by means of several techniques (such as spray pyrolysis, pulsed laser deposition, *etc.*), even if it is often very difficult to control the grains morphology and size during deposition or post-deposition annealing. Therefore, the result is a porous film containing multi- and mono-crystalline grains. In-between, particulate films, consisting of nanoparticle-network bridging the two electrodes, is usually found. The main advantage of this type of configuration with respect to dense films, is that it is not necessary to decrease the film thickness down to the MOS Debye length to reach high sensitivities. Notably, since the interactions with the gases take place on each grain, all the sensing material can participate to the detection. Such films are usually obtained by wet-deposition of pre-synthesized particles or by aerosol methods (such as FSP)[79].

Hence, an essential parameter that should be considered when fabricating a sensing film is its thickness. For dense layers, the thicker the film, the worse the response. Conversely, for porous and particulate films, two effects are expected by growing the thickness: a rise of the available active sites and a decrease of the gas permeation depth through the film. Nevertheless, these two consequences are strictly correlated with the MOS features, porosity

and also analyte composition/features; therefore, an optimization of the film thickness is always necessary to maximize the sensor response.

2.3.2.2. *Synthetic routes for MOS fabrication*

In order to produce films with controlled thickness and tailored morphology, the most suitable MOS synthetic route should be considered. Typically, two main fabrication ways can be pursued: dry and wet routes, which are reported to produce thin and thick layers, respectively[79]. Notably, regarding the former, MOS films are synthesized and deposited in a one-step process; whereas, wet routes contemplate several stages, comprising solvent evaporation and annealing processes, that require quite a long time[79] (Fig. 2.9). Going into detail, by means of dry methods, porous or nearly dense films with thicknesses lower than 1 mm are rapidly obtained. Conversely, sensing layers made by wet methods often show particulate morphology, despite it is possible to attain a certain degree of porosity even after calcination steps at elevated temperatures (*i.e.* high sintering degree). Besides, they are classified as thick-film sensors, since it is difficult to decrease the thickness below 1 mm, preserving the surface homogeneity.

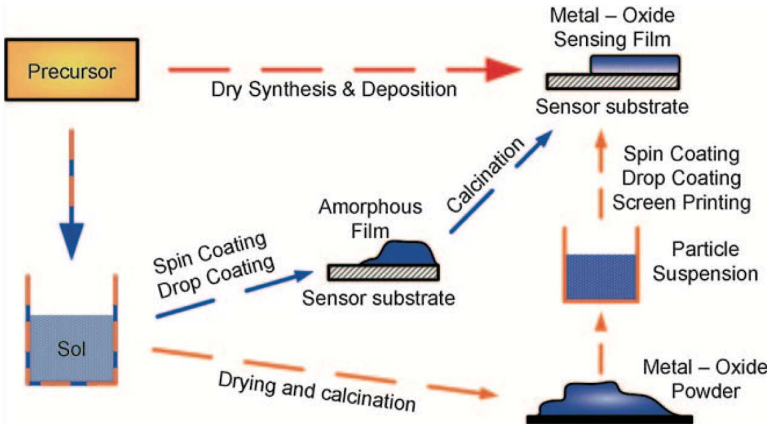

Figure 2.9. *Schemes of MOS dry (top red arrow) and wet (orange and blue arrows) synthetic pathways. Reproduced with permission[79], Copyright 2010, Wiley-VCH.*

Although particulate films show high sensing response, wet routes have some drawbacks, such as the limited control over layers porosity and thickness. Moreover, the reproducibility of these films is poor because of cracks formation, consequent to solvent evaporation.

Figure 2.10 displays some of the most used methods to fabricate gas sensing layers[79].

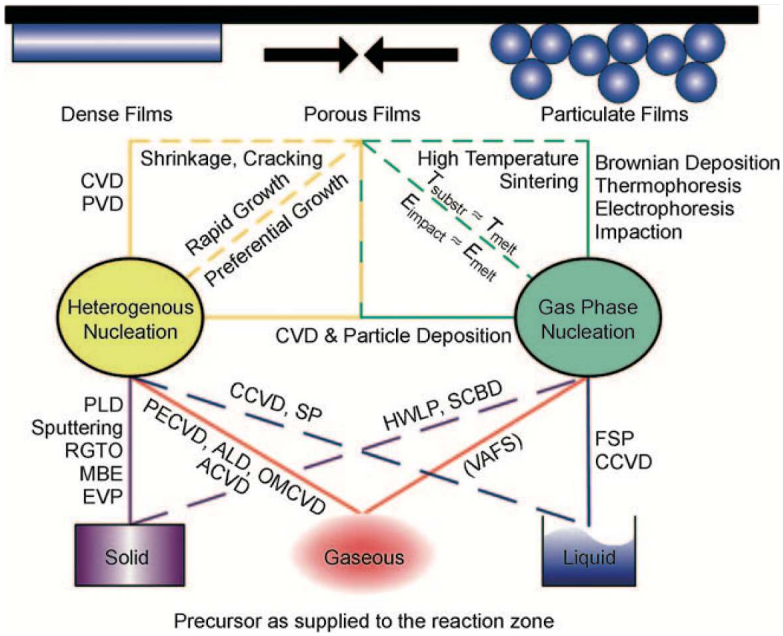

Figure 2.10. *Typical methods and pathways for the fabrication of dense, porous or particulate films. The vapor-fed aerosol flame synthesis (VAFS) method is uncommon for semiconductor gas sensors. Methods displayed: chemical vapor deposition (CVD), physical vapor deposition (PVD), pulsed layer deposition (PLD), rheotaxial growth and thermal oxidation (RGTO), molecular beam epitaxy (MBE), evaporation (EVP), combustion assisted chemical vapor deposition (CCVD), spray pyrolysis (SP), plasma enhanced chemical vapor deposition (PECVD), atomic layer deposition (ALD), organometallic chemical vapor deposition (OMCVD), atmospheric chemical vapor deposition (ACVD), hot wall aerosol reactor and low-pressure impactor (HWLP), supersonic cluster beam deposition (SCBD), flame spray pyrolysis (FSP). Reproduced with permission[79], Copyright 2010, Wiley-VCH.*

A first distinction can be made according to the nucleation step (Figure 2.10), which is subdivided into: heterogeneous (left side) and homogeneous (gas phase nucleation, right side) ones. Particularly, the former is mandatory for the synthesis of dense films, achieved through methods as sputtering or spray pyrolysis. The average porosity of such films is controlled by several parameters, *i.e.* pressure, substrate temperature, precursors feed rate. However, it is difficult to obtain homogeneous films with these techniques, hence a distribution of particulate regions in dense films is common. On the contrary, homogeneous nucleation in the gas phase leads to particle formation and growth. These particles can be deposited directly from the aerosol by Brownian deposition, thermophoresis or electrophoresis. With respect to the sensing properties, such films can be classified as particulate and, if sufficiently small particles are deposited, produce highly sensitive sensors[79]. Furthermore, post-annealing treatments of these particulate films cause sintering and grains growth, limiting the films porosity.

Particularly, chemical vapor deposition (CVD) is a robust tool to obtain dense or porous nanostructured films[79]. Generally, it is based on the direct synthesis of MOS on the substrate by providing the gaseous precursor straight onto the target region. Therefore, a minimum substrate temperature (ca. 100-200 °C) is required for the complete reaction. However, CVD-made sensing films has shown poor sensor responses, thus resulting in a less-performing method to produce MOS-based sensors[79]. This is reported to be due to the formation of multi-crystalline domains, with insufficiently depleted grains.

Alongside with CVD, spray pyrolysis (SP) has been widely exploited since the grain shape can be easily controlled by tailoring the deposition temperature and the film thickness. Notably, the substrate temperature has a pivotal role as it influences droplets vaporization, precursors oxidation, particles sintering and crystal growth[79]. Nevertheless, its main drawback is the poor penetration of gaseous analyte molecules into the sensing film[79]. Besides, a step forward with respect to the original aerosol methods has been achieved with flame spray pyrolysis (FSP) in which the temperature gradient between the hot flame fumes and a cooled substrate is used to increase the deposition rate by thermophoresis at atmospheric pressure. The as-deposited FSP-made films are highly porous (*e.g.* > 95%) and consist of fractal nanoparticles network, showing an average grain and crystal sizes of approximately 10 nm[79]. Thus, a nearly perfect particulate film can be obtained. In this way, the penetration of the analyte into the film is allowed, along with the depletion of all the grain surfaces.

Besides, the sputtering technique is another methodology widely exploited for the preparation of porous to nearly dense films, characterized by specific crystal plane orientations[79]. With this technique, it is possible to keep the target substrate at room temperature; however, there are two main shortcomings. Firstly, the necessity to operate at low pressure and, secondly, the scarce crystallinity when operating at low substrate temperatures. Hence, post-annealing treatments are mandatory to obtain fully crystalline materials. Besides, both radio frequency (RF) and direct current (DC) sputtering can be used, obtaining different performances according to the film porosity[79].

2.3.3. Metal oxide n-type semiconductors

Among the metal oxide semiconductors, SnO_2 and ZnO are the most extensively studied materials for chemoresistive gas sensors[51]. Other MOS such as titanium oxide (TiO_2), tungsten oxide (WO_3), iron oxide (Fe_2O_3) and indium oxide (In_2O_3) have also attracted much research attention (see Table 2.2). All these materials are n-type semiconductors, however several publications on p-type MOS (such as CuO, Co_3O_4, Cr_2O_3, NiO and TeO_2) are present in the literature[51].

Material	Operating temperature (°C)	VOC	Signal response, ($R_{air}/R_{analyte}$)-1[b]	LOD[a] (ppb)	Ref.
Hollow SnO_2	300	EtOH	28.2 (100 ppm)[c]	5000	[93]
rGO-SnO_2	300	EtOH	42.0 (100 ppm)[c]	5000	[93]
		Acetone	11.0 (100 ppm)[c]	–	[93]
0.1 wt% GO/SnO_2 nanocomposite	250	EtOH	22.5 (50 ppm)	1000	[94]
SnO_2 hollow spheres	200	Acetone	15.0 (50 ppm)[c]	5000	[95]
Rh-doped SnO_2 nanofibers	200	Acetone	59.6 (50 ppm)[c]	1000	[87]
3% CuO/SnO_2	280	EtBz	7.0 (50 ppm)[c]	2000 of BTEX	[96]
Co-doped ZnO branched nanorods	RT	Acetaldehyde	799 (10 ppm)[c]	10000	[97]
Hollow ZnO-SnO_2 nanofibers	200	Ethanol	~380 (100 ppm)[c]	5000	[39]
ZnO nanowires	300	Toluene	0.8 (0.1 ppm)[c]	100	[27]
SnO_2−ZnO nanowires (shell thickness = 50 nm)	300	Toluene	72 (0.1 ppm)[c]	100	[27]
Pt-functionalized SnO_2−ZnO nanowires (shell thickness = 80 nm)	300	Toluene	278 (0.1 ppm)[c]	100	[27]
ZnO-NiO nanoheterojunctions	RT	Ethanol	1.6[c]	10	[78]
Nanocoaxial p-Co_3O_4/n-ZnO heterojunction	260	Ethanol	38 (100 ppm)[c]	NA	[98]
GO-SnO_2-TiO_2	200	Acetone	~59 (5 ppm)[c]	250	[99]

[a] LOD, limit of detection; [b] always referred to 1 ppm, otherwise stated; [c] calculated from data reported in the reference.

Table 2.2. *Comparison of some recent literature data about n-type MOS or heterojunctions-based nanomaterials for the sensing of common VOCs.*

Notably, by both tailoring the nanoparticles morphology (*e.g.* hollow structure, nanowires, *etc.*) and combining/doping different semiconductors (*e.g.* CuO-SnO_2, GO-SnO_2, SnO_2-ZnO and Rh-SnO_2), peculiar sensing performances can be obtained, resulting in diverse optimal operating temperatures, LOD and signal intensity (as reported in Table 2.2).

2.3.3.1. *ZnO-based gas sensors*

Zinc oxide is a typical n-type semiconductor, which exhibits wide band-gap (3.37 eV), high electron mobility, high photocurrents, optimal chemical and thermal stability, and it is low

cost and non-toxic[85]. Conventionally, ZnO sensing performances are strictly correlated to its operating temperature, since it controls reactions kinetics, conductivity and electron mobility. Indeed, ZnO-based devices usually work at high temperatures (300-500 °C) in order to overcome the activation energy barrier for the surface redox reactions, responsible of the sensing behavior[85]. However, these high temperatures represent a limitation for ZnO usage, since they signify high energy consumption and poor long-term stability, along with the limitation to be used in portable devices. Hence, the urgent task is to reduce the operating temperatures.

At room temperature, a small amount of thermal electrons could be found on ZnO surface, forming few adsorbed oxygen species[85]. This very limited number of oxygen-containing compounds is thermally stable and difficult to be removed from the surface, due to the large adsorption energy, thus resulting in scarce sensing performances. Beyond these, relative humidity (RH) is one of the predominant interfering species of room-temperature sensing. Notably, in wet atmosphere, H_2O molecules compete for the surface reaction sites with oxygen molecules and, in-turn, limit the oxygen adsorption.

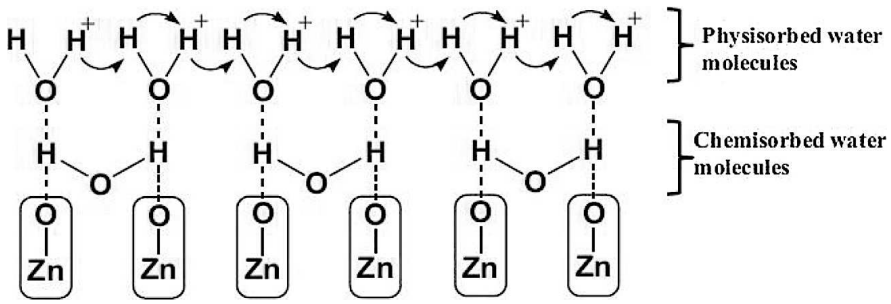

Figure 2.11. *Schematic representation of humidity sensing by ZnO semiconductor. Reproduced with permission*[85]*, Copyright 2017, Elsevier.*

As a consequence, the number of oxygen species will decrease with the increase of RH level, causing a decline of the baseline resistance with lower sensor response. Therefore, at lower level of RH, the charge carrier transport might be attributed to chemisorbed molecules; whereas, at higher RH, physisorption characterized by Grotthuss mechanism prevails (Fig. 2.11)[85]. Hence, the influence of RH should be taken into account while investigating room-temperature MOS gas sensors.

For instance, Guo[92] reported the successful synthesis of scroll-like, lung lobe-like, flower-like and sphere-like ZnO nanoparticles with different gas sensing performances according to their morphology. Figure 2.12 displays a comparison among the obtained sensors responses towards 10 ppm of ethanol molecules, operating at high temperatures (*i.e.* 300 °C). Clearly, the

most performing morphology seems to be the sphere-like one (Fig. 2.12d), and such enhancement has been attributed to its unique hierarchical structure, that has the largest specific surface area, thus promoting the adsorption of target gas[92].

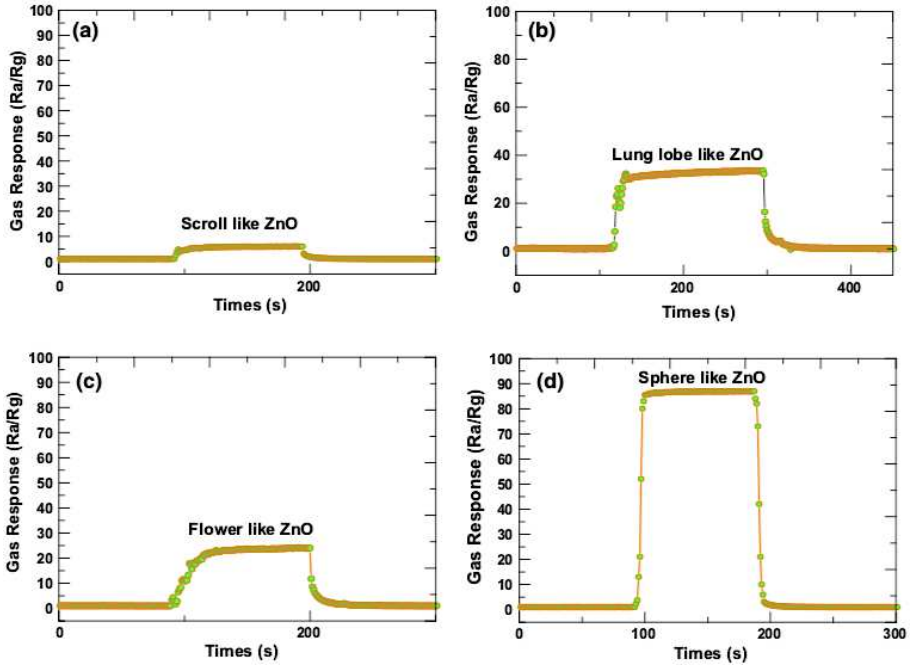

Figure 2.12. *Signals intensities and response/recovery times of the gas sensors made of ZnO with different morphologies. Measurements were conducted at working temperature of 300 °C under the ethanol concentration of 10 ppm. Reproduced with permission*[92]*, Copyright 2016, Springer.*

The previous outcomes have been further corroborated by Wang *et al.*[100] who fabricated ZnO spheres composed by flakes with high-density pores, having dimensions of tens of nanometers. These porous spheres showed both a very high response and great selectivity towards ethanol molecules (among ethanol, methanol, methanol and acetone) at 280 °C. Moreover, the signal is reproducible even after 15 weeks, thus underlining the sensor robustness. Besides, in order to decrease the operating temperature, Zhang *et al.*[101] demonstrated that the decoration of zinc oxide matrix with palladium nanoparticles can improve the VOC sensing. Indeed, compared to pristine ZnO NPs, 1 wt% Pd@ZnO has a twofold improvement in the sensing properties, at lower operating temperatures (340 *vs* 370 °C) towards acetone species. In addition, a further help for the room temperature sensing is represented by the light exploitation (see 2.3.1.1. Paragraph). Hence, Wongrat *et al.*[84] combined the ZnO decoration with gold NPs by sputtering technique (Fig. 2.13a), with the use

of UV illumination. Keeping the operating temperatures in the range 25–125 °C, it was found the sensor response was remarkably enhanced (Fig. 2.13b).

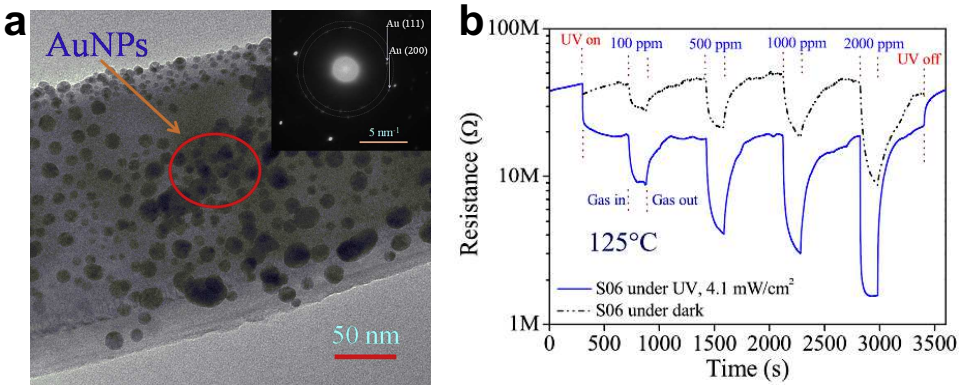

Figure 2.13. *(a) TEM image and selected area electron diffraction patterns (SAED, in the inset) of AuNPs adsorbed onto ZnO nanostructure surface at the sputtering time of 6 s. (b) Resistance trend upon exposure to ethanol vapor with various gas concentrations under dark condition and UV illumination intensity of 4.1 mW cm^{-2} (λ = 254 nm). Adapted and reproduced with permission[84], Copyright 2016, Elsevier.*

Then, it was reported the AuNPs added onto ZnO nanostructure strongly affect the oxygen adsorption reactions, resulting in a larger depletion layer width. Subsequently, the sensor response is enhanced with respect to pure ZnO one. Besides, the response enhancement, due to UV illumination, is explained by the formation of weakly bound oxygen ions thanks to the excitation of electrons from the MOS valence band to its conduction band. This produces a thinner depletion layer, characterized by weakly bound oxygen ions, which are easily removed from the ZnO surface resulting in high sensor responses[84].

2.3.3.2. *SnO_2-based gas sensors*

Tin dioxide is one of the most common metal oxide for gas sensing[96,102–104]. It is highly sensitive to many inorganic and organic gaseous compounds[50,96,105], but the scientific research about the improvement of its selectivity is still in its infancy[94,99,106]. Notably, many efforts have been made to overcome this shortcoming, for example by varying the crystal structure or morphology[99], by adding dopants[91] or by changing the operating temperature[107]. Furthermore, it is reported the application of SnO_2 for breath analysis is limited by its cross-sensitivity to humidity (*i.e.* the major component of the human breath)[81]. Besides, a further challenge is its scarce stability, typical of nano-sized MOS that usually operate at high temperatures. Indeed, this relatively poor stability may cause a drift of the baseline resistance and, hence, of the sensor response. A common solution to this problem is both the doping of

SnO_2 matrix with noble metal ions (such as silver[47] or gold[108] cations) and the coupling with other metal oxides (*e.g.* TiO_2[43,99]), due to the combined opportunities provided by these compounds. Moreover, 1D-SnO_2 nanostructures such as nanowires (Figs. 2.14a,b), nanorods and nanotubes have shown enhanced sensitivity and selectivity, particularly at lower temperatures (Figure 2.14)[51].

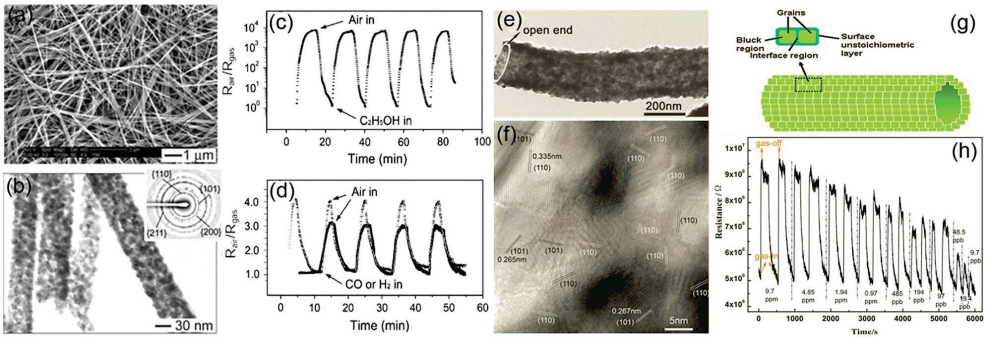

Figure 2.14. *(a) SEM and (b) TEM images of SnO_2 nanowires. Sensor response of SnO_2 nanowires to (c) 6% ethanol vapor and (d) 20 ppm CO (dashed line) and 500 ppm H_2 (solid line). (e,f) TEM images of SnO_2 nanotubes. (g) Schematic of the intergrain junctions in SnO_2 nanotubes. (h) Response curves of SnO_2 nanotube sensor from 9.7 ppm to 9.7 ppb of NOx at room temperature. Reproduced with permission[51], Copyright 2016, Wiley-VCH.*

For instance, Figures 2.14c,d display highly sensitive and reversible response towards ethanol, CO and H_2 by one-dimensional SnO_2 nanowires, owing to their small grain size, high surface-to-volume ratio and great network porosity[51]. Furthermore, SnO_2 nanotubes, prepared by electrospinning with subsequent thermal treatment, are also reported to be very promising for the detection of NOx at room temperature[51]. As shown in Figure 2.14e, the SnO_2 nanotubes consisting of 5–10 nm crystallites exhibiting {101} facets (Fig. 2.14f) has better performances with respect to nanotubes exhibiting {211} and {110) crystal facets. It was concluded that the {101} facets are the most active for NOx detection owing to their low/medium adsorption energy and the largest electron transfer[51]. The tubular structure can adsorb gas molecules on both the inner and outer surfaces of the tube. Notably, the SnO_2 crystallites in the tube wall are connected with four or more neighbors to form intergrain junctions (Fig. 2.14g), thus reaching a detection limit as low as 10 ppb NOx (Fig. 2.14h)[51]. Besides, Sharma *et al.* [109] recently reported highly sensitive SnO_2 nanostructures, grown by thermal solid evaporation of a mixture of anhydrous $SnCl_2$ and $ZnCl_2$ powders at 550°C, in air. The morphology and structural properties of the as-grown nanostructures were tuned by adjusting the weight ratio between the two salts, in which zinc chloride works as interspace separator between SnO_2 nuclei. The corresponding thin film showed ~85% sensitivity and 53

s of response time, at room temperature towards ethanol gaseous molecules. The authors stated the nanostructured material with small size and shape has better sensitivity on sensing compared to previously reported SnO_2-based sensors.

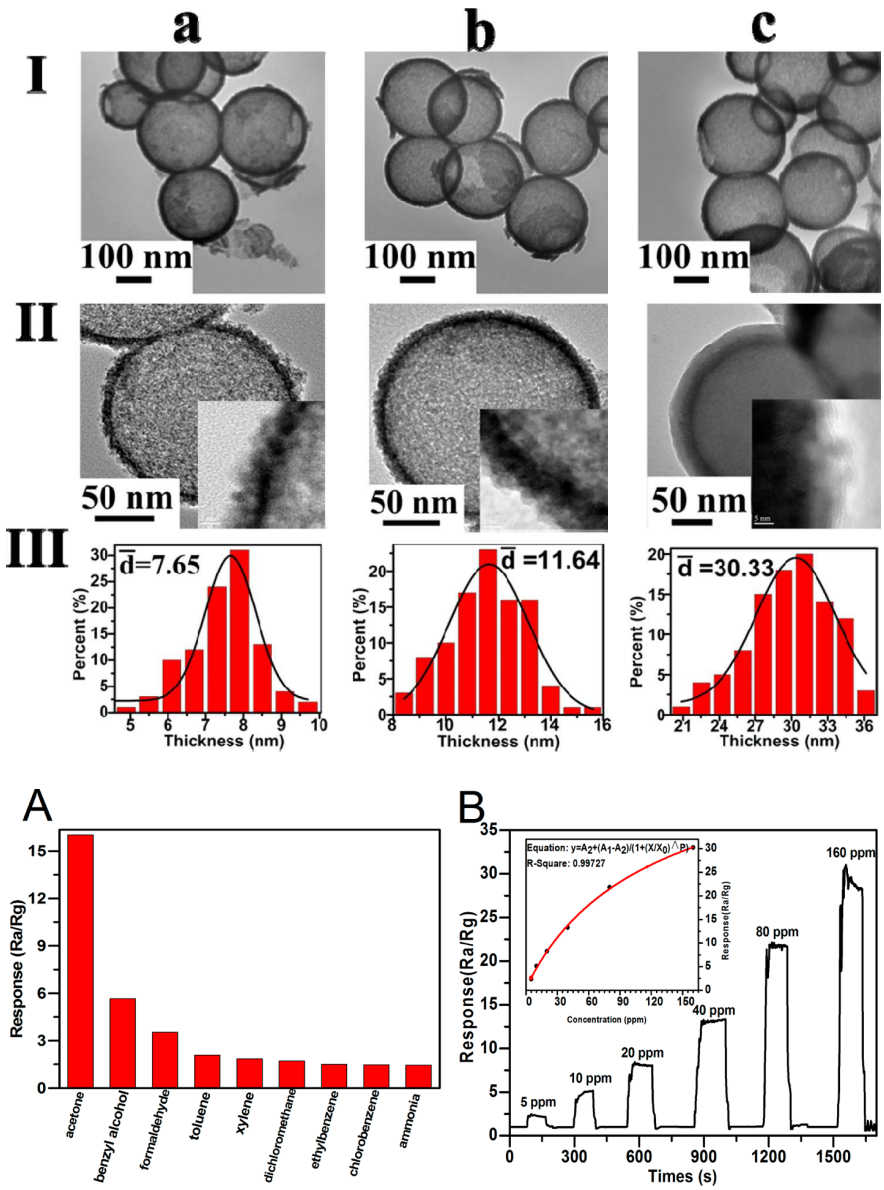

Figure 2.15. *(I) TEM images, (II) HRTEM images, and (III) shell thickness distribution of (a) SnO_2-200-0.5, (b) SnO_2-200-1 and (c) SnO_2-200-1.5; where 200 is the mean size of the SiO_2 microspheres (used as template), whereas 0.5-1-1.5 represent the Sn/Si molar ratio used in the preparation process. (A) Response of SnO_2-200-0.5 to various gases with concentration of 50 ppm at 200 °C; (B) responses towards acetone at 200 °C (inset: linear fitting curve of the sensing response). Reproduced with permission*[95]*, Copyright 2016, American Chemical Society.*

Furthermore, a facile method to prepare SnO_2 hollow microspheres (Figures 2.15I–III) has been proposed by Li and his co-workers[95], using SiO_2 microspheres as template and Na_2SnO_3 as tin precursor. They demonstrated that the diameter of SnO_2 hollow microspheres can be easily controlled in the range of 200−700 nm, and the shell thickness can be tuned from around 8 nm to 30 nm (Figures 2.15a–c). Notably, the sensing measurements showed that the as-prepared materials not only have high sensing response and excellent selectivity to acetone (Figure 2.15A), but also exhibit rapid response and recovery (Figure 2.15B), thanks to the small crystal size and thin shell structure. Therefore, the developed SnO_2 hollow microspheres are believed to represent one of the most promising materials for the preparation of high-performance gas sensors.

2.3.3.3. *WO_3-based gas sensors*

Tungsten oxide was reported to be used for the first time as H_2 sensor in 1967, for safety applications[81]. It has attracted much research attention, owing to its various crystal structures, such as monoclinic (ε and γ phases), triclinic (δ polymorph), orthorhombic (β phase) and tetragonal (α polymorph) one[81,110–113]. As SnO_2, also WO_3 is highly sensitive to many gaseous analytes. However, it is largely reported that different phases have different sensing properties[81,110–113].

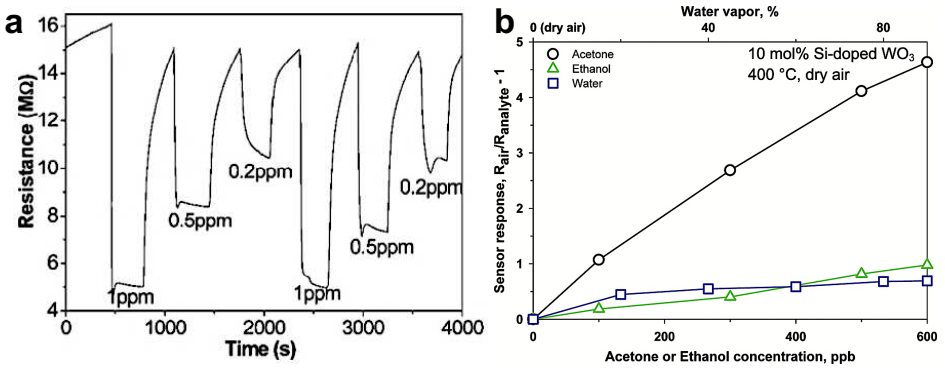

Figure 2.16. *(a) Resistance change with 10 atom % Cr-doped WO_3 upon exposure to acetone at 400 °C. Reprinted with permission[114], Copyright 2008, American Chemical Society. (b) Sensor response to acetone (circles), water (squares), and ethanol (triangles) vapors. Reprinted with permission[3], Copyright 2010, American Chemical Society.*

Specifically, the ε-WO_3 phase has been deeply investigated by Pratsinis's (Particle Technology Laboratory, ETH, Zurich) and Tricoli's (Nanotechnology Research Laboratory, ANU, Canberra) research groups, resulting in a very highly sensitive and selective to acetone sensing material (Figure 2.16)[3,110,114,115]. In particular, this polymorph is a metastable phase,

which has to be stabilized by doping with Cr (Fig. 2.16a) or Si (Fig. 2.16b) atoms, giving rise to a more stable material that shows a great selectivity towards acetone molecules (*i.e.* down to 20 ppb, at a relative humidity of 90%)[3,110,114,115]. Furthermore, the Si-doped WO_3 sensor response is only decreased by 4%, when increasing the RH from 80 to 90%, thus indicating sufficiently precise detection regardless of humidity fluctuations (Fig. 2.16b)[3].

Besides, Ya-Qiao *et al.*[116] proposed hexagonal WO_3 nanorods, fabricated by a facile hydrothermal process at 180°C, using sodium tungstate and sodium chloride as salts reagents. Hence, uniform WO_3 nanorods with diameters ranging from 100–150 nm and lengths up to several micrometers are obtained at acidic pH, prevalently showing a hexagonal phase structure. The nanostructures sensing properties were investigated by measuring the dynamic response to NO_2, with concentrations in the range 0.5–5 ppm and at working temperatures in the range 25–250 °C. Interestingly, the obtained WO_3 nanorods exhibited opposite sensing behaviors, depending on the operating temperature. Specifically, when exposed to an oxidizing gas such as NO_2 and at temperatures above 50 °C, the tungsten oxide behaves as an n-type semiconductor; whereas, it is a p-type one below 50 °C. The origin of this n- to p-type transition may be correlated with the formation of an inversion layer at the surface of the WO_3 nanorods at room temperature, resulting in much more holes that become the main charge carriers[116]. These findings are reported to be useful for making new room temperature gas sensors based on hexagonal WO_3 nanorods.

2.3.4. Heterojunctions to improve the sensing performances

As already mentioned, metal oxides have shown some lack in terms of sensitivity and selectivity, especially at low working temperatures. Hence, a typical method proposed to overcome these drawbacks consists in the MOS surface modification either with various dopants, such as Au[84], Ag[47], Pt[27] and Pd[83], or their coupling with other materials (both MOS[78] and carbonaceous matrixes[117,118]). Interestingly, there are many research work dealing with the fabrication of nano-heterojunctions, aiming at enhancing the room temperature sensing behavior[51]. For instance, Zhang *et al.*[51], in their almost recent review, give an overview on the plethora of complex existing heterojunctions at the nanoscale. Specifically, it is mandatory to define the possible mechanism underneath the improvement of the final sensing. Hence, the distinction between different classes of heterojunctions is necessary.

2.3.4.1. *Metal–Metal oxide heterojunctions*

In metal-metal oxide–based nano-heterojunctions, noble metals such as silver (Ag), gold (Au), palladium (Pd) or platinum (Pt) act as sensitizers to enhance the sensor performances, towards the target gaseous molecules[51]. The positive effect given by noble metals can be classified as *chemical* or *electronic sensitization*, depending on whether the noble metals change the work function of the interconnected MOS[51]. As concern the former, the noble metal plays its role activating the analyte molecules, in order to facilitate its reaction on the semiconductor surface. Therefore, in this case, it is a "promoter" since it does not affect the resistance of the system, but it helps to increase the sensor sensitivity by improving the reaction rate of the chemical reactions. On the other hand, electronic sensitization results from the direct interaction at the interface between the promoter and the semiconductor. For instance, Ag and Pd are known to form stable oxides (namely, AgO and PdO) in air, and produce an electron-depleted space charge layer in the interface. The electronic sensitization decreases when the oxide forms of metal promoters are reduced to metal by reductive gases.

2.3.4.2. *Metal oxide–Metal oxide heterojunctions*

Another effective strategy to improve the sensing behavior is the integration or coupling of nanocomposites, having two or more different phases[51]. Actually, the growth of a guest phase on a host metal oxide together with the coupling of MOS with another semiconductor can lead to the modification of acid/base properties, formation of interphase heterojunctions and boundaries, modulation of work functions, as well as of the surface properties (such as defects and active sites)[51]. Notably, the optimal integration of two different metal oxides is of particular interest, due to the synergic effects at the interface. Indeed, the appropriate combination of different metal oxides to produce heterostructures can result in enhanced charge transduction and modulated potential barriers at the grain boundaries, which are advantageous for gas sensors[51]. Chen *et al.*[78] reported a 3D network of NiO–ZnO p–n semiconductors with grain size of ≈20 nm and a porosity of around 98% (as observable in SEM images of Figs. 2.17b,c). They observed that the formation of the p–n heterojunctions, by decoration of ZnO nanoparticles with NiO (Fig. 2.17a), increases the sensor response by more than four times while lowering the limit of detection. Furthermore, under solar light irradiation, the optimal NiO–ZnO nano-heterojunction results in a strong and selective RT response to acetone and ethanol, being very promising the development of low-power solid-state chemical sensors.

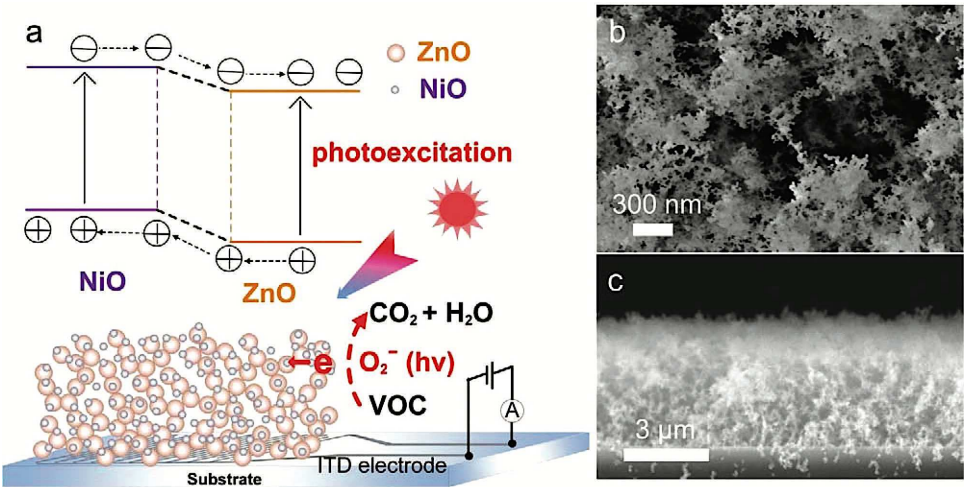

Figure 2.17. *(a) Scheme of the p–n NiO–ZnO nano-heterojunctions; (b) SEM images of films with NiO and ZnO thickness of 9 nm and 6 µm, respectively; (c) cross-sectional SEM of NiO-ZnO thin film. Reproduced with permission*[78]*, Copyright 2018, WILEY-VCH Verlag GmbH & Co.*

2.3.4.3. *Carbon-based materials–Metal oxide heterojunctions*

Carbon nanomaterials such as carbon nanotubes (CNTs) and fullerenes have been extensively used for VOCs detection[22]. Recently, to reach the goal of sensitivity increase, graphene-based gas sensors have attracted much attention due to the graphene fascinating properties such as thermo-electric conduction, surface area and mechanical strength. Hence, different structures have been developed and high sensing performances and room temperature working conditions have been achieved. Particularly, in the past decades, carbon nanotubes (CNTs) have been the most studied carbon materials for gas sensors. However, it seems that the dominance of CNTs in their application in gas sensors is now overtaken by graphene. Indeed, compared to the 1D structure of CNTs, graphene has a 2D planar surface with more flexibility.

It can be synthesized by several methods, as epitaxial growth[51], chemical vapor deposition (CVD)[51], and chemical or thermal reduction of graphene oxide[51]. Moreover, both graphene oxide and reduced graphene oxide bears different amounts of oxygen functional groups, which make them a versatile platform for further functionalization. Zhang *et al.*[51] reported that chemically reduced graphene oxide (rGO) film is a p-type semiconductor, suitable for electronic device applications. It should also be noted that graphene materials obtained from different synthetic routes lead to very different sensing properties. As stated by Novoselov *et al.*[35], graphene can detect a single gas molecule at room temperature, thanks to both the

complete exposure of carbon atom to the surrounding analytes, and its metallic conductivity. Nevertheless, its main shortcoming lies in the long recovery time, thus indicating that the gas molecules are strongly attached to the graphene at room temperature[35]. In general, carbon-based materials suffer from several problems, such as scarce selectivity, reversibility, recovery and scalability[51]. These can be partially overcome by functionalization with various guest components, as MOS nanoparticles. Notably, many studies have demonstrated that metal oxides, such as SnO_2[94,119], ZnO[120,121], TiO_2[33,99], can be good candidates for replacing noble metals in designing high-performing sensor materials. In Zhang *et al.*[51] review, it is claimed that p-type carbonaceous materials combined with n-type MOS form a heterojunction, which enhances the sensor conductivity. For instance, in CNT–SnO_2 heterostructures, two different depletion layers, and associated potential barriers, can coexist. The first one is at the surface of the metal oxide, whereas the second one at the interface between CNTs and the MOS. While the first depletion layer is due to the adsorption of ionized oxygen at the surface of the SnO_2 film, the second is due to the CNTs–SnO_2 heterojunction. Hence, when O_2 adsorbed onto the surface of the SnO_2 film, it modifies the width of the first depletion layer, which in turn alters the depletion layer at the p-CNTs–n-SnO_2 interface. The behavior has been explained by considering the various junctions involved in the sensing mechanism and their influence on the electric path: carbon nanotubes have numerous contacts among themselves, and potential barriers are formed at the crossing points, which can be modified by the presence of the metal oxide coating. Hence, by increasing the density of the SnO_2 particles on the CNT, the shortcuts between carbon nanotubes are reduced so the CNT–SnO_2–SnO_2–CNT junctions become more effective.

Besides, graphene oxide and reduced graphene oxide, with its large number of oxygen-containing functional groups, have been reported to be a successful platform for the synthesis of diverse composite nanomaterials[93,94,99]. Particularly, post-synthesis treatment of graphene oxide-metal oxides by either thermal or chemical reduction can result in reduced graphene oxide-based nanocomposites. As in the case of CNT-MOS coupling, also for graphene-based materials-MOS a synergistic effect can be hypothesized, which may enhance the sensing properties[122] (see Figure 2.18). Notably, graphene improves the conductivity of the composite materials by contributing to the charge transport, thus lowering the working temperature commonly needed for metal oxides. Secondly, graphene and metal oxides can have a strong electronic interaction by forming heterojunctions at the contact interface, which can modulate or affect the charge transfer during the gas sensing process. Thirdly, the growth of metal oxides on graphene can increase the reactive sites and better the adsorption of a particular gas, not detectable by pristine graphene.

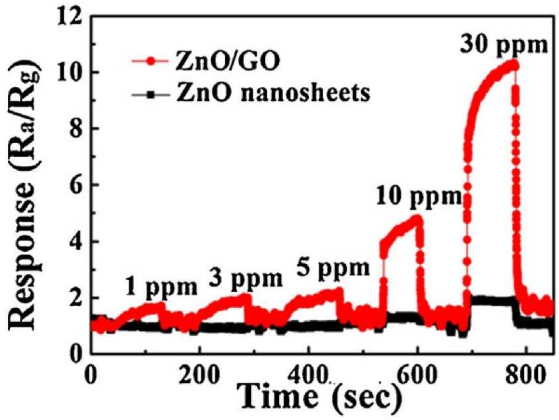

Figure 2.18. *Comparison between sensor responses towards acetone concentration by exploiting pure ZnO nanosheets and ZnO/GO nanocomposite, at the optimum operating temperature of 240 °C. Adapted with permission*[122]*, Copyright 2016, Elsevier.*

2.3.5. Future perspectives

If on one hand high sensitivity levels are not a major drawback anymore, due to the materials functionalization/engineering of nano-heterojunctions; on the other, poor selectivity, still high operating temperatures (and thus scarce materials stability), and the humidity interference do represent a challenge. In the case of metal oxide sensing materials, the control over morphology and structural properties have come into a matured state. Conversely, hybrid nanostructures should be much more investigated, owing to the more-complex sensing mechanisms, deriving from the additional interactions between the analyte molecules and the diverse material components. Notably, carbon-based nanostructures possess high sensitivity, but too poor selectivity. From a material perspective, the easy and straightforward synthesis of metal oxide nanostructures by wet chemistry is obviously a merit for the gas sensing field. Moreover, CNTs and graphene-based materials, due to their defect chemistry and versatile surface reactivity for functionalization, can represent the platform for carbon-metal oxide p-n heterojunctions, thus providing new opportunities to explore and optimize sensor properties and performances.

References

[1] A. Tricoli, N. Nasiri, S. De, *Adv. Funct. Mater.* **2017**, *27*, 1605271.

[2] S. Wang, Y. Zou, Q. Shan, J. Xue, Y. Dong, Y. Gu, J. Song, *RSC Adv.* **2018**, *8*, 33666.

[3] M. Righettoni, A. Tricoli, S. E. Pratsinis, *Anal. Chem.* **2010**, *82*, 3581.

[4] A. Tsukazaki, A. Ohtomo, T. Onuma, M. Ohtani, T. Makino, M. Sumiya, K. Ohtani, S. F. Chichibu, S. Fuke, Y. Segawa, H. Ohno, H. Koinuma, M. Kawasaki, *Nat. Mater.* **2004**, *4*, 42.

[5] D. Gedamu, I. Paulowicz, S. Kaps, O. Lupan, S. Wille, G. Haidarschin, Y. K. Mishra, R. Adelung, *Adv. Mater.* **2014**, *26*, 1541.

[6] M. Law, L. E. Greene, J. C. Johnson, R. Saykally, P. Yang, *Nat. Mater.* **2005**, *4*, 455.

[7] N. Nasiri, D. Jin, A. Tricoli, *Adv. Opt. Mater.* **2019**, *7*, 1800580.

[8] W. Zheng, R. Lin, J. Ran, Z. Zhang, X. Ji, F. Huang, *ACS Nano* **2018**, *12*, 425.

[9] R. Bo, N. Nasiri, H. Chen, D. Caputo, L. Fu, A. Tricoli, *ACS Appl. Mater. Interfaces* **2017**, *9*, 2606.

[10] J. Zou, Q. Zhang, K. Huang, N. Marzari, *J. Phys. Chem. C* **2010**, *114*, 10725.

[11] Y. L. Cao, Z. T. Liu, L. M. Chen, Y. B. Tang, L. B. Luo, J. S. Jie, W. J. Zhang, S. T. Lee, C. S. Lee, *Opt. Express* **2011**, *19*, 6100.

[12] J. Cai, X. Xu, L. Su, W. Yang, H. Chen, Y. Zhang, X. Fang, *Adv. Opt. Mater.* **2018**, *6*, 1800213.

[13] J. Chao, X. Sun, S. Xing, X. Zhang, S. Gao, Z. Du, *J. Alloys Compd.* **2018**, *753*, 212.

[14] A. Aldalbahi, E. Li, M. Rivera, R. Velazquez, T. Altalhi, X. Peng, P. X. Feng, *Sci. Rep.* **2016**, *6*, 23457.

[15] G. Nam, J.-Y. Leem, *RSC Adv.* **2015**, *5*, 94222.

[16] K. Liu, M. Sakurai, M. Liao, M. Aono, *J. Phys. Chem. C* **2010**, *114*, 19835.

[17] C. Chen, S. Zhang, B. Hu, H. San, Z. Cheng, W. Hofmann, *Compos. Part B Eng.* **2019**, *164*, 640.

[18] F. Malara, A. Minguzzi, M. Marelli, S. Morandi, R. Psaro, V. Dal Santo, A. Naldoni, *ACS Catal.* **2015**, *5*, 5292.

[19] J. K. Fong, J. K. Pena, Z.-L. Xue, M. M. Alam, U. Sampathkumaran, K. Goswami, *Anal. Chem.* **2015**, *87*, 1569.

[20] M. Z. Film, *Sensors* **2017**, *18*, 50.

[21] C. Chen, P. Zhou, N. Wang, Y. Ma, H. San, *Nanomaterials* **2018**, *8*, 26.

[22] S. Gupta Chatterjee, S. Chatterjee, A. K. Ray, A. K. Chakraborty, *Sensors Actuators B Chem.* **2015**, *221*, 1170.

[23] U. Latif, F. Dickert, *Sensors* **2015**, *15*, 30504.

[24] T. Wang, D. Huang, Z. Yang, S. Xu, G. He, *Nano-Micro Lett.* **2016**, *8*, 95.

[25] W. Li, X. Wu, N. Han, J. Chen, X. Qian, Y. Deng, W. Tang, Y. Chen, *Sensors Actuators B Chem.* **2016**, *225*, 158.

[26] V. K. Tomer, S. Devi, R. Malik, S. P. Nehra, S. Duhan, *Sensors Actuators B Chem.* **2016**, *229*, 321.

[27] J.-H. Kim, S. S. Kim, *ACS Appl. Mater. Interfaces* **2015**, *7*, 17199.

[28] D. Chen, Y. J. Yuan, S. Member, **2015**, *15*, 6749.

[29] Z. Song, Z. Wei, B. Wang, Z. Luo, S. Xu, W. Zhang, H. Yu, M. Li, Z. Huang, J. Zang, F. Yi, H. Liu, *Chem. Mater.* **2016,** *28*, 1205.

[30] A. M. K. Janghorban, B. H. G. Neri, *J. Nanoparticle Res.* **2015**, *17*, 1.

[31] R. Ab Kadir, Z. Li, A. Z. Sadek, R. Abdul Rani, A. S. Zoolfakar, M. R. Field, J. Z. Ou, A. F. Chrimes, K. Kalantar-Zadeh, *J. Phys. Chem. C* **2014**, *118*, 3129.

[32] X. Wei, Y. Luo, F. Xu, Y. Chen, *Synth. Met.* **2016**, *215*, 216.

[33] D. Acharyya, P. Bhattacharyya, S. Member, **2016**, *37*, 656.

[34] S. S. Varghese, S. Lonkar, K. K. Singh, S. Swaminathan, A. Abdala, *Sensors Actuators B Chem.* **2015**, *218*, 160.

[35] F. Schedin, A. K. Geim, S. V Morozov, E. W. Hill, P. Blake, M. I. Katsnelson, K. S. Novoselov, **2007**, *6*, 6.

[36] S. Dell'elce, S. Ligi, *La Chimica e l'Industria.* **2016,** 64.

[37] F. Meng, Z. Guo, X. Huang, *Trends Anal. Chem.* **2015**, *68*, 37.

[38] Y. Xu, P. Liu, D. Sun, Y. Sun, G. Zhang, D. Gao, *Mater. Lett.* **2015**, *161*, 495.

[39] W. Li, S. Ma, Y. Li, G. Yang, Y. Mao, J. Luo, D. Gengzang, X. Xu, S. Yan, *Sensors Actuators B Chem.* **2015**, *211*, 392.

[40] C. Marichy, P. A. Russo, M. Latino, J. Tessonnier, M. Willinger, N. Donato, G. Neri, N. Pinna, *J. Phys. Chem. C* **2013,** *117*, 19729.

[41] D. T. Phan, G. S. Chung, *J. Phys. Chem. Solids* **2013**, *74*, 1509.

[42] H. Liu, Y. Liu, D. Zhu, *J. Mater. Chem.* **2011**, *21*, 3335.

[43] D. Chen, L. Wei, L. Meng, D. Wang, Y. Chen, Y. Tian, S. Yan, L. Mei, J. Jiao, *J. Alloys Compd.* **2018**, *751*, 56.

[44] L. Li, C. Zhang, W. Chen, *Nanoscale* **2015**, *7*, 12133.

[45] V. K. Tomer, S. Duhan, *J. Mater. Chem. A* **2016**, *4*, 1033.

[46] J. Kim, P. Wu, H. W. Kim, S. S. Kim, *Appl. Mater. Interfaces* **2016,** *8*, 7173.

[47] Z. Wang, Y. Zhang, S. Liu, T. Zhang, *Sensors Actuators B Chem.* **2016**, *222*, 893.

[48] S. Cui, H. Pu, E. C. Mattson, G. Lu, S. Mao, M. Weinert, C. J. Hirschmugl, M. Gajdardziska-Josifovska, J. Chen, *Nanoscale* **2012**, *4*, 5887.

[49] L. Wang, B. Han, Z. Wang, L. Dai, H. Zhou, Y. Li, H. Wang, *Sensors Actuators B Chem.*

2015, *207*, 791.

[50] S. Choi, A. Katoch, G. Sun, P. Wu, S. S. Kim, *J. Mater. Chem. C* **2013**, *1*, 2834.

[51] J. Zhang, X. Liu, G. Neri, N. Pinna, *Adv. Mater.* **2016**, *28*, 795.

[52] Z. Wang, R. Yu, X. Wang, W. Wu, Z. L. Wang, *Adv. Mater.* **2016**, *28*, 6880.

[53] S. C. Rai, K. Wang, Y. Ding, J. K. Marmon, M. Bhatt, Y. Zhang, W. Zhou, Z. L. Wang, *ACS Nano* **2015**, *9*, 6419.

[54] Z. Zheng, L. Gan, H. Li, Y. Ma, Y. Bando, D. Golberg, T. Zhai, *Adv. Funct. Mater.* **2015**, *25*, 5885.

[55] X. Zhang, B. Liu, W. Yang, W. Jia, J. Li, C. Jiang, X. Jiang, *Nanoscale* **2016**, *8*, 17573.

[56] M. Sun, Z. Xu, M. Yin, Q. Lin, L. Lu, X. Xue, X. Zhu, Y. Cui, Z. Fan, Y. Ding, L. Tian, H. Wang, X. Chen, D. Li, *Nanoscale* **2016**, *8*, 8924.

[57] Y. Xie, L. Wei, G. Wei, Q. Li, D. Wang, Y. Chen, S. Yan, G. Liu, L. Mei, J. Jiao, *Nanoscale Res. Lett.* **2013**, *8*, 188.

[58] M. Wang, F. Liang, B. Nie, L. Zeng, L. Zheng, P. Lv, Y. Yu, C. Xie, Y. Y. Li, L.-B. Luo, *Part. Part. Syst. Charact.* **2013**, *30*, 630.

[59] T.-Y. Tsai, S.-J. Chang, W.-Y. Weng, C.-L. Hsu, S.-H. Wang, C.-J. Chiu, T.-J. Hsueh, S.-P. Chang, *J. Electrochem. Soc.* **2012**, *159*, J132.

[60] H. Chen, L. Hu, X. Fang, L. Wu, *Adv. Funct. Mater.* **2012**, *22*, 1229.

[61] Y. Qu, Z. Wu, M. Ai, D. Guo, Y. An, H. Yang, L. Li, W. Tang, *J. Alloys Compd.* **2016**, *680*, 247.

[62] B. Deka Boruah, A. Misra, *ACS Appl. Mater. Interfaces* **2016**, *8*, 18182.

[63] H. Zhang, X. Dai, N. Guan, A. Messanvi, V. Neplokh, V. Piazza, M. Vallo, C. Bougerol, F. H. Julien, A. Babichev, N. Cavassilas, M. Bescond, F. Michelini, M. Foldyna, E. Gautier, C. Durand, J. Eymery, M. Tchernycheva, *ACS Appl. Mater. Interfaces* **2016**, *8*, 26198.

[64] F. Xie, H. Lu, D. Chen, X. Ji, F. Yan, R. Zhang, Y. Zheng, L. Li, J. Zhou, *IEEE Sens. J.* **2012**, *12*, 2086.

[65] Y. Shen, X. Yan, H. Si, P. Lin, Y. Liu, Y. Sun, Y. Zhang, *ACS Appl. Mater. Interfaces* **2016**, *8*, 6137.

[66] Y. Zhang, J. Xu, S. Shi, Y. Gao, C. Wang, X. Zhang, S. Yin, L. Li, *ACS Appl. Mater. Interfaces* **2016**, *8*, 22647.

[67] J. Garnier, R. Parize, E. Appert, O. Chaix-Pluchery, A. Kaminski-Cachopo, V. Consonni, *ACS Appl. Mater. Interfaces* **2015**, *7*, 5820.

[68] L. Xu, X. Li, Z. Zhan, L. Wang, S. Feng, X. Chai, W. Lu, J. Shen, Z. Weng, J. Sun, *ACS Appl. Mater. Interfaces* **2015**, *7*, 20264.

[69] S. Sarkar, D. Basak, *ACS Appl. Mater. Interfaces* **2015**, *7*, 16322.

[70] D.-K. Kwon, S. J. Lee, J.-M. Myoung, *Nanoscale* **2016**, *8*, 16677.

[71] Z. Jin, Q. Zhou, Y. Chen, P. Mao, H. Li, H. Liu, J. Wang, Y. Li, *Adv. Mater.* **2016**, *28*, 3697.

[72] C. Ingrosso, G. V. Bianco, V. Pifferi, P. Guffanti, F. Petronella, R. Comparelli, A. Agostiano, M. Striccoli, I. Palchetti, L. Falciola, M. L. Curri, G. Bruno, *J. Mater. Chem. A* **2017**, *5*, 9307.

[73] H.-T. Ren, Q. Yang, *Appl. Surf. Sci.* **2017**, *396*, 530.

[74] M. Mallak, M. Bockmeyer, P. Löbmann, *Thin Solid Films* **2007**, *515*, 8072.

[75] G. Lan, J. Nong, W. Jin, R. Zhu, P. Luo, H. Jiang, W. Wei, *Surf. Coatings Technol.* **2019**, *359*, 90.

[76] F. Dejene, A. Ali, H. Swart, R. Botha, K. Roro, L. Coetsee, M. Biggs, *Open Phys.* **2011**, *9*, 1321.

[77] N. Nasiri, R. Bo, F. Wang, L. Fu, A. Tricoli, *Adv. Mater.* **2015**, *27*, 4336.

[78] H. Chen, R. Bo, A. Shrestha, B. Xin, N. Nasiri, J. Zhou, I. Di Bernardo, A. Dodd, M. Saunders, J. Lipton-Duffin, T. White, T. Tsuzuki, A. Tricoli, *Adv. Opt. Mater.* **2018**, *6*, 1800677.

[79] A. Tricoli, M. Righettoni, A. Teleki, *Angew. Chemie Int. Ed.* **2010**, *49*, 7632.

[80] S. S. Varghese, S. H. Varghese, S. Swaminathan, K. K. Singh, V. Mittal, *Electronics* **2015**, *4*, 651.

[81] M. Righettoni, A. Amann, S. E. Pratsinis, *Mater. Today* **2015**, *18*, 163.

[82] Z. Q. Zheng, J. D. Yao, B. Wang, G. W. Yang, *Sci. Rep.* **2015**, *5*, 1.

[83] Z. U. Abideen, J.-H. Kim, A. Mirzaei, H. W. Kim, S. S. Kim, *Sensors Actuators B Chem.* **2018**, *255*, 1884.

[84] E. Wongrat, N. Chanlek, C. Chueaiarrom, B. Samransuksamer, N. Hongsith, S. Choopun, *Sensors Actuators, A Phys.* **2016**, *251*, 188.

[85] L. Zhu, W. Zeng, *Sensors Actuators A Phys.* **2017**, *267*, 242.

[86] P. Zhang, G. Pan, B. Zhang, J. Zhen, Y. Sun, *Mater. Res.* **2014**, *17*, 817.

[87] X. Kou, N. Xie, F. Chen, T. Wang, L. Guo, C. Wang, Q. Wang, J. Ma, Y. Sun, H. Zhang, G. Lu, *Sensors Actuators, B Chem.* **2018**, *256*, 861.

[88] B. Bhangare, N. S. Ramgir, S. Jagtap, A. K. Debnath, K. P. Muthe, C. Terashima, D. K. Aswal, S. W. Gosavi, A. Fujishima, *Appl. Surf. Sci.* **2019**, *487*, 918.

[89] Y. Matsushima, R. Toyoda, H. Mori-Ai, A. Kondo, K. Maeda, *J. Ceram. Soc. Japan* **2014**, *122*, 96.

[90] M. Righettoni, A. Tricoli, S. Gass, A. Schmid, A. Amann, S. E. Pratsinis, *Anal. Chim. Acta* **2012**, *738*, 69.

[91] K. Govardhan, A. N. Grace, *Sens. Lett.* **2016**, *14*, 741.

[92] W. Guo, *J. Mater. Sci. Mater. Electron.* **2016**, *27*, 7302.

[93] C. A. Zito, T. M. Perfecto, D. P. Volanti, *Sensors Actuators B Chem.* **2017**, *244*, 466.

[94] M. Arvani, H. Mohammad Aliha, A. A. Khodadadi, Y. Mortazavi, *Sci. Iran.* **2017**, *24*, 3033.

[95] J. Li, P. Tang, J. Zhang, Y. Feng, R. Luo, A. Chen, D. Li, *Ind. Eng. Chem. Res.* **2016**, *55*, 3588.

[96] F. Ren, L. Gao, Y. Yuan, Y. Zhang, A. Alqrni, O. M. Al-Dossary, J. Xu, *Sensors Actuators B Chem.* **2016**, *223*, 914.

[97] G. K. Mani, J. B. B. Rayappan, *Sensors Actuators B Chem.* **2016**, *223*, 343.

[98] C. W. Na, H.-S. Woo, I.-D. Kim, J.-H. Lee, *Chem. Commun.* **2011**, *47*, 5148.

[99] R. Kalidoss, S. Umapathy, Y. Sivalingam, *Appl. Surf. Sci.* **2018**, *449*, 677.

[100] W. Wang, Y. Tian, X. Wang, H. He, Y. Xu, C. He, X. Li, *J. Mater. Sci.* **2013**, *48*, 3232.

[101] Y.-H. Zhang, C.-Y. Liu, B.-B. Jiu, Y. Liu, F.-L. Gong, *Res. Chem. Intermed.* **2018**, *44*, 1569.

[102] Y. He, P. Tang, J. Li, J. Zhang, F. Fan, D. Li, *Mater. Lett.* **2016**, *165*, 50.

[103] H. Keskinen, A. Tricoli, M. Marjamäki, J. M. Mäkelä, S. E. Pratsinis, *J. Appl. Phys.* **2009**, *106*, 084316.

[104] C. O. Blattmann, A. T. Güntner, S. E. Pratsinis, *ACS Appl. Mater. Interfaces* **2017**, *9*, 23926.

[105] Y. Chang, Y. Yao, B. Wang, H. Luo, T. Li, L. Zhi, *J. Mater. Sci. Technol.* **2013**, *29*, 157.

[106] M. N. Nasrabadi, Y. Mortazavi, A. A. Khodadadi, *Sensors Actuators B Chem.* **2016**, *230*, 130.

[107] S. H. Li, F. F. Meng, Z. Chu, T. Luo, F. M. Peng, Z. Jin, *Adv. Condens. Matter Phys.* **2017**, *2017*, 1.

[108] A. Larin, P. C. Womble, V. Dobrokhotov, *Sensors Actuators B Chem.* **2018**, *256*, 1057.

[109] A. P. Sharma, P. Dhakal, D. K. Pradhan, M. K. Behera, B. Xiao, M. Bahoura, *AIP Adv.* **2018**, *8*, 095219.

[110] A. T. Güntner, N. A. Sievi, S. J. Theodore, T. Gulich, M. Kohler, S. E. Pratsinis, *Anal. Chem.* **2017**, *89*, 10578.

[111] L. Saadi, C. Lambert-Mauriat, V. Oison, H. Ouali, R. Hayn, *Appl. Surf. Sci.* **2014**, *293*, 76.

[112] C. Lambert-Mauriat, V. Oison, L. Saadi, K. Aguir, *Surf. Sci.* **2012**, *606*, 40.

[113] K. Kanda, T. Maekawa, *Sensors Actuators, B Chem.* **2005**, *108*, 97.

[114] L. Wang, A. Teleki, S. E. Pratsinis, P. I. Gouma, *Chem. Mater.* **2008**, *20*, 4794.

[115] M. Righettoni, A. Tricoli, S. E. Pratsinis, *Chem. Mater.* **2010**, *22*, 3152.

[116] Y. Q. Wu, M. Hu, X. Y. Wei, *Chinese Phys. B* **2014**, *23*, 040704.

[117] E. Singh, M. Meyyappan, H. S. Nalwa, *ACS Appl. Mater. Interfaces* **2017**, *9*, 34544.

[118] K. M. Tripathi, T. Kim, D. Losic, T. T. Tung, *Carbon N. Y.* **2016**, *110*, 97.

[119] H. Chen, X. Pu, M. Gu, J. Zhu, L. Cheng, *Ceram. Int.* **2016**, *42*, 17717.

[120] C. N. Peter, W. W. Anku, S. K. Shukla, P. P. Govender, *Theor. Chem. Acc.* **2018**, *137*, 75.

[121] S. Liu, B. Yu, H. Zhang, T. Fei, T. Zhang, *Sensors Actuators B Chem.* **2014**, *202*, 272.

[122] P. Wang, D. Wang, M. Zhang, Y. Zhu, Y. Xu, X. Ma, X. Wang, *Sensors Actuators B Chem.* **2016**, *230*, 477.

Chapter 3

Graphene oxide

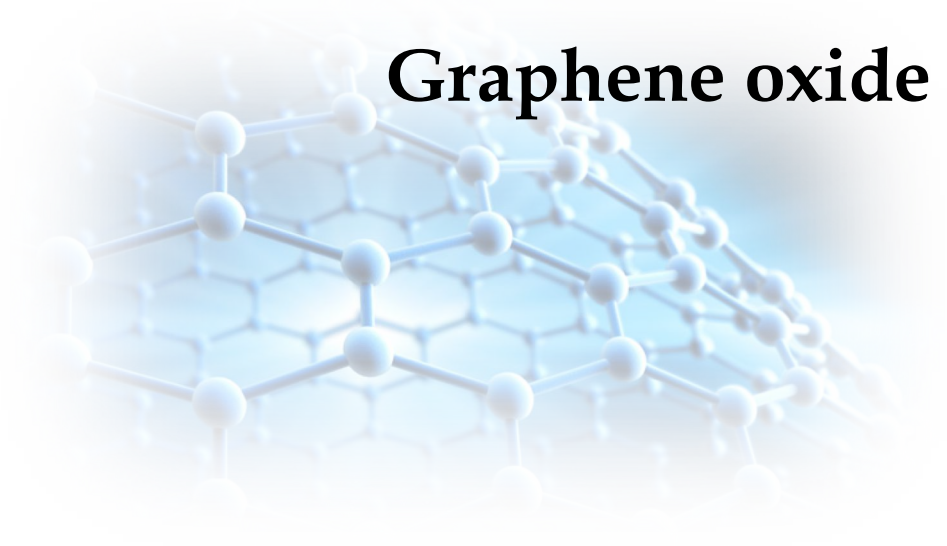

"A good head and a good heart are always
a formidable combination"

— Nelson Mandela

3.1. Introduction

As extensively discussed in Chapter 2, graphene and its oxides have attracted much attention, especially because of their enhanced electronic properties. In particular, graphene oxide (GO) is an important derivative of graphene with 2D-structure, having oxygen-containing functional groups, such as epoxy and hydroxyl groups, on the basal plane and carbonyl, carboxyl and hydroxyl groups on the edges of the graphene sheets[1]. Hence, the GO features mainly arise from the presence of various oxygenated groups and, thus, from its degree of oxidation[2]. Indeed, it has been demonstrated that either the optical properties or the electrical conductivity are affected by tailoring these oxygen-containing functional groups[3]. Notably, several recent studies[4–6] have suggested that the structure of GO is strongly influenced by its degree of oxidation which, in turns, depends on the adopted oxidizing agents, graphite source and reaction conditions. Starting by Brodie's attempts in 1859[7], several improvements in the formation of GO have been done so far. Particularly, Brodie explored the structure of graphite by investigating its reactivity. One of the performed reactions involved the addition of potassium chlorate to a slurry of graphite in fuming nitric acid. He determined that the resulting material was composed of carbon, hydrogen and oxygen, thus, resulting in an oxidized graphite. To obtain GO, that is a few-layered material, it is mandatory to overcome the interlayer Van der Walls forces. The exfoliation process has been focused primarily on intercalation, chemical derivatization, thermal expansion and oxidation of graphite, and the most common approach is the use of strong oxidizing agents[4]. Currently, there are four main methods of solution-based preparation of graphene oxide: *i)* the Staudenmaier[8] method that improves Brodie one by adding potassium perchlorate and sulfuric acid; *ii)* the Hofmann[8] method, which utilizes non-fuming nitric acid; *iii)* the Hummers[8] method, a safer alternative that produces nitric acid in the reaction vessels; and *iv)* the Tour[8] method, which omits the use of nitric acid through an oxidation mixture of potassium permanganate, concentrated sulfuric acid and phosphoric acid. Notably, all the above-mentioned synthetic routes may be grouped into permanganate oxidant-based (Hummers and Tour) and chlorate oxidant-based (Staudenmaier and Hofmann) methods. All

these synthetic methods highlight that, depending on the amount, type and location of the oxygen functional groups, GO will exhibit a different behavior, either when used directly (*e.g.* catalysis) or when it is subjected to further reduction treatment (groups located on the basal plane are most reactive on thermal reduction then groups located on the edges)[9]. For instance, Pumera and his group have deeply investigated the influence of different synthetic routes on the properties of graphene oxide[8,10]. These studies showed that GO synthesized by permanganate oxidant has a lower C-to-O ratio and a higher amount of carbonyl and carboxyl groups with respect to GO made by chlorate-based oxidant, as confirmed by XPS, elemental and ^{13}C -NMR analyses.

Thus, due to the fact that O-containing groups are the anchor point for the functionalization of GO, permanganate oxidant-based method will be adopted, in particular modified Hummers method will be used in the present research work. Specifically, this method makes use of the traditional Hummers reagents with an additional amount of $NaNO_3$, $KMnO_4$ and H_2O_2[9]. Despite intensive research, the mechanism of GO formation remains unclear. Most of the reported theoretical studies[11,12] focused on the changing in graphene structure, due to the introduction of oxygen atoms and the formation of C-O bonds. These studies consider both graphene and the oxidizing agent as free-standing species with no interaction with their surroundings. However, GO is produced from bulk graphite, where individual layers are closely aligned and stacked. To attack graphene layers, the oxidizing agent needs to first penetrate between those layers. Notably, in the conversion process of bulk graphite to GO, different steps can be identified[13]. The first step is the conversion of graphite to the sulfuric acid-graphite intercalation compound, which begins immediately upon exposing graphite to the acidic oxidizing medium. The second step involves the conversion of the intercalation compound into the oxidized form of graphite, a process significantly slow. In order to achieve a higher oxidation degree, $KMnO_4$ is added to the reaction. Then, the mixture becomes green due to the formation of the oxidizing agent MnO_3^+. The third step is the conversion of the oxidized form of graphite to GO by reaction with water: this is the exfoliation process, which involves sulphate hydrolysis from GO-sulphate structure[14]. $NaNO_3$ is an oxidizing agent and it is used to enhance the effect of H_2SO_4 in the presence of $KMnO_4$[15]. Residual permanganate and manganese dioxide are reduced by using hydrogen peroxide[16].

Nevertheless, the role of H_2O_2 has been recently studied and revised. Yoo *et al.*[2], actually, reported that hydrogen peroxide causes a large number of π-conjugated carbon radicals, by the reaction of hydroxyl radicals from the H_2O_2 to the double bonds of the disrupted p-conjugated plane of GO. This implies that excessive hydrogen peroxide would possibly affect the chemical structure of GO due to the large number of the radical generation. Kumar *et al.*[1]

verified that GO gets more exfoliated as the concentration of H_2O_2 increases. The exfoliation mechanism has been reported to follow these steps:

(a) when H_2O_2 is added to the mixed solution, KOH is formed;
(b) the OH^- ions, present in the aqueous solution of KOH, can react with other H_2O_2 molecules and form O_2^{2-} ions;
(c) the as-produced O_2^{2-} ions can intercalate into graphite layers and exfoliate it to the final graphene oxide;
(d) the oxidation of water also generates hydroxyl ($OH^\bullet$) and oxygen ($O^\bullet$) radicals. These radicals open up the edge sheets of graphite and subsequently promote the modification of interlayer thickness of the graphite sheets.

In this context, a fine investigation on the tailoring of GO features by tuning the starting graphite type and the concentration of hydrogen peroxide will be conducted herein, in order to elucidate their role and to fabricate a suitable support for the further growth of the MOS nanoparticles.

3.2. The role of graphite

In this paragraph, the role played by the starting graphite reagent will be deeply explored. Specifically, two different types were adopted: a powder (G) and a flake-like (GF) one (see SEM images in Fig. 3.1), by keeping constant the concentration of H_2O_2, *i.e.* 30 %wt (as widely reported for the modified Hummers method[8,17]).

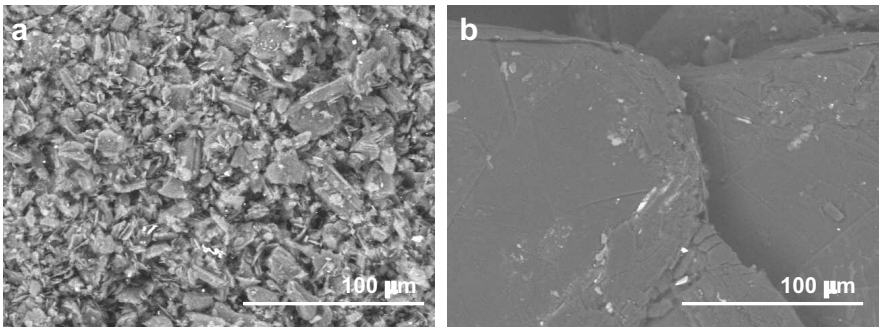

Figure 3.1. *SEM micrographs of pristine (a) powder and (b) flake-like graphite, used in the modified Hummers method.*

Herein, structural properties by XRPD analysis were mainly studied to verify the effective fabrication of graphene oxide sheets. Thus, Figure 3.2 shows a comparison among the x-ray lines of pure starting graphite samples (G and GF) and the relative synthesized GO.

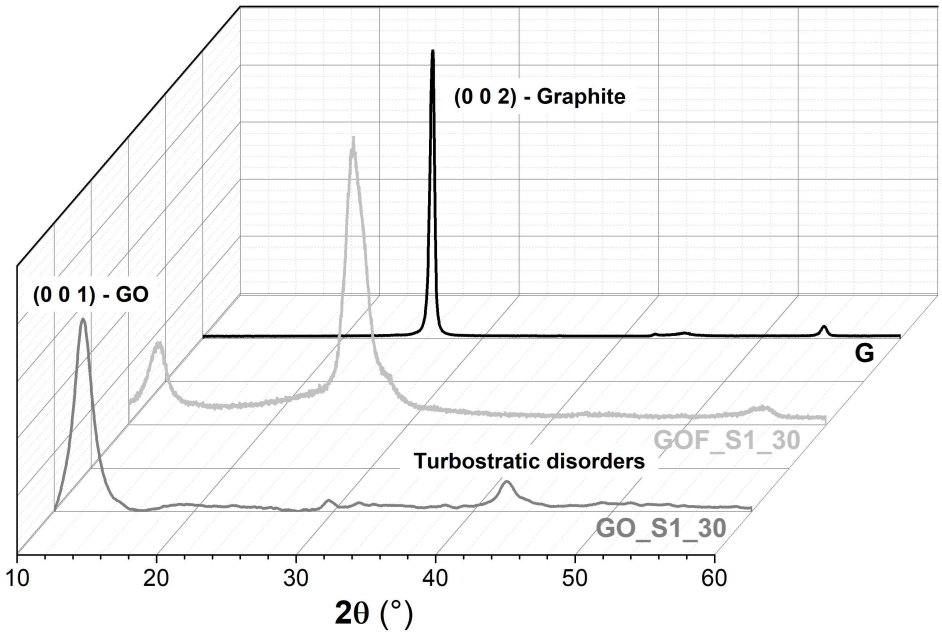

Figure 3.2. *Comparison of XRPD patterns relative to pure graphite (both powder, G and flake-like, GF have the same pattern), graphene oxide samples, fabricated starting from powder-graphite (GO_S1_30) and flake-like one (GOF_S1_30). The 100% reflection planes of the two compounds have been highlighted, accordingly. GOF_S1_30 spectrum clearly shows the presence of peak at around 26.7° ascribable to the starting graphite. The two graphene oxide samples were synthesized by adopting the modified Hummers method, that contemplates the use of H_2O_2 30 %wt.*

The main diffraction peak for graphite (both powder and flake-like) (0 0 2) is centred at 2θ = 26.7° with a corresponding layer-to-layer distance of about 0.333-0.335 nm (see in the following, Fig. 3.5c), as already reported in the literature (ca 0.340 nm)[1]. After the oxidation of powder graphite, the (0 0 1) diffraction plane peak of graphene oxide (GO_S1_30) appeared at around 2θ = 12.0° corresponding to a layer-to-layer distance of around 0.880 nm (Fig. 3.5d). The patterns showed a larger interlayer spacing probably due to the insertion of oxygen-containing functional groups between the layers[1]. Conversely, for GOF_S1_30, a well-observable peak (at ca 26.4°) relative to the starting graphite is still present, underlining an incomplete oxidation. This may be due to the morphology of the graphite materials: the contact area between spherical aggregates of ca 10 μm dimensions (G; Fig. 3.1a) and the oxidizing agents is much higher, than the one with few millimetres flakes (GF; Fig. 3.1b). Moreover, in GO_S1_30 pattern, a small and broad diffraction peak at around 42.3° appeared. According to Emiru *et al.*[18], it indicates that graphene oxide exhibits turbostratic disorders, *i.e.* the slipping

of basal planes out of alignment. Hence, since a well-defined XRPD spectrum was obtained starting from powder graphite, it will be used for the further investigations.

3.3. The role of hydrogen peroxide

To determine the contribution of the H_2O_2 to the structural, surface and optical features of the synthesized GO, XRPD, Raman, UV/Vis spectroscopy and BET-BJH analyses were carried out, respectively.

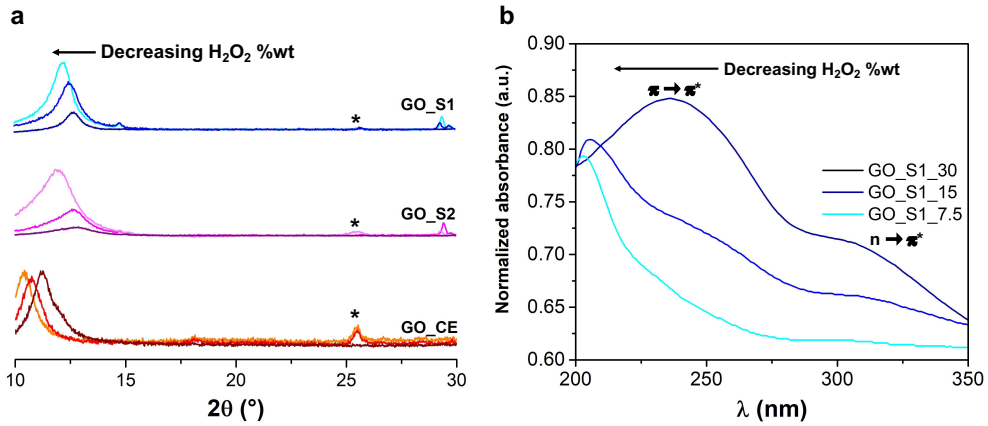

Figure 3.3. *(a) Comparison among XRPD lines of GO series prepared starting from the three adopted hydrogen peroxide reagents (see A.1.1 paragraph for the synthetic route). For each H_2O_2, three different concentrations were investigated (i.e. 7.5, 15.0 and 30.0 %wt). In the case of the lowest one, only a partial oxidation was observed, as the peak at around 26.7° ascribable to the starting graphite (0 0 2) is still observable (∗ in the spectra). (b) Comparison of UV/Vis spectra for the GO_S1 series. A blue-shift of the main peaks at around 230 nm ($\pi \rightarrow \pi^*$ transition in C=C bond) and 300 nm ($n \rightarrow \pi^*$ transition in C=O bond) was noticed by reducing of H_2O_2 concentration.*

Notably, three different H_2O_2 stocks (namely, Sigma-Aldrich S1, Sigma-Aldrich S2 and Carlo Erba CE) were adopted and, within the same stock, three different concentrations (*i.e.* 7.5, 15.0 and 30.0 %wt) were studied. Particularly, regarding the x-ray lines (Fig. 3.3a), as already observed by Yoo *et al.*[2], it is noticeable a small shift of the (0 0 1) GO peak towards lower 2θ values. This deviation can be attributed to several factors: *i*) it is known that the carbon atoms interactions become different depending on the oxidation degree. Thus, the different interlayer connectivity force between carbon atoms causes the deviation of the diffraction positions as a result of the different thermal vibrations[2]; *ii*) secondly, a reduced quantity of oxygen functional groups allows the vibrations across the horizontal-axis to be more violent than the vibrations along the vertical-axis. This leads to deviations of the diffraction peaks positions[2]. Furthermore, in lighter spectra of Figure 3.3a (corresponding to

7.5 %wt of H_2O_2), the peak at 2θ around 26.7° ascribable to the starting (0 0 2) graphite plane, is still observable. Hence, also here, an incomplete oxidation occurred.

Instead, as concern the GO optical features, Figure 3.3b displays the UV/Vis spectra with the decreasing of the hydrogen peroxide concentrations (herein, only Sigma-Aldrich S1 GO have been reported as a representative example). Firstly, the absorption spectrum of GO_S1_30 shows an absorption peak at 236 nm due to the π–π* transition of the C=C bonds and a shoulder at 299 nm, corresponding to the n-π* transition of the C=O bonds[1]. Interestingly, with the decreasing of H_2O_2 concentration (*i.e.* GO_S1_15 and GO_S1_7.5), a blue-shift was observed and, in GO_S1_7.5 spectrum, the shoulder relative to n-π* transition almost disappeared. Moreover, it can be seen from Figure 3.3b, that the peaks intensity gradually decreased with the reduction of H_2O_2 concentration. Kumar *et al.*[1] reported that the electronic properties of GO are profoundly affected by the charge distribution and the formation of hydrogen bonds, caused by the different amount of OH and O, relative to the oxygen-containing groups present on its surface. Hence, after oxidation, GO becomes a mixture of sp^2 and sp^3 carbon domains: the former is joined to the neighboring carbon atoms, the latter is bound to the adjacent oxygen-containing functional groups. Therefore, the presence of electronegative oxygen species can distort the π-network symmetry, leading to a strong change in the GO electronic features and, in particular, a band gap at the Brillouin Zone boundary can be formed[1]. It has been also reported that the presence of O-containing functional groups may induce localized states in π–π* band gap, causing transitions between these defect-induced states[1]. Therefore, the observed behavior reflects the changes in functional groups proportion after the treatment of different H_2O_2 concentrations, thus influencing the optical and the electronic features of GO. Notably, the blue-shifting of π–π* transition, with the decreasing of H_2O_2 concentration, suggests that the contribution of sp^3 hybridized domains (bound to -OH groups) gradually increases to the detriment of aromatic sp^2 ones (in particular -COOH moieties)[1].

Once investigated the structural and optical features, GO surface properties were elucidated. Specifically, the specific surface area (S_{BET}) of pristine graphite is about 11 $m^2\ g^{-1}$ (Table 3.1, 2nd column), in accordance with the reported literature[19]. After its oxidation/exfoliation process, two major observations can be made: *i*) by using three different stocks of H_2O_2, slightly diverse surface area values were obtained, and this may be due to the presence of some impurities in the starting reagent; *ii*) by decreasing the hydrogen peroxide concentration, S_{BET} seems to smoothly enhance.

Sample	S_{BET} ($m^2\ g^{-1}$)	$V_{tot.\ pores}$ ($cm^3\ g^{-1}$)
G	11	0.030
GO_S1_7.5	60	0.060
GO_S1_15	58	0.020
GO_S1_30	15	0.021
GO_S2_7.5	46	0.050
GO_S2_15	30	0.040
GO_S2_30	44	0.034
GO_CE_7.5	30	0.012
GO_CE_15	28	0.008
GO_CE_30	16	0.007

Table 3.1. *Specific surface area (S_{BET}) and total pores volume ($V_{tot.\ pores}$) relative to the as-synthesized GO (see A.1.1 paragraph for the synthetic route).*

Besides, notwithstanding this parameter should be much higher (about 500 $m^2\ g^{-1}$[20]), the obtained values could be explained since GO interlayer spaces are often inaccessible to N_2 molecules in a few-layered GO structure, thus underestimating the real active surface area[21]. Furthermore, the shape of the GO hysteresis loop has two distinctive behaviours (Fig. 3.4a): *i)* the adsorption branch resembles a Type II isotherm, in which the thickness of the adsorbed multilayer (at higher relative pressure) generally appears to increase without limit, when p/p_0 tends to 1; *ii)* the hysteresis loop is typical of Type IV isotherm and it could be explained by condensation of nitrogen molecules into mesopores that exceeds a certain critical width[22]. This type of isotherm is related to aggregates of platelet-like particles giving rise to slit-shaped pores[23] with an average pore diameter below 5 nm (Fig. 3.4b).

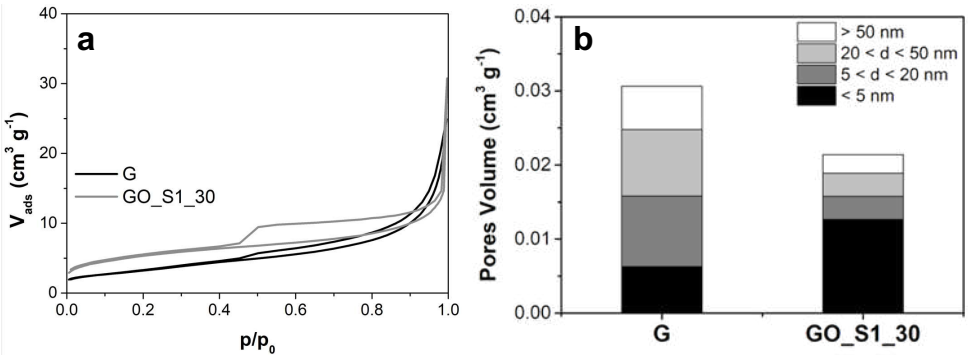

Figure 3.4. *(a) BET isotherms comparison between powder graphite (G) and GO_S1_30 (as representative sample). (b) A comparison of pores volume distribution between G and GO_S1_30 powders.*

In addition, the total pores volume decreases upon oxidation, and slightly increases with the reducing of H_2O_2 concentration (Table 3.1, 3rd column). As expected, both the oxidation and exfoliation processes are very strong treatments, giving rise to GO powders with lower

total pores volume (0.021 cm^3 g^{-1}; Table 3.1, 3rd column and Fig. 3.4b) with respect to the starting graphite (0.030 cm^3 g^{-1}); alongside with an increment of pores below 5 nm. This is a probable consequence of the very exothermic reaction leading to a collapse of the void space.

Hence, in the following and for the synthesis of all the composite nanomaterials, the 30 %wt H_2O_2 will be adopted, due the high content of oxygen-containing groups present on the relative synthesized GO material. Therefore, these O-pendants can represent the optimal anchoring points for the further growth of MOS nanoparticles.

3.4. Physico-chemical properties of GO_S1_30

GO_S1_30 was chosen to deeply study graphene oxide structural, morphological, surface and electrochemical features.

Firstly, the surface texture, displayed in SEM or TEM images of Figs. 3.5a–d, confirm the effective graphite oxidation and its exfoliation, resulting in the formation of clearly visible GO micrometric multi-stack sheets. Moreover, by SAED technique, the interlayer distances increase from 0.333-0.335 nm of the (0 0 2) peak relative to the starting graphite, to ca 0.880 nm of the (0 0 1) GO peak.

A further assessment of the fabrication of GO sheets was obtained by means of spectroscopic analyses (specifically FTIR and Raman ones). Regarding the former, Figure 3.5e (grey line) shows the typical GO bands at 1045, 1220, 1620 and 1715 cm^{-1} related to the stretching modes of C-O-C, C-O, C=C and C=O bonds, respectively[24], which are absent in the graphite spectrum (black line).

Furthermore, by deconvoluting the Raman spectra of both the precursor graphite and the as-prepared graphene oxide (Figs. 3.5g,h), the successful oxidation is corroborated by the shifting of the D and G bands as well as by the variation of their intensity ratio (I_D/I_G). Notably, the D band is connected to a disordered structure, originated by structural defects, edge effects and dangling sp^2 carbon bonds that break the symmetry, while the G peak results from the first order scattering of E_{2g} mode of the sp^2 carbon domains[25]. Both bands position and intensity depend on several factors, such as the doping level, the number of layers and the presence of structural defects[26]. Here, in the pristine graphite the D and G peaks positions are centered at 1347 and 1576 cm^{-1}, while for GO they appear at 1310 and 1564 cm^{-1}, respectively (Figs. 3.5g,h).

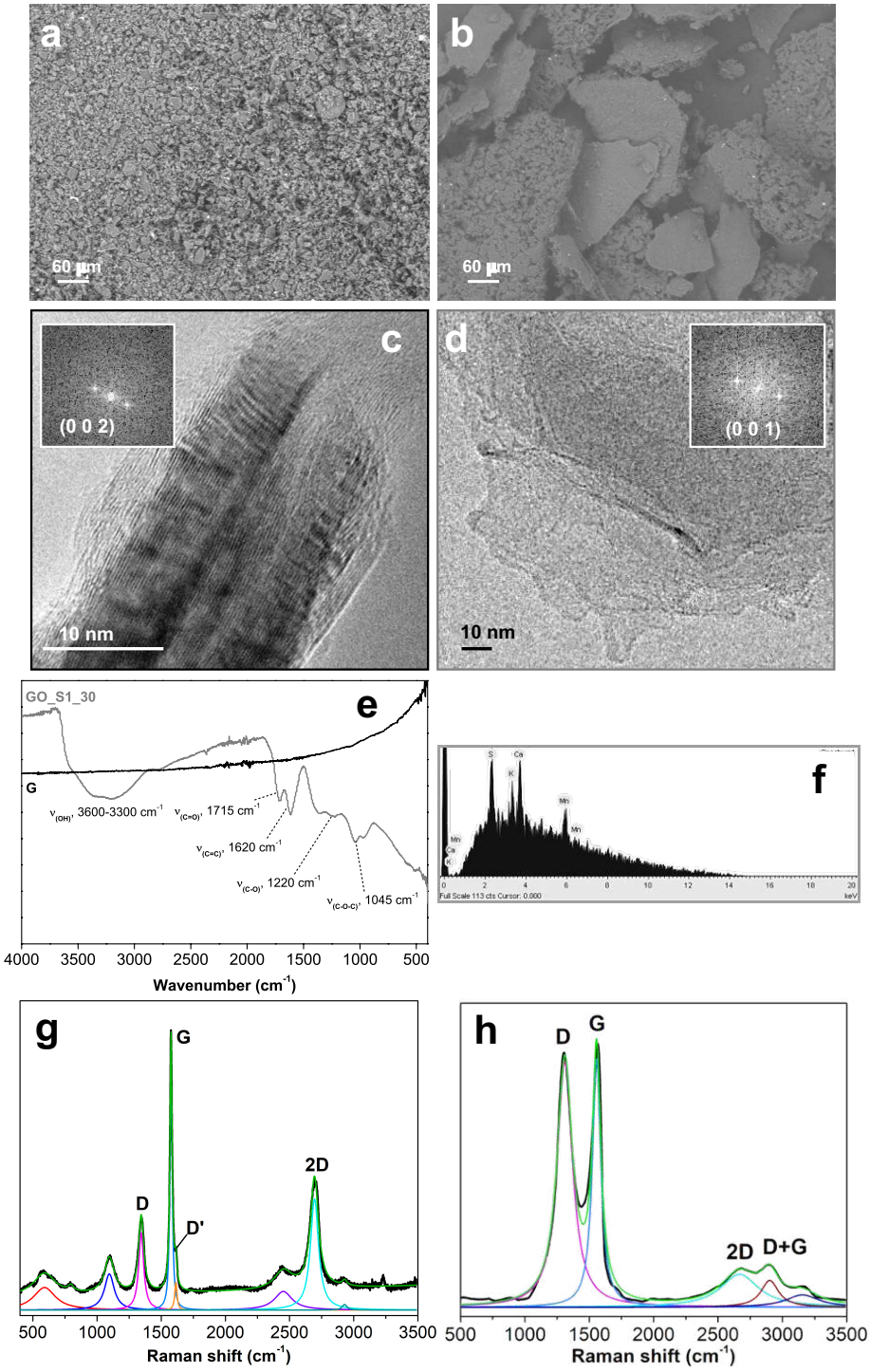

Figure 3.5. *SEM micrographs of (a) graphite and (b) graphene oxide powders. TEM images of (c) pristine graphite and (d) graphene oxide sheets (inset: SAED images of the main phases diffraction planes). (e) Corroboration of the*

effective fabrication of the graphene oxide material by means of FTIR spectroscopy. The main stretching modes have been highlighted, accordingly. (f) EDX output relative to GO_S1_30 powder. Fitted Raman spectra of (g) G graphite and (h) GO_S1_30 graphene oxide, with their relative deconvolution in eight and five modes by using the Lorentzian function.

Moreover, the GO I_D/I_G ratio is ~1 (*i.e.* about four times the one of graphite), a value typically reported for this compound since, during the oxidation process, oxygen functional groups were introduced into the graphitic chain causing a rise in the D band intensity[27]. Finally, EDX spectrum reported in Figure 3.5f reveals the presence of some impurities (such as manganese, potassium, sulfur), probably ascribable to the reagents used in the synthetic procedure.

Figure 3.6a shows the thermogravimetric plot relative to GO_S1_30 material. Notably, it decomposes in several stages. First a weight loss due to moisture and interstitial water occurs between 60 and 110 °C. The thermal stability of adsorbed water is influenced by its interaction with oxygen-containing groups on the GO surface[28]. A significant weight loss of ~30% is observed at around 200 °C, which corresponds to the pyrolysis of labile oxygen-containing groups with the generation of CO, CO_2 and water[29]. The sharp loss at around 480 °C is caused by the breakage of sp^2 carbon bonds in the hexagonal structure, thus indicating its thermal decomposition[28]. Alongside with TGA analysis, a potentiometric titration was carried out to estimate the acidity of the GO surface, giving an idea of the amount of hydroxyl, carbonyl, carboxylic moieties. Interestingly, Figure 3.6b displays two inflection points: the first one (at 1.35 mL of HCl 0.01 M) corresponds to the titration of the residual NaOH, remained in the solution after the neutralization of the total acidity. On the contrary, the second inflection point (at 4.95 mL) is characteristic of desorbed acid, *i.e.* acidic moieties intrinsically present on GO surface that, after basic treatment, have been released into the solution. Hence, in order to determine the covalent acidity, namely the acidity connected to the oxidation of graphite into GO, it is necessary to subtract the desorbed acidity (due to the released acid moieties) to the total acidity (total NaOH consumption). Therefore, the covalent acidity obtained for GO_S1_30 was equal to 4.1 mmol g_{GO}^{-1} (see Table 3.2).

To further provide a corroboration of the highest content of the O-terminating groups with the increasing of the H_2O_2 concentration, potentiometric titrations were carried out on GO_S1-series. The relative data are reported in Table 3.2.

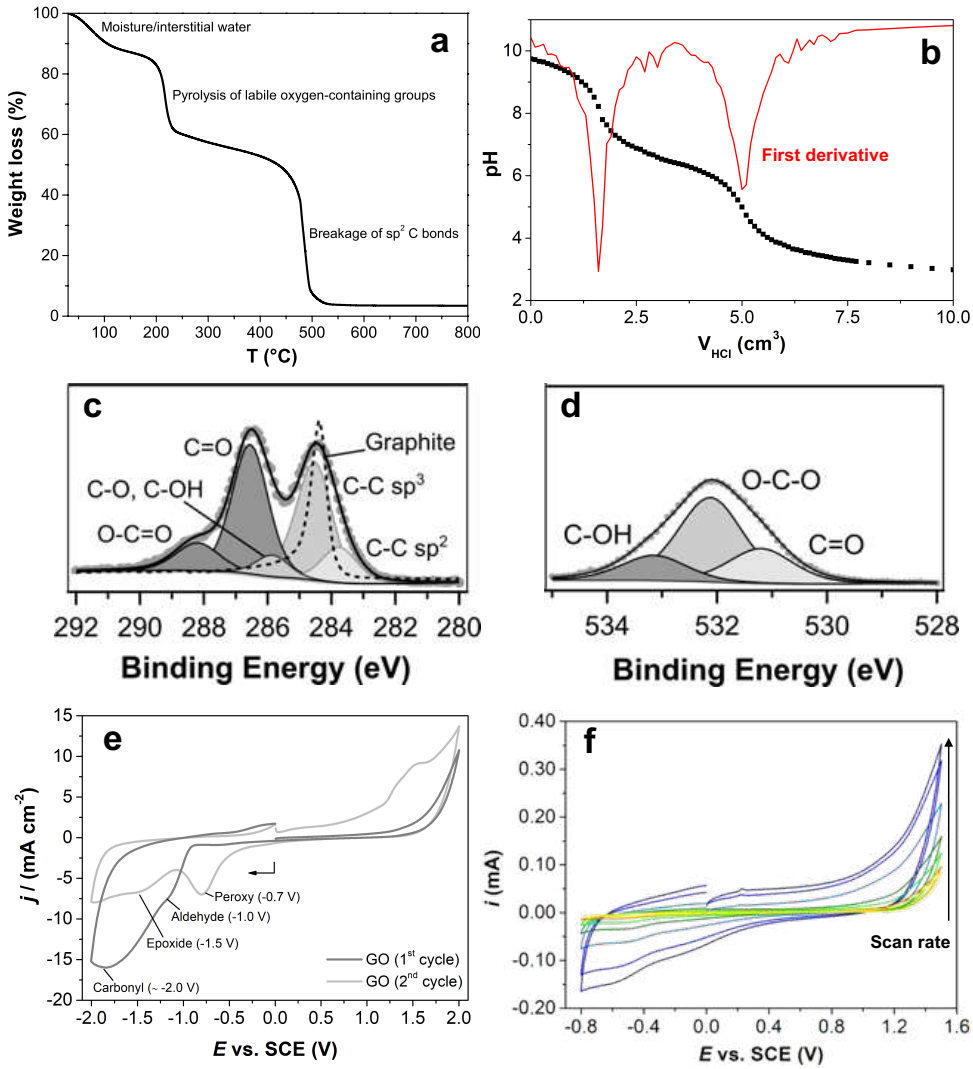

Figure 3.6. *(a) Thermogravimetric spectrum of GO_S1_30, alongside with the association of the weight losses to the physical/chemical decomposition steps. (b) Potentiometric titration plot, alongside with the relative first derivative of graphene oxide titrated with 0.1 M NaOH. The first peak on the left is related to the residual NaOH, whereas the one on the right to desorbed acid moieties. XP spectra of (c) C 1s (graphite, black dotted line) and (d) O 1s regions of GO_S1_30. (e) Cyclic voltammograms of GO-modified glassy carbon, performed in 0.1 M PBS electrolyte (pH 7.4) with a scan rate of 100 mV s^{-1}. The main oxygen-containing groups, present on the material surface, have been underlined, accordingly. (f) CVs relative to GO-modified glassy carbon in the presence of 3 mM $[Ru(NH_3)_6]Cl_3$ probe, at different scan rates (10, 20, 50, 100, 200, 500 and 750 mV s^{-1}). 0.1 M PBS electrolyte (pH 7.4).*

Once again, GO_S1_30 showed the greatest covalent acidity, resulting in the sample with the highest number of O-functional groups on the graphene oxide surface.

Sample	Covalent Acidity (mmol g_{GO}^{-1})
GO_S1_7.5	3.5
GO_S1_15	3.8
GO_S1_30	4.1

Table 3.2. *Covalent acidity by potentiometric titration of GO_S1-samples (with the increasing of H_2O_2 concentration in the synthetic route).*

Besides, an estimation of the types of the surface O-containing groups was obtained by XPS measurements. Figure 3.6c shows the C 1s core level high resolution spectrum, which is fitted by five components corresponding to carbon atoms in different functional groups. Especially, the C–C sp^3 band appears at 283.75 eV, the C–C sp^2 at 284.55 eV, the C in C–O, C–OH bonds at 285.85 eV, the carbonyl C=O at 286.55 eV and the carboxylate carbon O=C–O at 288.20 eV[30,31]. Similarly, the O 1s core level high resolution spectrum (Fig. 3.6d) consists of three components relative to C=O (at 531.20 eV), O–C–O (at 532.10 eV) and C–OH (at 533.15 eV)[32]. Once again, the effective accomplishment of graphite conversion into GO is well observable in Figure 3.6c, where G has a single peak (black dotted line) ascribable to C–C sp^3 bonds.

A further corroboration was acquired by electrochemical analyses. Indeed, the characteristic functional groups present on the surface of the graphene oxide were deeply investigated by cyclic voltammetric measurements (Figure 3.6e). GO is intrinsically electroactive since its great amount of oxygen functionalities can be electrochemically oxidized and reduced. Therefore, CV may be used to determine the nature of these oxygen-containing groups. As reported by Pumera *et al.*, by scanning the potentials from the negative (down to -2.0 V) to the positive (up to +2.0 V) values, peroxyl, aldehydic, epoxy and carbonyl groups can be assessed[33]. Particularly, the GO reduction begins at about -1.0 V with two identifiable peaks (*i.e.* -1.0 and -2.0 V) which may be related to aldehyde and carbonyl groups, respectively (Fig. 3.6e)[33]. However, these reduction peaks could be only observed during the initial reduction (Fig. 3.6e, dark grey line). Moreover, by further scanning the reductive sweep, two other peaks could be observed at around -0.7 and -1.5 V, ascribable to two other oxygen-containing moieties (*i.e.* peroxyl and epoxy groups) (Fig. 3.6e, light grey line)[33]. As a final characterization, since GO is widely reported to be a potential supercapacitor[1,22], the capacitance has been evaluated by performing CV measurements at different scan rates (Fig. 3.6f). Indeed, the presence of functional groups can increase the number of hydrophilic polar sites that, in turns, enhances the material capacitance[1]. In the present case, GO_S1_30 possesses an electrical capacitance of about 0.45 μF, a value comparable to the one reported in the literature[1].

3.5. Conclusions

Herein, graphene oxide powders, synthesized through a modified Hummers method by varying the starting graphite and the concentration of hydrogen peroxide, were reported. Notably, powder-like graphite seems to be better for its oxidation/exfoliation processes and 30 %wt of H_2O_2 guarantees the full accomplishment of the GO formation, as corroborated by structural, morphological, optical and surface properties. Moreover, thanks to both potentiometric titrations and electrochemical measurements, an estimation of the amount and type of oxygen-containing groups, present on the synthesized GO surface, was obtained. Starting from these outcomes, the as-prepared GO (30 %wt H_2O_2) represents a promising support for the further growth of metal oxide nanoparticles.

References

[1] S. Kumar, B. Baruah, A. Kumar, *Mater. Today Commun.* **2017**, *13*, 26.

[2] M. J. Yoo, H. B. Park, *Carbon N. Y.* **2019**, *141*, 515.

[3] R. Maiti, A. Midya, C. Narayana, S. K. Ray, *Nanotechnology* **2014**, *25*, 495704.

[4] D. C. D. Marcano, D. D. V. Kosynkin, J. M. J. Berlin, A. Sinitskii, Z. Sun, A. Slesarev, L. B. Alemany, W. Lu, J. M. Tour, *ACS Nano* **2010**, *4*, 4806.

[5] W. Gao, *Graphene Oxide*; Gao, W., Ed.; Springer International Publishing: Cham, 2015.

[6] Z. L. Chen, F. Y. Kam, R. G. S. Goh, J. Song, G. K. Lim, L. L. Chua, *Chem. Mater.* **2013**, *25*, 2944.

[7] B. C. Brodie, *Philos. Trans. R. Soc. London* **1859**, *149*, 249.

[8] H. L. Poh, F. Šaněk, A. Ambrosi, G. Zhao, Z. Sofer, M. Pumera, *Nanoscale* **2012**, *4*, 3515.

[9] C. Botas, P. Álvarez, P. Blanco, M. Granda, C. Blanco, R. Santamaría, L. J. Romasanta, R. Verdejo, M. A. López-Manchado, R. Menéndez, *Carbon N. Y.* **2013**, *65*, 156.

[10] C. K. Chua, Z. Sofer, M. Pumera, *Chem. - A Eur. J.* **2012**, *18*, 13453.

[11] C. N. Peter, W. W. Anku, S. K. Shukla, P. P. Govender, *Theor. Chem. Acc.* **2018**, *137*, 75.

[12] S. S. Varghese, S. H. Varghese, S. Swaminathan, K. K. Singh, V. Mittal, **2015**, 651.

[13] A. M. Dimiev, J. M. Tour, *ACS Nano* **2014**, *8*, 3060.

[14] A. Dimiev, D. V. Kosynkin, L. B. Alemany, P. Chaguine, J. M. Tour, *J. Am. Chem. Soc.* **2012**, *134*, 2815.

[15] S. A. El-Khodary, G. M. El-Enany, M. El-Okr, M. Ibrahim, *Electrochim. Acta* **2014**, *150*, 269.

[16] W. S. Hummers, R. E. Offeman, *J. Am. Chem. Soc.* **1958**, *80*, 1339.

[17] J. Song, X. Wang, C.-T. Chang, *J. Nanomater.* **2014**, *2014*, 1.

[18] T. F. Emiru, D. W. Ayele, *Egypt. J. Basic Appl. Sci.* **2017**, *4*, 74.

[19] M. P. Trammell, P. J. Pappano, **2011**, 1.

[20] S. Stankovich, D. A. Dikin, R. D. Piner, K. A. Kohlhaas, A. Kleinhammes, Y. Jia, Y. Wu, S. B. T. Nguyen, R. S. Ruoff, *Carbon N. Y.* **2007**, *45*, 1558.

[21] T. Szabó, E. Tombácz, E. Illés, I. Dékány, *Carbon N. Y.* **2006**, *44*, 537.

[22] T. Gao, W. Xu, L. Gong, Z. Wang, Z. Yang, Y. Song, Y. Xiong, *RSC Adv.* **2015**, *5*, 33767.

[23] K. S. W. Sing, D. H. Everett, R. A. W. Haul, L. Moscou, R. S. Pierotti, J. Rouquerol, T. Siemieniewska, *Pure Appl. Chem.* **1985**, *57*, 603.

[24] J. Chen, B. Yao, C. Li, G. Shi, *Carbon N. Y.* **2013**, *64*, 225.

[25] K. N. Kudin, B. Ozbas, H. C. Schniepp, R. K. Prud'homme, I. A. Aksay, R. Car, *Nano Lett* **2008**, *8*, 36.

[26] R. Ramachandran, M. Saranya, P. Kollu, B. P. C. Raghupathy, S. K. Jeong, A. N. Grace,

Electrochim. Acta **2015**, *178*, 647.

[27] A. A. Dubale, W.-N. Su, A. G. Tamirat, C.-J. Pan, B. A. Aragaw, H.-M. Chen, C.-H. Chen, B.-J. Hwang, *J. Mater. Chem. A* **2014**, *2*, 18383.

[28] E. T. Mombeshora, P. G. Ndungu, V. O. Nyamori, *New Carbon Mater.* **2017**, *32*, 174.

[29] X. Cai, Q. Zhang, S. Wang, J. Peng, Y. Zhang, H. Ma, J. Li, M. Zhai, *J. Mater. Sci.* **2014**, *49*, 5667.

[30] S. Muralikrishna, K. Sureshkumar, T. S. Varley, D. H. Nagaraju, T. Ramakrishnappa, *Anal. Methods* **2014**, *6*, 8698.

[31] L. Tang, X. Li, R. Ji, K. S. Teng, G. Tai, J. Ye, C. Wei, S. P. Lau, *J. Mater. Chem.* **2012**, *22*, 5676.

[32] M. C. Hsiao, C. C. M. Ma, J. C. Chiang, K. K. Ho, T. Y. Chou, X. Xie, C. H. Tsai, L. H. Chang, C. K. Hsieh, *Nanoscale* **2013**, *5*, 5863.

[33] A. Y. S. Eng, A. Ambrosi, C. K. Chua, F. Šaněk, Z. Sofer, M. Pumera, *Chem. - A Eur. J.* **2013**, *19*, 12673.

Chapter 4

3D – Metal oxides-based Nano-heterojunctions: synthesis and application

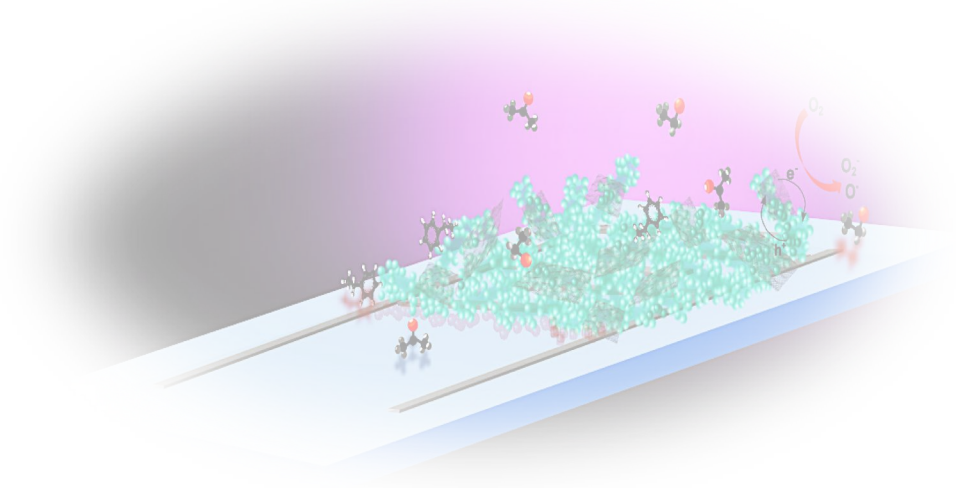

"Do not judge me by my successes, judge me
by how many times I fell down and got up again"

— Nelson Mandela

4.1. Zinc oxide-based materials

4.1.1. Introduction

As stated in Chapter 1, herein, nanostructured detectors based on an intimate incorporation of p-type GO nanodomains in an n-type 3D ZnO nano-architecture will be deeply investigated. The properties of these ultraporous nano-heterojunction networks will be finely characterized by a set of physical and chemical approaches, providing insights into the role of GO in enhancing or inhibiting the chemical sensing mechanism of the networks. Particularly, these nanocomposite materials will be used to sense some representative VOCs such as ethanol (EtOH), acetone, ethylbenzene (EtBz) and toluene, down to room temperature by exploiting the UV light activation of the sensing reactions[1].

4.1.2. ZnO-GO 3D-networks properties

In order to have an overview on the role played by the GO material, a comprehensive range of ZnO-GO nanocomposite structures were synthesized varying the ZnO/GO ratio from 4 to 32 (specifically, 4:1, 8:1, 16:1 and 32:1). Notably, within all this paragraph, the adopted graphene oxide will be GO_S1_30. Hence, for simplicity, it will be labelled as GO.

Specifically, zinc oxide nanoparticles were grown on the GO surface by exploiting its abundant oxidized groups. A set of structural analyses, comprising XRPD, FTIR and Raman ones (see Figure 4.1), evidenced the actual presence and progressive growth of the ZnO nanodomains by increasing the Zn salt precursor concentration-to-GO weight ratio from 4 to 32. In particular, the XRPD spectra (Fig. 4.1a) show the main zinc oxide polymorphic phase, *i.e.* wurtzite[2,3], for both the hybrid compounds with the ZnO crystal size increasing from 11 to 44 nm with the increasing ZnO/GO ratio from 0 to 32:1, thus approaching the value for pure ZnO of 77 nm (Table 4.1, 1st column; Fig. A.11 in the Appendix Chapter). Notably, as clearly observable in "difference spectra" of Figure A.11 (green line), experimental data are in accordance with the wurtzite structure fitting model (red line) and the calculated cell

parameters, obtained by Rietveld refinement, are consistent with the theoretical values (JCPDS n. 36-1451[4]).

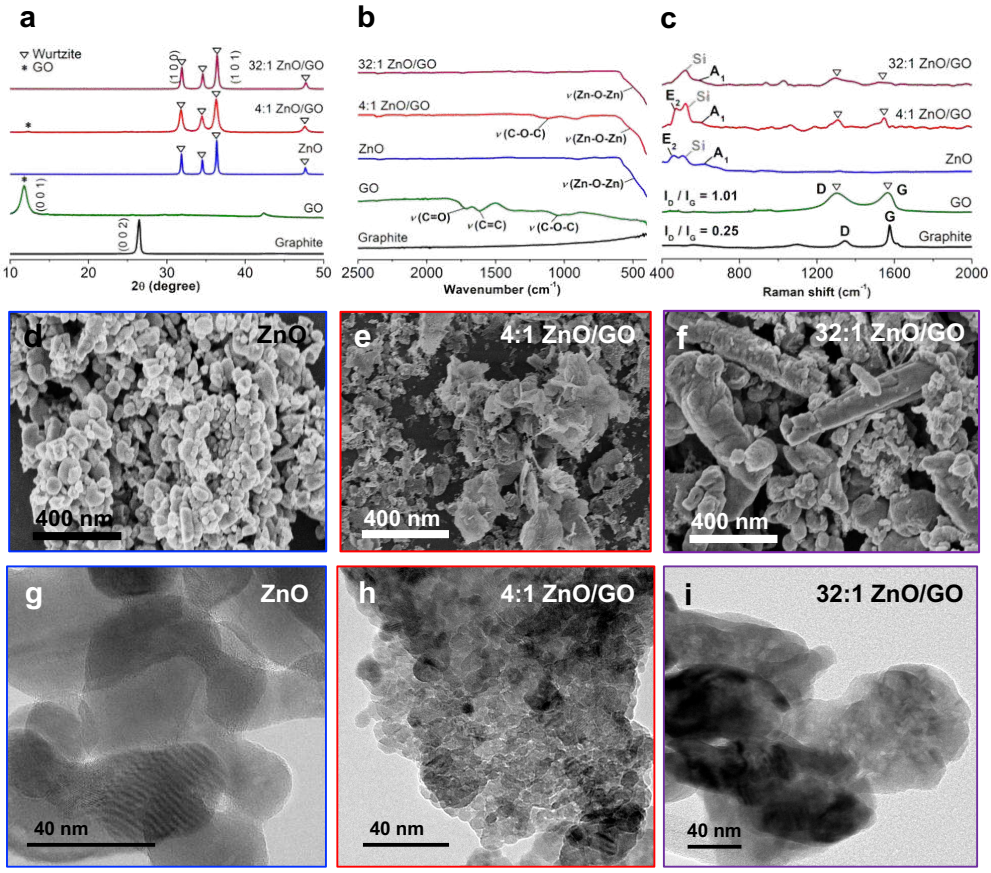

Figure 4.1. *(a) XRPD patterns of graphite (G), graphene oxide (GO), pure ZnO and hybrid ZnO/GO nanocomposites (100% intensity reflection planes have been assigned to the main phase of each compound). (b) FTIR and (c) Raman spectra (in the case of ZnO-based compounds, Si Raman band[5] due to the adopted support has been highlighted in grey color) of all the investigated samples. SEM micrographs and TEM images of (d,g) pure ZnO, (e,h) 4:1 ZnO/GO and (f,i) 32:1 ZnO/GO.*

The FTIR and Raman analyses further confirm the x-ray diffraction trend (Figs. 4.1b,c). Particularly, the infrared stretching mode of the Zn-O-Zn bonds (at ~500 cm^{-1}) appears in all the zinc oxide-containing samples. Parallelly, the Raman spectra of both pure ZnO and hybrid compounds show A_1 LO (at 594 cm^{-1}) and E_2 high (at 454 cm^{-1}) bands relative to ZnO particles[6]. However, especially in the case of the 4:1 ZnO/GO ratio, all the structural analyses reveal the presence of a small quantity of the graphene oxide sheets underneath the ZnO

nanoparticles (Fig. 4.1a–c, red line). In contrast, this is gradually less visible passing from 8:1 to 32:1 sample, in which GO is not detectable at all.

Sample	<d^{XRPD}> (nm)	S_{BET} ($m^2\ g^{-1}$)	$V_{tot.\ pores}$ ($cm^3\ g^{-1}$)	E_g (eV)	Capacitance ($F \cdot 10^5$)	Film thickness (μm)	% Film porosity
Graphite	27	11	0.030	–	–	–	–
GO	11	15	0.021	–	4.5	–	–
ZnO	77	9	0.040	3.11	2.4	2.1 ± 0.3	93 ± 1
4:1 ZnO/GO	22	25	0.077	3.07	2.0	5.0 ± 0.6	97 ± 1
8:1 ZnO/GO	33	7	0.025	3.12	2.5	2.5 ± 0.4	94 ± 1
16:1 ZnO/GO	38	6	0.018	3.14	3.0	2.3 ± 0.5	96 ± 1
32:1 ZnO/GO	44	11	0.055	3.10	3.4	2.0 ± 0.1	93 ± 1

Table 4.1. *Crystallite domain size by XRPD analysis (<d^{XRPD}>), surface area (S_{BET}), total pore volume ($V_{tot.\ pores}$), optical band gap (E_g, by Kubelka-Munk extrapolation) and capacitance of the synthesized materials by CV measurements. Thickness (by cross-sectional FESEM) and porosity percentage of the deposited layers (see section A.1.2, in the Appendix Chapter).*

Concerning the surface properties of the as-synthesized ZnO-GO composite materials, the specific surface areas of 4:1 and 32:1 ZnO/GO are higher (25 and 11 $m^2\ g^{-1}$) than that (9 $m^2\ g^{-1}$) of the pure ZnO[7], following a decreasing trend with the increase of ZnO content (Table 4.1, 3rd column). Conversely, 8:1 (7 $m^2\ g^{-1}$) and 16:1 (6 $m^2\ g^{-1}$) ZnO/GO show smaller S_{BET}, very close to the pristine zinc oxide matrix (Table 4.1, 3rd column). A similar trend is also observable for the total pores volume data (Table 4.1, 4th column). Notably, as Figure 4.2a displays, BET isotherms of the composite oxides are comparable to the pure ZnO one, evidencing a H3 hysteresis loop that corresponds to the presence of slit-shaped pores[8].

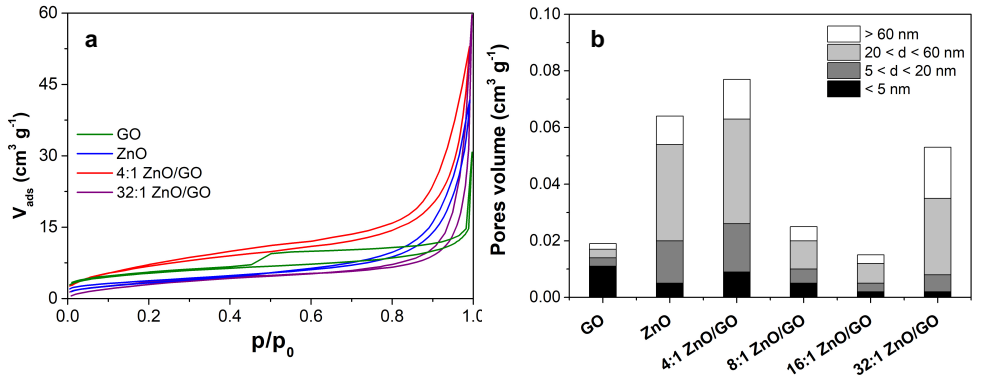

Figure 4.2. *(a) Comparison among BET isotherms relative to pristine GO, ZnO and two of the hybrid materials (namely, 4:1 and 32:1 ZnO/GO). (b) Trend of pores volume distribution with the decreasing of the GO amount integrated in the zinc oxide matrix.*

Furthermore, Figure 4.2b shows the pore volume distribution, which results in a reduction of pores having a diameter lower than 5 nm, with the decreasing of GO content in the zinc oxide matrix. Besides, pores in the range between 20 and 60 nm are predominant in all the composite oxides.

The growth of the ZnO nanoparticles is also confirmed by the SEM/TEM and EDX analyses. In particular, Figures 4.1d–f display a significant change in the material morphology switching from a pure ZnO to a 32:1 and 4:1 ZnO/GO composition. Specifically, the 4:1 sample analysis reveals the presence of flakes (Fig. 4.1e), probably arising by the GO presence, that are not completely covered by the metal oxide. Conversely, with the increasing of the ZnO content, particles tend to agglomerate forming nanorods with diameters of around 80-100 nm and length of up to several hundreds of nanometers (Fig. 4.1f). The 32:1 nanopowder resembles more the pure metal oxide (Fig. 4.1d), which is characterized by agglomerates made of spherical particles with diameters of ~100 nm. By TEM, the 4:1 ZnO/GO ratio shows packed agglomerates with dimensions of around 20 nm (Fig. 4.1h), which are smaller than the 32:1 ratio one, having a size of ~50-60 nm (Fig. 4.1i). Moreover, EDX spectra (Fig. A.12) effectively confirm the presence of zinc species for all the composite materials concentrations.

Besides, the optical properties of the zinc oxide-based compounds were investigated by UV/Vis absorption spectroscopy. Figure 4.3a shows the UV/Vis spectra revealing a broad rise in absorption at around 370 nm. To deduce the band gap, Kubelka-Munk (Fig. 4.3b) analyses were pursued (Table 4.1, 5th column), resulting in similar values of about 3.00–3.10 eV for all the ZnO-GO compounds, which are a little lower than the reported ZnO band gap of 3.37 eV[9].

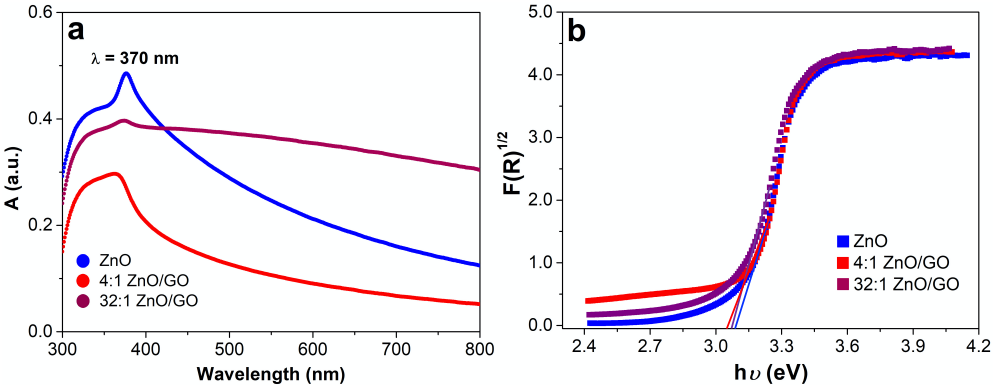

Figure 4.3. *(a) UV-Vis spectra of both pure and two GO-hybrid ZnO films on glass substrate, as representative samples; (b) relative band gap values determined by Kubelka-Munk elaboration.*

Thermogravimetric analyses reveal a very high stability of either pure ZnO[10] or hybrid ZnO-GO samples (Fig. 4.4a, red and purple lines; 4:1 and 32:1 ZnO/GO as representative

examples). Notably, even at temperatures up to 800 °C a mass loss of only ~2.5% is measured, probably ascribable to the elimination of physisorbed water molecules. In contrast, the pure GO (Fig. 4.4a, green line) decomposes in several stages (see Chapter 3). Therefore, the presence of ZnO grown onto GO provided thermal stability to the carbonaceous matrix, probably due to the passivation of the thermally degradable chemical functions by the formation of the hybrids.

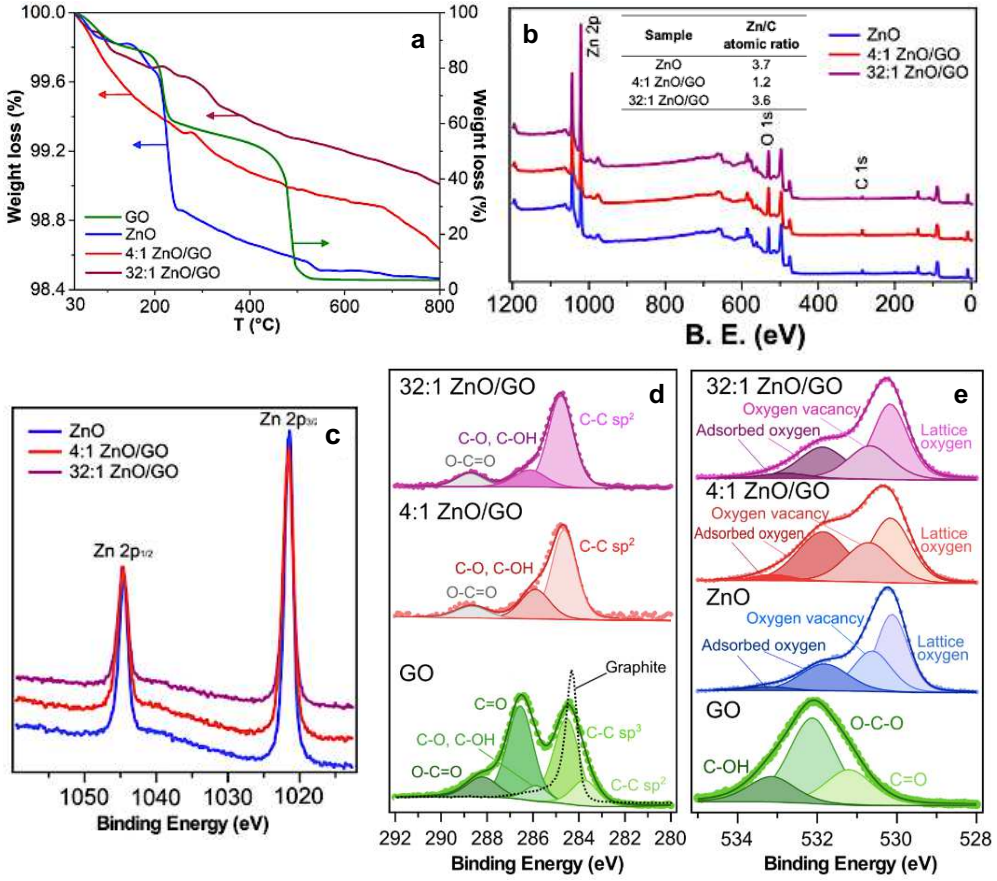

Figure 4.4. *(a) TGA spectra of GO, pure and hybrid 4:1 and 32:1 nanopowders. (b) XPS survey of ZnO-based samples (inset: Zn/C atomic ratios from XPS surveys; in the case of pristine ZnO carbon is an adventitious species always present in XPS measurements). XP spectra of (c) Zn 2p region of ZnO, 4:1 ZnO/GO and 32:1 ZnO/GO; (d) C 1s and (d) O 1s regions of GO (graphite, black dotted line) and hybrid samples.*

Furthermore, the surface properties of the materials were further investigated by XPS analysis (surveys spectra are reported in Figure 4.4b). Firstly, the gradual increase of zinc surface content was confirmed by Zn-to-C atomic ratios reported in the Table in inset of Figure 4.4b. Besides, Figure 4.4c shows the comparison of Zn 2p region relative to either pure ZnO or

the composite materials, resulting in almost superimposable signals. The C 1s region (Fig. 4.4d), conversely, shows only three components for the hybrid samples (instead of the five of the pristine GO), which are ascribable to C–C sp^2, C–O, C–OH and carbonyl C=O bonds. In particular, the last peak is mostly attributed to adventitious CO_2 although some potential contributions, rising from carbonyl groups remaining after the growth of the metal oxide, may not be excluded. The O 1s core level high resolution spectrum (Fig. 4.4e) have four components centered at around 530.10, 530.60, 531.80 and 533.20 eV. These correspond to lattice oxygen anions (O^{2-}) in the wurtzite structure, to oxygen ions (O^{2-} and O^{-}) in the oxygen-deficient regions, caused by oxygen vacancies, and to adsorbed oxygen species (especially water molecules)[11]. Interestingly, the content of adsorbed oxygen species is higher for the 4:1 ratio than for both the pure ZnO and the 32:1 ratio, suggesting a more hydrophilic nature of this compound than the others.

Hence, from all the above characterizations, it is possible to conclude that by adopting different zinc salt precursor-to-GO weight ratios a gradual coverage of the surface of graphene oxide sheets, creating strong bonds between the graphene and the metal oxide nanoparticles, occurs. This gradual growth can influence the surface properties, the morphology and crystal size of the as-prepared powders, thus affecting the final photo- and chemical sensing performances.

Moreover, in order to deeply investigate both the materials capacitance and the interfacial electron transfer properties, several electrochemical measurements were performed (see A.1.3 paragraph for the experimental set-up). In the following, the two composites 4:1 and 32:1 ZnO/GO will be considered, as representative cases. Firstly, Figure 4.5b displays a comparison among the calculated capacities according to the Ohm's law. As reported in Table 4.1 (6^{th} column), GO has the highest capacitance (45 μF), while a gradual increase of this parameter with the increasing of Zn-to-GO ratio can be observed. Indeed, 32:1 ZnO/GO (C = 34 μF) has the ability to accumulate charges intermediate between GO and pure ZnO (C = 24 μF). Besides, the interfacial electron transfer properties were investigated using an *outer-sphere* probe, *i.e.* a positively charged hexamine ruthenium (III) chloride ($[Ru(NH_3)_6]Cl_3$). CVs were, then, recorded at different scan, as shown in Figure 4.5c. The cathodic peak height was studied against the square root of the scan rate, according to the Randles-Sevčík equation (A.1.3.b equation), through which the relation between peak height and the scan rate in a diffusive system can be derived. Figure 4.5d displays a linear trend, thus indicating that the electrochemical reaction is controlled by diffusion. Moreover, in order to have a further corroboration, a logarithmic plot was investigated (Figure 4.5e). Similarly, all the samples

manifest a linear behavior and the slope value is similar to the ideal value (*i.e.* 0.5) of an electrochemical reaction controlled by diffusion[12].

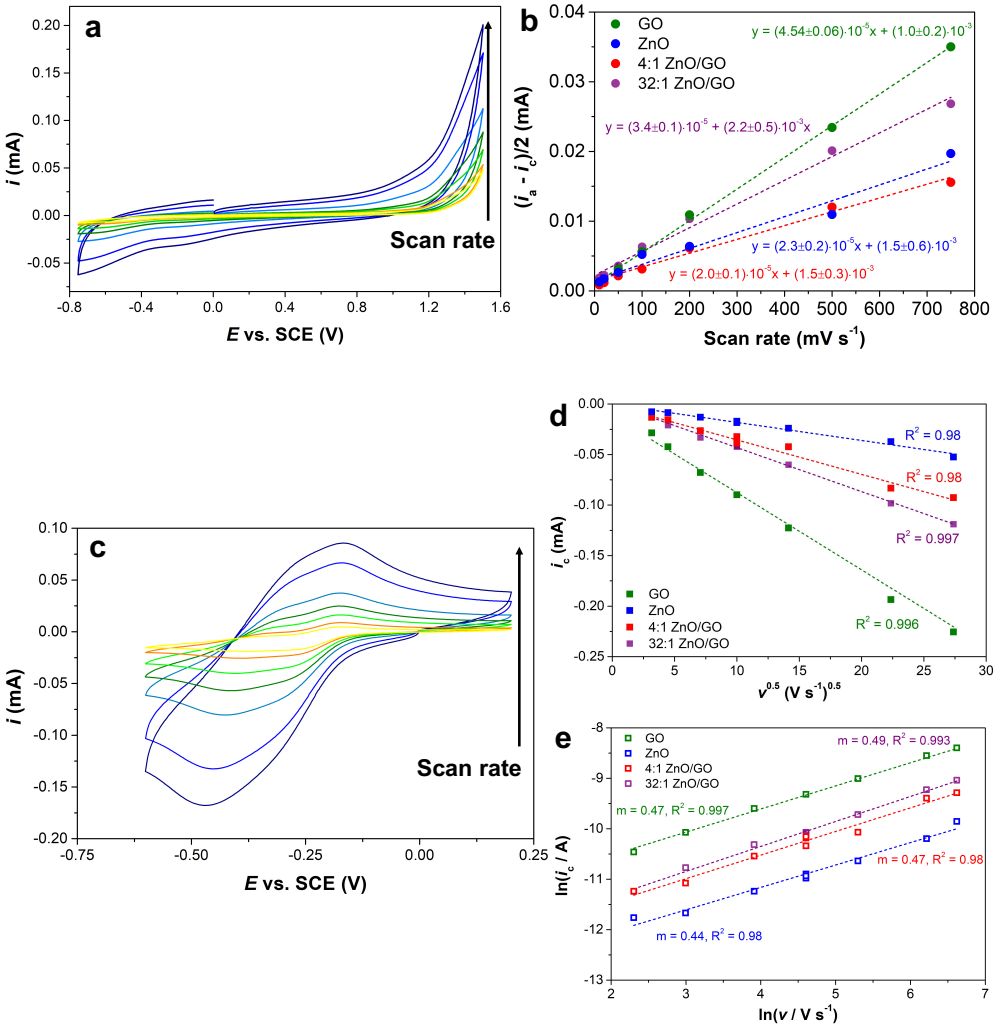

Figure 4.5. *(a) CVs relative to 32:1 ZnO/GO-modified glassy carbon (as representative case), at different scan rates (10, 20, 50, 100, 200, 500 and 750 mV s⁻¹). (b) Determination of materials capacitance through the Ohm's law, at fixed potential (+0.75 V). (c) CVs at different scan rates (10, 20, 50, 100, 200, 500 and 750 mV s⁻¹) for 32:1 ZnO/GO, in the presence of $[Ru(NH_3)_6]Cl_3$ (3 mM). (d,e) Randles-Sevčík plots, i_c vs. $v^{0.5}$ and $\ln(i_c)$ vs. $\ln(v)$, in the presence of $[Ru(NH_3)_6]Cl_3$ probe (3 mM). Electrolyte: 0.1 M PBS, pH 7.4.*

4.1.3. Chemical sensing

Before exploiting the as-synthesized materials for VOCs sensing, all the powders were deposited onto Pt-based interdigitated electrodes. Specifically, the deposition was via a scalable air-spraying method (see paragraph A.1.2), realizing homogeneous micrometric films (Figure A.3 in the Appendix Chapter). The cross-sectional FESEM images (Figure A.4 in the Appendix Chapter) reveal a layer thickness of around 2 μm for all the samples, with the exception of the 4:1 ratio that results in thicker films of ca ~5 μm (Table 4.1, 7th column). The films porosities were also computed indicating values above 90% for all the materials (Table 4.1, 8th column). Moreover, considering the nanoscale size of the ZnO and GO grains, the micrometer thickness of the ZnO/GO films provide a three-dimensional space for the electron and gas molecules transport. This is supported by the FESEM images of the ZnO/GO films showing a three-dimensional distribution of grains (Figures 4.1d–f). Previous modeling of the sensing mechanism of similarly three-dimensionally structured films has emphasized that the gas sensing reactions and the electrical transduction mechanisms are best represented by a three-dimensional network of sensing domains[13]. Specifically, Becker *et al*.[14] proposed that the contribution of the grains in the chemical sensing mechanism can be modeled as a three-dimensional network of parallel and series resistances distributed through the film thickness. Moreover, the individual contribution of the various part of the films change significantly as a function of the analyte concentration, sensing temperature and catalytic activity of the grains. As such, the sensing mechanism of the composite films is truly three-dimensional with contributions from the various parts and height of the film.

Figure 4.6 shows the chemical sensing responses of the pure ZnO (for the sake of comparison) and 32:1 ZnO/GO films towards acetone as a function of the temperature and UV light irradiation. Notably, the irregular shape of the response on 1 ppm may arise from limitations in transient response of the mass flow controllers in the experimental setup, utilized here. In particular, at high temperature (350 °C) without UV light, both pure and hybrid samples can detect acetone in air down to at least 20 ppb. Notably, the intensity of the 32:1 ZnO/GO response is around three times higher than the ZnO one (Figs. 4.6a and b). By decreasing the temperature to 150 °C and RT, it was possible to measure a sensor response towards these low concentrations (from 1 ppm to low-ppb) only with the ZnO/GO composite material and exploiting the UV light (Fig. 4.4c and d), whereas no response was obtained for ZnO and in dark conditions (Fig. 4.7a). Indeed, with the pristine zinc oxide only relatively high concentrations (8 ppm) of VOC (ethanol in Figure A.13, as representative analyte) can be detected at RT, showing a fairly low signal intensity (see the Appendix Chapter). This may be attributed to the relatively large size of the ZnO grains (77 nm) with respect to the high-

performing ones (d_P smaller than 40 nm), reported in the literature[15,16]. Indeed, to the increasing of nanoparticle size corresponds a reduction of the grain boundary density, thus resulting in a resistance to the electron conduction[16].

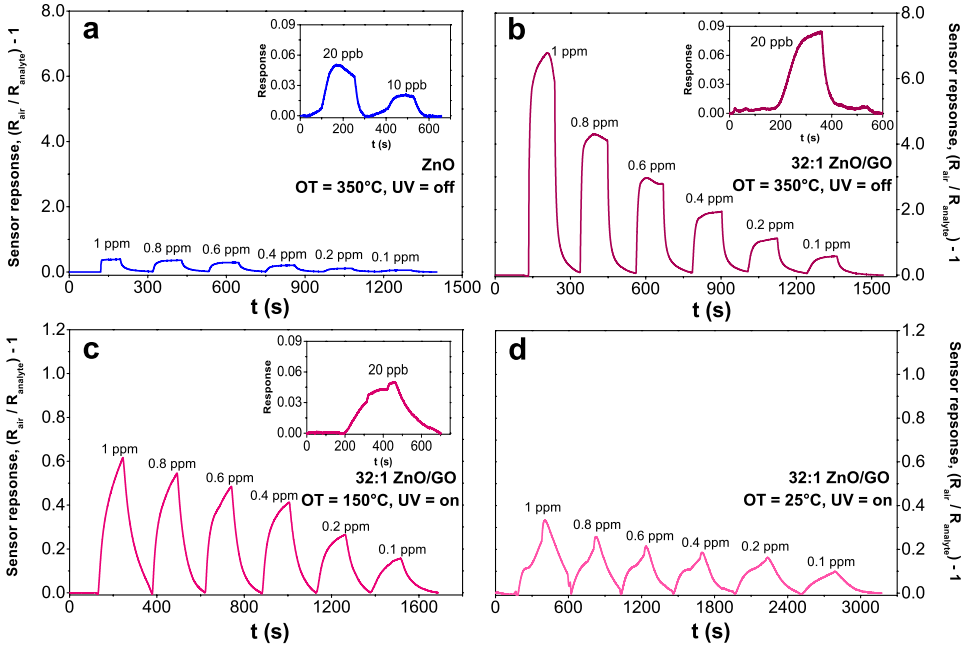

Figure 4.6. *(a) Pure ZnO and (b–d) hybrid 32:1 ZnO/GO sensors response when exposed to different ethanol concentrations (1 ppm to 10 ppb) in simulated air (20% O_2 – 80% N_2). OT = Operating Temperature.*

Moreover, for the hybrid compound, at these lower temperatures, the signal intensity was smaller than at 350 °C. However, a good signal-to-noise ratio was observed down to 100 ppb. Although an analogous sensor response behavior was also observed for ethanol and ethylbenzene (Figures A.14 and A.15), a different level of sensitivity was achieved. Ethanol resulted in the strongest sensing response followed digressively by acetone end ethylbenzene. Actually, the obtained signal at 1 ppm has an intensity two-times higher with respect to those recorded in presence of acetone or ethylbenzene gaseous molecules. Therefore, it is possible to conclude there is a moderate selectivity degree towards the EtOH species. This may be attributed to their different chemical structures, *i.e.* presence of polar groups (such as hydroxyl groups) or steric hindrance, thus leading to their different affinity with the zinc oxide surface[17–20]. Indeed, it has been already reported alcohols show higher sensing responses than aldehydes or ketones, and to a greater extent with respect to non-polar/low polar analytes, such as ethylbenzene[19–21]. Notably, selectivity may depend from the metal oxide

semiconductor used and ZnO is more selective towards ethanol molecules[22]. The interaction between ethylbenzene molecules and the metal oxide is much more difficult due to the phenyl ring presence, leading to lower sensitivity (600 ppb) and lower signal intensity for 32:1 ZnO/GO at RT (Figs. 4.7a and A.15). Moreover, the intensity signal trend obtained towards the increasing of ethanol and acetone concentration does not resemble a Langmuir-like behavior since no plateau is observable, resulting in agreement with what already reported in the literature[19,20]. Conversely, no oxygen-containing/low-polar compounds, such as ethylbenzene, are already reported to give much lower responses, since oxygen functionalities facilitate the adsorption on the metal oxide surfaces. Hence, its initial trend in Figure 4.7a may be due to its difficulty in interacting with the ZnO-GO material. Interestingly, the 4:1 ZnO/GO nanopowders resulted in an irreproducible sensor response (Figure A.16a). When the analyte gas molecules were injected into the sensing chamber (at RT with UV light), the current decreased revealing a bad signal recovery. This is probably due to the incomplete GO coverage by ZnO nanoparticles and, hence, the formation of a percolating GO network, which shortcuts the chemoresistive ZnO domains. Indeed, a similar behavior with a rapid decrease in current and no recovery, was also observed with the pure graphene oxide (Fig. A.16b), probably due to the many oxygen-containing functional groups, that give rise to stronger chemical interactions with the analyte molecules, hindering the gas desorption. Furthermore, as concern the other composite materials (8:1 and 16:1 ZnO/GO), no optimal responses were obtained. Particularly, Figures A.16c and d show the ethanol sensing by 16:1 compound. In this case, ethanol was adopted as the reference target gas, due to the higher responses obtained towards this species. Notably, the 16:1 ZnO/GO powder does not show a good signal both at 350°C and RT (under UV light). Therefore, since ratios lower than 32:1 do not have very promising features, 32:1 ZnO/GO hybrid can be considered the optimum combination of GO and ZnO due to the enhanced sensing performances, even with respect to pristine ZnO.

It is, therefore, suggested that the effective sensing material is zinc oxide, while GO helps to detect low VOCs concentrations at RT, under UV light irradiation. Moreover, upon purging of the target analyte molecules, both ZnO and 32:1 ZnO/GO readily recover showing fast response and recovery times (both below 50 s at 350 °C; Figs. 4.7b and c)[23,24]. Reducing the operating temperature, the response times increases to 80-340 s as a function of the analyzed gas. Interestingly, acetone (Fig. 5b and c, orange triangles) shows the fastest response (80 s) and recovery (90 s) times, also at RT.

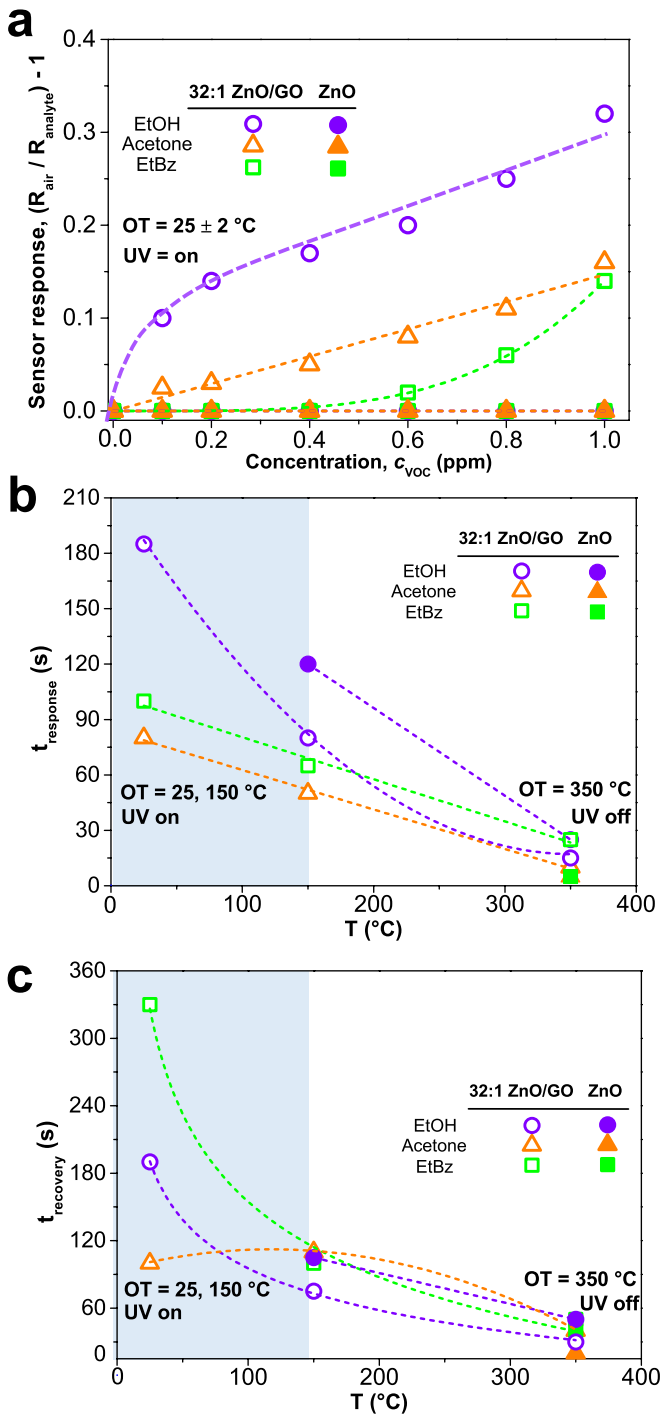

Figure 4.7. *(a) Signal response versus different VOCs concentrations obtained with either 32:1 ZnO/GO or pure ZnO. (b) Response and (c) recovery times as a function of the Operating Temperature (OT).*

4.1.4. Conclusions

Here, the fabrication of a three-dimensional network consisting of GO nanodomains well-integrated in a 3D zinc oxide matrix has been presented. By varying the GO content, tailored physico-chemical properties were obtained, tuning the final chemical sensing. Particularly, we observed that high amount of GO hinders the sensor response, due to the formation of interconnected GO domains which short-cut the chemical sensing ZnO regions. In contrast, low GO content results in an optimal combination, achieving room temperature detection of down to 100 ppb VOC concentrations. Notably, the highest sensitivity and fastest response and recovery times were obtained with the 32:1 ZnO/GO. A distinct sensitivity, and thus selectivity, was observed towards the various VOCs with the strongest response for ethanol, followed by acetone and ethylbenzene. This is possibly attributed to the gas molecules chemical structure and their affinity to the ZnO surface.

4.2. Tin dioxide-based materials

4.2.1. Introduction

Starting from the previous results, in the present paragraph, the fabrication of novel ultraporous networks based on well-integrated GO in a 3D SnO_2 networks will be finely studied, tailoring the amount of the p-type GO in the n-type SnO_2 matrix. The chemical sensing properties of these nano-networks will be deeply investigated to give insights into the role played by the graphene oxide in enhancing both the light-assisted sensors response at room temperature and the selectivity towards a specific VOC. Indeed, the same three different volatile compounds *i.e.* ethanol (EtOH), acetone and ethylbenzene (EtBz) will be adopted as target molecules. Finally, a deep electrochemical characterization, which may give a general comprehension of the synergistic effect between GO and the n-type semiconductor, will be assessed[25].

4.2.2. SnO_2-GO 3D-networks features

Also for SnO_2-based nanocomposites, a comprehensive range of structures were synthesized varying the SnO_2/GO ratio from 4 to 32 (specifically, 4:1, 8:1, 16:1 and 32:1). Moreover, within all this paragraph, the adopted graphene oxide will be GO_S1_30. Hence, for simplicity, it will be labelled as GO.

From structural and surface points of view, the effective accomplishment of graphene oxide optimal integration in a three-dimensional SnO_2 network have been ascertained.

Sample	$<d^{XRPD}>$ (nm)	S_{BET} ($m^2\ g^{-1}$)	$V_{tot.\ pores}$ ($cm^3\ g^{-1}$)	E_g (eV)	Capacitance ($F \cdot 10^5$)	Film thickness (μm)	% Film porosity
Graphite	27	11	0.030	–	–	–	–
GO	11	15	0.021	–	4.5	–	–
SnO_2	80	67	0.210	3.6	4.4	1.8 ± 0.2	93 ± 1
4:1 SnO_2/GO	5	29	0.074	3.0	1.5	3.2 ± 0.4	97 ± 1
8:1 SnO_2/GO	9	27	0.069	3.1	1.6	2.3 ± 0.3	94 ± 1
16:1 SnO_2/GO	15	51	0.086	3.2	1.7	1.9 ± 0.2	92 ± 1
32:1 SnO_2/GO	10	55	0.133	3.4	1.7	1.4 ± 0.4	94 ± 2

Table 4.2. *Crystallite domain size by XRPD analysis ($<d^{XRPD}>$), surface area (S_{BET}), total pore volume ($V_{tot.\ pores}$), optical band gap (E_g, by Kubelka-Munk extrapolation) and capacitance of the synthesized materials by CV measurements. Thickness (by cross-sectional FESEM) and porosity percentage of the deposited layers (see paragraph A.1.2).*

In particular, Figures 4.8a,b show a comparison of x-ray diffraction lines and Raman spectra of the pristine graphite and GO, along with the structural data of bare SnO_2 and the hybrid materials (herein, 4:1 and 32:1 SnO_2/GO will be described in detailed, as samples with the lowest and highest ratios). As previously reported, the effective transformation of graphite material into graphene oxide was assessed, since both the main GO diffraction peak (at 2θ value of 12°) and the intensity increase of the ratio between the D and G Raman bands (1.01 of GO *vs.* 0.25 of the starting graphite) can be clearly highlighted (Figs. 4.8a,b; red line). Moreover, the gradual integration of GO particles into SnO_2 matrix was demonstrated by both the presence of Raman bands relative to the graphene oxide material and tin dioxide, *i.e.* the appearance of A_{1g} (624 cm^{-1}), A_{2u} (640 cm^{-1}) and B_{2g} (766 cm^{-1}) peaks (Fig. 4.8b; blue and violet spectra), and the very small XRPD crystallites diameter (ca 5-10 nm; Fig. 4.8a and Table 4.2, 1st column) with respect to bare cassiterite SnO_2[26] (80 nm, Table 4.2).

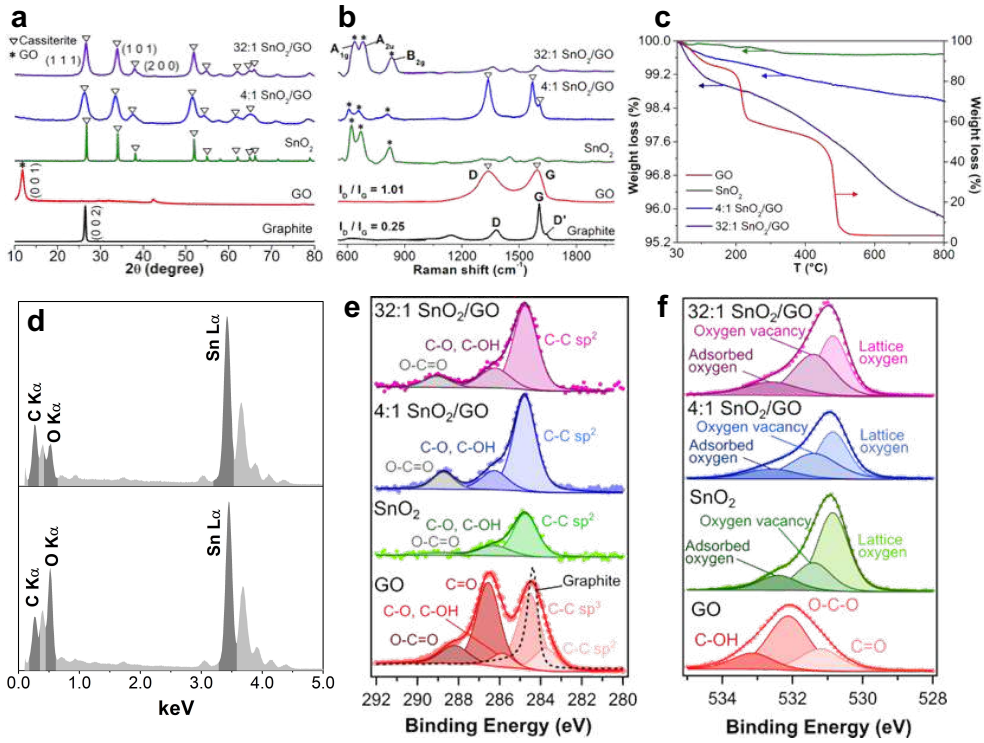

Figure 4.8. *(a) XRPD spectra of graphite, graphene oxide (GO), pure SnO_2 and two hybrid SnO_2-GO samples, as representative cases (100% intensity reflection planes have been assigned to the main phases of each compound). (b) Raman spectra of the investigated samples. (c) TGA spectra of GO, pure and hybrid nanopowders. (d) EDX spectra of 4:1 SnO_2/GO and 32:1 SnO_2/GO. XP spectra of (e) C 1s and (f) O 1s regions relative to graphite, GO, 4:1 and 32:1 SnO_2/GO.*

Actually, the domain sizes of the hybrid compounds resemble much more the graphene oxide one (11 nm, Table 4.2), further underlining the effective integration of the carbonaceous material into the metal oxide network. This integration conversely leads to a lower SnO_2 crystallinity degree[25]. Besides, x-ray diffraction lines by Rietveld refinement are in accordance with the experimental data (see Figure A.17 in the Appendix Chapter), resulting in calculated cell parameters consistent with the theoretical values (JCPDS n. 41-1445[27]). Moreover, a further corroboration was obtained by means of infrared spectroscopy. Indeed, in Figure A.18, all the composite oxides show the characteristic FTIR peaks of tin dioxide at around 500 cm^{-1}, ascribable to O–Sn–O and Sn–O stretching modes[28].

Thermogravimetric analyses reveal that either pristine SnO_2 or hybrid samples are very stable (Fig. 4.8c) even at temperatures of up to 800 °C. Indeed, as already seen for ZnO-based materials, the formation of the MOS on GO sheets may passivate its degradable chemical functions.

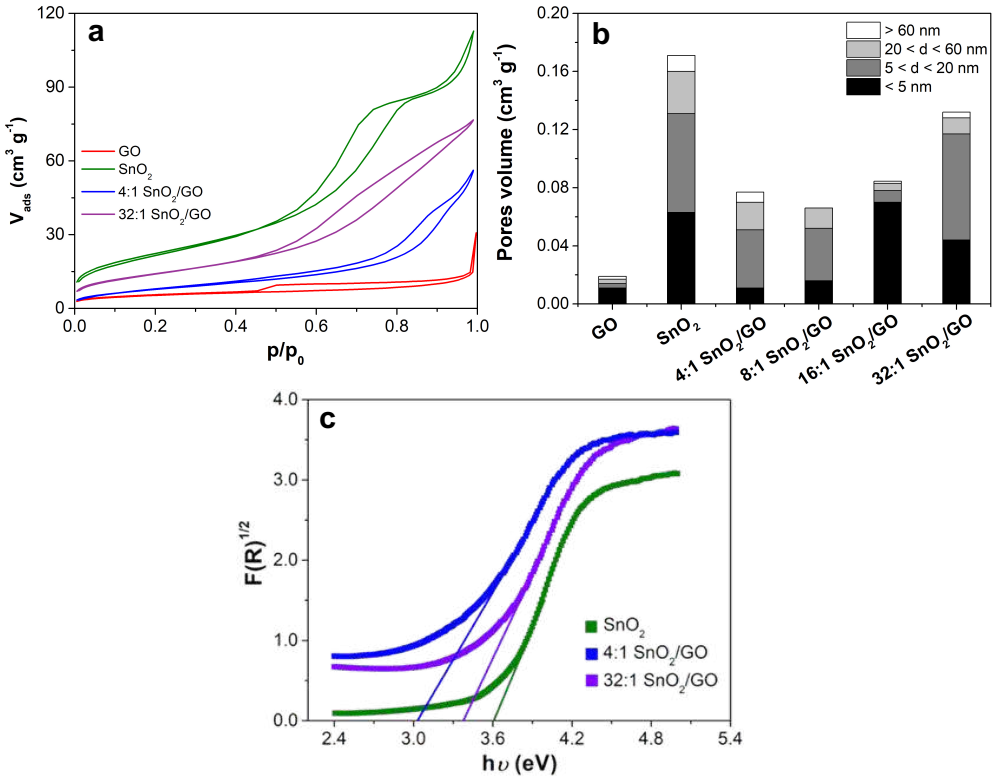

Figure 4.9. *(a) Comparison among BET isotherms relative to pristine GO, SnO_2 and two of the hybrid materials (namely, 4:1 and 32:1 SnO_2/GO). (b) Trend of pores volume distribution with the decreasing of the GO amount integrated in the tin dioxide matrix. (c) Kubelka-Munk elaboration of DRS spectra to determine the SnO_2, 4:1 and 32:1 SnO_2/GO band gaps.*

Notably, a mass loss of only ~4% was measured, probably due to the water molecules physisorbed on the materials surface, as well as occurred in hybrid ZnO-based compounds (see the previous 4.1. paragraph). Furthermore, the effective presence of tin element in the hybrid samples was also confirmed by EDX analysis, as shown in Figure 4.8d.

Once evaluated the materials structural features, the surface properties were further investigated by XPS and BET-BJH analyses. XPS surveys spectra are reported in Figure A.19a. Firstly, the gradual increase of tin content was confirmed by Sn-to-C atomic ratios reported in the Table in inset of Figure A.19a. Besides, Figure A.19b shows the comparison of Sn 3d region relative to either pure SnO_2 or the composite materials (4:1 and 32:1 as representative samples), resulting in almost superimposable signals. The C 1s and O 1s core level high resolution spectra of GO compound (Fig. 1e–f, red spectra) were deeply discussed in Chapter 3. Besides, the C 1s region of both pure and composite SnO_2-GO materials shows three components (Fig. 4.8e), referable to C–C sp^2 (284.75 eV), C–O/C–OH (286.20 eV) and O–C=O (289.00 eV) bonds[29,30]. Notably, even if the last peak can be mostly attributed to adventitious CO_2, the fact that it is much more visible in the hybrid samples can be assigned to the effective GO presence. Figure 4.8f displays the O 1s core level high resolution spectrum, which can be deconvoluted into three components centered at around 530.75, 531.40 and 532.60 eV. These bands correspond respectively to: *i*) the lattice oxygen anions (O^{2-}) in the cassiterite structure; *ii*) the oxygen ions (O^{2-} and O^-) in the oxygen-deficient regions, caused by oxygen vacancies; and *iii*) the adsorbed oxygen species (especially water molecules)[31,32]. As expected, the amount of oxygen vacancies in the SnO_2-GO compounds is higher than in the pure SnO_2, suggesting a more defective structure as a result of the graphene oxide integration into the metal oxide matrix. Furthermore, the specific surface areas of the composite materials are close (29 and 55 $m^2\ g^{-1}$) to the pure SnO_2 one (67 $m^2\ g^{-1}$), following a decreasing trend with the increase of the GO content (S_{BET} GO equal to 15 $m^2\ g^{-1}$; Table 4.2, 3rd column). The same trend was observed for the total pores volume data (Table 4.2, 4th column). Besides, Figure 4.9a shows the N_2 adsorption-desorption isotherms of the synthesized materials. Interestingly, pure SnO_2 (green line) displays its typical H2-type hysteresis loop, corresponding to bottle-necked shaped pores[8]. Conversely, nanocomposite materials (blue and violet lines) are characterized by isotherm shape intermediary between that of SnO_2 and the one of GO. Therefore, these powders possess either bottle neck-shaped pores (of SnO_2) or slit-shaped ones (typical of GO). As regard the pores distribution, Figure 4.9b shows a comparison among the fabricated materials. Notably, nanocomposite samples have a high number of micropores ($d < 20$ nm), resembling much more the pure SnO_2 matrix, than that of the graphene oxide material.

Since we found that VOCs sensing at lower temperatures is greatly improved by light exploitation[25,33], the optical properties of tin dioxide-based compounds were initially investigated by diffuse reflectance spectroscopy. Figure 4.9c shows the Kubelka-Munk elaboration of the DRS spectra, revealing that by decreasing the GO integration into SnO_2 matrix, band gap values slightly increase reaching 3.4 eV for 32:1 SnO_2/GO (similar to pure SnO_2 one of 3.6 eV[25]; Table 4.2, 5th column).

Figure 4.10 shows the morphology of pristine and composite samples by TEM and FESEM analyses. Notably, both the 4:1 and 32:1 SnO_2/GO ratios seem to have spherical nanoparticles with dimensions of around 8 nm (Fig. 4.10b,c), which are bigger than pure oxide ones, having a size of ~5 nm (Fig. 4.10a)[25]. Also scanning electron micrographs display the presence of spherical agglomerates with dimensions of hundreds of nanometers for all the three SnO_2-based samples (Fig. 4.10g–i).

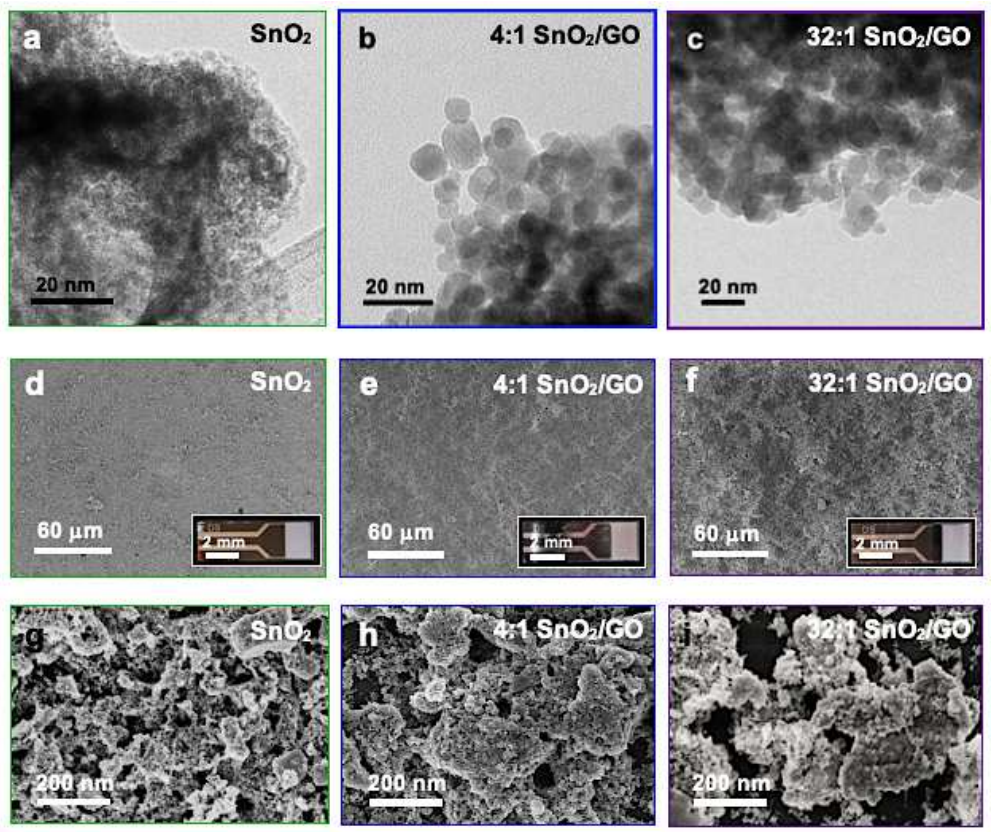

Figure 4.10. *(a–c) TEM images of pristine SnO_2 and hybrid SnO_2-GO compounds. (d–i) Top view FESEM micrographs and (l–n) cross-sectional images of both pure and composite samples. Insets: photos of the relative interdigitated electrodes.*

Hence, it is possible to conclude that from all the above physico-chemical characterizations the gradual coverage of the graphene oxide sheets by SnO_2 can be achieved, creating strong bonds between the graphene and the metal oxide nanoparticles. This tailored GO presence in the tin dioxide matrix can influence the structural and surface properties, the morphology and crystal size of the as-prepared powders, thus possibly affecting their behavior as chemoresistive materials.

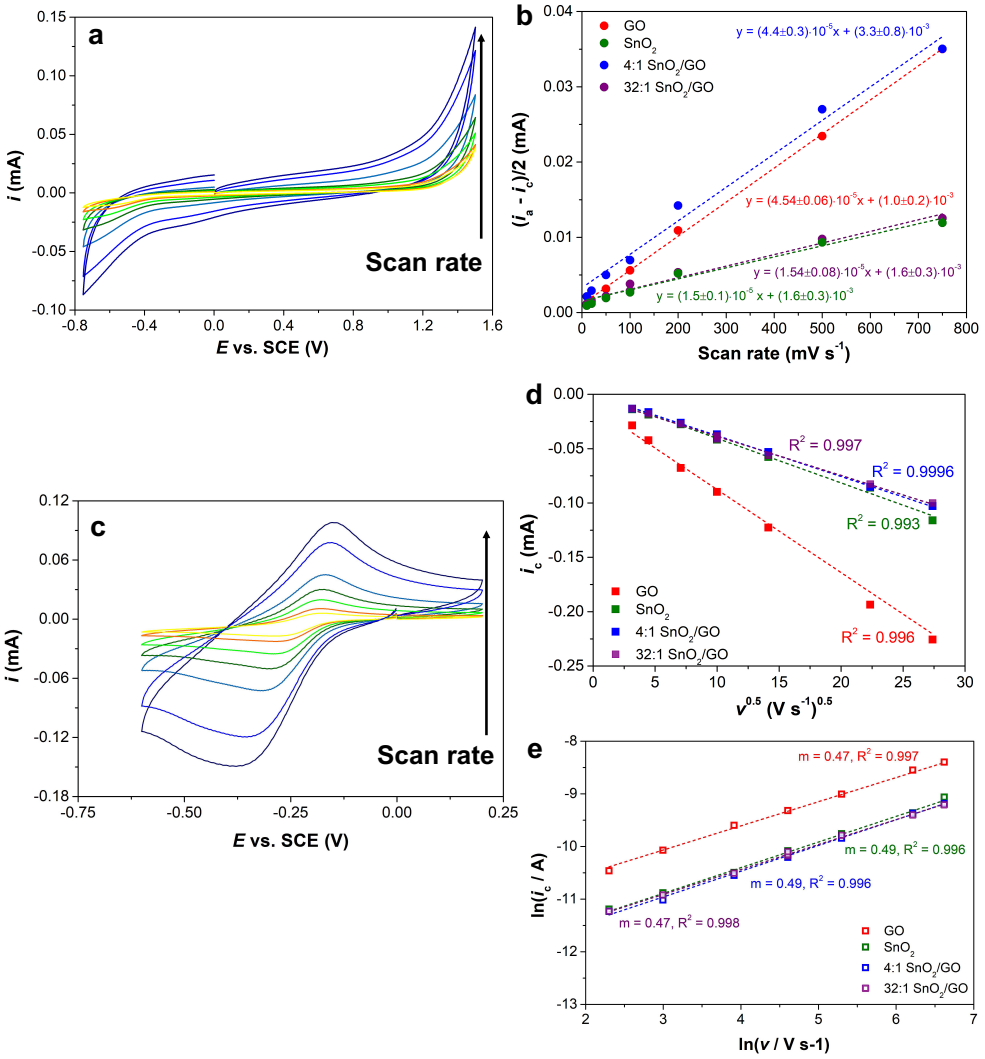

Figure 4.11. *(a) CVs relative to 32:1 SnO_2/GO-modified glassy carbon (as representative case), at different scan rates (10, 20, 50, 100, 200, 500 and 750 mV s^{-1}). (b) Determination of materials capacitance through the Ohm's law, at fixed potential (+0.75 V). (c) CVs at different scan rates (10, 20, 50, 100, 200, 500 and 750 mV s^{-1}) for 32:1 SnO_2/GO, in the presence of $[Ru(NH_3)_6]Cl_3$ (3 mM). (d,e) Randles-Sevčík plots, i_c vs. $v^{0.5}$ and ln(i_c) vs. ln(v), in the presence of $[Ru(NH_3)_6]Cl_3$ probe (3 mM). Electrolyte: 0.1 M PBS, pH 7.4.*

Moreover, as for ZnO-based composites (paragraph 4.1), in order to deeply investigate both the materials capacitance and the interfacial electron transfer properties, electrochemical measurements were performed (see A.1.3 paragraph for the experimental set-up). In the following, the two composites 4:1 and 32:1 SnO_2/GO will be considered as representative samples, and the relative results discussed. Firstly, Figure 4.11b displays a comparison among the calculated capacities according to the Ohm's law. As reported in Table 4.2 (6th column) and already discussed (paragraph 4.1), GO has the highest capacitance (45 μF), even if, in this case, comparable to that of pristine SnO_2 (44 μF). Moreover, a decrease of this parameter occurs by combining GO and SnO_2 materials. Indeed, all the composites show a lower ability to accumulate charges, resulting in capacities of about 15–17 μF. Besides, the interfacial electron transfer properties were investigated using an *outer-sphere* probe, *i.e.* $[Ru(NH_3)_6]Cl_3$. CVs were recorded at different scan (Figure 4.11c), and the cathodic peak height was studied against the square root of the scan rate, according to the Randles-Sevčík equation (A.1.3.b equation). Figure 4.11d displays a linear trend, thus indicating that the electrochemical reaction is controlled by diffusion. Moreover, similarly to ZnO-based samples, all the SnO_2-materials manifest a diffusion-controlled electrochemical reaction, since a linear behavior (Figure 4.11e) and a slope value very close to 0.5 were obtained[12].

4.2.3. Chemical sensing

In order to investigate the powders performances, they were firstly deposited on Pt-IDEs via a scalable air-spraying method, obtaining very homogeneous micrometric films (Figures 4.10d–f). The cross-sectional FESEM images (Figure A.20), reveal layers thickness in the range between 1.5 and 3.2 μm for either SnO_2 or the other composite materials (Table 4.2, 7th column). Besides, as for ZnO-based compounds, the films porosities were estimated (Table 4.2, 8th column) resulting in very porous layers (above 90% for all the synthesized samples).

Hence, starting from the previous results about zinc oxide nanocomposites, gaseous ethanol was firstly chosen as analyte molecule, due to its easiness of detection. Indeed, the tin dioxide sensing performances towards gaseous ethanol molecules has been widely reported, already showing good results[34,35]. However, herein, the significant step forward consists in the amplification of the final signal, obtained with the integration of GO into the n-type semiconductor matrix, giving the possibility to reach very low VOC concentrations, even at room temperature. Figures A.21, A.22 and 4.12 compare the responses achieved increasing the GO surface coverage by tin dioxide (Sn salt precursor-to-GO weight ratio from 0 to 32:1). All the as-synthesized powders were tested either at high operating temperatures (350 and 150°C) or at RT, UV light-aided with the decreasing of the temperature. Figures A.21 and 4.12g show

the response to 1 ppm or lower concentrations of gaseous ethanol for all the hybrid compounds, at RT. Notably, by decreasing the GO content in the 3D-SnO_2 matrix, an improvement of the signal was noticed, especially concerning the response intensity and the sensitivity. Indeed, only with 32:1 SnO_2/GO, 100 parts-per-billion ethanol concentration was reached. Moreover, for the sake of comparison, the same tests were performed with the pristine tin dioxide, resulting in good signal down to 2 ppb only at 350 °C (see Fig. 4.12a). Besides, higher concentrations (*i.e.* 8 ppm) were sensed till 150 °C (UV light-assisted; Fig. A.22); below this temperature no signal was detectable. Notably, the reported materials have shown quite fast response and recovery (about 70-90 s) towards ethanol.

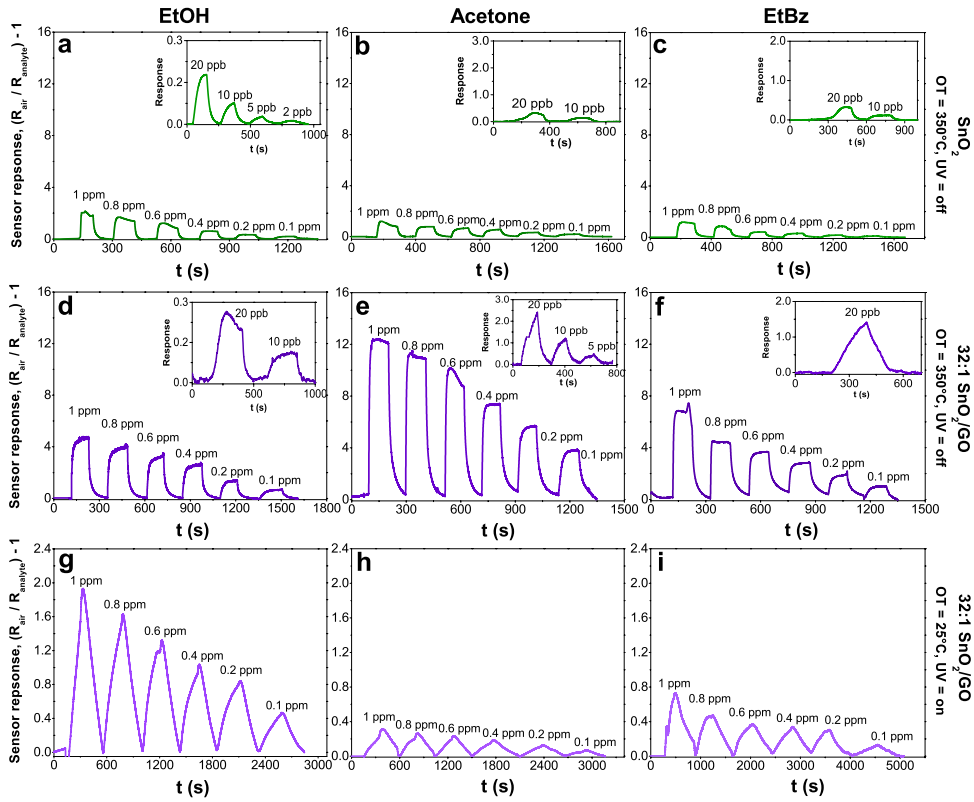

Figure 4.12. *(a–c) Pure SnO_2 and (d–f) hybrid 32:1 SnO_2/GO sensors response when exposed to different low-ppm concentrations of ethanol, acetone and ethylbenzene at 350°C, without UV light. (g–i) Same tests performed with hybrid 32:1 SnO_2/GO materials at RT, UV-assisted. All the measurements were carried out in simulated air (20% O_2 – 80% N_2). OT = Operating Temperature.*

Once deeply investigated the ethanol analyte sensing, the research was focused on the evaluation and the enhancement of either sensitivity or selectivity towards different VOCs.

Therefore, acetone and ethylbenzene were further tested. Figures 4.12a,d,g display the sensor responses for either pure and 32:1 SnO_2/GO, as a function of both the operating temperature (OT) and the UV exploitation. The greatest ratio was initially adopted due to the above-mentioned higher ethanol sensing performances. Notably, at high temperature (350 °C) without UV light, both pure and hybrid sample can detect acetone and EtBz in air down to ppb concentrations. Remarkably, the intensity of the 32:1 SnO_2/GO responses are almost three, six and seven times higher than the SnO_2 ones, in the case of EtOH, acetone and EtBz, respectively (Figs. 4a and d). By decreasing the temperature to 150 and 25 °C, it was possible to measure a sensor response only with the composite sample and by exploiting the UV light, whereas no response was obtained for the bare oxide compound (Figs. 4.12 and A.23). Even if at these lower temperatures the signal intensity was smaller than at 350 °C, a very good signal-to-noise ratio was observed down to 100 ppb at RT, for the three tested species. However, the signals intensities were quite different among the analytes, thus resulting in a possible selective discrimination among the studied VOCs (Figure 4.13a). Notably, as seen for ZnO-based materials, at RT ethanol seems to be the easiest species to be detected by 32:1 SnO_2/GO and it is followed digressively by acetone and ethylbenzene. This may resemble the VOCs chemical structure, since EtBz possesses a sterical hindrance, given by the phenyl ring, that can hinder its interaction with the sensing material[19–21]. Moreover, both SnO_2 and 32:1 SnO_2/GO readily respond and recover upon purging all the three analytes (response and recovery times below 80 s at 350 °C; Figs. 4.13b,c). However, reducing the operating temperature, the response times increase by three/four times, depending on the analyzed molecule. Interestingly, all the materials presented here have superior sensing abilities than those already reported in the literature[35–39] (see the comparative Table in Chapter 6) and, in particular, 32:1 SnO_2/GO exhibits significantly higher sensitivity (very low-ppb values of detection limit) and a quite high response intensity, even at RT, than the other studied compounds[35,38]. Moreover, we can also remarkably observe the very promising results obtained towards EtBz, for which very few studies have been conducted so far[39].

By deeply investigating the responses of all the as-synthesized composites, 4:1 SnO_2/GO material interestingly showed a "reversed" behavior in the case of acetone and to a greater extent for ethylbenzene (Figure A.24). Specifically, upon purging these species, a drop of the current was recorded. This phenomenon is reported to be typical of p-type semiconductors[33] and it might be due to the greater content of the highly hydrophilic GO (p-type) inside the metal oxide matrix. As stated by Chen *et al.*[33], the negative response may be caused by the interaction between the moisture adsorbed on the sensing material surface and the VOCs molecules and it is lost when the operating temperature is above the water condensation point. Hence, to demonstrate this hypothesis, tests at high temperatures were carried out (Fig. A.24).

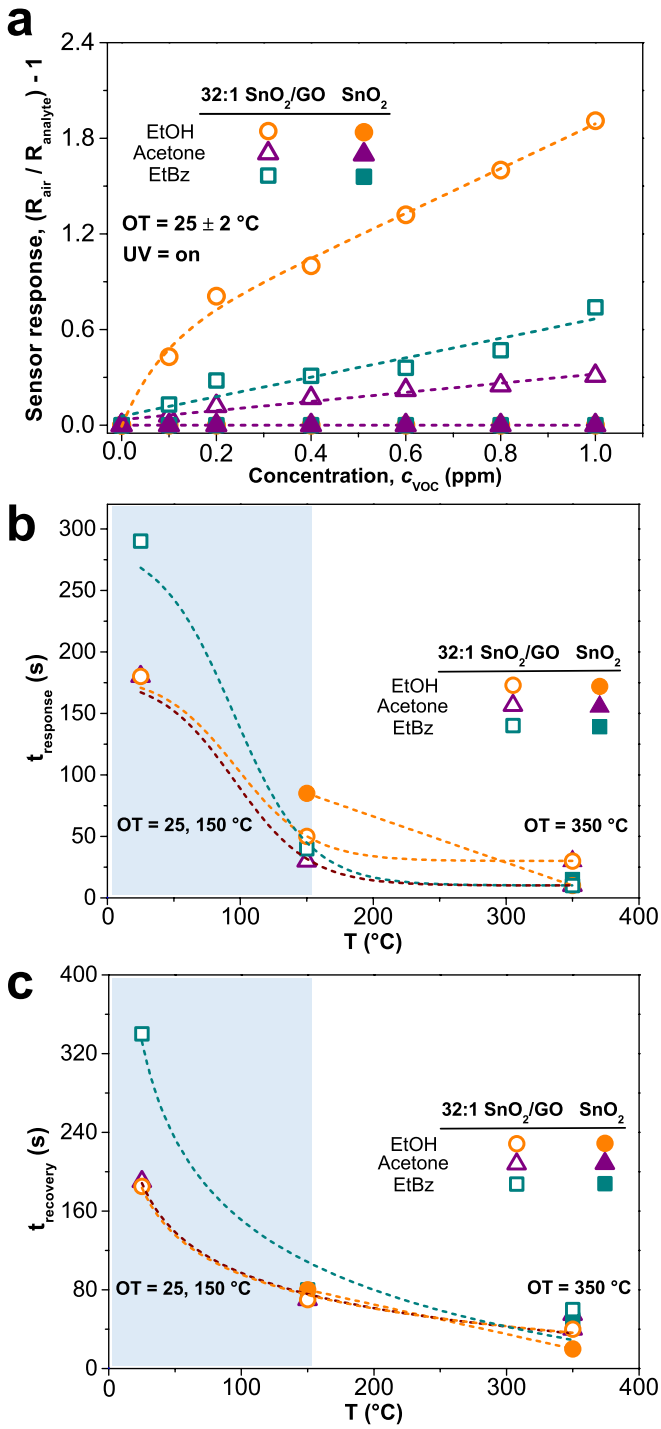

Figure 4.13. *(a) Signal response versus different VOCs concentrations obtained with either 32:1 SnO_2/GO or pure SnO_2. (b) Response and (c) recovery times as a function of the Operating Temperature (OT).*

It is possible to notice that the signals both for acetone and ethylbenzene switch from negative to positive values by increasing the OT above 100 °C, along with an increase in the relative intensities. Thus, since this behavior was particularly stressed for ethylbenzene molecules only in the case of 4:1 SnO_2/GO, it can be used as a tool to selectively sense this species at RT, in a humid environment, as the human breath.

Hence, the tailoring of the GO content in a 3D SnO_2 network can allow to either achieve very high sensitivities or enhance the selectivity towards different VOCs, even at room temperature with the aid of the UV light.

4.2.3.1. *Aqueous ethanol electrochemical detection*

In order to give a preliminary explanation of the synergistic effect between graphene oxide and n-type semiconductors, ethanol adsorption and detection onto powders modified-glassy carbon electrodes have been evaluated. To achieve this goal, the use of aqueous ethanol was mandatory due to the nature of the tests (*i.e.* cyclic voltammetric ones).

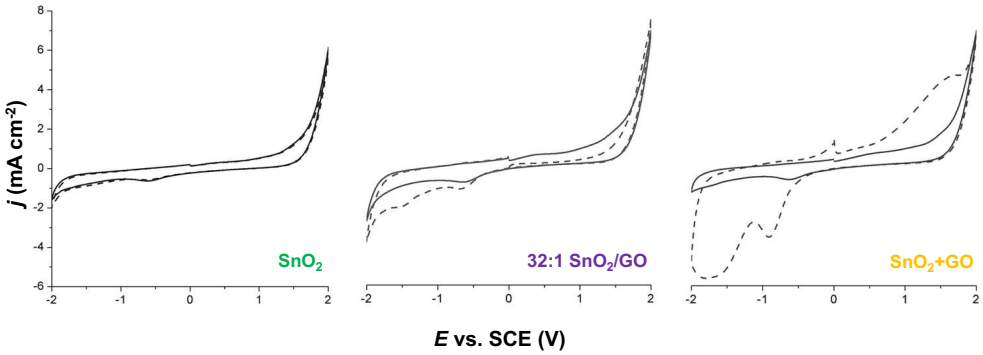

Figure 4.14. *Cyclic voltammograms obtained with modified glassy carbon in the absence (dotted line) and presence (continuous line) of 1 mM aqueous ethanol. SnO_2+GO label stands for mechanically mixed sample, in which the weight ratio is comparable to the one in 32:1 SnO_2/GO compound. All the tests were conducted in 0.1 M PBS electrolyte, at scan rate of 100 mV s^{-1}. Adapted with permission*[25]*, Copyright 2019, Elsevier.*

Specifically, pure liquid ethanol was added to PBS electrolyte to have a final concentration of 1 mM. In the case of pristine SnO_2, the addition of the alcohol molecules has no influence (as shown in the relative CVs; Figure 4.14, green sample) remaining similar to the background, thus indicating that no observable electroactivity is detected for the molecule on this electrode material. The situation is different for SnO_2+GO sample (*i.e.* the mechanically mixed one; Fig. 4.14, orange sample), where in the background we can observe, as expected, the typical graphene peaks (see Chapter 3) that disappear after ethanol addition. This is probably due to

the analyte adsorption on the functional groups of GO, therefore irreversibly blocking their electrochemical reactions. On the other hand, the presence of SnO_2 has no effect, as demonstrated in the case of pure tin dioxide, and only the electrochemistry of graphene is observable. On the contrary, in the case of the hybrid material 32:1 SnO_2/GO, after ethanol addition we can observe the increase of the oxidation current with respect to the background (Fig. 4.14, violet sample), pointing out that ethanol can be detected at positive potentials. Moreover, since the majority of the graphene functional groups are occupied by SnO_2 nanoparticles, the irreversible adsorption of the analyte is prevented. Hence, starting from these significant electrochemical outcomes, the improvement of the gaseous ethanol sensing by the nanocomposites could be further corroborated and deeply explained as the result of the synergistic effect between graphene oxide and n-type semiconductor.

4.2.4. Conclusions

Novel nano-3D layouts based on GO domains integrated in a three-dimensional tin dioxide matrix were proposed for the room temperature UV-assisted VOCs sensing. The composites were synthesized tailoring the graphene oxide amount in the SnO_2 network. Thus, taking into account all the outcomes reported so far, the pivotal role of graphene oxide underneath metal oxide nanoparticles has been assessed and the controlled growth of tin dioxide revealed to be fundamental in order to achieve high sensitivity/good signal-to-noise ratio, even at lower operating temperatures. In particular, it has been demonstrated that sensor signal can be amplified by chemically coupling GO with the suitable amount of SnO_2 (so that an almost complete coverage of GO surface is obtained). In this context, 32:1 SnO_2/GO has a higher selectivity towards ethanol if compared to acetone and ethylbenzene. On the contrary, a high amount of GO hinders the ethanol sensing at room temperature, inducing an opposite negative response with acetone and, above all, with ethylbenzene, thus preserving an optimal selectivity towards the latter species. Hence, we believe that these findings can provide guidelines for the engineering of novel chemoresistors with high selectivity to be used in portable and point-of-care devices.

4.3. Composite Sn/Ti mixed oxides-based materials

4.3.1. Introduction

This paragraph gives a review of the research carried out for SnO_2-TiO_2-GO mixed oxides system in VOCs sensing. Indeed, simple metal oxides such as ZnO, SnO_2 and TiO_2 show remarkable sensitivity towards reducing and oxidizing gases. However, their major drawback is the lack of selectivity, *i.e.* the parameter defined as the ratio of the partial sensitivity to the analyte with respect to the interfering species. Unfortunately, most MOS-based gas sensors and, especially those operating on changes in the electrical conductivity upon interaction with gases, are non-specific. In this context and with the promising results previously reported about the synergistic effect between SnO_2 and GO, SnO_2-TiO_2-GO mixed oxide was believed to be an efficient active material with improved selectivity. There are already several works[40–44] on the synthesis and successful application of SnO_2-TiO_2 mixed oxides as either photocatalysts or sensing materials. Tricoli *et al.*[41] reported the preparation of a SnO_2-TiO_2 solid solution with limited cross-sensitivity towards humidity, thanks to the replacement of some tin cations by titanium ones. Chung *et al.*[45] suggested that the enhancement of the gas sensing performance relies on the Schottky barrier formation at the grain boundaries of well-formed SnO_2 particles embedded in a finely dispersed TiO_2 matrix. Hence, starting from these prior studies, novel co-synthesized materials, based on SnO_2, TiO_2 and GO, will be presented here. Notably, the effect of substitution of tin ions by titanium cations will be fully elucidated on structural, surface, morphological and optical points of view. Finally, toluene (*i.e.* big and non-polar molecule) sensing will be deeply investigated as a function of titanium content in the solid solution, both at 350 °C and at lower operating temperatures (by exploiting the UV light). Then, the most performing sample will be tested towards acetone molecules (*i.e.* smaller and polar species), in order to evidence its possible enhanced selectivity towards one of the target analytes.

4.3.2. Nanostructured Sn/Ti oxides solid solution: composition and properties

Starting from all the previous results, the same wet chemical method was used for the fabrication of novel ultraporous nanostructured SnO_2-TiO_2-GO mixed oxides. Within this paragraph, the adopted graphene oxide material is GO_S2_30 (due to its slightly higher surface area). Nevertheless, as before, it will be simply labelled as GO.

Wide-angle XRPD analyses were performed to determine the crystal structure and to corroborate the formation of a Sn/Ti solid solution. Figure 4.15 displays the as-synthesized

nanostructured metal oxides with a controlled Sn/Ti ratio. Notably, no GO traces were observable in all the x-ray spectra.

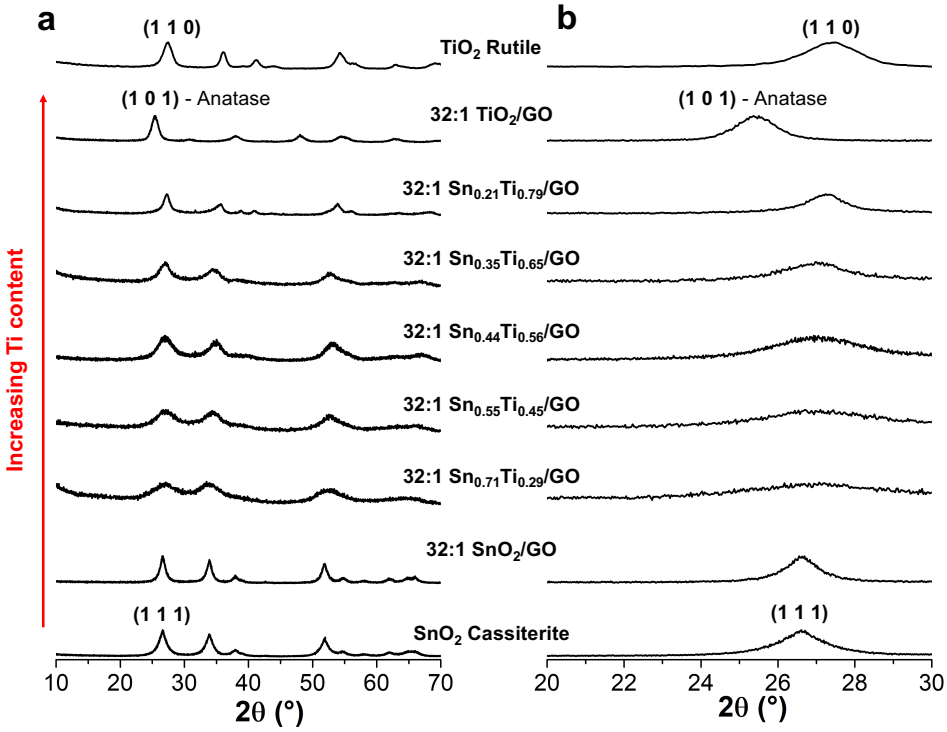

Figure 4.15. *(a) Comparison of x-ray lines relative to pure cassiterite SnO_2, rutile TiO_2, 32:1 SnO_2/GO, 32:1 TiO_2/GO and all the SnO_2-TiO_2 mixed oxides (32:1 Sn_xTi_{1-x}/GO, with x = Sn/(Sn+Ti)) with the increasing of the titanium content. (b) Magnification of the XRPD spectra to investigate the shift of the peak from 26.6°[44] of pure cassiterite SnO_2 to 27.4° of pure rutile TiO_2[44] (100% intensity reflection planes have been assigned to the main phases of each compound).*

Moreover, the crystallinity degree of 32:1 Sn_xTi_{1-x}/GO composites seems to slightly increase with the increasing of titanium content (*i.e.* sharper peaks), having estimated grain sizes from about 6 to 10 nm. In particular, all the mixed oxides do not show any phase segregation (as clearly visible in Figures 4.15b and A.25): the main cassiterite SnO_2 peak (1 1 1) slightly shifts from 26.6° (of pure SnO_2 and 32:1 SnO_2/GO) to 27.4° typical of rutile TiO_2 (JCPDS n. 21-1276), with the increasing of Ti content. Interestingly, in the investigated solid solutions, the anatase polymorph (JCPDS n. 21-1272) was not observed contrarily to 32:1 TiO_2/GO sample. This may be due to the fact that cassiterite and rutile-TiO_2 are isostructural phases, both having a tetragonal cell[46]: hence, Sn atoms could have been substituted by Ti

ions, maintaining the structural configuration more similar to cassiterite (rutile-type) polymorph, without drastic cell distortions.

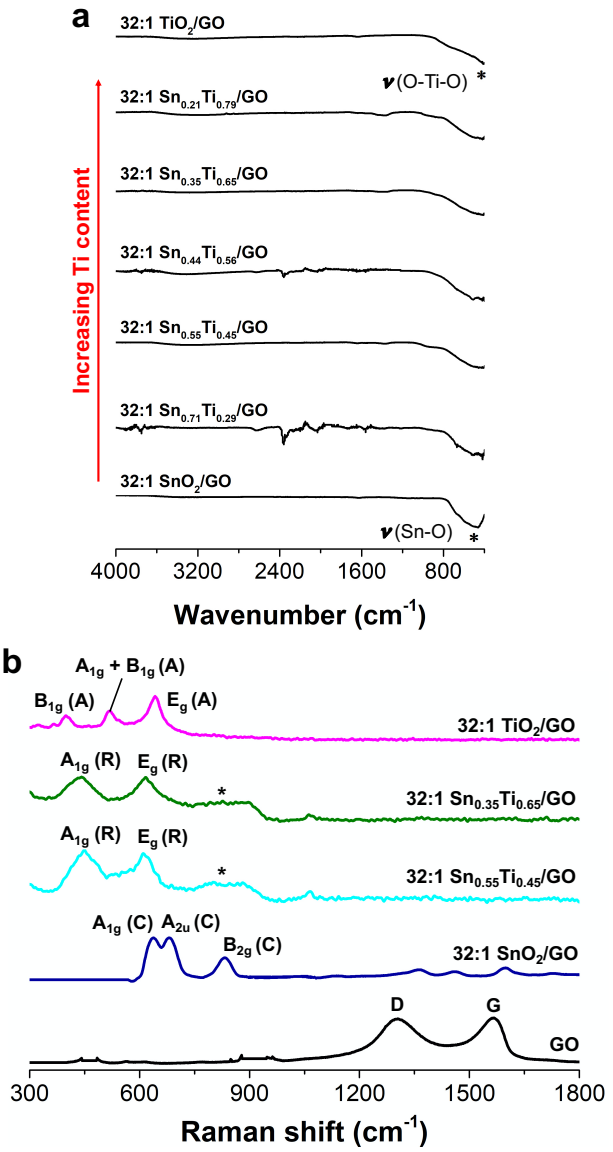

Figure 4.16. *(a) FTIR spectra comparison with the gradual shift of the broad band at 600-500 cm-1 towards lower wavenumber values. (b) Raman analysis of 32:1 SnO_2/GO, 32:1 TiO_2/GO, 32:1 $Sn_{0.55}Ti_{0.45}$/GO, 32:1 $Sn_{0.35}Ti_{0.65}$/GO samples, in which the main bands have been highlighted (A = anatase, R = rutile and C = cassiterite). GO Raman spectrum has been reported to evidence its absence in all the hybrid materials.*

Furthermore, the effect of Ti-content was also investigated by FTIR and Raman spectroscopies (Figure 4.16). Figure 4.16a displays the non-linear, very rapid transition from

SnO_2 (~500 cm^{-1}, ascribable to Sn–O stretching[28]) to TiO_2 (~470 cm^{-1}, ascribable to O–Ti–O stretching[42]) infrared modes, which is already almost finished in the 32:1 $Sn_{0.71}Ti_{0.29}$/GO sample. According to Tricoli *et al.*[41], even 9% Ti-doping into SnO_2 matrix can have implications to the ionic transport in the crystal, to the molecular bond length and, thus, to the surface adsorption properties/sensing performances. Besides, a further corroboration of the previous XRPD results was obtained by Raman spectroscopy. In particular, spectral analysis shows one main transition by decreasing the Ti content, *i.e.* from the anatase polymorph of 32:1 TiO_2/GO to the rutile one of the mixed oxides (Fig. 4.16b). Notably, 32:1 TiO_2/GO displays the four Raman modes of anatase TiO_2: the E_g at 641 cm^{-1}, the A_{1g} and B_{1g} at 524 cm^{-1} and the B_{1g} one at 398 cm^{-1}[41]. Conversely, with the decreasing of the titanium content, the E_g and A_{1g} rutile peaks of TiO_2 are detected at 612 and 445 cm^{-1}, respectively[41]. This abrupt transition from anatase to rutile is consistent with either XRPD (Figure 4.15) or FTIR (Figure 4.15) results. Moreover, a further reduction of the Ti amount gradually shifts the TiO_2 rutile Raman modes to the SnO_2 cassiterite ones, clearly visible in the 32:1 SnO_2/GO spectrum (*i.e.* A_{1g} at 624 cm^{-1}, A_{2u} at 640 cm^{-1} and B_{2g} at 766 cm^{-1}).

Concerning the specific surface area (S_{BET}), it increases (from 60 $m^2\ g^{-1}$ of 32:1 SnO_2/GO; Table 4.3, 2nd column) with the increasing of Ti-content, reaching a maximum of 178 $m^2\ g^{-1}$ for the 32:1 $Sn_{0.44}Ti_{0.56}$/GO. Then, a drastic reduction of this parameter occurred by further increasing the titanium amount. This might be due to the much more presence of TiO_2 rutile polymorph, which has a very small surface area (< 10 $m^2\ g^{-1}$), even compared to the anatase phase (132 $m^2\ g^{-1}$ for pure TiO_2 and 159 $m^2\ g^{-1}$ for 32:1 TiO_2/GO; Table 4.3, 2nd column). Interestingly, the same trend was observed for the total pores volume (see Table 4.3, 3rd column).

Sample	S_{BET} ($m^2\ g^{-1}$)	$V_{tot.\ pores}$ ($cm^3\ g^{-1}$)	E_g (eV)
Graphite	11	0.030	–
GO	44	0.034	–
SnO_2	67	0.210	3.60
32:1 SnO_2/GO	60	0.130	3.40
32:1 $Sn_{0.71}Ti_{0.29}$/GO	65	0.048	3.25
32:1 $Sn_{0.55}Ti_{0.45}$/GO	117	0.119	3.26
32:1 $Sn_{0.44}Ti_{0.56}$/GO	178	0.170	3.23
32:1 $Sn_{0.35}Ti_{0.65}$/GO	44	0.070	3.15
32:1 $Sn_{0.21}Ti_{0.79}$/GO	34	0.120	3.05
32:1 TiO_2/GO	159	0.303	3.20
TiO_2 anatase	132	0.250	3.00
Commercial TiO_2 rutile	< 10	0.033	2.90

Table 4.3. *Surface area (S_{BET}), total pore volume ($V_{tot.\ pores}$) and optical band gap (E_g, by Kubelka-Munk extrapolation).*

Specifically, BET isotherms (Fig. 4.17a) reveal the presence of bottle-necked shaped pores[8], with a typical H2-type hysteresis loop for pure TiO_2, SnO_2 and 32:1 TiO_2/GO. On the contrary, mixed oxides materials, along with 32:1 SnO_2/GO (as already seen in paragraph 4.2) are characterized by an isotherm shape intermediary between that of pure SnO_2 or TiO_2 and the one of GO. Therefore, some of these powders possess bottle neck-shaped pores (typical of SnO_2), others slit-shaped ones (typical of GO). Instead, regarding the pores distribution, Figure 4.17b reports a comparison among the synthesized materials. Notably, by increasing the titanium amount, pores tend to get smaller, showing the distribution peak at around 3-4 nm. Nevertheless 32:1 $Sn_{0.44}Ti_{0.56}$/GO compound represents an exception, since it has a very small total pores volume and the corresponding Gaussian curve has a very broad band centered at around 12 nm. Besides, either 32:1 SnO_2/GO or 32:1 TiO_2/GO possess pores with a slightly higher average dimensions, of ca 5-6 nm.

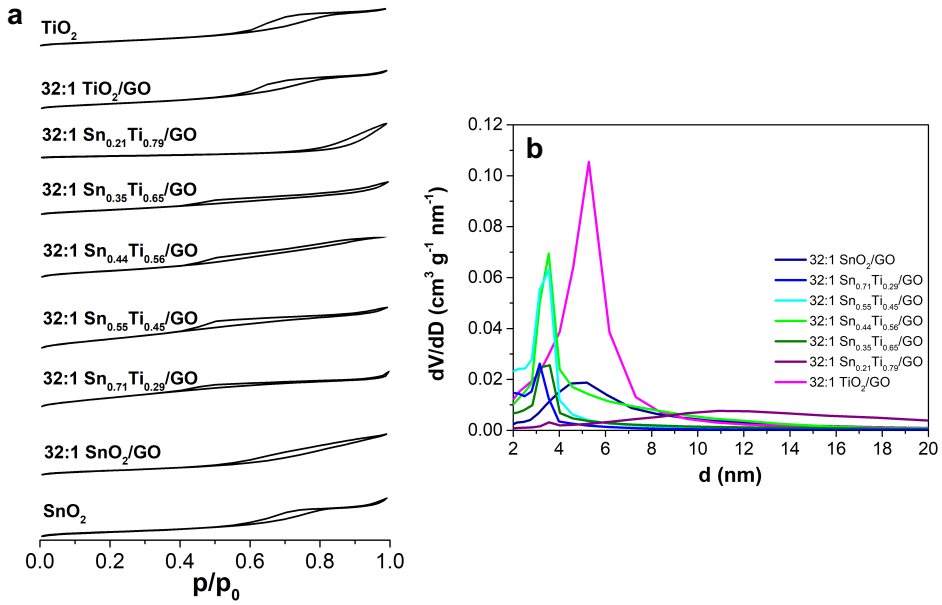

Figure 4.17. *(a) Comparison of BET isotherms from pure cassiterite SnO_2, 32:1 SnO_2/GO to 32:1 TiO_2/GO, pure anatase TiO_2. (b) Pores size distribution by BET analysis for all the composite oxides.*

Figures 4.18 and A.26 display the surface texture and morphology of the as-prepared powders, by both SEM and TEM measurements. Specifically, from SEM micrographs, it is possible to observe the presence of micrometric spherical aggregates, even of about 200 μm (see Fig. A.26a), especially for low Ti-content. Conversely, by increasing the titanium amount, these agglomerates tend to become smaller (< 100 μm), showing a characteristic sponge-like morphology (Fig. A.26e), that is much more similar to 32:1 TiO_2/GO one (Fig. A.26f). In

addition, by EDX analysis, the corroboration of the amount of Sn and Ti in the mixed oxides was obtained, as reported in Figure A.26. Parallelly, TEM images reveal the presence of nanometric crystalline particles in either cassiterite 32:1 SnO_2/GO or anatase TiO_2/GO (Fig. 4.18). On the contrary, the solid solutions SnO_2-TiO_2-GO display a lower powders crystallinity, as a further corroboration of XRPD results. In particular, for these last samples, it seems that SnO_2 behaved as seeds for the further growth of the rutile titania nanoparticles.

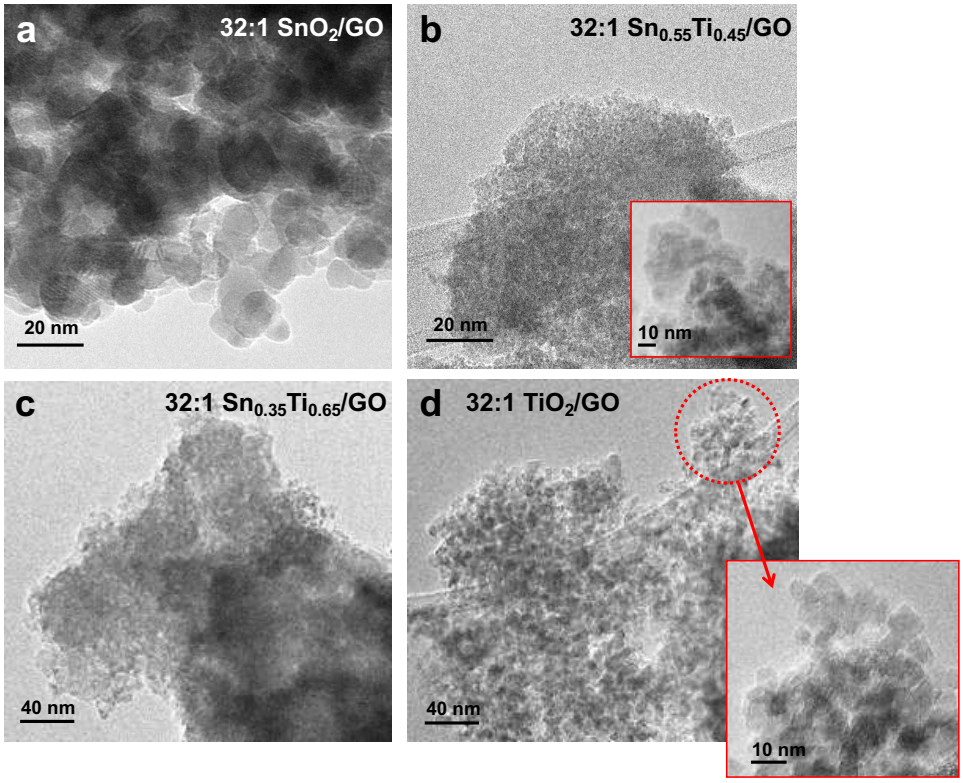

Figure 4.18. *TEM images of (a) 32:1 SnO_2/GO, (b) 32:1 $Sn_{0.55}Ti_{0.45}$/GO, (c) 32:1 $Sn_{0.35}Ti_{0.65}$/GO and (d) 32:1 TiO_2/GO, as representative samples (inset: relative magnifications).*

As concern the powders optical properties, DRS analyses were performed and, subsequently, elaborated by Kubelka-Munk equation. Notably, with the increasing of titanium ions into tin dioxide lattice, the band gap value tends to decrease (Table 4.3, 4th column and Figure 4.19a). Indeed, from 3.40 eV of 32:1 SnO_2/GO, E_g decreases till 3.05 eV of 32:1 $Sn_{0.21}Ti_{0.79}$/GO, reaching a value much more similar to the pure TiO_2 one (*i.e.* 2.90-3.00 eV). These results are further confirmed by literature (see Fig. 4.19b): the same trend has been already reported by Zakrzewska *et al.*[43], pointing out the systematically change of the solid solutions band gap with the increasing of titanium content.

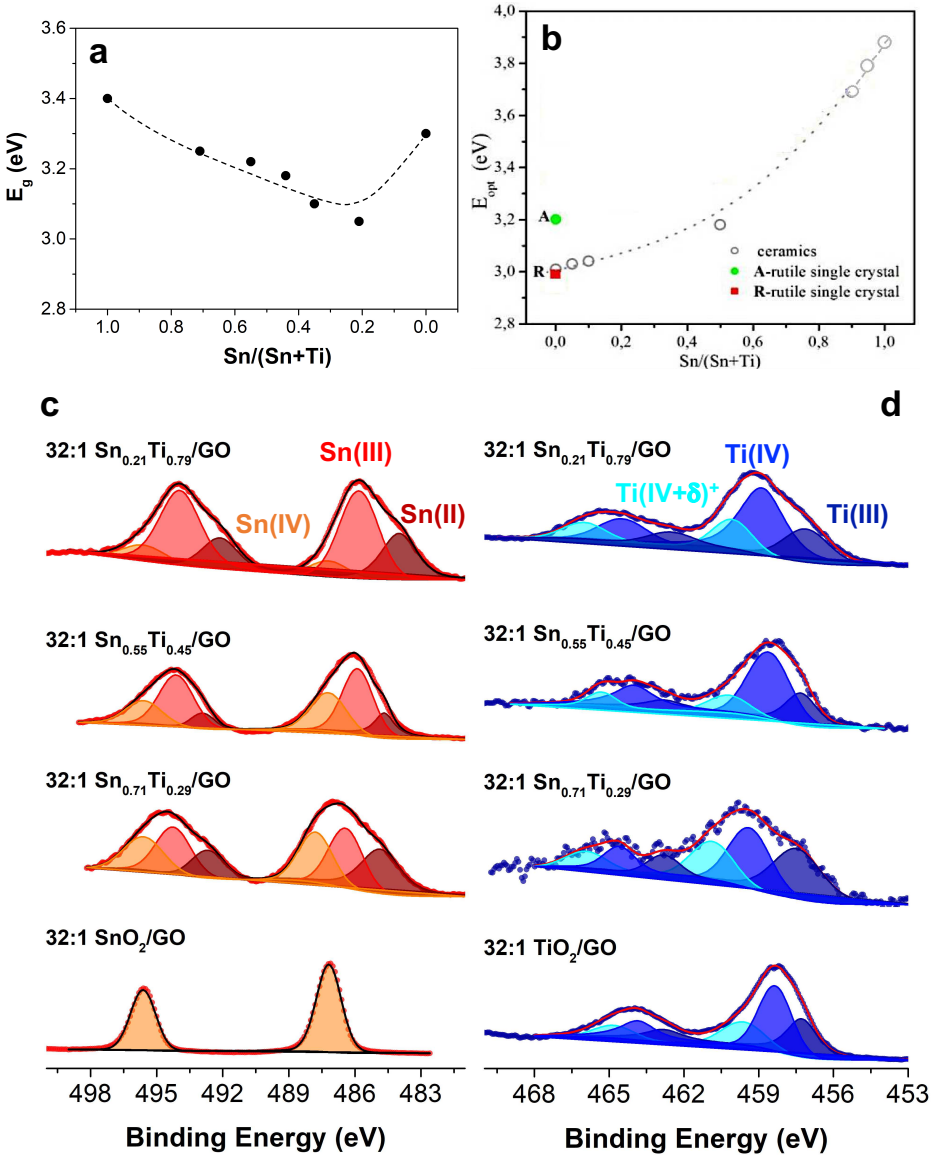

Figure 4.19. *(a) Band gap (E_g) trend as a function of the Sn/(Sn+Ti) ratio. (b) Optical band gap E_{opt} as a function of composition for solid solutions of $Ti_xSn_{1-x}O_2$ (Adapted with permission[43], Copyright 2012, Elsevier, open access). XP spectra of (c) Sn 3d and (d) Ti 2p regions relative to three mixed oxides (with x = 0.71, 0.55 and 0.21) as representative samples. 32:1 SnO_2/GO and TiO_2/GO have been reported for comparison.*

Furthermore, surface properties by XPS measurements were finely investigated to give insights into powders composition by varying the Ti content. Hence, three different Sn/(Sn+Ti) ratios, *i.e.* the lowest 0.21, an intermediate 0.55 and the highest 0.71 ones, were studied. Particularly, Sn $3d_{5/2}$ region (Fig. 4.19c) shows the presence of a peak at around 486.90

eV, typical of Sn(IV) species[46], in all the composites samples. However, while 32:1 SnO_2/GO signal can be deconvoluted with only this peak, the mixed oxides interestingly possess broader spectra, which underline the presence of other bands. Particularly, with the addition of titanium ions, XP spectra tend to smoothly shift towards lower binding energies and two other peaks (at ca 485.90 and 484.20 eV) appear, that can be ascribable to Sn(III) and Sn(II) species, respectively[46]. Therefore, these spectral changes prove that the Sn atoms are gradually substituted by Ti cations, resulting in the formation of tin ions with lower oxidation states, probably due to oxygen vacancies[46]. This observation is further corroborated by the area of these peaks: by increasing the Ti content, lower Sn valence states become more and more. Besides, focusing on the Ti $2p_{1/2}$ region (Fig. 4.19d), a confirmation of the previous outcomes was obtained. Indeed, for all the three mixed oxides, the peaks relative to defective Ti species[32], Ti(III) (at ca 456.40 eV) and $Ti(IV+\delta)^+$ (at ca 459.20 eV) are observable. In particular, with the increasing of titanium atoms, their area rises due to the presence of Sn(III) and Sn(II) species and, hence, to the much higher lattice defectivity.

4.3.3. Chemical sensing

As widely reported previously, both ZnO- and SnO_2-based compounds possess optimal features as sensing materials for very small and high-polar molecules, such as gaseous ethanol. Herein, instead, the solid solution oxides will be tested towards a bigger and non-polar analyte, as toluene. Notably, gas sensing measurements were conducted firstly at high temperatures (350 °C, without UV light), and, in a second moment, at decreased T by exploiting the synergistic effect between n-type semiconductors and GO. For the sake of comparison, tests were also performed using pure SnO_2 and TiO_2: in both cases, no reproducible and good responses were obtained. Furthermore, also in the present case, the adopted scalable air-spraying method led to very homogeneous micrometric films, having a thickness of about 1.5 – 3.0 μm and a very high porosity, *i.e.* above 90% for all the tested materials.

Hence, Figures 4.20a and A.27 show the responses obtained with 32:1 SnO_2/GO, 32:1 TiO_2/GO and the mixed oxides materials towards different toluene concentrations (from 4 to ppb-level), at 350 °C. Interestingly, by increasing the titanium amount, the sensors response gets worsen and worsen (see Fig. A.27e relative to 32:1 $Sn_{0.21}Ti_{0.79}$/GO), even resulting in no conductivity for the 32:1 $Sn_{0.44}Ti_{0.56}$/GO sample. The reason for this behavior has been already unravelled by Tricoli *et al.*[41], who investigated the electrical and chemical properties of SnO_2-TiO_2 solid solutions. Specifically, they observed that the resistivity of these materials increases up to 7 orders of magnitude by increasing the Ti-content from 0 to 80%. Thus, this strong

increase in resistivity may indicate the dominant role of the surface states in determining the solid solution conductivity. Hence, the most performing samples, in terms of either sensitivity (down to 100 ppb of toluene, Fig. A.27) or signal intensity (see histograms in Fig. 4.20a) seem to be 32:1 SnO_2/GO, 32:1 TiO_2/GO and 32:1 $Sn_{0.55}Ti_{0.45}$/GO. Furthermore, also concerning the response and recovery behaviors, all these three chemoresistors have shown very sharp signals, indicating short response/recovery times (of about 20-35 and 30-60, respectively; inset of Fig. A.27).

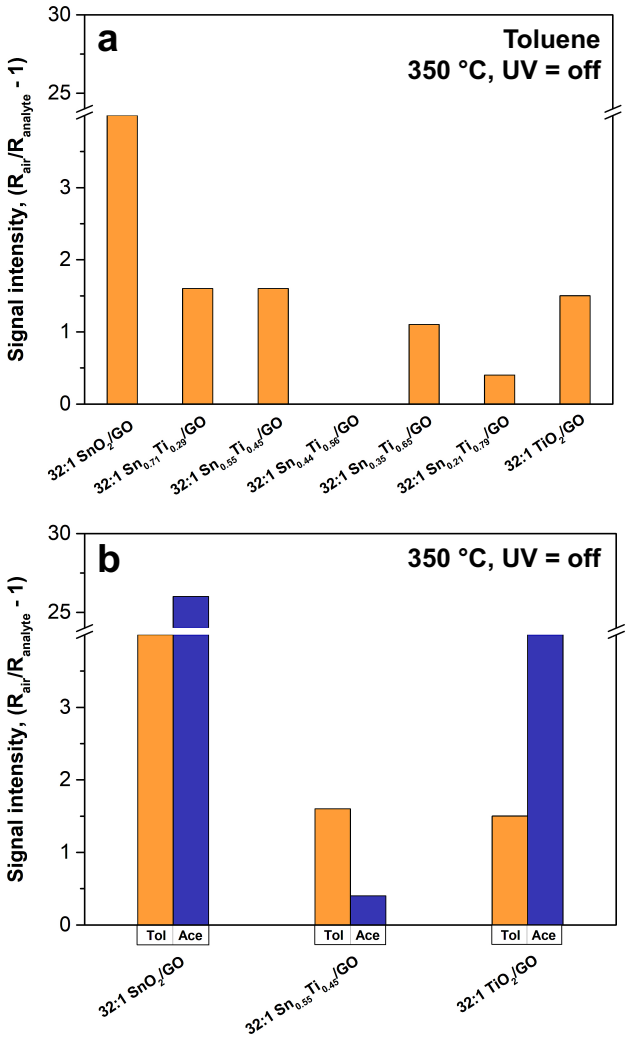

Figure 4.20. *(a) Histograms displaying a comparison of the response intensity obtained with the composite oxides towards 4 ppm of toluene analyte. (b) 32:1 SnO_2/GO, 32:1 TiO_2/GO and 32:1 $Sn_{0.55}Ti_{0.45}$/GO (as one of the most performing samples) sensor signals towards acetone molecules. Tests were carried out in simulated air (20% O_2 – 80% N_2) at 350 °C, without UV light.*

Starting from all the previous findings, the optimal samples were tested towards acetone analyte, to eventually elucidate their potential for selectively sensing a specific biomarker. Thus, Figure 4.20b shows the comparison of the 4 ppm-signal intensity for all the three compounds (always at high operating temperatures, 350 °C). Moreover, the relative sensor responses are reported in Figure A.28. Interestingly, two main observations can be made: regarding the sensitivity and the signal intensities, 32:1 SnO_2/GO (Figs. A.27a and A.28a) and 32:1 TiO_2/GO (Figs. A.27f and A.28b) seems to better sense acetone with respect to toluene gaseous molecules. Indeed, even if in both cases 100 ppb are detected, either the two composites display a six-fold signal intensity with respect to the ones achieved in the presence of toluene analyte (at the same concentration and experimental conditions; see Fig. 4.20b). Secondly, the mixed oxide 32:1 $Sn_{0.55}Ti_{0.45}$/GO seems to have a much more selectivity towards toluene than acetone, as noticeable in Fig. 4.20b, notwithstanding the low signal intensities. Interestingly, also the sensitivity appears to be affected, since in the case of acetone, 200 ppb were the lowest detectable concentration (instead of 100 ppb for toluene; Figs. A.27c and A.28c). Finally, response and recovery times are well-comparable to the ones reached towards toluene, and all below 70 s (inset of Fig. A.28).

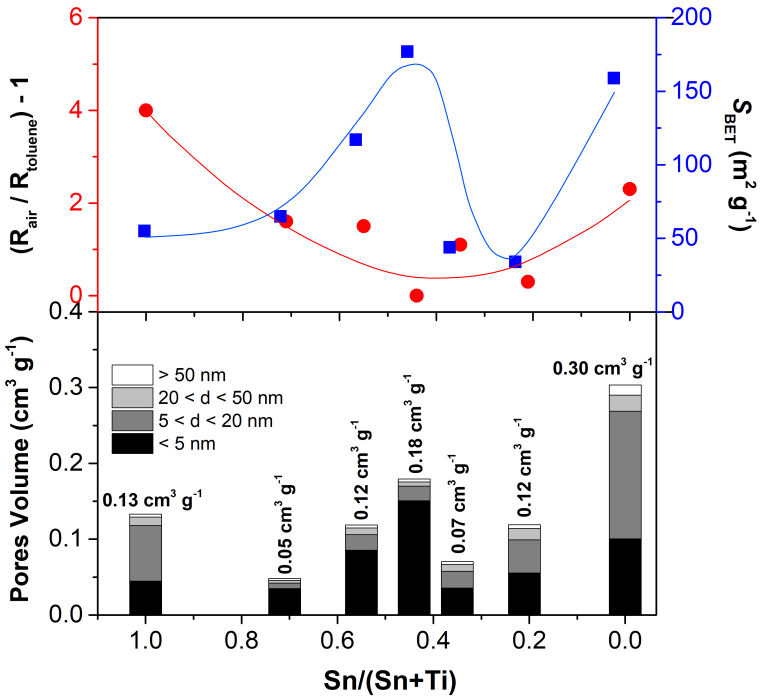

Figure 4.21. *Comparison among surface area (S_{BET}) and pores volume distribution ($V_{tot.\ pores}$) trend with respect to the sensor signal intensity (at 4 ppm) towards toluene molecules, at 350 °C (without UV light).*

One of the most decisive factors, influencing the materials sensing behavior, is certainly their surface, and especially the specific surface area and the pores features. Hence, in order to unravel the role played by these parameters, a comparison of them with the sensors responses intensity (at 4 ppm) has been drawn (Fig. 4.21). Notably, by increasing the Ti content, the surface area increases, has a maximum at Sn/(Sn+Ti) equal to 0.44, and then decreases till 32:1 TiO_2/GO sample, in which it rises up to ca 160 $m^2\ g^{-1}$, again (blu line). The same trend is also observable for the total pores volume (histograms). Conversely, the sensors response shows an opposite tendency, highlighting the fact that the worst behavior is obtained with the Sn/Ti solid solution having the highest surface area (177 $m^2\ g^{-1}$). However, already Zakrzewska *et al.*[43] described an analogous performance trend, evidencing a minimum of H_2 sensing for Sn/(Sn+Ti) of 0.5 (Figure 4.22).

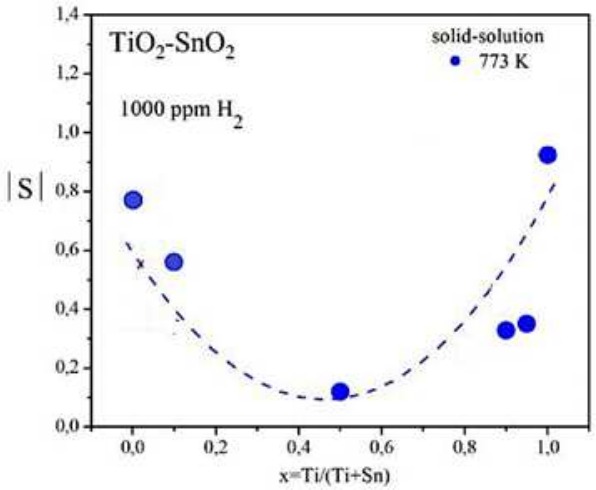

Figure 4.22. *Sensor response as a function of Sn/(Sn+Ti) in microcrystalline solid solutions. Adapted with permission*[43]*, Copyright 2012, Elsevier (open access).*

Therefore, samples with a slightly higher Sn content seem to be preferable for VOCs sensing. This further corroborates our choice to adopt 32:1 $Sn_{0.55}Ti_{0.45}$/GO solid solution for both selectivity investigation and sensing at lower working temperatures. Hence, Figures 4.23a and A.29 display a comparison between toluene and acetone sensing by the adopted 32:1 $Sn_{0.55}Ti_{0.45}$/GO mixed oxide, at 250 °C (with the aid of the UV light). Notably, with this sample, it was not possible to reduce the operating temperature further, even exploiting the UV irradiations. For either the two gases, 200 ppb were detected. Nevertheless, the signal obtained towards toluene unlikely shows a low signal-to-noise ratio (Fig. A.29a). Notwithstanding this fact, interestingly, the selectivity towards big and non-polar analytes, as toluene, has been preserved.

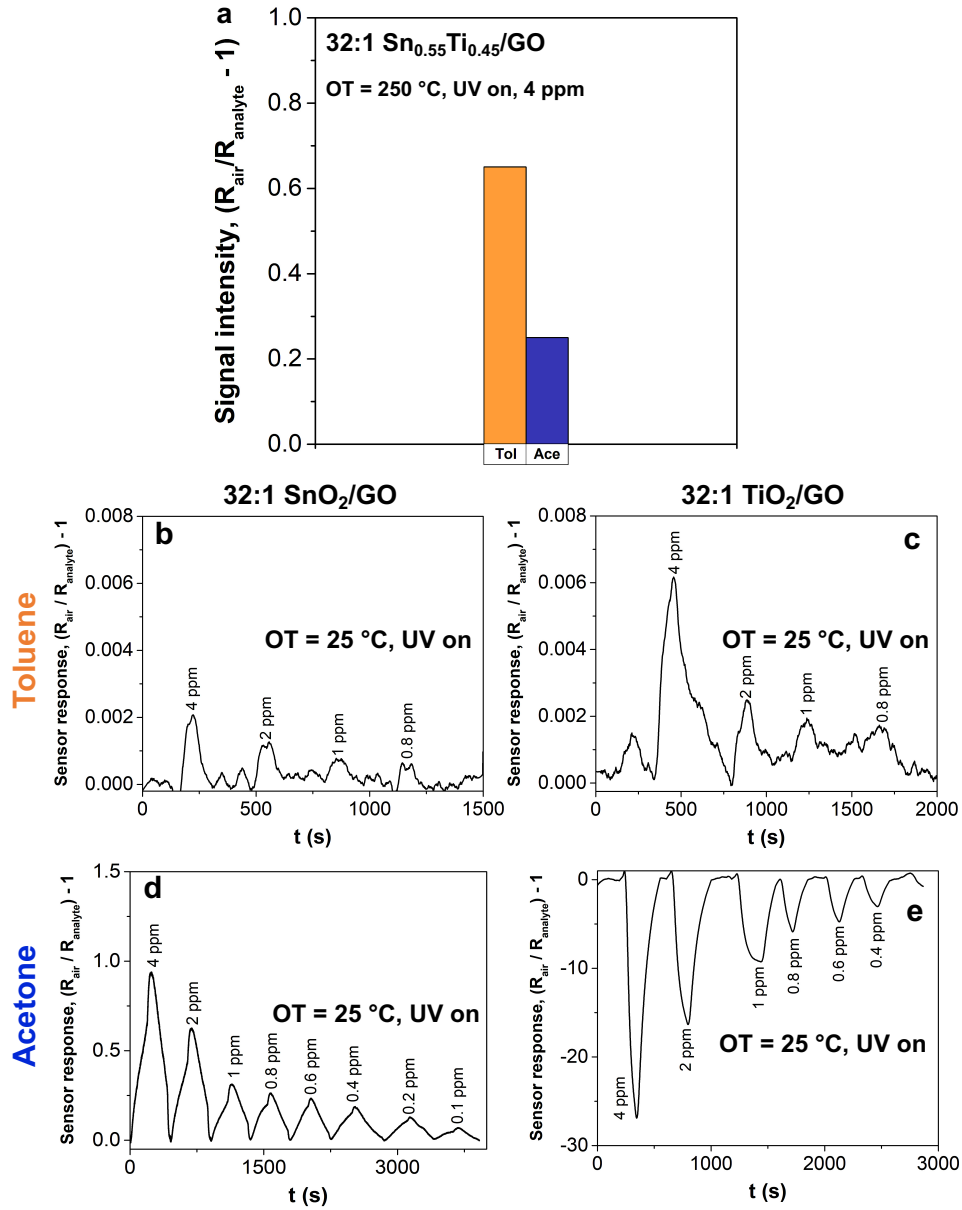

Figure 4.23. *(a) Histogram showing the higher selectivity towards toluene with respect to acetone, exploiting the composite 32:1 $Sn_{0.55}Ti_{0.45}$/GO sample, at 250 °C (UV-light aided). Sensor responses obtained towards (b,c) toluene and (d,e) acetone for 32:1 SnO_2/GO and 32:1 TiO_2/GO, at RT with UV irradiation. All the measurements were carried out in simulated air (20% O_2 – 80% N_2). OT = Operating Temperature.*

On the contrary, with 32:1 SnO_2/GO and 32:1 TiO_2/GO (Figs. 4.23b–e) composites, a signal was obtained even at RT (UV light-aided). Specifically, both samples conserve the higher sensitivity and goodness of sensor signal towards acetone molecules, rather than toluene gas.

However, as previously noticed for 4:1 SnO_2/GO material (see 4.2.3 paragraph), 32:1 TiO_2/GO shows a "reversed" behavior (see the Chapter 6) in the case of small and polar molecules, such as acetone (Figure 4.23e), maybe caused by the interaction between the moisture adsorbed on the sensing material highly-hydrophilic surface and the VOCs molecules and it is lost when the operating temperature is above the water condensation point, as reported by Tricoli *et al*.[33]. Hence, once more, this interesting behavior could be exploited for the engineering of materials with higher sensing performances in terms of selectivity degree.

4.3.4. Conclusions

In this study, 32:1 SnO_2-TiO_2-GO-based materials have been synthesized via a simple hydrothermal route, varying the titanium content in the tin dioxide matrix. All these materials have been finely investigated on structural, morphological, surface and optical points of view. Furthermore, the toluene and acetone gas sensing performances of the as-prepared sensors were systematically investigated and compared with 32:1 SnO_2/GO and 32:1 TiO_2/GO nanocomposites. At 350 °C, mixed oxides, having a higher content of tin with respect to titanium (as 32:1 $Sn_{0.55}Ti_{0.45}$/GO), showed promising sensing behavior towards bigger and non-polar gaseous molecules, such as toluene. In particular, these solid solutions seem to be much more selective towards this species rather than acetone one; even if, in both cases, hundreds of ppb concentrations were detected. Unfortunately, the lowest operating temperature, achieved by exploiting the UV light, was 250 °C, still too high to possibly use these materials in point-of-care devices. Hence, further studies, especially concerning different synthetic routes, are required to improve the sensing at RT. Indeed, only with 32:1 SnO_2/GO and 32:1 TiO_2/GO, room temperature conditions were achieved showing, however, a greater selectivity towards acetone analyte (see Chapter 6).

References

[1] E. Pargoletti, U. H. Hossain, I. Di Bernardo, H. Chen, T. Tran-Phu, J. Lipton-Duffin, G. Cappelletti, A. Tricoli, *Nanoscale* **2019**.

[2] E. Pargoletti, S. Mostoni, G. Rassu, V. Pifferi, D. Meroni, L. Falciola, E. Davoli, M. Marelli, G. Cappelletti, *Environ. Sci. Pollut. Res.* **2017**, *24*.

[3] G. Cappelletti, V. Pifferi, S. Mostoni, L. Falciola, C. Di Bari, F. Spadavecchia, D. Meroni, E. Davoli, S. Ardizzone, *Chem. Commun.* **2015**, *51*, 10459.

[4] K. Al Abdullah, S. Awad, J. Zaraket, C. Salame, *Energy Procedia* **2017**, *119*, 565.

[5] Z. Q. Zheng, J. D. Yao, B. Wang, G. W. Yang, *Sci. Rep.* **2015**, *5*, 1.

[6] R. Atchudan, T. N. J. I. Edison, S. Perumal, M. Shanmugam, Y. R. Lee, *J. Photochem. Photobiol. A Chem.* **2017**, *337*, 100.

[7] S. Mostoni, V. Pifferi, L. Falciola, D. Meroni, E. Pargoletti, E. Davoli, G. Cappelletti, *J. Photochem. Photobiol. A Chem.* **2017**, *332*.

[8] S. Lowell, *Introduction to powder surface area*; John Wiley and Sons, 1979.

[9] N. Nasiri, R. Bo, F. Wang, L. Fu, A. Tricoli, *Adv. Mater.* **2015**, *27*, 4336.

[10] A. H. Moharram, S. A. Mansour, M. A. Hussein, M. Rashad, *J. Nanomater.* **2014**, *2014*.

[11] Y. Tu, S. Chen, X. Li, J. Gorbaciova, W. P. Gillin, S. Krause, J. Briscoe, *J. Mater. Chem. C* **2018**, *6*, 1815.

[12] D. A. Skoog, J. F. Holler, S. R. Crouch, *Chimica analitica strumentale*; Edises, 2009.

[13] A. Tricoli, M. Righettoni, A. Teleki, *Angew. Chemie Int. Ed.* **2010**, *49*, 7632.

[14] T. Becker, S. Ahlers, C. Bosch-v.Braunmühl, G. Müller, O. Kiesewetter, *Sensors Actuators, B Chem.* **2001**, *77*, 55.

[15] S.-P. Chang, K.-Y. Chen, *ISRN Nanotechnol.* **2012**, *2012*, 1.

[16] R. Bo, N. Nasiri, H. Chen, D. Caputo, L. Fu, A. Tricoli, *ACS Appl. Mater. Interfaces* **2017**, *9*, 2606.

[17] R. Zhang, Z. Liu, L. Ling, B. Wang, *Appl. Surf. Sci.* **2015**, *353*, 150.

[18] M. M. Rahman, S. B. Khan, A. M. Asiri, K. A. Alamry, A. A. P. Khan, A. Khan, M. A. Rub, N. Azum, *Microchim. Acta* **2013**, *180*, 675.

[19] H. Gong, Y. J. Wang, S. C. Teo, L. Huang, *Sensors Actuators B Chem.* **1999**, *54*, 232.

[20] B. P. J. de Lacy Costello, R. J. Ewen, N. M. Ratcliffe, P. S. Sivanand, *Sensors Actuators B Chem.* **2003**, *92*, 159.

[21] R. Rella, J. Spadavecchia, M. G. Manera, S. Capone, A. Taurino, M. Martino, A. P. Caricato, T. Tunno, *Sensors Actuators B Chem.* **2007**, *127*, 426.

[22] C. P. Gupta, S. K. Sharma, B. Bhowmik, K. T. Sampath, C. Periasamy, S. Sancheti, *J. Electron. Mater.* **2019**, *48*, 3686.

[23] M. Righettoni, A. Tricoli, S. Gass, A. Schmid, A. Amann, S. E. Pratsinis, *Anal. Chim. Acta* **2012**, *738*, 69.

[24] M. Righettoni, A. Tricoli, S. E. Pratsinis, *Anal. Chem.* **2010**, *82*, 3581.

[25] E. Pargoletti, A. Tricoli, V. Pifferi, S. Orsini, M. Longhi, V. Guglielmi, G. Cerrato, L. Falciola, M. Derudi, G. Cappelletti, *Appl. Surf. Sci.* **2019**.

[26] A. Kumar, L. Rout, L. S. K. Achary, A. Mohanty, R. S. Dhaka, P. Dash, *RSC Adv.* **2016**, *6*, 32074.

[27] A. D. Bhagwat, S. S. Sawant, B. G. Ankamwar, C. M. Mahajan, *J. Nano- Electron. Phys.* **2015**, *7*, 7.

[28] M. K. Singh, R. K. Pandey, R. Prakash, *Org. Electron.* **2017**, *50*, 359.

[29] S. Muralikrishna, K. Sureshkumar, T. S. Varley, D. H. Nagaraju, T. Ramakrishnappa, *Anal. Methods* **2014**, *6*, 8698.

[30] L. Tang, X. Li, R. Ji, K. S. Teng, G. Tai, J. Ye, C. Wei, S. P. Lau, *J. Mater. Chem.* **2012**, *22*, 5676.

[31] L. Jin, W. Chen, H. Zhang, G. Xiao, C. Yu, Q. Zhou, *Appl. Sci.* **2016**, *7*, 19.

[32] E. Pargoletti, G. Cappelletti, A. Minguzzi, S. Rondinini, M. Leoni, M. Marelli, A. Vertova, *J. Power Sources* **2016**, *325*, 116.

[33] H. Chen, R. Bo, A. Shrestha, B. Xin, N. Nasiri, J. Zhou, I. Di Bernardo, A. Dodd, M. Saunders, J. Lipton-Duffin, T. White, T. Tsuzuki, A. Tricoli, *Adv. Opt. Mater.* **2018**, *6*, 1800677.

[34] B. A. Vessalli, C. A. Zito, T. M. Perfecto, D. P. Volanti, T. Mazon, *J. Alloys Compd.* **2017**, *696*, 996.

[35] C. A. Zito, T. M. Perfecto, D. P. Volanti, *Sensors Actuators B Chem.* **2017**, *244*, 466.

[36] M. Arvani, H. Mohammad Aliha, A. A. Khodadadi, Y. Mortazavi, *Sci. Iran.* **2017**, *0*, 0.

[37] L. Xiao, S. Shu, S. Liu, *Sensors Actuators B Chem.* **2015**, *221*, 120.

[38] X. Kou, N. Xie, F. Chen, T. Wang, L. Guo, C. Wang, Q. Wang, J. Ma, Y. Sun, H. Zhang, G. Lu, *Sensors Actuators, B Chem.* **2018**, *256*, 861.

[39] F. Ren, L. Gao, Y. Yuan, Y. Zhang, A. Alqrni, O. M. Al-Dossary, J. Xu, *Sensors Actuators B Chem.* **2016**, *223*, 914.

[40] S. M. And, V. Thangadurai, *Soil Mech. Found. Eng.* **1978**, *26*, 73.

[41] A. Tricoli, M. Righettoni, S. E. Pratsinis, *Nanotechnology* **2009**, *20*, 315502.

[42] R. Kalidoss, S. Umapathy, Y. Sivalingam, *Appl. Surf. Sci.* **2018**, *449*, 677.

[43] K. Zakrzewska, M. Radecka, *Procedia Eng.* **2012**, *47*, 1077.

[44] L. Trotochaud, S. W. Boettcher, *Chem. Mater.* **2011**, *23*, 4920.

[45] C. WY, L. DD, S. BK, *Thin Solid Films* **1992**, *221*, 304.

[46] Q. Tian, W. Wei, J. Dai, Q. Sun, J. Zhuang, Y. Zheng, P. Liu, M. Fan, L. Chen, *Appl.*

Catal. B Environ. **2019**, *244*, 45.

Chapter 5

Tungsten trioxide: preliminary experimental and theoretical outcomes

"A winner is a dreamer who never gives up"

— Nelson Mandela

5.1. Synthesis of pure WO_3 and sensing applications

5.1.1. Introduction

The acetone concentration in the breath increases from 300-900 ppb for healthy humans to more than 1800 ppb in diabetic patients. Hence, acetone has been accounted as a selective breath biomarker to type-1 diabetes[1–3]. Therefore, the detection of this small concentration difference (around 900 ppb) between healthy and ill people, in such a complex gas mixture as the human breath, requires a highly sensitive and selective acetone sensor.

Among the various chemoresistors, SnO_2, TiO_2, ZnO, In_2O_3 and WO_3 have been widely exploited[4–6]. Particularly, crystalline WO_3 has been extensively studied for many reasons: *i*) it exists in a series of stable solid polymorphs at different temperatures, from α phase to ε one[2,3]; *ii*) γ-WO_3 has been greatly investigated because it is stable at either room or higher temperatures, at which most devices are designed to operate[7,8]; *iii*) it showed high sensitivity towards VOCs species, such as acetone[2,9].

In this context, herein, a preliminary and systematic study on the synthesis of WO_3 nanoparticles to be used as acetone sensing materials will be conducted. The attention will be focused on tuning the powders physico-chemical features in order to achieve the optimal conditions, in terms of sensing performances, rather than synthesizing composites able to detect gases at low operating temperatures. Hence, different synthetic routes will be adopted (see in the Appendix Chapter, A.1.1 paragraph) and the resulting WO_3 materials will be finely characterized.

5.1.2. Tailoring the physico-chemical properties by tuning the synthetic route

As stated by Woodward *et al.*[10], the structure of WO_3 is best described as a 3D-network of corner-sharing WO_6 octahedra, in which the symmetry of the tungsten trioxide is lowered by the tilting of these WO_6 octahedra[10]. Notably, variations in these distortions give rise to several phase transitions. Indeed, tungsten trioxide adopts, at least, five distinct

crystallographic modifications between absolute zero and its melting point at 1700 K[10] (see Table 5.1).

Phase	Symmetry	Space group	Z	Temperature range (K)
α-WO_3	Tetragonal	$P4/nmm$	2	1010–1170
β-WO_3	Orthorhombic	$Pmnb$	8	600–1170
γ-WO_3	Monoclinic	$P2_1/n$	8	290–600
δ-WO_3	Triclinic	$P\bar{1}$	8	230–290
ε-WO_3	Monoclinic	Pc	4	0–230

Table 5.1. *Known polymorphs of WO_3, according to crystallographic data. Z is the number of atoms in the unit cell*[10].

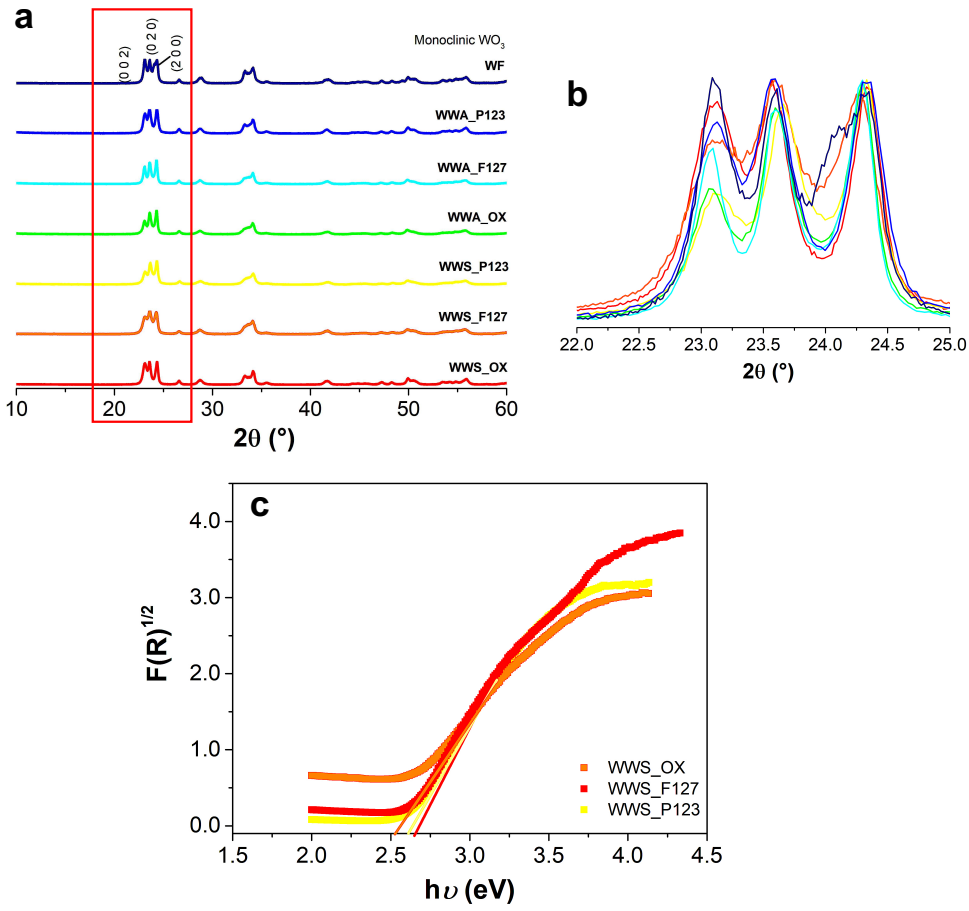

Figure 5.1. *(a) Comparison among XRPD spectra of the synthesized WO_3. All the powders show the characteristic monoclinic phase, as highlighted by the three main diffraction peaks at 23.1, 23.7 and 24.3°; (b) magnification of 2θ region between 22.0 and 25.0° (red rectangle). (c) Kubelka-Munk elaboration of diffuse reflectance spectra relative to WWS-series (as a representative example).*

Hence, starting from the literature data, structural properties were firstly evaluated. Figure 5.1a displays a comparison among the x-ray patterns of all the synthesized WO_3 powders. WWS- and WWA-series represent tungsten trioxide samples obtained by hydrothermal and sol-gel methods, respectively, in which different stabilizing/templating agents were added, principally to increase the surface area and the pores volume. Besides, other two powders were prepared: one by flame spray pyrolysis (WF) and the other by magnetron sputtering (WS) technique[1]. As clearly observable from XRPD spectra, all the nanopowders show the characteristic monoclinic phase, displaying the three WO_3 main peaks at $2\theta = 23.1°$ (0 0 2), 23.7° (0 2 0) and 24.3° (2 0 0). In particular, especially WWS_P123 (yellow line) and WWA_OX (green line) samples appear to be grown along a preferential direction, *i.e.* (2 0 0) one, since this peak is more intense that the other two (see Fig. 5.1b). Furthermore, each pattern seems to have a good degree of crystallinity, as witnessed by the crystallite domains size reported in Table 5.2 (2nd column).

Sample	$\langle d^{XRPD} \rangle$ (nm)	E_g (eV)	S_{BET} ($m^2\ g^{-1}$)	$V_{tot.\ pores}$ ($cm^3\ g^{-1}$)	t_{res} (s)	t_{rec} (s)
WWS_OX	49	2.63	24	0.35	50	70
WWS_F127	36	2.51	17	0.38	55	65
WWS_P123	15	2.64	21	0.10	33	100
WWA_OX	25	2.66	12	0.05	25	10
WWA_F127	30	2.64	7	0.03	33	50
WWA_P123	27	2.63	16	0.05	30	45
WF	24	2.73	20	0.07	30	20
WS_1000‡	–	–	–	–	27	30
WS_500+500‡	–	–	–	–	30	15

Table 5.2. *Crystallite domain size by XRPD analysis ($\langle d^{XRPD} \rangle$), optical band gap (E_g, by Kubelka-Munk extrapolation), surface area (S_{BET}) and total pores volume ($V_{tot.\ pores}$) for all the synthesized materials of the synthesized materials. Response and recovery times (calculated for 1 ppm signal) have been reported for measurements at 300 °C, towards acetone molecules. ‡For the sputtered samples (WS), the powders were directly deposited onto IDEs, thus no physico-chemical characterizations were performed.*

Indeed, crystallite domains are all in the range between 15 and 35 nm, with the exception of WWS_OX sample, for which they are smoothly bigger (ca 50 nm). On the structural point of view, also FTIR analyses were performed. Figure A.30 reports a comparison among the WWA-WO_3 series (as representative examples). Actually, for all the samples the main stretching modes relative to W–O–W and W–O_{inter}–W bonds are clearly visible at around 620 and 815 cm^{-1}, respectively, fully in accordance with the literature[12].

[1] The WS materials was directly synthesized onto interdigitated electrodes, due to the nature of the fabrication route, thus no physico-chemical characterizations were carried out on them, but previous studies[11] showed the high crystallinity of the as-prepared samples.

As regards the optical properties, band gap values have been determined by Kubelka-Munk elaboration of DRS spectra (Fig. 5.1c and Table 5.2, 3rd column). The obtained data are in the range ~2.50-2.70 eV comparable to those already reported[13] for WO_3 material.

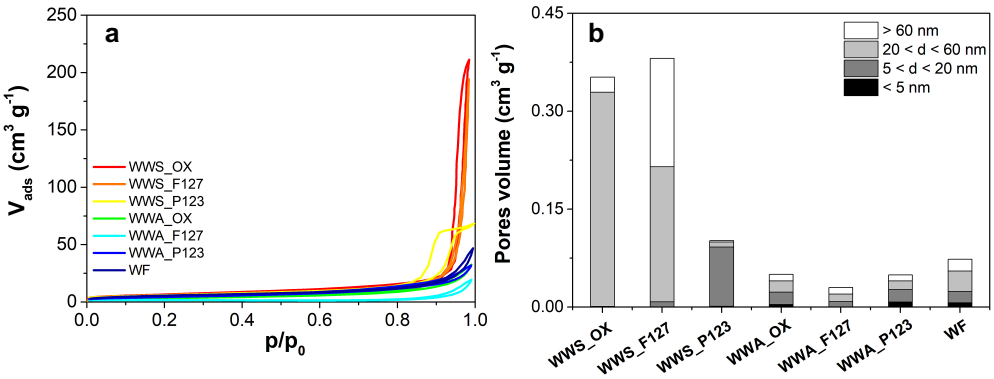

Figure 5.2. *(a) Comparison among BET isotherms relative to the synthesized pure WO_3. (b) Corresponding trend of pores volume distribution.*

Besides surface properties have been evaluated, focusing on how the surface area and the total pores volume can be tuned by tailoring the synthetic route. Firstly, all the specific surface areas are lower than 25 m^2 g^{-1}, as expected for tungsten oxide materials[12,14,15] (Table 5.2, 4th column). However, powders prepared *via* hydrothermal route and flame spray pyrolysis possess a slightly higher value. Specifically, the highest one was obtained by adding, in the preparation procedure, oxalic acid as both structure-directing and templating agent, according to Li *et al.* work[14]. Furthermore, almost all the BET isotherms display the same hysteresis loop, *i.e.* H3 type, that corresponds to the presence of slit-shaped pores[16] (Fig. 5.2a). Conversely, WWS_P123 (yellow line) shows a hysteresis loop typical of Mc Bain's pores, namely bottle-neck ones[16]. As regard the total pores volume and pores distribution, Figure 5.2b reports a comparison among the synthesized materials. Specifically, WWS_OX (0.35 cm^3 g^{-1}) and WWS_F127 (0.35 cm^3 g^{-1}) have a very high total pores volume (Table 5.2, 5th column) with respect to that of the other samples. Moreover, together with WF compound, they show a greater percentage of pores larger than 20 nm which, on the contrary, are very few in all the other materials (histograms in Fig. 5.2b).

Hence, since either the specific surface area/pores volume or the grain sizes play a pivotal role in the sensing of gaseous molecules, which contemplates an adsorption/desorption mechanism, it is mandatory to bear in mind that the final performances might result from a combination of all these parameters.

Finally, morphological properties were investigated. Figures 5.3a–e display SEM micrographs of some representative WO_3 samples.

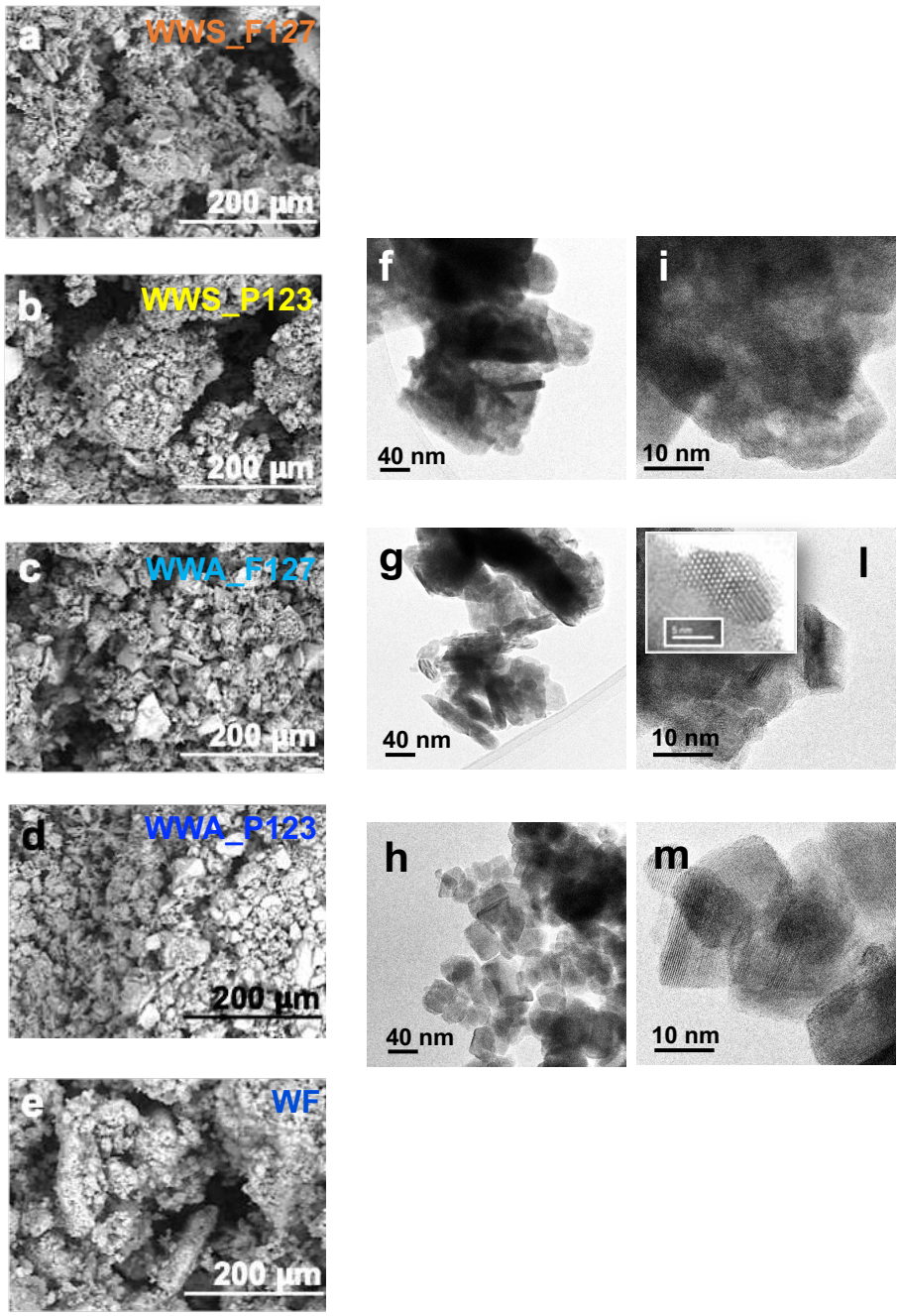

Figure 5.3. *(a–e) SEM micrographs of WWS_F127, WWS_P123, WWA_F127, WWA_P123 and WF samples. TEM images of (f) WWA_F127, (g) WWA_P123 and (h) WF. (i–m) Corresponding higher magnifications.*

All the powders have a similar surface texture, made of about 50 μm spherical agglomerates and, especially for samples prepared by adopting F127 tenside, platelet-like aggregates are clearly visible (Figs. 5.3a and c). Parallelly, high-resolution TEM images display highly crystalline particles for all the synthesized materials. Specifically, WWA_F127 is formed by dense aggregates having micrometric and sub-micrometric sizes, whereas WWA_P123 shows elongated nanoparticles of about 20-100 nm, with smoothed edges. WF sample has very smooth particles with heterogeneous dimensions, ranging from 5 to 50 nm.

5.1.3. Acetone sensing: results and discussion

As briefly above-mentioned, the as-synthesized WO_3 powders were tested towards acetone molecules, firstly at 300 °C (without the UV light). The working temperature was chosen according to the literature, as it is reported to be the optimal one for WO_3 material[8]. All the powders films on IDEs are around 1-2 μm in thickness. In the case of sputtered WO_3, 1000 nm was chosen due to the fact that previous tests revealed that thinner films are not so performing, giving very small current values, and thicker layers do not enhance the sensing responses. Concerning the films porosity, sprayed powders showed a very high value > 90%, as already reported for all the other sensing materials, previously discussed (see Chapter 4).

Hence, Figure 5.4 displays a comparison among the obtained results. Interestingly, each material has a specific response, with analogous sensitivity but different response/recovery times (Table 5.2, 8th and 9th column). Juxtaposing samples prepared with the same synthetic route, in the WWS-series the most performing one, in terms of signal intensity, is WWS_P123 (yellow line) *i.e.* the one synthesized with Pluronic® P123 as dispersing agent. On the contrary, among WWA-compounds, WO_3 prepared with oxalic acid (green line) seems to be the most performing, even if there is no a huge difference among the sensors responses. Finally, between the two sputtered samples, WS_500+500 (violet line) and WS_1000 (dark green line) show a similar signal intensity, even if with the former a smooth faster recovery was recorded (Table 5.2, 9th column). Furthermore, by comparing all the obtained responses, both WWS_P123 and WF (dark blue line) resulted to be the optimal ones, showing a very high signal response at the same VOC concentration.

In order to formulate a possible explanation of the previous observations, it is fundamental to notice that the optimal materials have the same surface area (21 and 20 $m^2 g^{-1}$; Table 5.2) and similar total pores volume (0.10 and 0.07 $cm^3 g^{-1}$), thus evidencing the non-randomness of the parameters influencing the sensing behavior. According to Tamaki *et al.*[17], grain sizes may affect the WO_3 sensing. Indeed, they tuned the synthetic route in order to fabricate nanopowders with crystallite sizes in the range between 16 and 57 nm. Notably, they have

found that at grain dimensions below 25 nm, the signal intensity and sensitivity increase up to about three/four times. Interestingly, also in the present case, both WWS_P123 and WF possess an average grain size of 15 and 24 nm, respectively, thus resulting consistent with the Tamaki's observations[17].

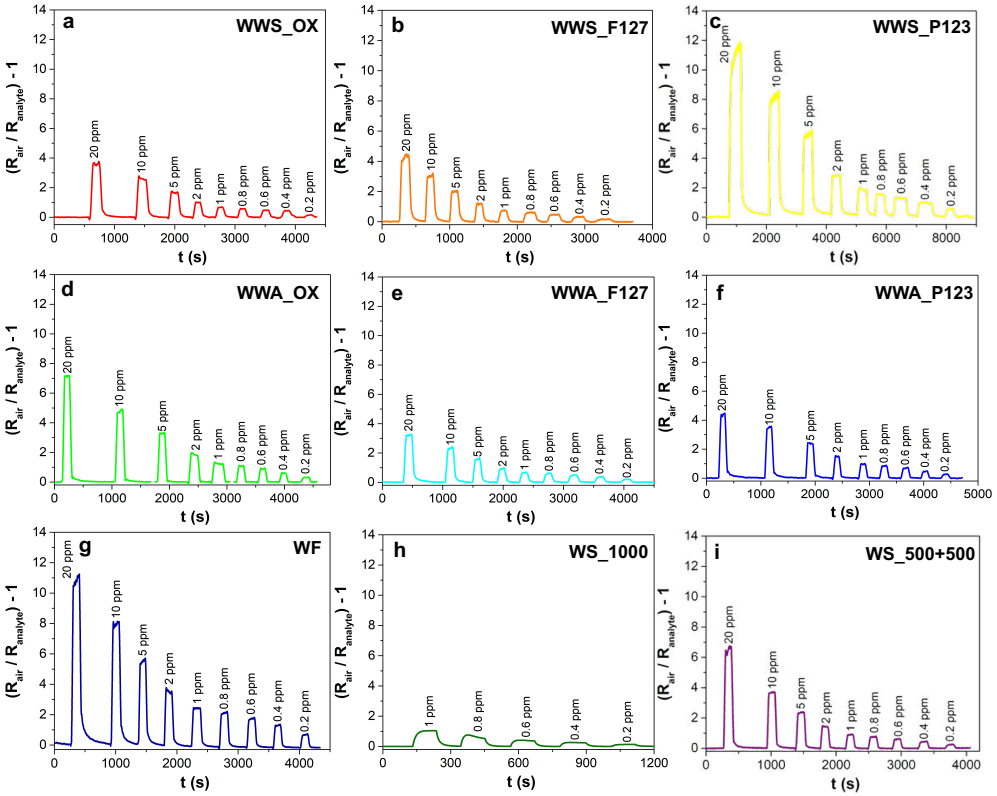

Figure 5.4. *Acetone sensing by tailored synthesized pure WO_3 samples. All the measurements were carried out in simulated air (20% O_2 – 80% N_2), at 300 °C, without UV light.*

Besides, response and recovery times (Table 5.2) are around 20-50 s and 10-70 s respectively (in the case of WWS_P123, a longer recovery time of about 100 s was computed), according to the materials used, and they can be considered optimal and comparable to those reported in the literature[1–3]. Going into details, it can be inferred that the response/recovery times are mainly influenced by the pores size distribution, since the sensing mechanism is based both on gas adsorption on the materials surface and on the desorption of the reaction products and by-products. Indeed, WWA_OX and WF have a similar percentage of pores lower than 20 nm and between 20-60 nm (Fig. 5.2b). Thus, this range may be considered the optimal one in the specific WO_3/acetone case. Conversely, WWS_P123 showed a quite high recovery time due to the great percentage (almost 90%) of pores with diameters smaller than 20 nm. The presence

of these micro-pores may have hindered the products desorption, therefore resulting in an increase of the recovery time.

By comparing the present results with the available data[2,18,19], it is possible to conclude that these powders have well approached the performances of tungsten trioxide-based chemoresistors already discussed. Figure 5.5 displays an exemplifying comparison with two research works, in which WO_3 materials were used for acetone sensing at high operating temperatures.

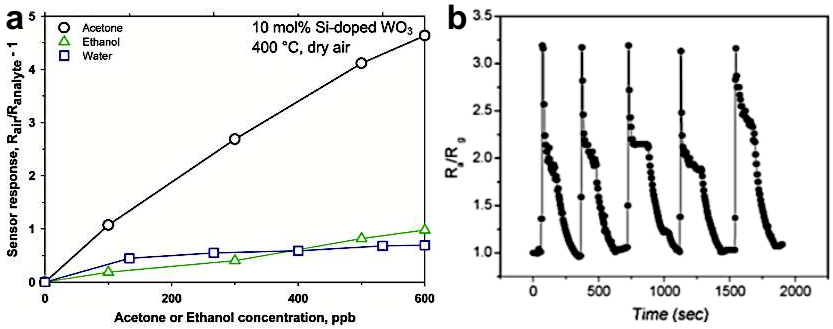

Figure 5.5. *(a) Sensor response to acetone, water and ethanol vapors. (b) chematic energy-level diagram of an n-type semiconductor. Reproduced with permission[2], Copyright 2010, American Chemical Society. (b) Repetitive response of screen printed WO_3 films upon exposure to 50 ppm acetone vapor at 300 °C. Reproduced with permission[18], Copyright 2007, Elsevier (open access).*

Moreover, even if the focus of the present Chapter is not the achievement of the low temperature-sensing, an attempt to reduce the operating conditions, by exploiting the UV light, has been performed. WWS_P123 was used as representative sample, being one of the most performing sensors at 300 °C. Hence, Figure 5.6 shows its sensing towards acetone with the decreasing of the operating temperature (*i.e.* 150 °C and RT). In both cases, 2 ppm was the lowest detectable concentration. However, at 150 °C, the signal has a very low signal-to-noise ratio; whereas at RT a "reversed" signal was observed. As already justified in Chapter 4, this may be due to the conductivity-type change from n-type to p-type, with the decreasing of the working temperature (for a detailed discussion see Chapter 6). In the case of WO_3, there are several works reporting this unusual behavior[20–23]. For instance, it is stated that WO_3 nanorods showed a p-type response behavior (*i.e.* resistance increase) to reducing gases including ethanol, methanol and propanol at room temperature, in the presence of a high concentration of oxygen species[20]. Besides, Gurlo *et al.*[21] pointed out that the anomalous change of metal oxide semiconductors conductance mainly occurs when exposed to different gaseous atmospheres, especially under different oxygen concentrations.

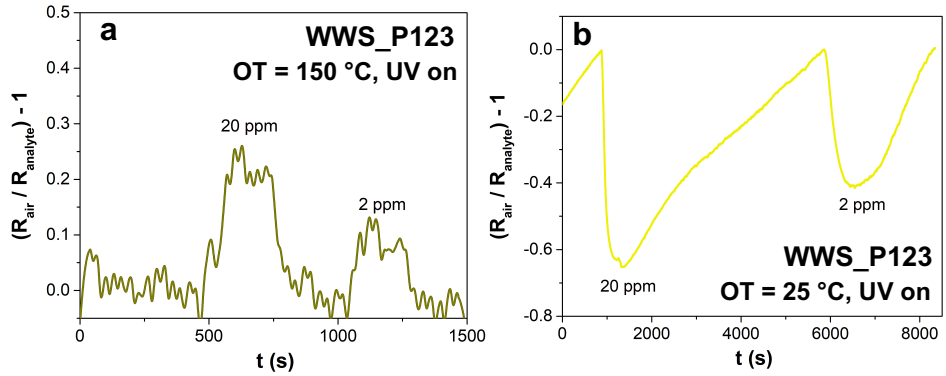

Figure 5.6. *Acetone sensing by WWS_P123 powder, with the decreasing of the working temperature (by exploiting the UV light). The measurements were carried out in simulated air (20% O_2 – 80% N_2).*

Finally, WO_3-based sensors selectivity has been preliminarily studied always with WWS_P123, at 300 °C, without UV irradiations. Figures 5.7 and A.31 display the results achieved towards a bigger and non-polar molecule, such as toluene.

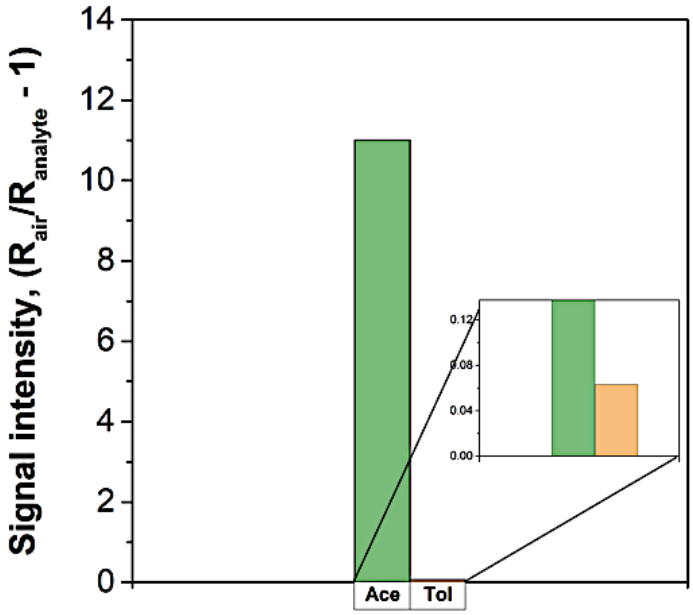

Figure 5.7. *Comparison between signal intensities obtained towards 20 ppm of acetone and toluene, by WWS_P123 material. Inset: magnification to evidence the response obtained towards toluene species. The measurements were carried out in simulated air (20% O_2 – 80% N_2), at 300 °C, without UV light.*

The sensor response is quite good, with a high signal-to-noise ratio, reaching 5 ppm as the lowest detectable concentration. However, at the same experimental conditions (Fig. 5.8), the

intensity is very small if compared to the one obtained towards acetone analyte. Hence, it is possible to infer the as-prepared WWS_P123 material is much more selective to smaller and polar molecules, as acetone.

5.2. Synchrotron results and computational investigation

5.2.1. Introduction

In this Chapter, besides preliminary studies on acetone sensing by WO_3 material, the aim was to fully understand, at a structural level, the sensing mechanism by n-type MOS. To pursue this target, either *in situ* synchrotron tests or computational investigations were carried out. Particularly, the intent was the theoretical corroboration of ESRF experimental results. As described in detail in the Appendix Chapter (A.1.5 paragraph), the Modulated Excitation X-Ray Adsorption Spectroscopy (ME-XAS)[24] was performed to endow x-ray adsorption with surface sensitivity, making this powerful bulk technique able to provide information concerning the local structure and the coordination state of metallic centers located on the surface of inorganic materials. Herein, the applied external stimulus was represented by acetone adsorption on WO_3 surface.

Besides, by means of computational simulations, a reasonable model of WO_3 surface will be reported in order to reproduce the most probable adsorption configurations involved in the actual sensing process. Hence, starting from these configurations, the ESRF ME-XANES experimental output will be theoretically reproduced as close as the level of approximation allows. Finally, theoretical and experimental results will be compared. If the model will be accurately conceived, the features of the theoretical analogue and the demodulated spectra will approximately match, validating the computational predictions.

5.2.2. *In situ* synchrotron tests

As reported in detailed in the Appendix Chapter (A.1.5 paragraph), acetone sensing tests were conducted at 300 °C, without UV light, both in the absence and presence of oxygen species. Oxygen is, indeed, adopted as a carrier gas together with helium. The resulting responses are reported in Figure 5.8.

Notably, the presence of oxygen drastically increases the signal intensity of about four times, evidencing its possible role in the sensing mechanism. Hence, the elaboration of the corresponding XANES spectra may elucidate this aspect, that is currently under debate. Figure 5.9 displays a superimposition of XANES spectra, acquired during the tests, and the phase sensitive-demodulated ones, in which the maximum amplitudes (at 330° and the exact opposite at 150°) have been highlighted. Notably, all the following observations are referred to the 330°-demodulated spectra and they should be inverted for the 150° demodulated ones.

For the sake of clarity, a "blank" experiment in the absence of both oxygen and acetone species was carried out (Figure 5.9a). As expected, no current variation was recorded.

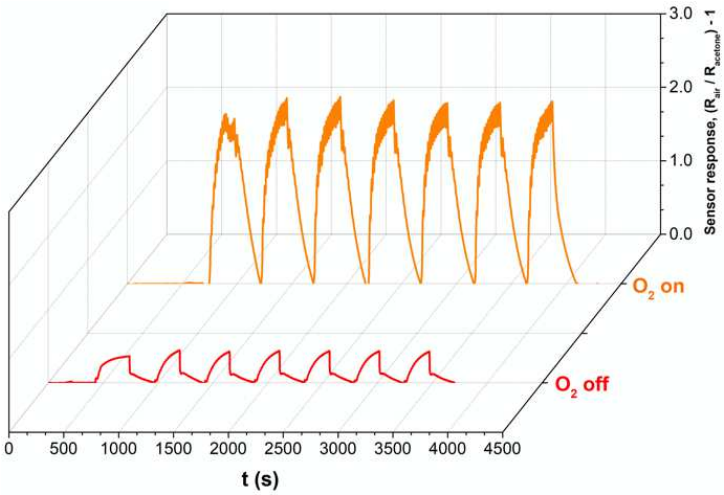

Figure 5.8. *Effect of oxygen species in the sensing behavior of WWS_OX towards 2000 ppm of acetone. Tests were carried out at 300 °C, without UV light. To simulate air, helium was used as inert gas instead of nitrogen species, due to the facilities available at ESRF-ID26.*

Considering firstly the case without oxygen when acetone was purged (red spectrum in Fig. 5.8 and Fig. 5.9b), the sharp positive and negative profiles of the demodulated spectra seem to be balanced. Two negative peaks are observed at the right and left portions (at ca 10.208 and 10.216 keV), whereas two more intense positive peaks appear in the middle (at 10.210 and 10.213 keV, respectively). Conversely, by adding oxygen species during the acetone sensing, the relative demodulated spectra have a shape significantly different from the previous ones. Specifically, a negative peak appears in the middle of the edge (at ca 10.212 keV), while two intense peaks rise in correspondence with the two XANES broad bands (at ca 10.210 and 10.214 keV; Fig. 5.9c). Afterwards, the signal decreases resulting in a downward bend at about 10.208 and 10.216 keV. Although formally being difference spectra, in the present case, the demodulation does not integrate to zero: the positive portion outweighs the negative one, as if an upward vertical translation is applied. This fact may be due to a significant x-ray absorption and/or scattering by atmospheric species (as oxygen for instance), thus preventing the detector to collect all the reflected radiation. Indeed, in an ideal 330°-demodulated spectrum, the positive portion should exactly balance the negative one. Finally, considering the blank experiment (Fig. 5.9a), a very scattered profile can be noticed, without showing a significant shape as in the other two cases.

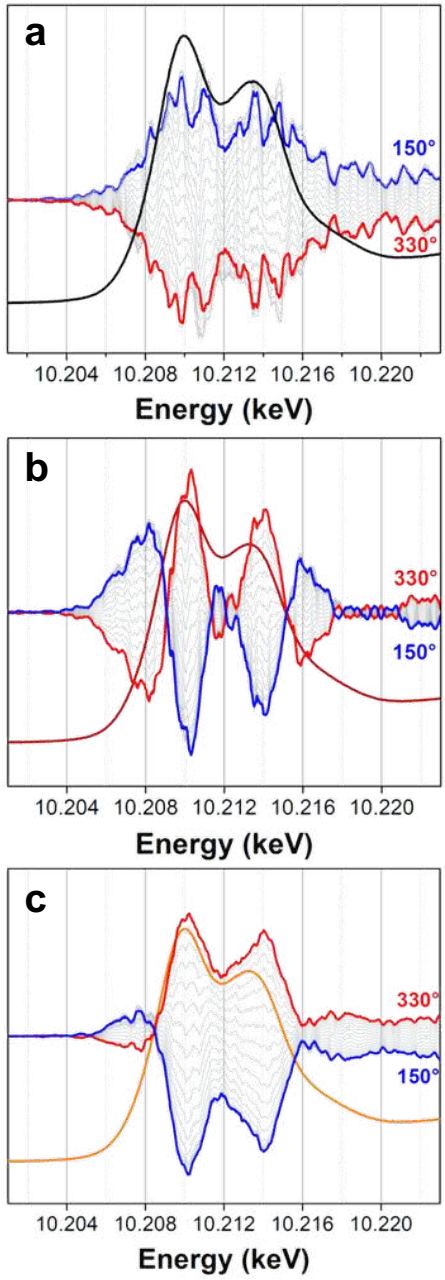

Figure 5.9. *PS-demodulated spectra of (a) blank experiment (without O_2 and acetone), and acetone sensing tests by WWS_OX both (b) in the absence and (c) presence of oxygen molecules. The averaged XANES spectra have been superimposed, while 330° (red) and 150° (blue) angle values have been highlighted, as they show the maximum amplitude. The other demodulations are reported in grey color, at 10° phase shift. All the measurements were performed at 300 °C, without UV light.*

Hence, we can infer the features just described are reasonably produced by alterations in the electronic structure of those superficial tungsten atoms whose coordination sphere is modified during the sensing mechanism. Indeed, changes either in bond lengths or in the nature/number of the adsorbed species do produce rearrangements in the empty t_{2g} and e_g states energy distributions. These changes will be explained in detail by the performed computational simulations. Therefore, after reproducing (within the limits of the involved approximations) an *ab initio* version of the aforementioned experimental results, a comparison will be carried out in order to better clarify the VOCs sensing mechanism.

5.2.3. Theoretical results

5.2.3.1. *From bulk to surface perspective*

As explained in 5.1.2 paragraph, the operating temperature of the WO_3-based sensor is 300 °C (573 K). Hence, the monoclinic γ-WO_3 polymorph, described by the CIF file provided by Vogt *et al.*[25], was selected as the starting point. Its unit cell, displayed in Figure 5.10, can be seen as a distortion from the ideal cubic ReO_3 structure and it consists in eight WO_6 octahedral units, connected one to each other by the vertexes and tilted in various directions.

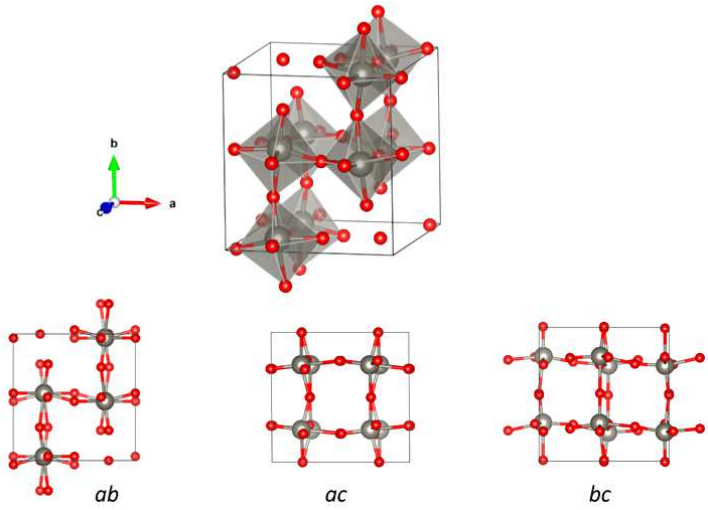

Figure 5.10. *Overview of the γ-WO_3 structure adopted for the theoretical calculations, with projections over the three fundamental planes.*

Subsequently, this structure was optimized in order to both define the final computational parameters and to obtain useful bulk properties, thus leading to bond lengths and angles slightly different from the starting experimental ones. Notably, some of the already reported

computational studies on tungsten oxide[26,27] are carried out on a particular monoclinic structure, which does not seem to strictly reproduce the experimental one. Since our aim is to use theoretical calculations as a tool to explain experimental observations, fully matching the real one.

Hence, the first step contemplated the modelling of the WO_3 surface, whose atomic and electronic structure differ largely from the bulk phase. Specifically, the bulk phase represents the fundamental building block for the achievement of a reasonable surface model. Besides, the relative electronic properties, such as the band structure and the density of states (DOS) constitute a commonly used benchmark, that have to be comparable with the ones already reported in the literature[26,27].

a (Å)	*b* (Å)	*c* (Å)	*β* (°)	V (Å^3)
7.4565	7.6837	7.9033	90.46	452.8

Table 5.3. *Structural parameters of the computed γ-WO_3 bulk structure, obtained by using the computational set-up defined in A.1.6 paragraph and by relaxing the experimental unit cell.*

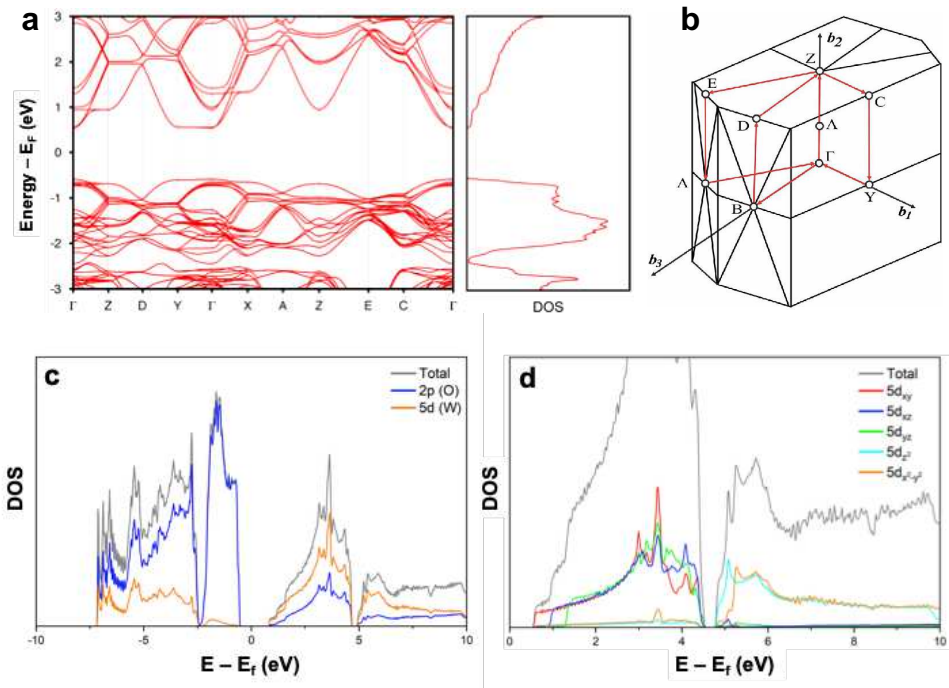

Figure 5.11. *(a) Calculated band structure and total DOS of γ-WO_3 bulk structure. (b) Representation of monoclinic lattice Brillouin zone, in which the path used for band structure calculation has been evidenced in red*[28]*. (c) PDOS over O 2p (blue line) and W 5d (orange line) orbitals. (d) PDOS over W 5d orbitals (namely xy, xz, yz, z^2 and x^2-y^2) in the region above the Fermi level.*

In this way, we can be sure about the goodness of the obtained results. Therefore, starting from the bulk shown in Figure 5.10, whose structural parameters are listed in Table 5.3, its electronic and band structure were then computed (Figure 5.11).

Before proceeding with further calculations, the results were compared to the literature data, obtaining good agreement except for the band gap which, as stated in A.1.6 paragraph, gets systematically underestimated by pure functionals. Together with the band structure, the total (Figs. 5.11a,b) and projected DOS (PDOS, Fig. 5.11c) calculations were performed. As seen in Figure 5.11c, the occupied states near the band gap are almost totally localized on oxygen 2p orbitals, whereas the unoccupied ones mainly belong to the tungsten 5d orbitals, with some hybridization by oxygen 2p. The empty states (Fig. 5.11d) consist in two broad bands separated by a tiny gap (of around 4 eV): the least energetic one shows a strong t_{2g} (d_{xz}, d_{xy} and d_{yz}) character, conversely the one at higher energies has a strong e_g (d_{x2-y2} and d_{z2}) character.

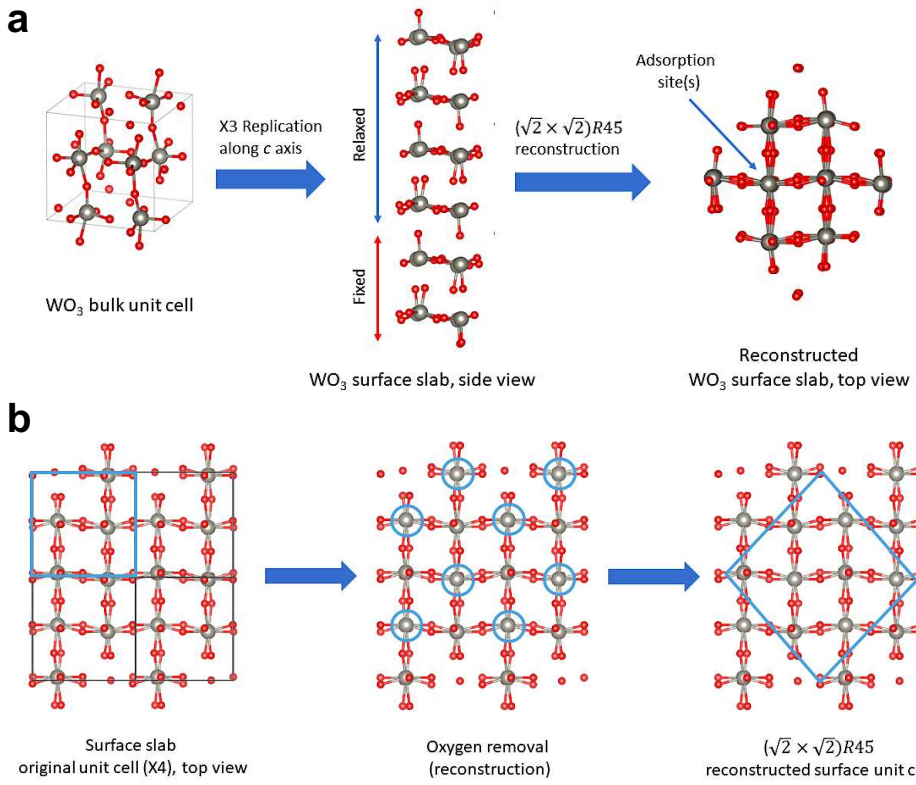

Figure 5.12. *(a) Schematic representation of the whole surface slab building process. (b) Schematics of the surface reconstruction process.*

Once obtained the equilibrium bulk structure, we started building the most stable surface for γ-WO_3 which, according to literature[26,29], is the $(\sqrt{2}\times\sqrt{2})R45°$ reconstructed (001) one. As

clearly visible in Figure 5.10, the unit cell is composed by alternating layers of O atoms and WO_2 networks. To isolate the surface, we first exposed an only-oxygen layer and replicated the unit cell three times along the *c* axis, while increasing the cell parameter in the same direction, obtaining a slab of six WO_6 octahedra layers. Then, we proceeded with the relaxation of the first four layers, keeping fixed the last two except for the terminating O atoms. Finally, the surface reconstruction was obtained by removing half of the exposed oxygen atoms as shown in Figure 5.12. Since these atoms are connected to the below W atoms, by alternating long and short W-O bonds, we decided to remove the long-bonded O atoms, supposing it would speed up the optimization process. As the surface morphology changes, the same does the unit cell, which now contains twice as much atoms as the starting surface slab. Moreover, since the *ab* plane is large enough to prevent interactions of the adsorbed molecules between adjacent cells, we did not need to produce any supercell. As displayed in Figure 5.12a, the top layer contains four adsorption sites centered on W atoms, which are not bound to the terminating O atoms. Besides, as concern the bottom of the slab, three different approaches were considered: *i*) the complete saturation of the final oxygen atoms with hydrogen ones positioned parallel to the long axis; *ii*) the hydrogen atoms were placed at the typical 109° angle. Since both these two situations gave rise to undesired mid-gap states, *iii*) the adoption of a symmetrical slab where, at the bottom, oxygen atoms on the opposite positions with respect to the top layer were removed.

In this way, we succeeded in reconstructing the WO_3 surface, that represents the starting point for the further steps. The task was then to corroborate the observed tungsten trioxide intrinsic n-type semiconductor behavior. As widely stated in the literature[30,31], this feature is commonly attributed to the presence of abundant material defects, such as the oxygen vacancies.

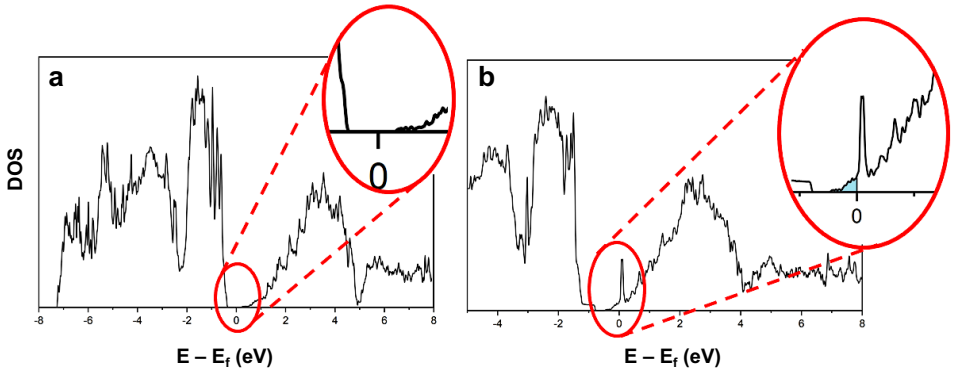

Figure 5.13. *Density of states relative to (a) the clean surface and (b) the defective surface. Inside the red circle is highlighted, in blue, the portion of the conduction band populated by the O vacancy.*

Indeed, since the clean surface is an insulant (as seen in Fig. 5.13a), we expected that including this type of defects would cause the Fermi level to shift towards the conduction band, populating it and producing the observed intrinsic n-doping. Our system can be seen as a network of W-O-W chains oriented in the same directions as the cell axes. According to Le *et al.*[27], for low defect concentrations (0.5%, $WO_{2.984}$) the most stable vacancies in the bulk phase are obtained by removing an O atom on the W-O-W chain parallel to the *c* axis. Since we decided to include a single defect in the surface slab, producing a 0.6% defect concentration ($WO_{2.983}$), we proceeded accordingly. In order to prevent any future interaction between the oxygen vacancy and the adsorbed atoms, we positioned it on the fourth layer. The Basis Set Superpositioned Error (BSSE) was corrected by placing a ghost atom in the same position, then an optimization of the first and second neighbors was performed. As expected, a sharp peak appears and the conduction band of the defective surface gets populated (Figure 5.13b), thus resulting in the desired n-doping.

Finally, a spin- polarized calculation was performed in order to verify whether the vacancy was charged, exhibiting magnetic properties.

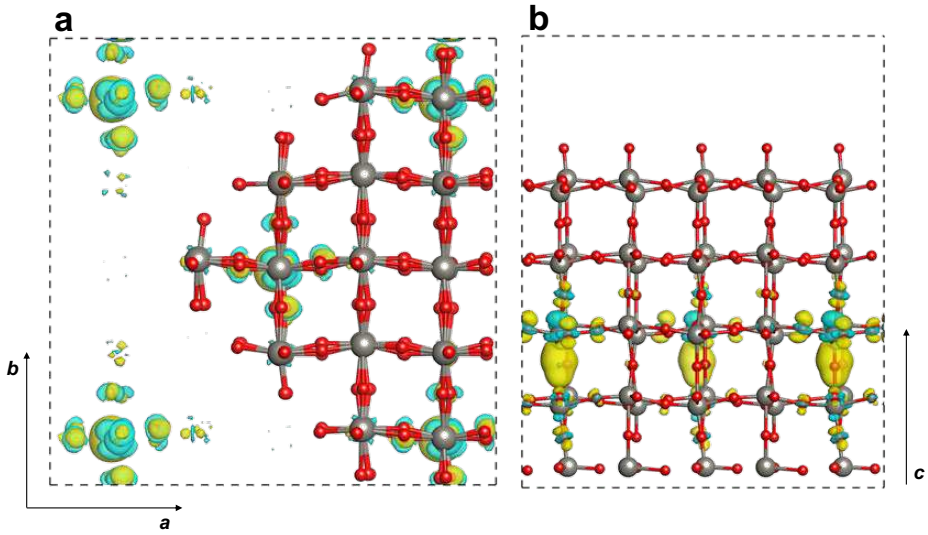

Figure 5.14. *Charge displacement maps relative to oxygen vacancies formation in WO_3 surface slab. (a) Top view, (b) side view. Yellow regions indicate charge accumulation, blue ones indicate charge depletion. The charges have been plotted on a 0.03 $Å^{-3}$ electron density isosurface.*

Since no energy difference was observed between the polarized and non-polarized solution, the vacancy is not magnetic. As seen in the charge displacement maps displayed in Figure 5.14, the electron density redistribution following vacancy formation is mostly localized on the defect site, with slight propagation along the *c* axis and negligible in-plane propagation.

Despite the yellow area around the vacancy indicates charge accumulation, no significant amount of charge is trapped inside, thus the defect is considered to be in a neutral state.

5.2.3.2. *Adsorption of the molecules in play*

Once obtained the oxygen-deficient surface slab, it is finally possible to adsorb on it the species that are supposed to take part in the sensing process. We recall that the commonly reported mechanism[8,32] for transition metal oxide sensors consists in two main steps: *i*) the formation of oxygen species (*e.g.* O^-, O^{2-} and O_2^-), which drains electrons from the conducting surface; *ii*) these reactive species interact with the surrounding acetone molecules, exchanging electrons with the surface, resulting in the final sensor response. After reacting, adsorbed products, such as CO_2 and H_2O are desorbed from the surface[33]. When acetone is removed from the atmosphere, the original electronic properties are progressively restored. Our aim is to give an elucidation on this mechanism, through the modelling and simulation of the experimental observations. Specifically, as soon as the surface is exposed to O_2 we observe an abrupt decrease of the measured current. When acetone is flowing in the sensing chamber, instead, the current increases proportionally to the gas concentration. Hence, in the light of both our observations and the already reported mechanism, we decided to simulate four different situations:

- adsorption of acetone molecules;
- adsorption of O_2 molecules;
- adsorption of atomic oxygen (which may recall the oxygen species that form upon UV irradiations, at RT conditions);
- simultaneous adsorption of acetone and atomic oxygen molecules.

The molecules were adsorbed on the top layer of the final slab, which contains four adsorption sites (as seen in the previous paragraph). After obtaining the equilibrium configurations we compared DOS, adsorption energies and charge transfer in order to have the necessary parameters to interpret our experimental data and support our considerations about the mechanism.

Regarding acetone molecule, we optimized three different starting configurations called *tilted*, *vertical* and *bridge*. The first two were adsorbed on both clean and defective surface, leading to slightly different properties and almost identical geometries. In order to calculate the binding energy, we applied the following equation:

(5.2.3.2.a) $$E_{binding} = E_{complex} - (E_{surface} + E_{molecule})$$

where $E_{complex}$, $E_{surface}$ and $E_{molecule}$ are the energies associated, respectively, to the surface with the adsorbed molecule on it, the surface alone and the molecule alone. The charge transfer was obtained as the difference between the valence charge of the isolated molecule and the sum of its atomic Mulliken charges, when adsorbed.

Concerning the molecules adsorption, *i.e.* acetone and oxygen species, Figure 5.15 shows the possible acetone configurations. In particular, in the tilted configuration (Fig. 5.15a), acetone points its oxygen atom towards a surface oxygen-free W atom. Notably, the associated distance is 2.32 Å, evidencing that the interaction is non-covalent. The plane, identified by the C and O atoms, is approximately bent by a 23°-angle with respect to the *c* axis. Furthermore, four out of six H atoms point towards three O atoms surrounding the adsorption site.

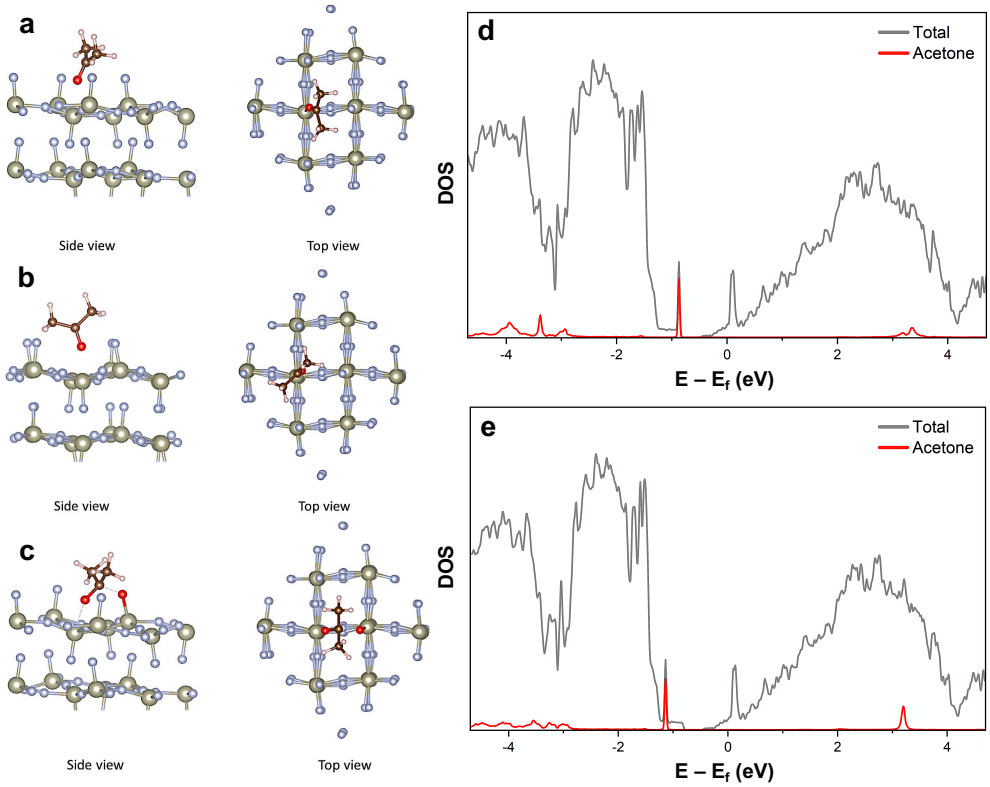

Figure 5.15. *Side and top views of (a) tilted, (b) vertical and (c) bridge adsorption configuration for acetone molecules. Total DOS of the surface-molecule complex relative to (d) tilted and (e) vertical configurations (grey lines). In red, PDOS over acetone atoms.*

The calculated binding energies are 0.78 eV on the clean surface and 0.82 eV on the oxygen-deficient surface, highlighting a slight reactivity increase caused by the presence of the vacancy. Mulliken population analysis reveals a net 0.128 electrons transfer from the molecule

to the surface in the former case, whereas 0.133 in the latter. Among the H atoms, the ones pointing towards O surface atoms are less charged by approximately 0.030 electrons with respect to the ones pointing outwards, thus suggesting a slight polarization induced by the electronegative O atoms. The density of states of the complex, shown in Figure 5.15d, is almost identical in its structure to the DOS of the isolated surface (Figure 5.13b), except for the presence of an acetone peak near the top of the valence band (red line in Fig. 5.15d). On the contrary, in vertical configuration (Figure 5.15b), acetone carbon-oxygen plane lays almost parallel to the *c* axis. Nevertheless, the C=O group forms a 34° angle with the tungsten atom below. The distance between the latter and the acetone oxygen is 2.27 Å suggesting, once again, a non-covalent interaction. The methyl groups are rotated by approximately 45° with respect to the W-O mesh below, exposing four H atoms towards all O atoms surrounding the adsorption site. Similarly to the previous case, these hydrogen atoms are less charged than the remaining ones. Overall, the molecule transfers 0.149 electrons to the clean surface and 0.154 to the defective one, slightly more than the tilted configuration probably due to the shorter W-O distance. The binding energies are higher as well, being 0.89 and 0.93 eV for the clean and defective surface, respectively. Moreover, the relative density of states does not differ too much from the previous case, except for the acetone peak, which appears at slightly lower energies (Fig. 5.15e). We finally tried an adsorption configuration in which central C atom is forced in a sp^3 hybridization acting as a bridge between the surface and the acetone oxygen atoms, the latter directly connected to the surface (Figure 5.15c). After running some optimization cycles on the clean surface, central C atom returned in the typical sp^2 planar hybridization observed in acetone molecule, moving away from the O surface atom. Since the whole molecule clearly pointed towards the already tested tilted geometry; this last configuration was not taken into account.

Furthermore, as concern the oxygen species adsorption, both atomic and molecular oxygen were adsorbed on WO_3 surface. We decided to use different adsorption sites with respect to the one used for acetone. Since both these species carry two unpaired electrons, being in a triplet state, spin-polarized calculations were required. Two oxygen atoms were adsorbed on adjacent adsorption sites as shown in Figure 5.16a. Indeed, the initial hypothesis was that an O_2 molecule could adsorb and then dissociate directly on the surface leaving two O atoms, one next to each other (namely, O_1^{ads} and O_2^{ads}). As expected, atomic oxygen adsorbs stronger and closer to the surface with respect to acetone molecule due to the lower steric hindrance, acting as an electron acceptor because of its high electronegativity. In the equilibrium configuration, the W-O distance is 2.09 Å for both adsorbed atoms, ca 0.4 Å longer than the average bond length of surface O atoms. The average binding energy is 1.34 eV per oxygen atom; hence we can consider these species to be chemisorbed.

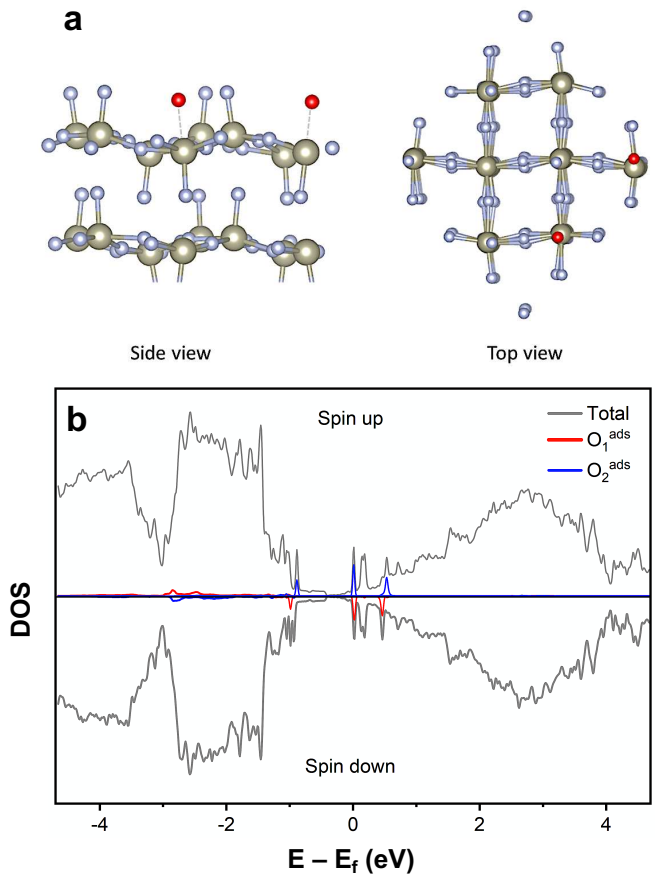

Figure 5.16. *(a) Side and top views of the atomic oxygen adsorption configurations. (b) DOS of WO_3 surface with two adsorbed oxygen atoms, calculated in a 10 eV range. Since the calculation is spin-polarized, spin up and spin down populations have been mirrored. The PDOS over O_1^{ads} is shown in red, the one over O_2^{ads} in blue.*

The associated charge transfer, now directed from the surface to the atoms, is 0.232 for one oxygen and 0.244 for the other one (Figure 5.17). Indeed, the charge redistribution induced by adsorption of these species is evidenced in Figure 5.17, in which there is a significant electron accumulation along the just formed W-O bond (propagating to reticular O atoms along the *c* axis), accompanied by a charge depletion localized on the W atom below. Moreover, concerning the density of states, shown in Figure 5.16b, spin up and spin down states are practically superimposed. Since the system is antiferromagnetic, O_1^{ads} spin up population is almost identical to O_2^{ads} spin down one. Specifically, for each adsorbed oxygen, we can observe three sharp peaks with the same spin and a broad band with opposite spin, all attributed to 2p orbitals. Interestingly, population analysis highlights that the most populated spin state for O_1^{ads} and O_2^{ads} is the one associated to the broad band. The latter contains states having the

highest degree of hybridization with surface band structure, in particular with the O 2p band. Among the sharp peaks, the one attributed to $2p_x$ orbital is situated just next the Fermi level, basically in the same position for O_2^{ads} (spin down states) and O_1^{ads} (spin up states). Since it does not seem to present any type of hybridization, it may act as a trap state preventing electrons from conducting, when populated, thus contributing to the conductivity decrease experimentally observed when WO_3 is exposed to oxygen.

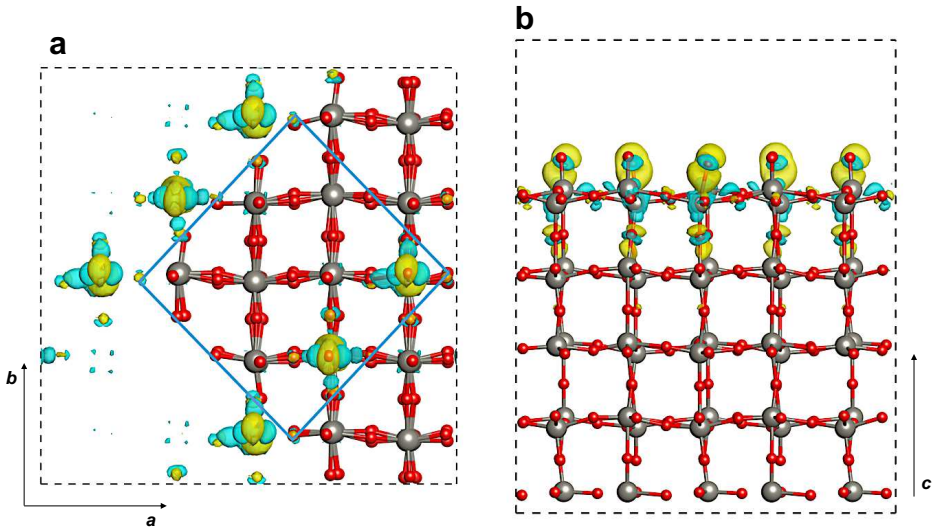

Figure 5.17. *Charge displacement maps relative to the adsorption of two O atoms. (a) Top view (on the left side, all atoms have been hidden to highlight the charge displacement), (b) side view. Yellow regions indicate charge accumulation, blue ones indicate charge depletion. The charges have been plotted on a 0.03 Å^{-3} electron density isosurface.*

Finally, as regard the molecular oxygen (O_2), after several optimization cycles, no stable adsorption configuration was obtained. The molecule was constantly repulsed from the surface until it detached. We concluded that, even if this species adsorbed in the real experimental conditions, it would do it very weakly and without a significant interaction with the surface electronic structure. Moreover, no optimization step evidenced any charge transfer from the molecule to the surface but, instead, a slight transfer in the opposite direction. This shows that O_2 molecule tends to act as an electron acceptor in closed-shell interactions. This observation is in line with some previous studies, already reported in the literature[34,35]. Specifically, in the case of the n-type SnO_2 reported by Abokifa *et al.*[34], *ab initio* molecular dynamics simulations show that, at room temperature, the less active superoxide molecules O_2^- constitute the majority of the pre-adsorbed oxygen species, which are formed by the direct adsorption of oxygen molecules from the ambient atmosphere on the defective surfaces,

whereby they ionize by pulling the localized charge at the vacancy site. It is appropriate to specify that the level of the theory used in our modeling does not take into account slight dispersive contributes that could possibly lead to a weak physisorption of O_2 species.

The last case we treated in depth was the simultaneous adsorption of an acetone molecule and an oxygen atom, in order to investigate the possibility of a reaction taking place directly on the surface. We found only one configuration (see paragraph 5.2.3.3) in which the species can get close enough to potentially allow an effective interaction. As seen, only two of the four adsorption sites are suited for this case, with the acetone molecule adsorbed in the tilted configuration. Initially, the adsorbates were forcefully placed one close to each other, in order to allow an interaction. After performing many optimization steps, however, they returned to their original positions, suggesting that, once adsorbed, any direct charge transfer between the species in play may not happen.

5.2.3.3. *The ME-XANES computational model*

A XANES spectrum collects all the intensities associated to the electronic transitions from a specific core level of a metallic species to unoccupied states above the Fermi level. The starting core level is defined by selecting a proper range of x-ray energies around a specific adsorption edge of the metal. The transition intensity between two states with energies E_i and E_f by means of a photon with energy $h\nu$ is described by the Fermi's golden rule (Eq. 5.2.3.3.a).

$$I(E_f - E_i) \propto |H_{fi}|^2 \rho(E_f)\, \delta(E_f - E_i - h\nu) \qquad \text{(5.2.3.3.a)}$$

where

$$|H_{fi}|^2 = |\langle f|\hat{\boldsymbol{\varepsilon}}\mathbf{r}|i\rangle|^2 \qquad \text{(5.2.3.3.b)}$$

is the matrix element of the perturbation between the final state f and the initial state i, in the electric dipole approximation. $\rho(E_f)$ is the density of states at E_f and $\delta(E_f - E_i - h\nu)$ is a Kronecker delta, which extracts only the photon with proper energy $h\nu = E_f - E_i$. The matrix elements weigh the intensity, based on the relative shape and symmetry of the involved wavefunctions. Calculating them would have been computationally taxing with respect to the resources available at the time these calculations were performed. Hence, the zero-order approximation was considered, in which all the matrix elements are assumed to be constant, *i.e.* all empty states are equally accessible. However, the associated selection rules ($\Delta l = \pm 1$, where l is the orbital angular momentum) were taken into account by only considering the DOS projected

on tungsten 5d orbitals (l = 2). Indeed, at the L_3−edge used in our experiments, the initial state is the $2p_{3/2}$ orbital (l = 1). Within this approximation, Equation 5.2.3.3.a becomes:

(5.2.3.3.c) $$I(E_f - E_i) \propto \rho(E_f)$$

in which only the photons with proper energies (*i.e.* $\delta(E_f - E_i - h\nu)$) are considered. Subsequently, the shape of the XANES spectra is assumed to be an image of tungsten 5d density of states multiplied by a constant. Notably, an actual XANES spectrum and the corresponding density of states only share their general shape, as shown in Figure 5.18a. The reason is that DOS resolution can be decided arbitrarily, while XANES measurements are affected by experimental broadening. Since our aim is to replicate the experimental output at best, this broadening was artificially introduced in the density of states by convolution with a gaussian function ($g(x)$) having the following equation:

(5.2.3.3.d) $$g(x) = \frac{1}{\sigma\sqrt{2\pi}} \exp\left[-\frac{1}{2}\left(\frac{x}{\sigma}\right)^2\right]$$

The width parameter σ was selected in order to reach a reasonable agreement between the convoluted DOS of WO_3 bulk phase and a reference XANES spectrum. We finally opted for σ equal to 0.4 eV. The result illustrated in Figure 5.18b is satisfying, considered the high degree of approximation involved. Specifically, for clarity, the elements of approximation in this model are:

- the consideration of all the matrix elements as constant parameters, ignoring the different values deriving from loss of 5d orbital degeneration due to the crystalline field. This affects the relative heights of t_{2g} and e_g broad peaks;
- the ignoring of the eventual linear or circular polarization of x-rays in the synchrotron light, which would also introduce selection rules on the magnetic quantum numbers;
- the omittance of the eventual surface core level shifts, *i.e.* the variations of surface W L_3−edges, due to energy shifts of the starting $2p_{3/2}$ states. This effect should be cancelled for all W atoms that remain unchanged during the experiment but it cannot be eliminated for those atoms interested by acetone adsorption. However, if the latter does not determine an excessive rearrangement of tungsten core states, this effect may be negligible.

Hence, the case reported here represents the bulk contribution to XANES intensity, which is completely eliminated by the modulated excitation procedure.

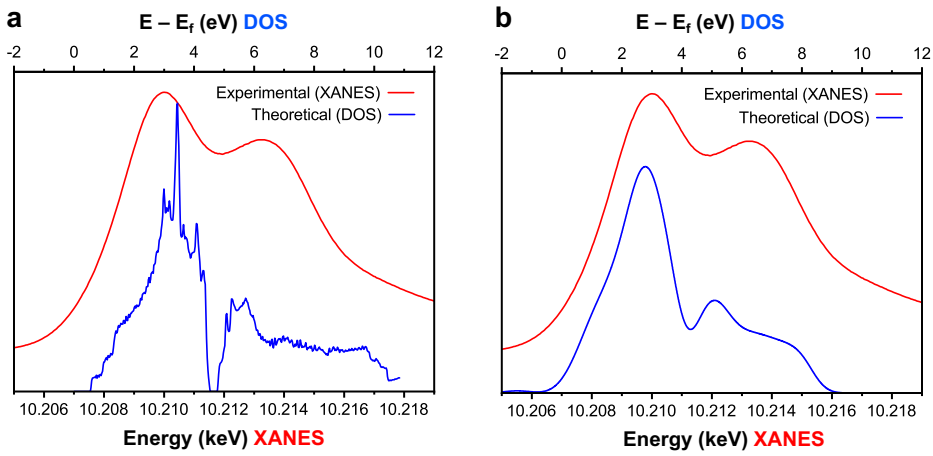

Figure 5.18. *Comparison between the experimental XANES spectrum (red line) and its theoretical counterpart (blue line), represented by the DOS projected on W 5d empty orbitals, before (a) and after (b) convolution with a gaussian function. The x axes for XANES and DOS plots span the same energy range. The former is referred to the L_3–edge, the latter to the Fermi level. On the y axes the intensities have been omitted, since they are not comparable.*

All the relevant contributions come from the surface, whose electronic properties deeply differ from those of the bulk one. Moreover, due to surface reconstruction and molecule adsorption, several "types" of tungsten atoms can be found on our slab, each one presenting unique features.

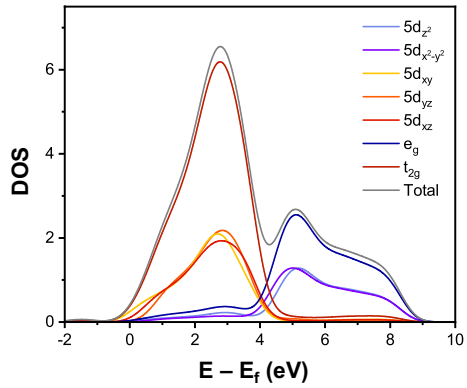

Figure 5.19. *Projection of tungsten 5d bands, convoluted with a gaussian function, in the bulk phase.*

Anyway, most of their contributions will be also cancelled. In our simulations, indeed, adsorption generally modifies just one tungsten atom on the slab, with a negligible effect on its neighbors. However, by analyzing in detail the empty states structure of specific surface W atoms can be very useful in order to understand the effect of surface reactivity on the

adsorption properties. This analysis will be performed in the following, utilizing the convolution procedure above-mentioned.

Hence, concerning the bulk phase, all the tungsten atoms are substantially equivalent. As can be seen in Figure 5.19, where the contributions of the single 5d bands has been isolated, t_{2g} states are almost degenerate, as well as the e_g ones.

Regarding, instead, the clean surface, when the bulk structure is cut along the (0 0 1) plane, a surface is formed and the reconstruction occurs.

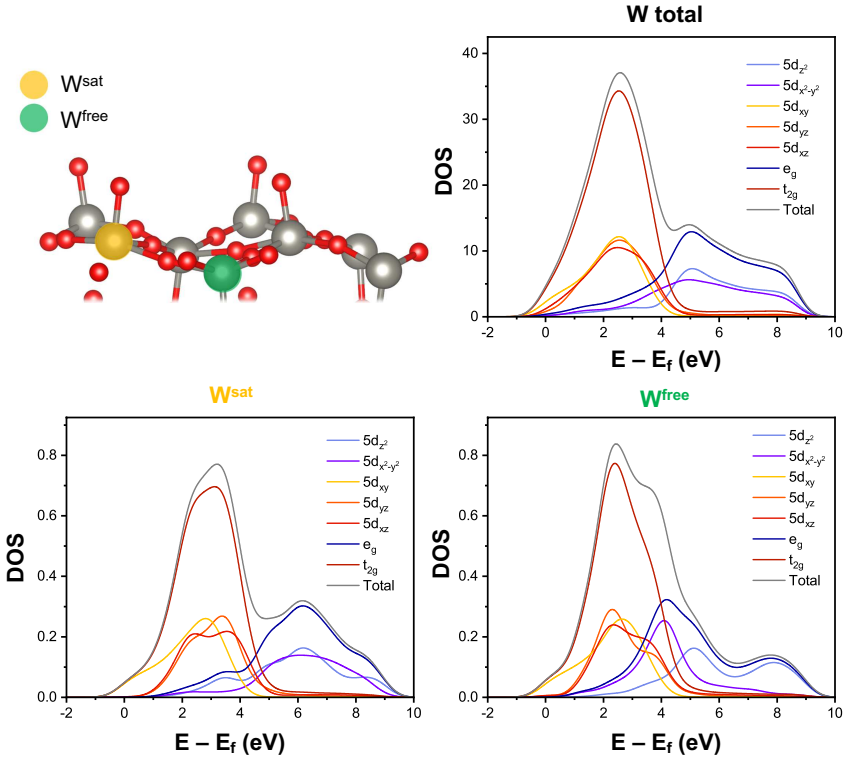

Figure 5.20. *Comparison between the gaussian-convoluted DOS for the clean surface. The top left image highlights the different W atom types.*

This process generates two different types of surface tungsten atoms: *i*) W^{sat}, whose coordination sphere is saturated by an apical O atom and *ii*) W^{free}, available for adsorption, in which the apical O is missing. Figure 5.20 shows a comparison between the total density of states projected on all W atoms of the surface slab, and the ones projected on the W^{sat} and W^{free} atoms. As expected, the total tungsten empty DOS recalls the one of the bulk phases, although with a less prominent e_g band. If a surface slab of infinite thickness was used, the two DOS would be practically identical. Therefore, the contributions of single W^{sat} and W^{free} atoms are

significantly different. In both cases, d_{xz} and d_{yz} states are found at higher energies with respect to d_{xy} states because they possess a *z* component pointing out of the surface. In addition, their energetic distribution is more contracted. Besides, d_{z2} states of W^{free} possess the typical profile of a dangling bond, with a pronounced peak between the t_{2g} and d_{x2-y2} states, because the apical O atom is missing. W^{sat}, whose coordination sphere is similar to the one of bulk W atoms, differs from the latter because no W-O layers are found above it.

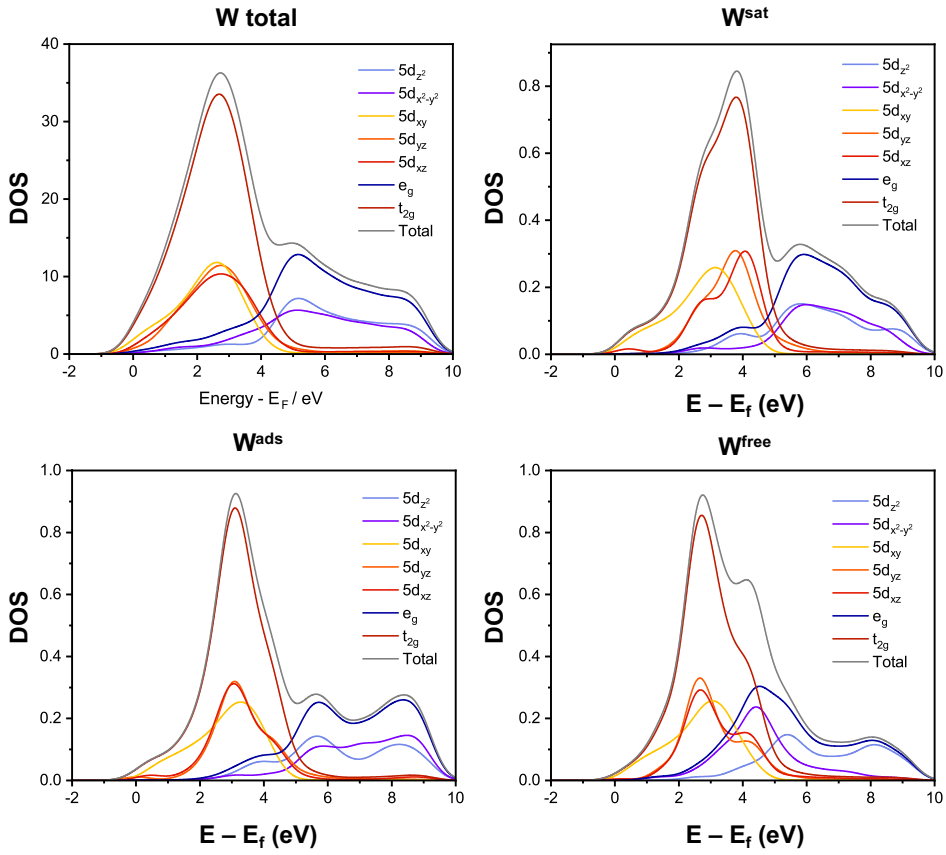

Figure 5.21. *Comparison between the gaussian-convoluted DOS for the adsorption of two oxygen atoms. The DOS have been projected on all W atoms (W total) and on single tungsten atom types (W^{sat}, W^{ads} and W^{free}).*

Conversely, when atomic oxygen is adsorbed on the WO_3 surface, another tungsten type is generated (Figure 5.21). These atoms, called W^{ads}, are found directly below the adsorbed species. Their DOS is significantly different from the one of W^{sat}, whose coordination sphere appears to be very similar to the previous case. This observation underlines the difference between the electronic properties of the structural and the adsorbed O atoms. Since the system is magnetic, densities of states were calculated for both spin populations. No significant

differences can be observed between them in all cases except for W^{ads}, whose spin-down DOS has a shoulder right after the Fermi level that is not observable for spin-up population. This feature is due to slight peaks exhibited in that region by d_{xz} and d_{yz} spin-down states, probably mixed with the near-gap sharp state of the oxygen atom above (see Figure 5.17b), which possesses a net spin-down polarization. The splitting of d_{z2} states is probably due to interactions with a high-energy state of atomic oxygen. As expected, the density of states of W^{sat} and W^{free} are almost identical to their analogues on the clean surface, highlighting the fact that adsorption effects are strictly localized on the W^{ads}.

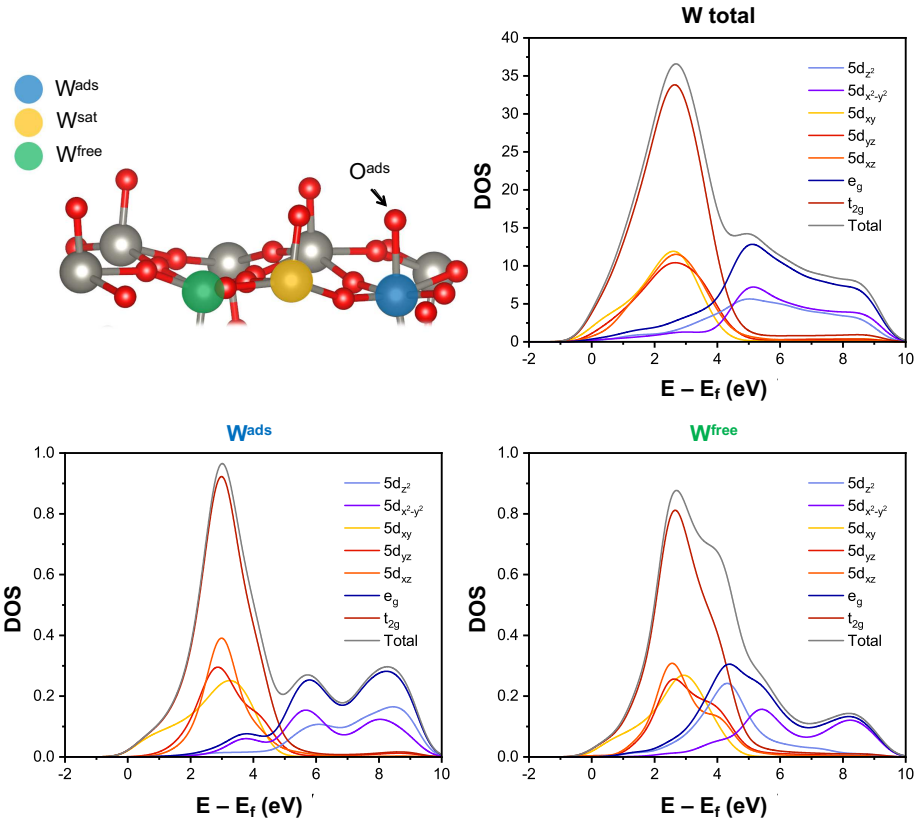

Figure 5.22. *Comparison between the gaussian-convoluted DOS for the adsorption of a single oxygen atom adsorption. The DOS have been projected on all W atoms (W total) and on single tungsten atom types (W^{ads} and W^{free}).*

Thus, the Gaussian-convoluted DOS were calculated, along with the double atom adsorption, described in 5.2.3.2. paragraph. No significant difference was noticed between the single tungsten atom types in the two cases. This additional configuration has been useful in order to obtain a complete casuistry, producing all the necessary difference spectra for a

detailed analysis. All the Gaussian-convoluted for two oxygen atoms adsorption are reported in Figure 5.21, while the single atom adsorption case is illustrated in Figure 5.22.

Once simulated the adsorption of oxygen species, acetone molecules were considered.

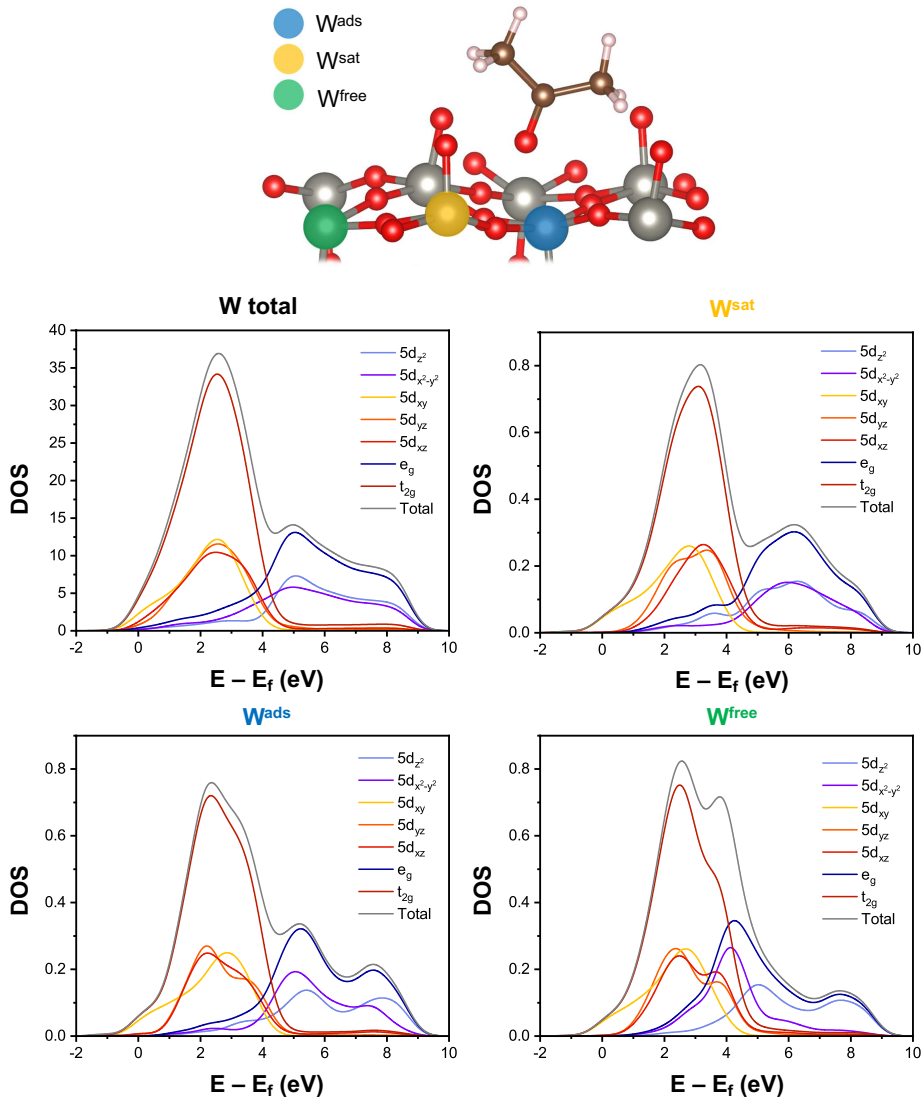

Figure 5.23. *Comparison between the gaussian-convoluted DOS for acetone adsorption. The DOS have been projected on all W atoms (W total) and single tungsten atom types (W^{sat}, W^{ads} and W^{free}).*

Hence, for the VOC adsorption in vertical configuration, W^{ads} is found below the acetone O atom. As seen in Figure 5.23, its DOS differs a lot from the analogue cases above-mentioned, due to the different effect on the electronic surface properties of acetone O atom, with respect

to the atomic oxygen. In this case, the first peak is wider, while the other two have higher intensities.

Finally, the acetone and oxygen co-adsorption was investigated, where these two species are adsorbed on adjacent sites. Specifically, Figure 5.24 displays the empty states DOS of the system, highlighting the difference between W atoms below the two different adsorbed species.

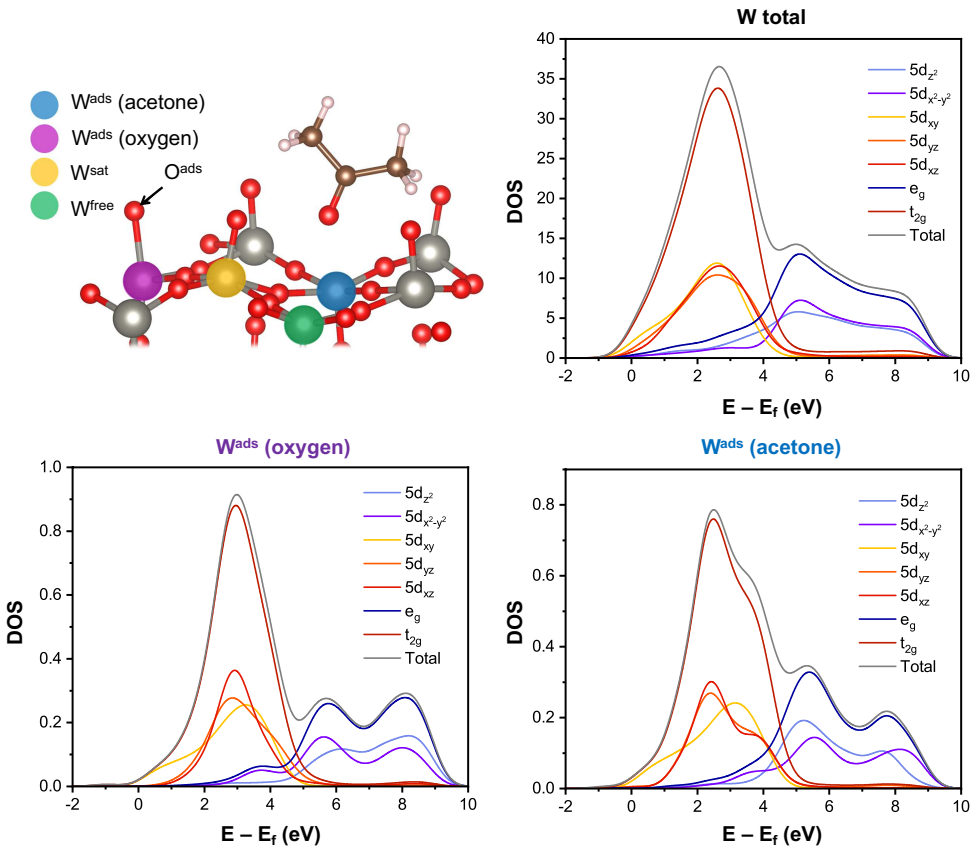

Figure 5.24. *Comparison between the gaussian-convoluted DOS for acetone and atomic oxygen co-adsorption. The DOS have been projected on all W atoms (W total) and single tungsten atom types (W^{ads} below acetone molecule and W^{free} below the adsorbed O atom).*

Now that the adsorption scenario is completed, all difference spectra can be obtained.

5.2.3.4. *Simulation of the experimental ME-XANES data*

As already explained in the Appendix A.1.5 paragraph, the modulated excitation procedure consists in a manipulation of the raw XANES spectra acquired at different times during acetone adsorption-desorption cycle. The resulting demodulated spectra (see Figure 5.9) are basically equivalent to a difference between two of the XANES spectra, recorded while two limit conditions occur:

a) WO_3 surface before acetone exposure. This case is represented either by the clean surface or by atomic oxygen adsorption;
b) WO_3 surface after acetone exposure, when the analyte surface concentration is at the equilibrium. This case is represented either by acetone adsorption or acetone-oxygen co-adsorption.

After adsorption, the associated adsorption sites will be certainly occupied by an acetone molecule. Before adsorption, instead, these sites can be either empty or occupied by a pre-adsorbed oxygen atom. By exploiting the available adsorption configurations, three different cases were reproduced in the difference spectra.

1. *Acetone adsorption on a free site, in presence of a spectator O atom*
   This case is reproduced by subtracting the 5d DOS of the single oxygen adsorption from the one of the co-adsorption. Here, a W^{free} site in the former case will be occupied by an acetone molecule, while the pre-adsorbed O is left untouched.

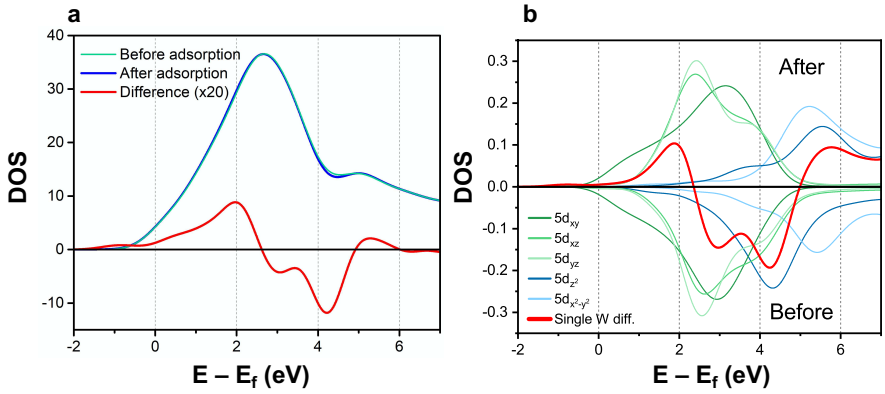

Figure 5.25. *(a) Difference between the DOS projected on all W atoms; (b) difference between the DOS projected on the specific W atoms interested by acetone adsorption (W^{mod}, red line). The contributes of the single 5d states in the co-adsorption are reported on the positive portion of the graph; the same contributes for single oxygen adsorption are reported with opposite sign in the negative portion.*

Two difference spectra can be obtained: one considers all the W atoms in the surface slab, eventually taking into account the long-range adsorption effects; the other considers only the W atom influenced by the acetone adsorption (namely W^{mod}). Figure 5.25a illustrates the total difference spectra. Generally, the difference between two horizontally shifted bell-shaped function produces a minimum followed by a maximum if the first term of the subtraction is shifted to the left. In the opposite case, the sign of the difference peaks is inverted. In our total difference spectrum, we observe the combination of a left shift of the t_{2g} band and a right shift of the e_g band, due to acetone adsorption (Fig. 5.25a). A detailed analysis can be performed by comparing the 5d states projected on W^{mod} alone (Fig. 5.25b), which contributes to half of the total difference spectrum intensity. Hence, its specific difference spectrum has a similar shape, and considerations based on its DOS can be extended to the whole surface. All the remaining contributes are due to long-range effects exerted by the nearby W atoms. Notably, from Figure 5.25b, it can be deduced that the e_g right shift is due to a redistribution of d_{z2} states towards higher energies, accompanied by a local intensity reduction. On the contrary, the t_{2g} left shift is determined by a more complex redistribution of the corresponding states, whose barycenter is totally moved towards lower energies.

2. *Acetone adsorption on a free site*

This case was simulated by comparing the free surface state and the vertical configuration adsorption process. Herein, the acetone molecule simply occupies a free surface site.

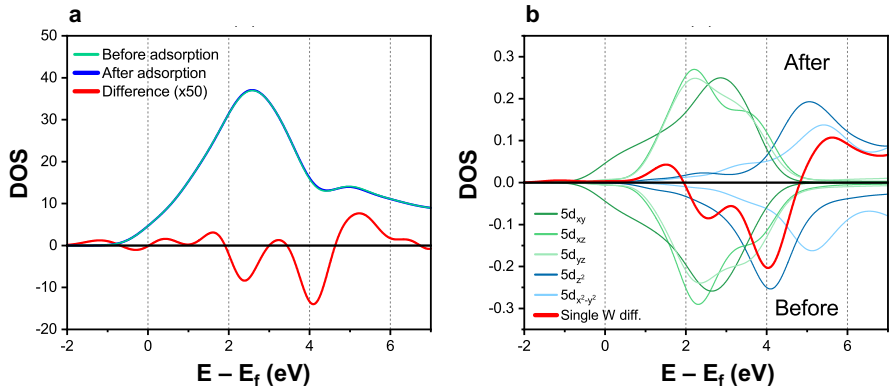

Figure 5.26. *(a) Difference between the DOS projected on all W atoms; (b) difference between the DOS projected on the specific W^{mod} (red line).*

The differences observed in the total W difference spectrum (Figure 5.26a) are analogous to the ones observed in the previous case, although little changes in intensities and energy distributions of the 5d states produce occur. W^{tot} now contributes to about 70% of the total difference spectrum, suggesting that a large part of the long-range contributions in the previous case (where W^{tot} contribution was about 50%) came from the spectator O atom.

3. *Acetone adsorption with replacement of a previously adsorbed O atom*

This third case was simulated by comparing the single oxygen adsorption and the acetone adsorption in vertical configuration. The O atom occupying the W^{mod} site in the former will be replaced by an acetone molecule. Conversely from the previous cases, a significant difference can be seen in the original DOS (blue and green lines in Figure 5.27a), especially in the initial portion of the spectra.

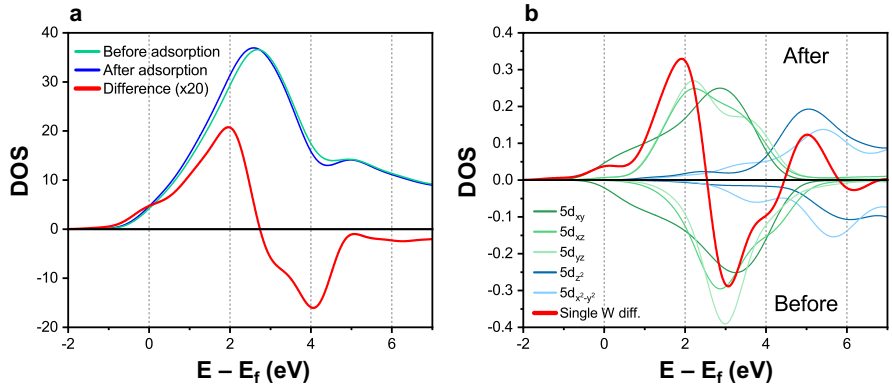

Figure 5.27. *(a) Difference between the DOS projected on all W atoms; (b) difference between the DOS projected on the specific W^{mod} (red line).*

The cause is the heavy impact on the density of states arising from the removal of an oxygen atom, which significantly modifies the states next to the Fermi level. Most of the difference spectrum intensity comes from this region, significantly shifted towards lower energies after oxygen replacement with acetone. As seen in Figure 5.27b, the d_{z2} states are now down-shifted, as well. Parallelly, the long-range contributions to the intensity get higher, reaching 60%. It can be concluded that the acetone adsorption, by replacing an adsorbed O atom, leads to a scenario completely different form the experimental case.

Hence, once optimized and widely investigated these three particular cases, the final goal is the matching between the computed and the experimental outputs, in order to give an

interpretation of the VOCs sensing mechanism by n-type semiconductor materials, as WO_3 (for a detailed discussion see Chapter 6).

5.3. Conclusions

Herein, WO_3 sensors able to detect acetone gas in atmosphere were successfully obtained, reaching low ppb concentrations at the operating temperature of 300 °C. In addition, under the same experimental conditions, the samples were able to effectively discriminate between acetone and toluene molecules, suggesting their higher selectivity towards small and polar species. Parallelly, theoretical simulations were carried out to study in depth the n-type MOS sensing mechanism, to eventually give an interpretation of it. Indeed, it represents a current hot topic still under debate. Specifically, computational results have firstly confirmed that oxygen vacancies do induce the n-type doping observed experimentally. Subsequently, after simulating atomic oxygen adsorption, a strong interaction with the surface has been observed. This species attracts a significant portion of the charge and introduces in the system a trap state, partially populated. Acetone, on the other hand, adsorbs as an electron donor, with a very small surface DOS perturbation. Finally, a comparison between the demodulated spectra, obtained from the experimental XANES data, and their theoretical counterpart has been made, resulting in a preliminary explanation of the atomic and electronic surface rearrangements arising from the adsorption/sensing of gaseous molecules.

References

[1] M. Righettoni, A. Tricoli, S. Gass, A. Schmid, A. Amann, S. E. Pratsinis, *Anal. Chim. Acta* **2012**, *738*, 69.

[2] M. Righettoni, A. Tricoli, S. E. Pratsinis, *Anal. Chem.* **2010**, *82*, 3581.

[3] M. Righettoni, A. Tricoli, S. E. Pratsinis, *Chem. Mater.* **2010**, *22*, 3152.

[4] M. Righettoni, A. Tricoli, S. E. Pratsinis, *Chim. Int. J. Chem.* **2011**, *65*, 105.

[5] H. Chen, R. Bo, A. Shrestha, B. Xin, N. Nasiri, J. Zhou, I. Di Bernardo, A. Dodd, M. Saunders, J. Lipton-Duffin, T. White, T. Tsuzuki, A. Tricoli, *Adv. Opt. Mater.* **2018**, *6*, 1800677.

[6] H. W. Kim, Y. J. Kwon, A. Mirzaei, S. Y. Kang, M. S. Choi, J. H. Bang, S. S. Kim, *Sensors Actuators, B Chem.* **2017**, *249*, 590.

[7] K. Kanda, T. Maekawa, *Sensors Actuators, B Chem.* **2005**, *108*, 97.

[8] R. S. Khadayate, J. V. Sali, P. P. Patil, *Talanta* **2007**, *72*, 1077.

[9] A. T. Güntner, N. A. Sievi, S. J. Theodore, T. Gulich, M. Kohler, S. E. Pratsinis, *Anal. Chem.* **2017**, *89*, 10578.

[10] P. M. Woodward, A. W. Sleight, T. Vogt, *J. Solid State Chem.* **1997**, *131*, 9.

[11] G. L. Chiarello, M. Bernareggi, M. Pedroni, M. Magni, S. M. Pietralunga, A. Tagliaferri, E. Vassallo, E. Selli, *J. Mater. Chem. A* **2017**, *5*, 12977.

[12] P. Periasamy, T. Krishnakumar, M. Sathish, M. Chavali, P. F. Siril, V. P. Devarajan, *J. Mater. Sci. Mater. Electron.* **2018**, *29*, 6157.

[13] P. P. González-Borrero, F. Sato, A. N. Medina, M. L. Baesso, A. C. Bento, G. Baldissera, C. Persson, G. A. Niklasson, C. G. Granqvist, A. Ferreira da Silva, *Appl. Phys. Lett.* **2010**, *96*, 061909.

[14] L. Li, J. Zhao, Y. Wang, Y. Li, D. Ma, Y. Zhao, S. Hou, X. Hao, *J. Solid State Chem.* **2011**, *184*, 1661.

[15] H. Chen, R. Bo, T. Tran-Phu, G. Liu, A. Tricoli, *Chempluschem* **2018**, 1.

[16] S. Lowell, *Introduction to powder surface area*; John Wiley and Sons, 1979.

[17] J. Tamaki, *J. Electrochem. Soc.* **1994**, *141*, 2207.

[18] A. Bajtarevic, C. Ager, M. Pienz, M. Klieber, K. Schwarz, M. Ligor, T. Ligor, W. Filipiak, H. Denz, M. Fiegl, W. Hilbe, W. Weiss, P. Lukas, H. Jamnig, M. Hackl, A. Haidenberger, B. Buszewski, W. Miekisch, J. Schubert, A. Amann, *BMC Cancer* **2009**, *9*, 348.

[19] M. Esmaeili, G. Kiani, F. S. Nogorani, S. Boroomand, *Int. J. Nano Dimens.* **2016**, *7*, 254.

[20] J. Zhang, X. Liu, G. Neri, N. Pinna, **2016**, 795.

[21] A. Gurlo, N. Bârsan, A. Oprea, M. Sahm, T. Sahm, U. Weimar, *Appl. Phys. Lett.* **2004**,

85, 2280.

[22] T. Siciliano, A. Tepore, G. Micocci, A. Genga, M. Siciliano, E. Filippo, *Sensors Actuators, B Chem.* **2009**, *138*, 207.

[23] K. Galatsis, L. Cukrov, W. Wlodarski, P. McCormick, K. Kalantar-Zadeh, E. Comini, G. Sberveglieri, *Sensors Actuators, B Chem.* **2003**, *93*, 562.

[24] G. L. Chiarello, D. Ferri, *Phys. Chem. Chem. Phys.* **2015**, *17*, 10579.

[25] T. Vogt, P. M. Woodward, B. A. Hunter, *J. Solid State Chem.* **1999**, *144*, 209.

[26] F. Wang, C. Di Valentin, G. Pacchioni, *J. Phys. Chem. C* **2012**, *116*, 10672.

[27] H. M. Le, N. H. Vu, B.-T. Phan, *Comput. Mater. Sci.* **2014**, *90*, 171.

[28] D. I. Bletskan, V. V. Vakulchak, V. M. Kabatsii, *Open J. Inorg. Non-metallic Mater.* **2015**, *05*, 31.

[29] P. M. Oliver, S. C. Parker, R. G. Egdell, F. H. Jones, *J. Chem. Soc. Faraday Trans.* **1996**, *92*, 2049.

[30] C. Lambert-Mauriat, V. Oison, L. Saadi, K. Aguir, *Surf. Sci.* **2012**, *606*, 40.

[31] C. Lambert-Mauriat, V. Oison, *J. Phys. Condens. Matter* **2006**, *18*, 7361.

[32] J. Li, P. Tang, J. Zhang, Y. Feng, R. Luo, A. Chen, D. Li, *Ind. Eng. Chem. Res.* **2016**, *55*, 3588.

[33] A. Tricoli, M. Righettoni, A. Teleki, *Angew. Chemie Int. Ed.* **2010**, *49*, 7632.

[34] A. A. Abokifa, K. Haddad, J. Fortner, C. S. Lo, P. Biswas, *J. Mater. Chem. A* **2018**, *6*, 2053.

[35] L. Zhao, F. H. Tian, X. Wang, W. Zhao, A. Fu, Y. Shen, S. Chen, S. Yu, *Comput. Mater. Sci.* **2013**, *79*, 691.

Chapter 6

Discussion

"Education is the most powerful weapon which
you can use to change the world"

— Nelson Mandela

6.1. Exploring the sensing mechanism of MOS-GO nano-heterojunctions

6.1.1. Introduction

To elucidate the sensing mechanism of the as-synthesized 3D-nanonetworks, widely described in the previous Chapters, materials electrochemical and optoelectronic features were deeply investigated. Specifically, we believe that the enhanced sensing behavior, especially at room temperature and by exploiting the UV light, should be addressed to the formation of p-n heterojunctions when MOS nanoparticles were directly grown on the graphene oxide sheets. Hence, several analyses were carried out to corroborate our hypothesis, accompanied with a possible sensing mechanism of the aforementioned chemoresistive powders, on the basis of the computational findings. Finally, a matching attempt between the theoretical and the ESRF experimental outcomes will be made.

6.1.2. Electrochemical and optoelectronic properties

Electrochemical and optoelectronic features of the prepared MOS-GO powders have been evaluated mainly by means of cyclic voltammetries, electrochemical impedance spectroscopy and photocurrent measurements.

Firstly, in order to explain the synergistic effect between graphene oxide and n-type metal oxide semiconductors (such as ZnO, SnO_2, or TiO_2), a characterization of the relative photocurrents, upon UV light exposure, was carried out. Starting from ZnO materials, Chen *et al.*[1] have demonstrated the incorporation of low-dimensional carbon material into ZnO nanowires effectively enhances the separation efficiency of photo-generated electron-hole pairs, providing efficient carrier transport pathways. Moreover, they stated that rGO/ZnO-based photodetector has high photoresponsivity (~16 $A \cdot W^{-1}$), high on/off current ratio (2.81×10^4) and great specific detectivity (1.14×10^{14} Jones), under low UV irradiation (< 10 $\mu W\ cm^{-2}$) at +1.0 V bias. Besides, uniform and oriented GO/ZnO nanorods have been obtained

thanks to the presence of GO, that influences the growth process of ZnO nanorods, giving rise to less light scattering and, thereby, stronger absorption and enhanced photocurrent. When the growth time is 1 h, the optimum photocurrent of GO/ZnO nanorods is about 10 times than pure ZnO one, whereas the detectivity reaches 7.17 × 10^{11} cm $Hz^{1/2}$ W^{-1}[2]. Hence, starting from these findings, herein, the current response was acquired by applying a bias potential of +1.0 V and by irradiating with UV light at 370 nm (light power density of 19 μW cm^{-2}), using both pure and composite ZnO-GO materials (Fig. 6.1a).

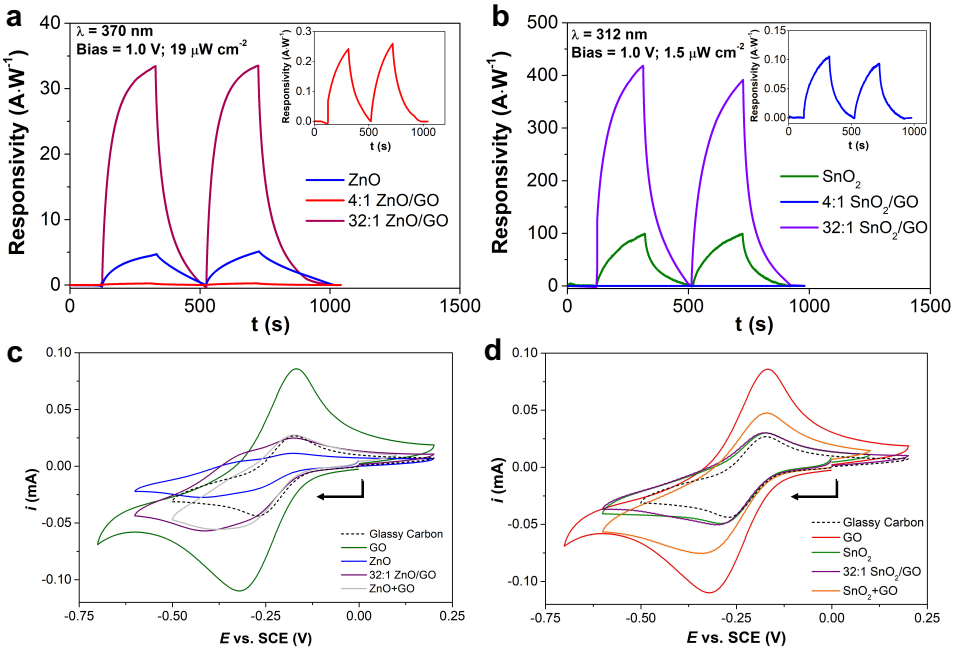

Figure 6.1. *Dynamics of photodetectors responsivity for (a) Zn- and (b) Sn-based compounds. Cyclic voltammograms relative to both bare and (c) Zn- or (d) Sn-modified glassy carbon electrodes, in the presence of 3 mM $[Ru(NH_3)_6]Cl_3$ probe (electrolyte 0.1 M PBS, scan rate: 100 mV s^{-1}). For the sake of comparison, mechanically mixed MOS+GO (with a MOS/GO weight ratio consistent to 32:1 hybrid materials) are reported.*

The major figures of merit for photodetectors are the magnitudes of the photo- and dark-currents, responsivity and detectivity (Table 6.1)[3]. Especially the last parameter quantitatively characterizes the photodetectors performances[3]. Photocurrent values are comparable with data reported in the literature for ZnO[1–3] and, among the investigated samples, 32:1 ZnO/GO shows the highest value followed digressively by ZnO and 4:1 ZnO/GO (Fig. 6.1a and Table 6.1, 3rd column). In contrast to the other ZnO-GO composite materials, at a 32:1 ZnO/GO ratio, we observed that the dark-current is decreased while the photo-current is increased (Table 6.1, 2nd column). The drop in dark-current has been attributed in the literature to the formation of

a heterojunction at the surface of n-type semiconductor and p-type material, which decreases the available free carriers[4,5]. Specifically, Retamal *et al.*[6] stated the occurrence of nanoscale heterojunctions between p-type NiO and n-type ZnO enhances the surface band bending of ZnO nanowires, improving the spatial separation efficiency of photogenerated electrons and holes, thus resulting in a larger number of free electron carriers in the ZnO. Here, the presence of more conductive GO domains in the ZnO matrix as the latter would result in an increase of the dark-current, as observed at greater GO ratios of 4:1. Therefore, these values led to higher I_{photo}/I_{dark} of around 1400 for the 32:1 ZnO/GO (Table 6.1, 4th column). Furthermore, the rise and decay times (5th and 6th columns) were comparable to data obtained with highly performing ZnO ultraporous nanoparticle networks[3] and slightly lower for the 32:1 compound. Among the investigated parameters, the responsivity achieved with the 32:1 ZnO/GO ratio is very high at ca 33 A W^{-1} with respect to the literature, while the detectivities (Table 6.1, 8th column) are comparable to the most performing materials in this field[1–3].

Sample	Dark-current (μA)	Photocurrent (μA)	I_{Photo}/I_{Dark}	Rise time (s)	Decay time (s)	Responsivity (A·W^{-1})	Detectivity (Jones)
ZnO	1.08	39	37	≈160	≈190	5.2	5.5×10^{12}
4:1 ZnO/GO	0.01	≈2	167	≈150	≈160	≈0.3	2.6×10^{12}
32:1 ZnO/GO	0.18	257	1426	≈100	≈120	33.4	8.7×10^{12}
SnO_2	540	58	108	≈160	≈130	100	1.5×10^{14}
4:1 SnO_2/GO	1	0.057	52	≈130	≈110	0.100	3.4×10^{12}
32:1 SnO_2/GO	100	240	2380	≈120	≈100	395	1.4×10^{15}

Table 6.1. *Figures of merit of photodetectors made by Zn- (λ = 370 nm, light power density = 19 μW cm^{-2}) and Sn-based (λ = 312 nm, light power density = 1.5 μW cm^{-2}) samples. In both cases, the applied bias was +1.0 V.*

Notably, as clearly visible from Figure 6.1b and Table 6.1, an analogous behavior was observed for SnO_2-GO composites (λ = 312 nm, light power density = 1.5 μW cm^{-2}). Indeed, among the investigated samples, 32:1 SnO_2/GO shows the highest value followed digressively by SnO_2 and 4:1 SnO_2/GO (Fig. 6.1b and Table 6.1, 3rd column). Dark-currents of 32:1 and bare SnO_2 are very similar and they are two orders of magnitude higher than that of 4:1 sample. Therefore, these values led to a very high I_{photo}/I_{dark} of around 2400, for the 32:1 SnO_2/GO. Furthermore, the rise and decay times (Table 6.1, 5th and 6th columns) were almost comparable or slightly higher to data obtained with highly performing SnO_2-based photodetectors[3,7]. Among the studied parameters, the responsivity reached with the 32:1 ratio is very high (around 400 A·W^{-1}) with respect to the recent literature[8], as well as the detectivities (Table 6.1, 8th column) are greater than those of the most performing materials[8–10].

Lan *et al.*[8] proposed a high-performance UV photodetector combining the SnO_2 semiconductor with three-dimensional graphene nanowalls (GNWs). The as-prepared

nanocomposite films show strong absorption in the wide UV region, owing to the presence of the 3D-GNWs network that efficiently suppresses the recombination of the photo-induced electron-hole pairs. This results in a great enhancement of GNWs/SnO_2 photoresponse compared to pure SnO_2 one. Notably, the responsivity of GNWs/SnO_2 photodetector is reported to be 8.6 mA W^{-1} (light power density of 32 mW cm^{-2}) at a bias voltage of +1.0 V, which is around 8 times higher than that of the pristine tin dioxide.

Hence, the observed photo-responsivity trend (*i.e.* 32:1 > pure MOS > 4:1) and the very high responsivity/detectivity, measured with the 32:1 ratio, suggest a potential enhancement mechanism for the chemical and UV light sensing[11], probably thanks to the p-n heterojunction formation between GO (p-type) and MOS (n-type) materials. Indeed, GO has been reported to behave as a p-type semiconductor[12–14] (see Chapter 3), especially when coupled to an n-type material.

Therefore, to have a confirmation of our hypothesis, either CV (Figs. 6.1c,d) or EIS (Fig. 6.2) measurements were performed. Particularly, CV measurements were carried out exploiting glassy carbon electrodes, differently covered by GO, pure MOS, 32:1 MOS/GO, and mechanically mixed MOS+GO (where MOS represents ZnO or SnO_2), in the presence of a positively charged outer-sphere electrochemical probe[15] (*i.e.* hexamine ruthenium (III) chloride, $[Ru(NH_3)_6]Cl_3$). We observed a peculiar and specific behavior of the hybrid 32:1 ZnO/GO with respect to mechanically mixed ZnO+GO. The ZnO+GO composite (Figure 6.6c, grey line) displays a major contribution of graphene oxide (peak at -0.31 V) and a separated, partially masked, ZnO contribution (peak at -0.33 V). This indicates that, in these mechanically mixed samples, the GO and the ZnO act as separate electrical domains with no intimate electron/hole exchange. In contrast, the hydrothermally grown 32:1 ZnO/GO samples (Figure 6.6c, purple line) exhibits a miscellaneous electrochemical behavior between that of ZnO and GO. This indicates an intimate interaction between GO and ZnO, suggesting the formation of p-n heterojunctions between these two materials. Instead, concerning the SnO_2-based samples (Fig. 6.1d), a further interesting observation can be made. Actually, the reductive sweep shows two diverse behaviors: *i*) a defined peak-shaped curve in the case of GO (red line), pristine SnO_2 (green line) and SnO_2+GO (orange line) materials (at around -0.3 V); *ii*) a tendency to step-shaped curve for the hybrid 32:1 SnO_2/GO (violet line). Actually, by focusing on the potential range between -0.25 and -0.50 V, only 32:1 SnO_2/GO displays a flat behavior. From these experimental evidences, it may be inferred that the contribution of convergent diffusion seems to become smoothly predominant[16] in the case of this composite material, with respect to either pristine SnO_2 or mixed SnO_2+GO. The growth of tin oxide on the graphene oxide sheets by forming catalytic isles, almost widely spaced, guarantees their independency in the experimental timescale and thus promotes convergent diffusion, already visible also with an

outer-sphere probe[17]. The predominance of convergent diffusion allows to obtain higher sensitivities and low detection limits, thanks to high faradaic and low capacitive currents[18-21], important features of more performing sensors[15]. Hence, we can infer that an intimate interaction between GO and MOS nanoparticles might be assumed, proving the existence of an optimally integrated p-n heterojunctions.

However, to have a further corroboration, EIS measurements were carried out, always in the presence of the same outer-sphere probe (Figure 6.2 and Table 6.2).

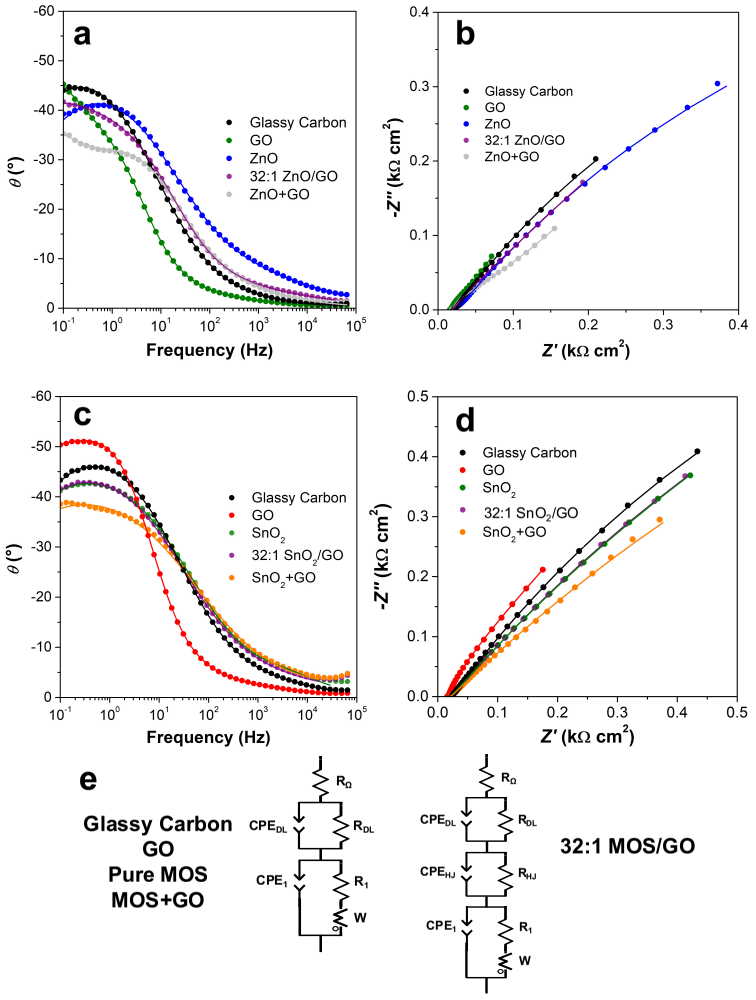

Figure 6.2. *(a,c) Bode plots and (b,d) complex plane plots for Zn- or Sn-modified glassy carbon electrodes at -0.15 V (potential at which the adopted probe, $[Ru(NH_3)_6]Cl_3$, is oxidized. See dotted lines in Figs. 6.1c,d). Points are the experimental values, while continuous lines are the simulated data according to the equivalent circuits, shown in (e). Supporting electrolyte: PBS 0.1 M, pH 7.4.*

Comparing the Bode plots for both ZnO- and SnO_2-based materials (Figs. 6.2a and c), their relative shape seems to be quite different. To get quantitative information on the electrical behavior (Table 6.2), the EIS data of glassy carbon/investigated materials/electrolyte interfaces were fitted according to the equivalent circuits shown in Figure 6.2e. Starting from ZnO-based materials, a series resistor (R_Ω, ca 15-20 Ω cm^{-2}) was introduced to describe the electrolyte resistance and another R_{DL}/CPE_{DL} parallel circuit was necessary to model the electrode/electrolyte double layer: R_{DL} is the charge transfer resistance, whereas CPE_{DL} represents a non-ideal double layer capacitance. Notably, a constant phase element (CPE) was used instead of a real capacitance due to the presence of defects and impurities that introduce inhomogeneities in the electrical properties of the investigated materials. Moreover, an open Warburg element (R_W) was also added in the fitting circuits of GO, 32:1 ZnO/GO and ZnO+GO to take into account the probe mass transfer process. Specifically, the charge transfer resistance (R_{DL}) at the solid-liquid interface (the parameters that changes more when the probe reacts), showed similar values for the 32:1 ZnO/GO (0.05 kΩ cm^{-2}) and GO (0.03 kΩ cm^{-2}), and it is two orders of magnitude smaller with respect to the ZnO one (ca 3.50 Ω cm^{-2}; Table 3), which was in line with the literature[22–24]. The ZnO+GO, on the contrary, exhibited a behavior close to the ZnO, with a charge transfer resistance of about 1.10 kΩ cm^{-2}. These results show that 32:1 ZnO/GO composite, notwithstanding the almost complete coverage of GO by the zinc oxide nanoparticles, has an efficient charge transfer, and a strongly different behavior than the ZnO. Besides, the CPE_{DL} was very high for the conductive GO material (ca 14 mF cm^{-2} $s^{\alpha-1}$) and quite low for the pure ZnO (ca 1 mF cm^{-2} $s^{\alpha-1}$). Interestingly, the 32:1 ZnO/GO showed an intermediate behavior with a capacitance of ca 5 mF cm^{-2} $s^{\alpha-1}$, which is greater than that of the ZnO+GO one of ca 2 mF cm^{-2} $s^{\alpha-1}$. The EIS technique has been previously used to provide information about the actual presence of a p-n heterojunction, modelling it as a parallel combination of a resistance (R_{HJ}), accounting for the leakage and recombination paths through the p/n-type MOS interface, and a constant phase element (CPE_{HJ}), due to the non-ideal capacitance resulting from the depletion region of the p-n junction[22–24]. Notably, 32:1 ZnO/GO plot fitted well this model, while the other investigated materials could be not modelled with the above-described heterojunction circuit. This was particularly evident for the mechanically mixed ZnO-GO. Furthermore, a third circuit (R_1/CPE_1, *i.e.* the polarization capacitance) is present representing the interface between the powders and the glassy carbon support. CPE_1 values similar or higher than that of the bare glassy carbon indicate the easiness of the polarization processes. This is the case only for the GO and 32:1 ZnO/GO materials.

For SnO_2-based samples (Figs. 6.2c,d), the same electrical circuits used in the case of ZnO compounds were adopted (Figs. 6.2e). Also, in this case, GO is the less resistive sample.

Interestingly, herein, *i*) the 32:1 SnO_2/GO material is the only compound that has all the electrochemical impedance parameters closer to the GO ones (see Table 6.2); *ii*) its behavior is quite different from the one obtained with mechanically mixed SnO_2+GO; *iii*) also for 32:1 SnO_2/GO an additional R_{HJ}/CPE_{HJ} circuit was added to better fit the EIS data.

Modified-GCE	R_Ω (Ω cm²)	R_{DL} (kΩ cm²)	CPE_{DL}‡	α_{DL}	R_{HJ} (Ω cm²)	α_{HJ}	CPE_{HJ}‡	R_1 (kΩ cm²)	CPE_1‡	α_1	R_W (Ω cm²)	τ_W (s)	α_W
Bare	21.90	2.95	1.41	0.60	–	–	–	1.96	1.98	0.60	–	–	–
GO	15.73	0.03	13.70	0.43	–	–	–	4.50	2.01	0.93	0.02	>0.01	0.25
ZnO	19.27	3.48	1.05	0.50	–	–	–	11.20	0.83	0.59	–	–	–
32:1 ZnO/GO	17.47	0.05	4.84	0.45	1.40	0.70	0.30	5.57	1.60	0.77	3.07	92.00	0.36
ZnO+GO	17.81	1.10	2.15	0.46	–	–	–	7.59	0.62	0.73	3.23	143.00	0.36
Bare	21.90	2.95	1.41	0.60	–	–	–	1.96	1.98	0.60	–	–	–
GO	15.73	0.03	13.70	0.43	–	–	–	4.50	2.01	0.93	0.02	>0.01	0.25
SnO_2	20.23	3.90	0.17	0.77	–	–	–	2.37	2.14	0.54	–	–	–
32:1 SnO_2/GO	20.45	0.90	4.00	0.41	3.55	0.70	0.03	2.45	2.15	0.55	0.05	0.06	0.45
SnO_2+GO	19.70	3.76	1.24	0.45	–	–	–	3.68	2.05	0.49	0.11	0.09	0.42

Table 6.2. *Comparison among values obtained by EIS analyses for both Zn- and SnO_2-based materials, at -0.15 V. Supporting electrolyte: PBS 0.1 M, pH 7.4. Adopted probe: $[Ru(NH_3)_6]Cl_3$, 3 mM. ‡CPE values are reported in mF cm^{-2} $s^{\alpha-1}$.*

Hence, by means of EIS, it has been possible to either compare the different behavior, especially for composite 32:1 MOS/GO and mechanically mixed MOS+GO or corroborate the direct growth of MOS nanoparticles on GO, leading to the formation of a p-n heterojunction. Conversely, this phenomenon does not occur when powders are physically mixed.

Starting from all the previous outcomes, gas sensing tests towards ethanol molecules (as representative VOC) by a composite SnO_2/GO (16:1 as representative one) and the corresponding SnO_2+GO were carried out, at the same experimental conditions. Figure 6.3 displays the results obtained. As expected, even with a less performing sample as 16:1 SnO_2/GO, in the case of composite material, an enhancement of both the signal intensity and sensitivity was achieved.

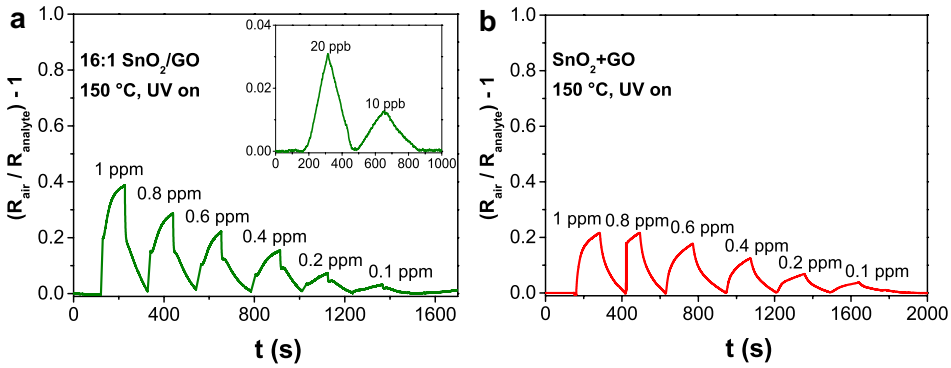

Figure 6.3. *Ethanol sensor responses achieved by using (a) hybrid 16:1 SnO_2/GO and (b) mechanically mixed SnO_2+GO, having a weight ratio comparable to the composite 16:1 SnO_2/GO. The tests were carried out in simulated air (80% N_2 – 20% O_2), at 150°C, under UV light. Adapted with permission[15], Copyright 2019, Elsevier.*

An additional validation of our hypothesis was also given by TEM analysis. Figure 6.4 displays transmission microscopy images of 16:1 and 32:1 SnO_2/GO, as indicative examples. In both cases, it is possible to notice the simultaneous presence of tin dioxide nanoparticles, with a spherical morphology, in contact with graphene oxide material, with its typical sheet-like texture (as clearly visible in the magnified image).

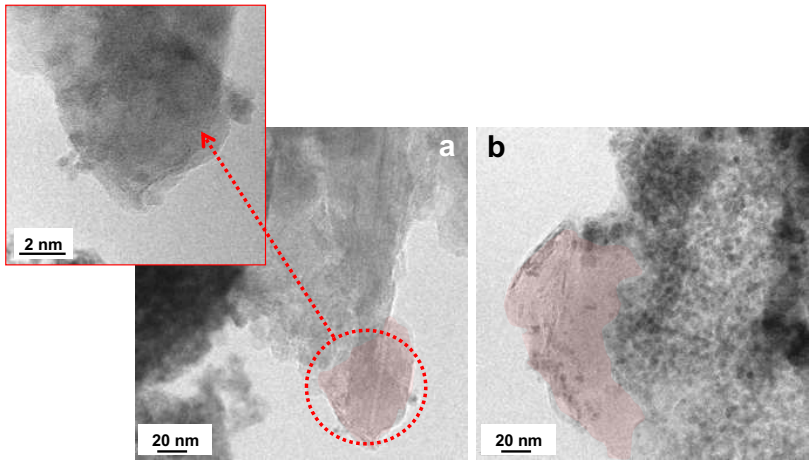

Figure 6.4. *TEM images of (a) 16:1 SnO_2/GO and (b) 32:1 SnO_2/GO (as representative and most performing samples among SnO_2-GO series), in which it is clearly visible the simultaneous presence of GO (reddish region and in the magnification in inset) and MOS nanoparticles.*

Hence, an intimate interaction between p-type GO and n-type metal oxide nanoparticles can be assumed, proving the existence of an optimally integrated p-n heterojunctions. As such,

this heterojunction formation is the key for the enhancement of the material performances in both light and low-temperature chemical sensing.

6.1.3. The sensing mechanism

The proposed mechanism is an extension of the one reported by Chen *et al.*[4], who explained the sensing behavior of only n-type semiconductor both under dark and UV conditions[4,15,25]. In summary, they reported that, when MOS is exposed to air, oxygen molecules are adsorbed on its surface withdrawing electrons from the conduction band of the semiconductor, thus forming negatively charged oxygen ions (*i.e.* O_2^-, O^- and O^{2-} depending on the operating temperature[26,27]), which are the effective reactive species. This phenomenon gives rise to a low-conductivity depletion layer at the MOS surface. However, since the adsorption energy is high[25], the oxygen species are thermally stable and difficult to be removed from the MOS surface at room temperature, therefore they may not react with the VOCs molecules. Hence, no gas sensing response in the dark occurs. To overcome this drawback, the coupling of the metal oxide with graphene oxide-based material can represent an optimal alternative. In particular, since GO shows a p-type semiconductor behavior[12–14], especially in the presence of a n-type material, a possible heterojunction creation may occur, as widely confirmed in the previous paragraph.

Figures 6.5 shows either the density of states of WO_3 surface with oxygen deficient sites (see Chapter 5), or a schematic representation of the junction between GO and a generic n-type MOS (with UV light and by applying a bias of +1.0 V). Specifically, Figure 6.5a is mandatory since it displays the appearance of populated states near the conduction band (highlighted in blue in the magnified image), thus corroborating the intrinsic n-doping of the metal oxide semiconductor. Figure 6.5b, instead, explains the sensing mechanism by exploiting the UV light. Particularly, when the device is irradiated, the separation of the photo-excited electron-hole couples occurs. Hence, some of these holes can desorb the adsorbed oxygen ions forming O_2 gaseous molecules, resulting in either a decrease of the depletion layer width or an increase in the free carrier concentration, *i.e.* a rise in the photocurrent upon UV irradiation[25,28]. Besides, the higher carrier density can cause more ambient oxygen species to adsorb onto the MOS surface, thus creating photo-induced oxygen ions that are less strongly bound and can react more easily with the VOCs molecules[25]. When the reaction occurs, electrons are released back to the conduction band of the metal oxide, decreasing the MOS surface depletion layer and, then, increasing the final conductivity.

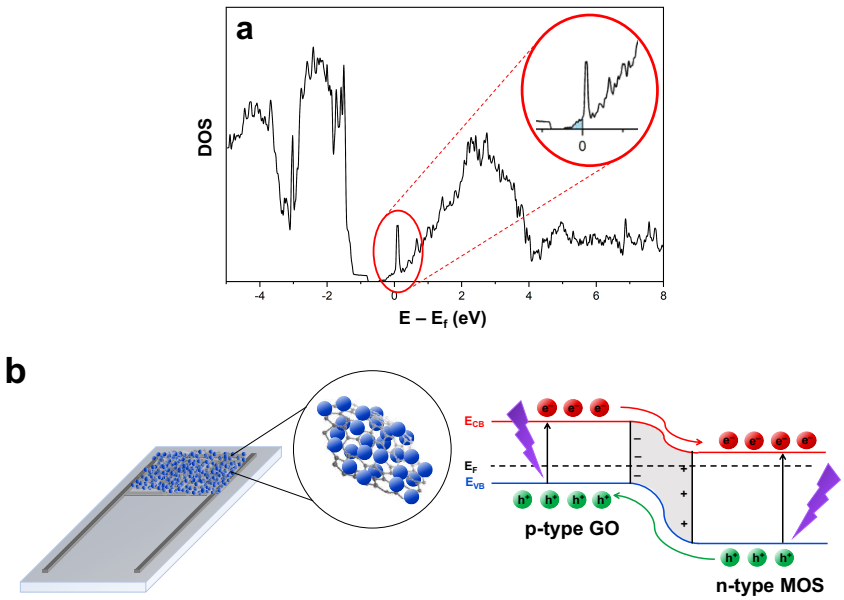

Figure 6.5. *(a) DOS of WO_3 surface with oxygen deficient sites: the appearance of populated states at Fermi level (highlighted in blue in the magnified image) corroborates the intrinsic n-doping of the semiconductor. (b) Hypothesized mechanism underneath the sensing behavior for the composite n-type MOS-GO powders.*

To corroborate the effective reaction of VOCs molecules on the chemoresistor material surface, mass spectrometry analyses were conducted (concomitantly to the *in situ* synchrotron acetone sensing measurements). Figure 6.6a shows the obtained results. As expected, acetone (as the representative VOC) and oxygen were detected when purged into the sensing chamber. According to the reactions, already reported in the literature[25,29], the sensing ionosorption mechanism (see Chapter 2, 2.3.1 paragraph) is supposed to produce CO_2 and water molecules, according to the following reaction[25,29–31]:

(6.1.3.a) $(CH_3)_2CO + 8O^- \rightarrow 3CO_2 + 3H_2O + 8e^-$

As such, mass spectrometry results reveal the formation of these products, confirming the mechanism hypothesized. In addition, the proposed sensing mechanism was further validated by measurement of the 32:1 ZnO/GO sensor response to 8 ppm of NO_2 showing an opposite response direction (resistance increase) with respect to reducing gases, as ethanol, acetone and ethylbenzene (Fig. 6.6b). This is in line with the expected charge exchange at the nanomaterial surface, where oxidant species would decrease the concentration of free-carriers in the metal oxide[32].

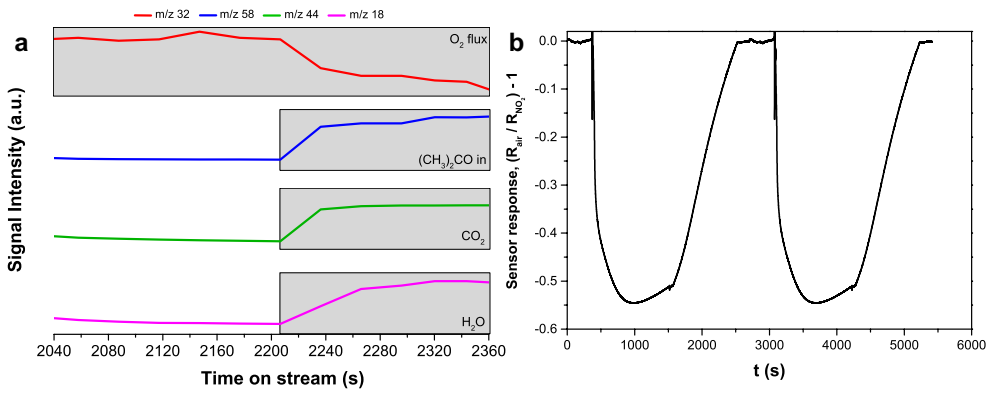

Figure 6.6. *(a) Mass spectrometry results relative to a single modulation cycle (in situ ESFR measurement), showing O_2 (m/z 32, red line), $(CH_3)_2CO$ (m/z 58, blue line), and the hypothesized products CO_2 (m/z 44, green line), H_2O (m/z 18, magenta line). The grey boxes highlight the formation of CO_2 and H_2O during the acetone purging, whereas O_2 is consumed. (b) Example of 32:1 ZnO/GO response (as representative sample) to oxidizing species such as NO_2, at RT by exploiting the UV light. Tests were conducted in simulated air (20% O_2 – 80% N_2).*

Up to now, the described mechanism contemplates the presence of only one n-type metal oxide semiconductor, such as ZnO, SnO_2, WO_3 or TiO_2. The following paragraph focuses on the SnO_2-TiO_2-GO mixed oxides.

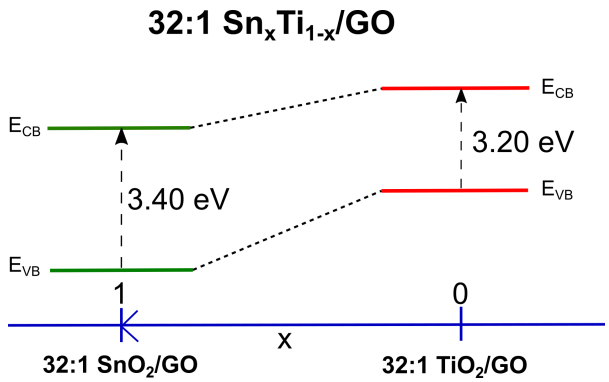

Figure 6.7. *Variation of the electronic properties (band gap values) with the decreasing of titanium content. In the case of solid solutions, no n-n type heterojunctions are formed, thus no band bending occur.*

Starting from both the results of the physico-chemical characterizations and the available literature[33–37], it is possible to infer that there is not an n-n type heterojunction formation and, so, any band bending but simply a variation of the band gap, as clearly described in Figure 6.7. Indeed, rather than composite materials, Sn/Ti oxides solid solutions were synthesized. Hence, we believe that the aforementioned mechanism is valid also for the investigated 32:1 Sn_xTi_{1-x}/GO materials.

6.1.3.1. *When the theory meets the experiment*

The theoretical approach is fundamental to obtain a more thorough understanding behind the VOCs sensing by pure MOS nanoparticles. A set of factors that control the sensing process, including the materials atomic structure, surface oxygen defects, and the polarity of the analyte gas should be considered. For this reason, the adsorption of oxygen species and acetone molecules (as representative gas target) on WO_3 (as representative MOS) have been investigated, along with the role of both surface oxygen defects and pre-adsorbed oxygen species. As already mentioned, the final goal was the attempt to corroborate the ESRF data by computational results.

Generally, the obtained theoretical predictions concord with some experimental observations. In particular, when oxygen adsorbs on WO_3 as an atomic species it acts as an electron acceptor, withdrawing electrons from the surface and decreasing its conductivity (Figure 6.8a). On the other hand, when acetone is present in the environment, due its electron donor properties it transfers some charge to the surface, partially restoring the natural surface conductivity (see Figure 6.8b).

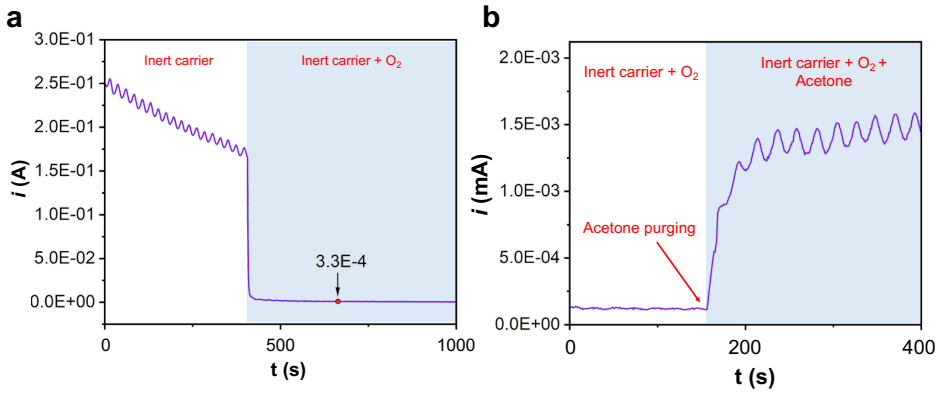

Figure 6.8. *WO_3 current variation (a) in the presence of oxygen molecules and (b) upon acetone purging into the sensing chamber, under simulated air (80% N_2 – 20% O_2).*

Notably, the effect due to oxygen is greater with respect to the acetone case. This fact can be justified by comparing the adsorption energies and the charge transfer values. Indeed, the oxygen binding energy is higher than the acetone ones of ca 63% for tilted and 44% for vertical adsorption configurations; whereas, the charge transfer is 78% and 54% greater, respectively.

Once investigated the molecules adsorption, difference PDOS spectra were simulated to obtain outputs comparable to ME-XANES results. As can be noticed in graphs reported in Chapter 5 (Figs. 5.25, 5.26 and 5.27), the local and total difference spectra have significantly different intensities, suggesting that the perturbations induced by the adsorbed species on the

nearby W atoms DOS are not negligible. Hence, we selected only the total difference spectra for comparison with the ME-XANES data, since the latter takes into account these long-range effects, while providing a better representation of the experimental output. Figure 6.9 displays a comparison between the theoretical and the experimental difference spectra. Notably, in all the investigated cases, the stress should not be put on the t_{2g}-e_g gap values, but on the general shape of the computed curves. Therefore, a satisfying agreement was obtained in the case of: *i*) acetone adsorption on a free site in the presence of a spectator O atom (Fig. 6.9a); *ii*) acetone adsorption on a free site (Fig. 6.9c). In particular, the first case should be compared to ESRF experiment in which both the two species (*i.e.* acetone and oxygen) are purged into the chamber (Chapter 5, Fig. 5.9c).

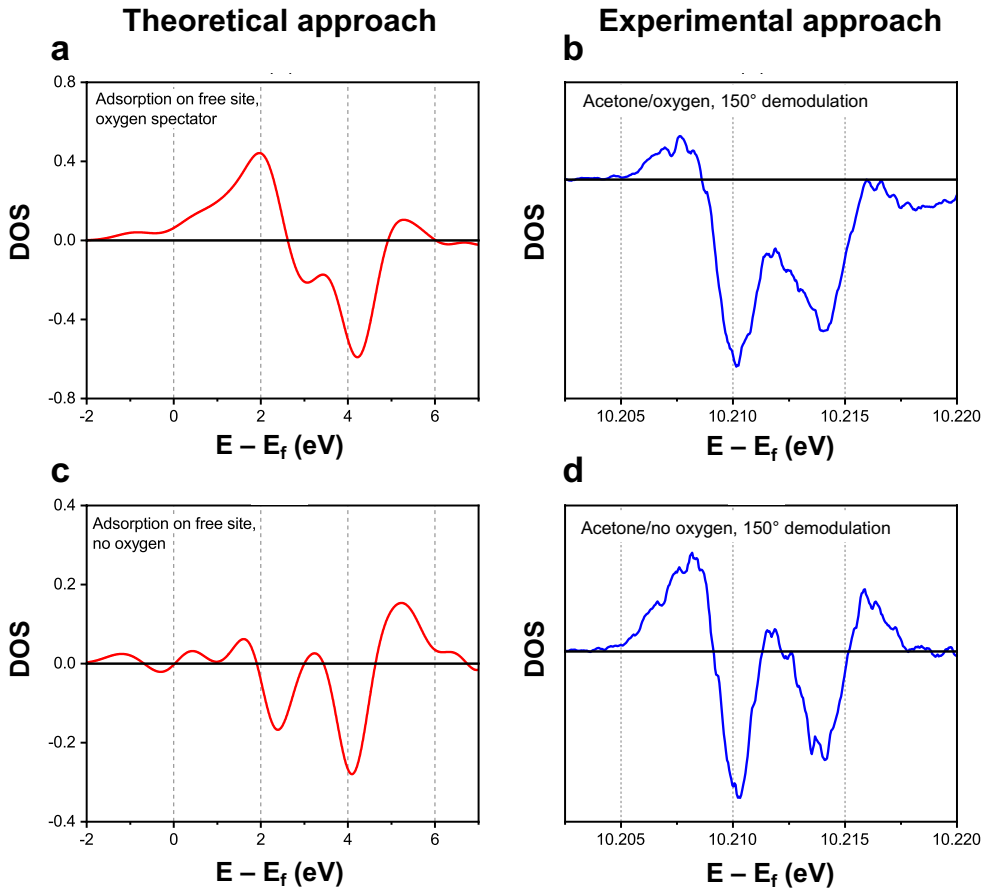

Figure 6.9. *Total difference spectra associated to acetone adsorption (a) in the presence of oxygen and (c) in the absence of oxygen. (b, d) Experimental demodulated spectra relative to (a) and (c) theoretical cases, respectively.*

On the contrary, the second case may reasonably recall the experiment in which only acetone gas was purged together with the inert He carrier (Chapter 5, Fig. 5.9b). The comparison in Figure 6.9 allows to conclude that the 150° demodulation spectra correspond to the differences between two XANES spectra obtained after and before the gas adsorption. Hence, we can reasonably hypothesize that acetone adsorption does not occur by replacing a pre-adsorbed oxygen atom. Moreover, a detailed analysis of the theoretical difference spectra suggests that the oscillations observed in the experimental demodulated spectra, due to acetone adsorption, are caused by the shift of the d_{z2} states towards higher energies and a simultaneous rearrangement of the t_{2g} states that shifts their barycenter towards lower values.

In conclusion, we can infer that when the sensor is in inert environment (N_2 or He atmosphere) the surface conductivity is at its maximum. As soon as O_2 molecules are introduced in the environment, an abrupt conductivity decrease is observed. From our theoretical findings, atomic oxygen may be the responsible of this phenomenon, since it adsorbs strongly, behaving as an electron acceptor. This behavior can be explained either in terms of simple charge transfer, since it attracts a significant amount of charge, or by observing the surface density of states in its presence. Indeed, a sharp state appears just next to the Fermi level, acting as an electron trap. This oxygen species may derive from O_2 dissociation in proximity of the surface, eventually induced by the long-range interactions. Thus, when acetone reaches the sensor, it does not provoke atomic oxygen desorption, but it adsorbs on the remaining sites thanks to its affinity to the WO_3 surface. Due to its weak electron donor properties, the effect is a slight conductivity increase, partially restoring the pristine surface conductivity and determining the sensor response. This mechanism can be also applicable in the case of oxidative reactions taking place at the oxygen-occupied sites, with the gaseous analyte. Indeed, as long as the reaction products are electron donors and possess affinity towards the surface, a conductivity increase proportional to the analyte concentration would be observed as well. Hence, so far, we cannot exclude neither any oxidative reaction in the presence of oxygen species and reducing gases, nor a mere adsorption/desorption mechanism at the base of the chemoresistive sensing. Certainly, the pivotal role of oxygen species has been confirmed on either experimental (see Chapter 5, Fig. 5.8) or theoretical points of view. However, further studies (*i.e.* molecular dynamics) are required to simulate the majority of the experimental conditions, especially for what concerns the higher operating temperature. Nevertheless, this novel work can be the starting point for further investigations, principally because Abokifa *et al.*[31] recently demonstrated, *via ab initio* molecular dynamics simulations at RT, that the adsorption of acetone on SnO_2 semiconductor is energetically favorable and this process is accompanied by a charge release from the adsorbed gas to the material surface. Furthermore, they evidenced that an interaction may take place between the pre-adsorbed

oxygen species (in their case they evidenced the presence of O_2^- species) and the studied polar VOCs, upon their adsorption on the defective surface. Hence, from both theoretical and experimental approaches, their results suggested that the sensing mechanism of SnO_2 towards polar VOCs at room temperature can be explained by their direct adsorption on the semiconductor surface, similarly to what we obtained herein.

6.2. Sensitivity and selectivity: a comparison with the literature

The novel three-dimensional nano-heterojunction networks, presented in this PhD research work, showed very promising sensing properties, both at high and low temperature working conditions, resulting in great sensitivities (*i.e.* down to concentrations of parts-per-billions) towards either small and polar molecules (such as ethanol and acetone) or bigger and non-polar ones (*e.g.* ethylbenzene and toluene). Moreover, the most promising materials exhibit a good degree of selectivity. Indeed, besides mixed oxides solid solutions did operate at only quite high temperatures (the lowest one was 250 °C, under UV light), SnO_2/GO and ZnO/GO sensors seem to be well-performing even at RT and, as displayed in Figure 6.9, they possess different and specific selectivity.

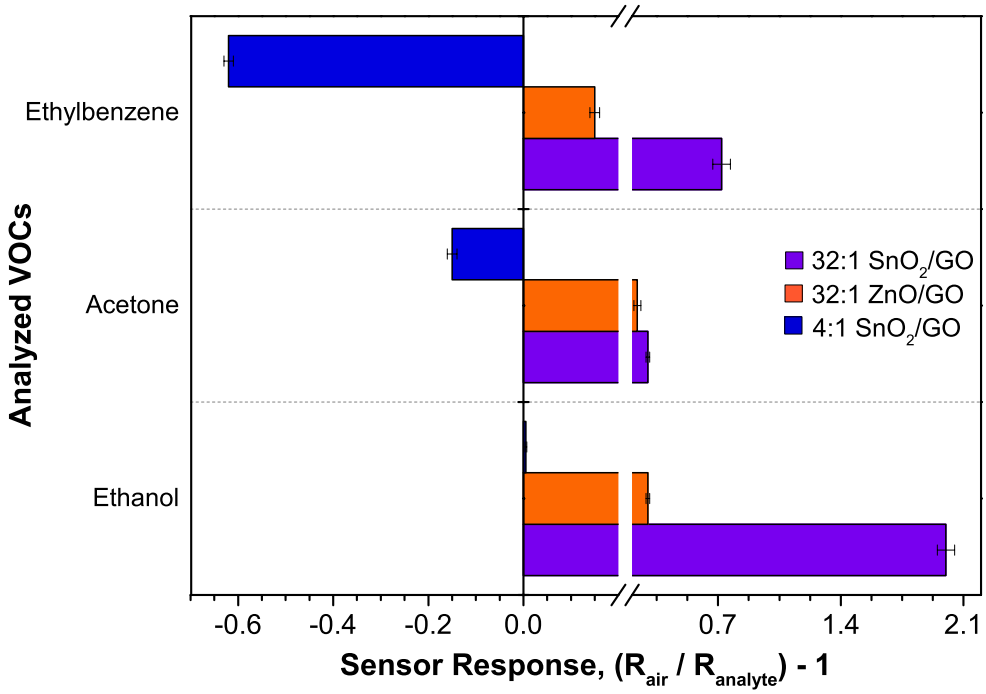

Figure 6.9. *Comparison among 32:1, 4:1 SnO_2/GO and 32:1 ZnO/GO sensors, in terms of signal response intensity to 1 ppm of VOCs, at 25°C under UV irradiation. Each response is an average on at least five different measurements.*

Notably, the above comparison considers the two optimal composites, namely 32:1 ZnO/GO and 32:1 SnO_2/GO, and 4:1 SnO_2/GO which exhibited a very interesting behavior, revealing exploitable for selectivity purposes. Particularly, 32:1 SnO_2/GO has an excellent selectivity for ethanol than the other species, showing a response about four times higher than that of acetone. According to our results, at constant GO amount, tin dioxide matrix seems to

be more performing than zin oxide one. This may be attributed to the different grain boundary density of the two nanonetworks, which is in turn affected by the nanoparticles dimensions. Indeed, the mechanism that controls the materials resistance change depends mainly on the ratio between the grain size (D) and the Debye length (δ, see Chapter 2). As stated by Tricoli *et al.*[38], if D is slightly lower or equal to 2δ, the whole grains are depleted and modifications in the surface oxygen species concentration can affect the entire semiconductor, thus resulting in higher sensitivity. In our case, particles sizes of both hybrid SnO_2-GO (~5-8 nm; see Chapter 4, 4.2 paragraph) and ZnO-GO (~50 nm; see Chapter 4, 4.1 paragraph) compounds are very close to twice of the Debye length of tin dioxide (~3 nm[39–41]) and zinc oxide (~30 nm[42]), respectively. Hence, an improvement of the sensing behavior was expected. However, recently Bo *et al.*[3] reported that the further increase of ZnO nanoparticles dimensions beyond 42 nm limits the photo-sensing due to slightly greater backscattering phenomena, causing reduced performances and, in the present case, decreased chemical sensing.

Furthermore, as previously said, 4:1 SnO_2/GO shows an interesting "reversed" behavior, *i.e.* upon purging these species a drop of the measured current was recorded, especially in the case of ethylbenzene. In Chapters 4 and 5, a rough explanation has been given, mainly based on recent literature results[4], in which the same phenomenon has occurred. Going deeply into the matter in question, Gurlo *et al.*[43] have hypothesized the switching in an n-or p-type MOS from n- to p-conductivity or *vice versa*. Therefore, they have proposed the following mechanism, according to their theoretical model. Formally, for a semiconductor material, one can distinguish among five different situations (see Figure 6.10):

1. *inert atmosphere*: flat band situation;
2. *low oxygen concentrations*: the band bending due to oxygen adsorption is not high enough to change the surface conductivity, which remains n-type;

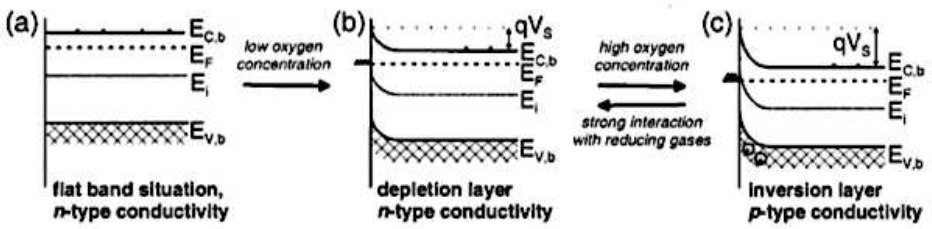

Figure 6.10. *Schematic energy-level diagram of an n-type semiconductor. (a) Flat band situation in the presence of only inert gases. (b) Oxygen adsorption leading to depletion layer formation and reduced n-type surface conductivity. (c) Inversion layer formation, since the Fermi level (E_F) lies below the intrinsic level (E_i), and occurrence of a p-type surface conductivity. Reproduced with permission[43], Copyright 2004, American Institute of Physics.*

3. *high oxygen concentrations*: oxygen adsorption leads to the formation of an inversion layer at the semiconductor surface, hence its conductivity changes from n to p. The concentration of holes (normally minority carriers in n-type MOS) becomes larger than the concentration of electrons;
4. *interaction with low concentrations of reducing gases*: reducing gases react with the surface oxygen ions, releasing electrons that can return to the MOS bands. Electron concentration is increased, and holes concentration is decreased. Downward bending is small, so the Fermi level is still below the intrinsic level and dominant free charge carriers are still holes;
5. *Interaction with high concentrations of reducing gases*: in this case the band bending is large enough to bring the Fermi level above the intrinsic level and the electrons become the dominant surface charge carriers.

Hence, Gurlo and his co-workers successfully explained the possible MOS conductivity inversion that causes the switching of the sensing behavior: at RT the exploitation of UV light increases the amount of atomic oxygen[44] adsorbed on the MOS surface, leading to a greater concentration of holes than electrons and, thus, giving rise to a p-type behavior. Hence, this phenomenon is quite interesting, since it allows to selectively sense a specific analyte, thus representing a powerful tool for the engineering of next-generation sensors.

Moreover, starting from all the obtained data, a comparison with literature results is mandatory if we want to highlight the real potentialities of our 3D-nanostructures. Table 6.3 shows a comparative summary of either pristine MOS or MOS-graphene based materials chemiresistors, already present in the literature[40,45–48]. As widely stated, all the pure metal oxide nanoparticles have shown good responses towards both smaller/polar molecules and bigger/non-polar ones. However, the sensing measurements were feasible only at high operating temperatures, which allow to activate the MOS itself. Particularly, we can infer that crystallites size, surface area and pores volume/shape are the key parameters that influence the final materials performances, especially in terms of sensitivity and response/recovery times. Indeed, this conclusion has been brought especially by the study on how the synthetic strategy can influence the powders properties and, so, the sensing behavior in the representative case of WO_3 material (discussed in Chapter 5). Furthermore, all the materials presented here have superior sensing abilities than those already reported and, in particular, 32:1 SnO_2/GO exhibits significantly higher sensitivity (very low-ppb values of detection limit) and a quite high response intensity, even at RT, than the other studied compounds[40,45]. Finally, we can also remarkably observe the very promising results obtained towards EtBz, for which very few studies have been conducted so far[48].

Material	Operating temperature (°C)	VOC	Signal response, ($R_{air}/R_{analyte}$)-1[b]	LOD[a] (ppb)	Ref.	
Hollow SnO_2	300	EtOH	28.2 (100 ppm)[c]	5000	[45]	Literature results
rGO-SnO_2	300	EtOH	42.0 (100 ppm)[c]	5000	[45]	
		Acetone	11.0 (100 ppm)[c]	–	[45]	
SnO_2-rGO composites	250	EtOH	~50.0 (50 ppm)[c]	5000	[49]	
0.1 wt% GO/SnO_2 nanocomposite	250	EtOH	22.5 (50 ppm)	1000	[46]	
ZnO with 10% GO	240	EtOH	~10.0 (100 ppm)[c]	–	[50]	
		Acetone	~34.0 (100 ppm)[c]	1000		
rGO-ZnO	RT	EtOH	~0.03 (100 ppm)	20000	[51]	
		Acetone	~0.04 (100 ppm)	20000		
SnO_2 hollow spheres	200	Acetone	15.0 (50 ppm)[c]	5000	[52]	
Rh-doped SnO_2 nanofibers	200	Acetone	59.6 (50 ppm)[c]	1000	[40]	
GO/SnO_2/TiO_2	200	Acetone	~12.0[c]	250	[53]	
		Toluene	~11.0 (5 ppm)[c]	–		
3% CuO/SnO_2	280	EtBz	7.0 (50 ppm)[c]	2000 of BTEX	[48]	
10% mol Si-doped WO_3	400	Acetone	~4.5 (600 ppb)	100	[54]	
WO_3 core-shell microspheres	300	Acetone	~9.0 (10 ppm)[c]	1800	[55]	
Rh-WO_3	400	Acetone	~12.0 (4 ppm)[c]	40	[56]	
ZnO	350	EtOH	0.4	10		This work
		Acetone	0.5	20		
		EtBz	0.3	20		
32:1 ZnO/GO	350	EtOH	7.0	20		
		Acetone	3.0	20		
		EtBz	2.7	100		
	RT (UV)	EtOH	0.4	100		
		Acetone	0.3	100		
		EtBz	0.2	600		
SnO_2	350	EtOH	2.0	2		
		Acetone	1.8	10		
		EtBz	1.5	10		
32:1 SnO_2/GO	350	EtOH	5.1	10		
		Acetone	12.5	5		
		EtBz	7.2	20		
	RT (UV)	EtOH	2.0	100		
		Acetone	0.4	100		
		EtBz	0.8	100		
4:1 SnO_2/GO	350	EtOH	0.1	100		
		Acetone	0.6	100		
		EtBz	0.4	100		

	RT (UV)	EtOH[d]	0.006	1000
		Acetone	-0.1	100
		EtBz	-0.6	100
32:1 $Sn_{0.55}Tn_{0.45}$/GO	350	Toluene	1.5	100
		Acetone	0.5	200
	250 (UV)	Toluene	0.6	200
		Acetone	0.2	200
32:1 TiO_2/GO	350	Toluene	0.9	100
		Acetone	6.0	100
WO_3 (WWS_P123)	300	Acetone	1.7	200
	RT (UV)		-0.4 (2 ppm)	2000
	300	Toluene	0.06 (20 ppm)	2000
WO_3 (WWS_OX)	300	Acetone	0.9	200
WO_3 (WWS_F127)			0.8	200
WO_3 (WWA_P123)			1.1	200
WO_3 (WWA_OX)			1.2	200
WO_3 (WWA_F127)			0.6	200
WO_3 (WF)			2.3	200
Sputtered WO_3 1000 nm thick			1.0	200
Sputtered WO_3 500+500 nm thick			1.2	200

[a] LOD, limit of detection; [b] always referred to 1 ppm, otherwise stated; [c] calculated from data reported in the reference. [d] Ref. [15].

Table 6.3. *Comparison of pure MOS and MOS-graphene based nanomaterials sensing performances, towards different VOCs.*

6.3. Conclusions

Herein, a deep discussion of the most outstanding results has been pursued. Particularly, optoelectronic and electrochemical properties of the 3D MOS-GO nanonetworks were finely investigated to corroborate the effective presence of p(GO)–n(MOS) heterojunction at the nanoscale. As a matter of fact, enhanced photo- and chemical sensing were achieved, resulting in very promising materials for VOCs detection, in terms of sensitivity, selectivity and low temperature operating conditions by exploiting the UV light. Besides, computational studies on pure WO_3 have demonstrated the plausible adsorption of either oxygen or acetone species by n-type semiconductor, thus resulting in a material conductivity change giving some highlights on the sensing mechanism. Parallelly, starting from the mechanism already reported in the literature, the one proposed herein for composite materials is an extension, taking into account the presence of both p-n nano-heterojunctions and the UV light.

References

[1] C. Chen, S. Zhang, B. Hu, H. San, Z. Cheng, W. Hofmann, *Compos. Part B Eng.* **2019**, *164*, 640.

[2] C. Chen, P. Zhou, N. Wang, Y. Ma, H. San, *Nanomaterials* **2018**, *8*, 26.

[3] R. Bo, N. Nasiri, H. Chen, D. Caputo, L. Fu, A. Tricoli, *ACS Appl. Mater. Interfaces* **2017**, *9*, 2606.

[4] H. Chen, R. Bo, A. Shrestha, B. Xin, N. Nasiri, J. Zhou, I. Di Bernardo, A. Dodd, M. Saunders, J. Lipton-Duffin, T. White, T. Tsuzuki, A. Tricoli, *Adv. Opt. Mater.* **2018**, *6*, 1800677.

[5] N. Nasiri, R. Bo, L. Fu, A. Tricoli, *Nanoscale* **2017**, *9*, 2059.

[6] J. R. D. Retamal, C. Y. Chen, D. H. Lien, M. R. S. Huang, C. A. Lin, C. P. Liu, J. H. He, *ACS Photonics* **2014**, *1*, 354.

[7] D. Chen, L. Wei, L. Meng, D. Wang, Y. Chen, Y. Tian, S. Yan, L. Mei, J. Jiao, *Nanoscale Res. Lett.* **2018**, *13*, 92.

[8] G. Lan, J. Nong, W. Jin, R. Zhu, P. Luo, H. Jiang, W. Wei, *Surf. Coatings Technol.* **2019**, *359*, 90.

[9] J. Chao, X. Sun, S. Xing, X. Zhang, S. Gao, Z. Du, *J. Alloys Compd.* **2018**, *753*, 212.

[10] J. Cai, X. Xu, L. Su, W. Yang, H. Chen, Y. Zhang, X. Fang, *Adv. Opt. Mater.* **2018**, *6*, 1800213.

[11] M. K. Singh, R. K. Pandey, R. Prakash, *Org. Electron.* **2017**, *50*, 359.

[12] D. T. Phan, G. S. Chung, *J. Phys. Chem. Solids* **2013**, *74*, 1509.

[13] T.-F. Yeh, J. Cihlář, C.-Y. Chang, C. Cheng, H. Teng, *Mater. Today* **2013**, *16*, 78.

[14] M. Siyar, A. Maqsood, S. B. Khan, *Mater. Sci.* **2014**, *32*, 292.

[15] E. Pargoletti, A. Tricoli, V. Pifferi, S. Orsini, M. Longhi, V. Guglielmi, G. Cerrato, L. Falciola, M. Derudi, G. Cappelletti, *Appl. Surf. Sci.* **2019**.

[16] Compton, Banks, *Understanding voltammetry* **2010**.

[17] C. Ingrosso, G. V. Bianco, V. Pifferi, P. Guffanti, F. Petronella, R. Comparelli, A. Agostiano, M. Striccoli, I. Palchetti, L. Falciola, M. L. Curri, G. Bruno, *J. Mater. Chem. A* **2017**, *5*, 9307.

[18] G. Herzog, V. Beni, *Anal. Chim. Acta* **2013**, *769*, 10.

[19] G. Soliveri, V. Pifferi, G. Panzarasa, S. Ardizzone, G. Cappelletti, D. Meroni, K. Sparnacci, L. Falciola, *Analyst* **2015**, *140*, 1486.

[20] A. O. Simm, S. Ward-Jones, C. E. Banks, R. G. Compton, *Anal. Sci.* **2005**, *21*, 667.

[21] S. Daniele, M. Baldo, C. Bragato, *Curr. Anal. Chem.* **2008**, *4*, 215.

[22] M. Santamaria, G. Conigliaro, F. Di Franco, F. Di Quarto, *Electrochim. Acta* **2014**, *144*,

315.

[23] K. P. Musselman, A. Marin, A. Wisnet, C. Scheu, J. L. MacManus-Driscoll, L. Schmidt-Mende, *Adv. Funct. Mater.* **2011**, *21*, 573.

[24] G. Di Liberto, V. Pifferi, L. Lo Presti, M. Ceotto, L. Falciola, *J. Phys. Chem. Lett.* **2017**, *8*, 5372.

[25] Z. Q. Zheng, J. D. Yao, B. Wang, G. W. Yang, *Sci. Rep.* **2015**, *5*, 1.

[26] H. J. Kim, J. H. Lee, *Sensors Actuators, B Chem.* **2014**, *192*, 607.

[27] H. W. Kim, Y. J. Kwon, A. Mirzaei, S. Y. Kang, M. S. Choi, J. H. Bang, S. S. Kim, *Sensors Actuators, B Chem.* **2017**, *249*, 590.

[28] M. Z. Film, *Sensors* **2017**, *18*, 50.

[29] P. Zhang, G. Pan, B. Zhang, J. Zhen, Y. Sun, *Mater. Res.* **2014**, *17*, 817.

[30] H. Zhang, Y. Cen, Y. Du, S. Ruan, *Sensors (Switzerland)* **2016**, *16*, 1.

[31] A. A. Abokifa, K. Haddad, J. Fortner, C. S. Lo, P. Biswas, *J. Mater. Chem. A* **2018**, *6*, 2053.

[32] S. Liu, B. Yu, H. Zhang, T. Fei, T. Zhang, *Sensors Actuators B Chem.* **2014**, *202*, 272.

[33] K. Zakrzewska, M. Radecka, *Procedia Eng.* **2012**, *47*, 1077.

[34] R. Kalidoss, S. Umapathy, Y. Sivalingam, *Appl. Surf. Sci.* **2018**, *449*, 677.

[35] L. Trotochaud, S. W. Boettcher, *Chem. Mater.* **2011**, *23*, 4920.

[36] S. M. And, V. Thangadurai, *Soil Mech. Found. Eng.* **1978**, *26*, 73.

[37] C. WY, L. DD, S. BK, *Thin Solid Films* **1992**, *221*, 304.

[38] A. Tricoli, M. Righettoni, A. Teleki, *Angew. Chemie Int. Ed.* **2010**, *49*, 7632.

[39] B. Bhangare, N. S. Ramgir, S. Jagtap, A. K. Debnath, K. P. Muthe, C. Terashima, D. K. Aswal, S. W. Gosavi, A. Fujishima, *Appl. Surf. Sci.* **2019**, *487*, 918.

[40] X. Kou, N. Xie, F. Chen, T. Wang, L. Guo, C. Wang, Q. Wang, J. Ma, Y. Sun, H. Zhang, G. Lu, *Sensors Actuators, B Chem.* **2018**, *256*, 861.

[41] Y. Matsushima, R. Toyoda, H. Mori-Ai, A. Kondo, K. Maeda, *J. Ceram. Soc. Japan* **2014**, *122*, 96.

[42] A. Kolmakov, M. Moskovits, *Annu. Rev. Mater. Res.* **2004**, *34*, 151.

[43] A. Gurlo, N. Bârsan, A. Oprea, M. Sahm, T. Sahm, U. Weimar, *Appl. Phys. Lett.* **2004**, *85*, 2280.

[44] K. Hänninen, *Environ. Ecol. Res.* **2018**, *6*, 74.

[45] C. A. Zito, T. M. Perfecto, D. P. Volanti, *Sensors Actuators B Chem.* **2017**, *244*, 466.

[46] M. Arvani, H. Mohammad Aliha, A. A. Khodadadi, Y. Mortazavi, *Sci. Iran.* **2017**, *0*, 0.

[47] L. Xiao, S. Shu, S. Liu, *Sensors Actuators B Chem.* **2015**, *221*, 120.

[48] F. Ren, L. Gao, Y. Yuan, Y. Zhang, A. Alqrni, O. M. Al-Dossary, J. Xu, *Sensors Actuators B Chem.* **2016**, *223*, 914.

[49] Y. Chang, Y. Yao, B. Wang, H. Luo, T. Li, L. Zhi, *J. Mater. Sci. Technol.* **2013**, *29*, 157.

[50] P. Wang, D. Wang, M. Zhang, Y. Zhu, Y. Xu, X. Ma, X. Wang, *Sensors Actuators B Chem.* **2016**, *230*, 477.

[51] Y. Zhou, X. Lin, Y. Wang, G. Liu, X. Zhu, Y. Huang, Y. Guo, C. Gao, M. Zhou, *Sensors Actuators, B Chem.* **2017**, *240*, 870.

[52] C. Zhao, H. Gong, W. Lan, R. Ramachandran, H. Xu, S. Liu, F. Wang, *Sensors Actuators B Chem.* **2018**, *258*, 492.

[53] A. Kumar, L. Rout, L. S. K. Achary, A. Mohanty, R. S. Dhaka, P. Dash, *RSC Adv.* **2016**, *6*, 32074.

[54] M. Righettoni, A. Tricoli, S. E. Pratsinis, *Anal. Chem.* **2010**, *82*, 3581.

[55] M. Esmaeili, G. Kiani, F. S. Nogorani, S. Boroomand, *Int. J. Nano Dimens.* **2016**, *7*, 254.

[56] K.-I. Choi, S.-J. Hwang, Z. Dai, Y. Chan Kang, J.-H. Lee, *RSC Adv.* **2014**, *4*, 53130.

Chapter 7

Conclusions & future perspectives

"All our dreams can come true,
if we have the courage to pursue them"

— Walt Disney

7.1. Conclusions

In this PhD Thesis, novel three-dimensional nanoarchitectures, based on well-integrated GO nanodomains in a metal oxide network, have been proposed and deeply studied as VOCs sensing materials. Specifically, different MOS such as ZnO, SnO_2, TiO_2 and WO_3 have been reported herein, firstly focusing on *i*) sensitivity along with room temperature chemical sensing and, then, on *ii*) gas selectivity trying to discern among smaller/polar analytes (namely, ethanol and acetone) and bigger/non-polar ones (as ethylbenzene and toluene). Thus, the synthetic routes of both pristine and composite materials were tuned in order to prepare nano-networks with enhanced photo- and chemical properties. Particularly, we interestingly observed that the crystallite dimensions, the surface area, the volume and shape of the pores play a key role in determining the final performances. Indeed, focusing on tungsten trioxide study, even if it is still in its infancy, by tailoring the dispersing/structuring agents we succeeded in both smoothly increasing the active surface area and producing the majority of the powders having slit-shaped pores, which could potentially favour the desorption of the in play gaseous species.

Furthermore, in order to reach one of the main Thesis's goal, *i.e.* the lower operating temperatures, the most performing MOS matrixes as ZnO and SnO_2 were selected to be grown onto GO sheets. Specifically, different MOS-GO ratios were investigated and we observed that a high amount of GO hinders the sensor response, especially in the case of zinc oxide, due to the formation of interconnected GO domains which short-cut the chemical sensing of ZnO regions. In contrast, low GO content results in an optimal p-n type nano-heterojunctions architecture with enhanced photodetectivity and chemical sensing properties. These optimal ZnO-based materials achieve a UV light responsivity of about 33 $A \cdot W^{-1}$ and room temperature detection of down to 100 ppb VOC concentrations. Notably, the highest sensitivity and fastest response and recovery times (of around hundreds of second at RT) were obtained with the 32:1 ZnO/GO. Interestingly, the case of tin dioxide matrix is even better. Indeed, alongside with a very high sensitivity (down to 100 ppb at RT), quite fast response/recovery (around

100 s) and UV light responsivity of ca 400 $A \cdot W^{-1}$, a marked selectivity was obtained towards different VOCs. Notably, at RT, 32:1 SnO_2/GO has the strongest response for ethanol, followed by acetone and ethylbenzene. This is probably attributed to the gas molecules chemical structure and their affinity to the SnO_2 surface. Moreover, conversely to what happens with ZnO, in the case of tin dioxide a high amount of GO hinders the ethanol sensing at room temperature and induces an opposite negative response with acetone and, above all, with ethylbenzene, thus resulting in an optimal selectivity towards the latter species. On the basis of some recent literature, we hypothesized that the switching in the selectivity is mainly due to either the moisture interfering presence or, to a major extent, the different oxygen concentration. Indeed, at RT the exploitation of UV light increases the amount of oxygen species adsorbed on the MOS surface, leading to a greater concentration of holes than electrons and, thus, giving rise to a p-type behavior. This phenomenon is quite interesting since it allows to selectively sense a specific analyte, thus representing a powerful tool for the engineering of next-generation sensors.

Always with a view to reaching a quite high selectivity, the well-performing SnO_2 matrix was combined with the TiO_2 one, since their coupling has been reported to enhance the materials affinity to apolar VOC molecules. In this context, the greatest MOS-GO ratio (*i.e.* 32:1) was adopted. Interestingly, at 350 °C, the prepared solid solutions revealed to be more selective to bigger/non-polar molecules (as toluene) and they keep this feature down to 250 °C (by exploiting the light). Unluckily, no good signal was detectable below this temperature.

Hence, a mechanism for the enhanced sensing behavior achieved with the MOS-GO nanocomposite structure was suggested based on the formation of a nanostructured network of p(GO) – n(MOS) junctions. Furthermore, in order to better understand the sensing mechanism by MOS nanoparticles, either an experimental *in situ* XANES study or computational simulations were carried out. Notably, the matching between the experiment and the theory is mandatory to fully elucidate the mechanism for which there is not a unique vision. From both the two approaches, an evidence of the pivotal role of the oxygen species in modifying the system conductivity was obtained since, once adsorbed, it behaves as an electron acceptor. Conversely, acetone molecules (as representative VOC) tend to restore the decreased conductivity by donating electrons to the MOS surface, giving rise to the recorded signals. Our results are very preliminary, therefore a deeper investigation and comprehension, for example by molecular dynamics, are strictly necessary.

7.2. Future perspectives

We believe that the findings, shown so far, can pave the way for the development of composite carbon/metal oxide-based devices, for applications extending from optoelectronics to chemical sensing. Moreover, they can provide guidelines for the engineering of novel chemoresistors with high sensitivity, high selectivity, fast response/recovery times and room temperature operating conditions, likely to be used in point-of-care devices.

Nevertheless, although the present PhD Thesis has spanned different types of MOS, their coupling with graphene oxide in diverse ratios and their application to various volatile organic compounds, from smaller/polar ones to bigger/non-polar analytes, some aspects should be deepened more and more, in order to engineer a final portable device. Firstly, the selectivity aspect is still a weakness, especially when the chemoresistor has to operate in a complex real system where the humidity interference is quite high. Therefore, to improve this feature, preliminary studies were focused on the decoration of the most performing composite materials, such as 32:1 SnO_2/GO, with noble metal nanoparticles (*e.g.* Ag; see Figure 7.1).

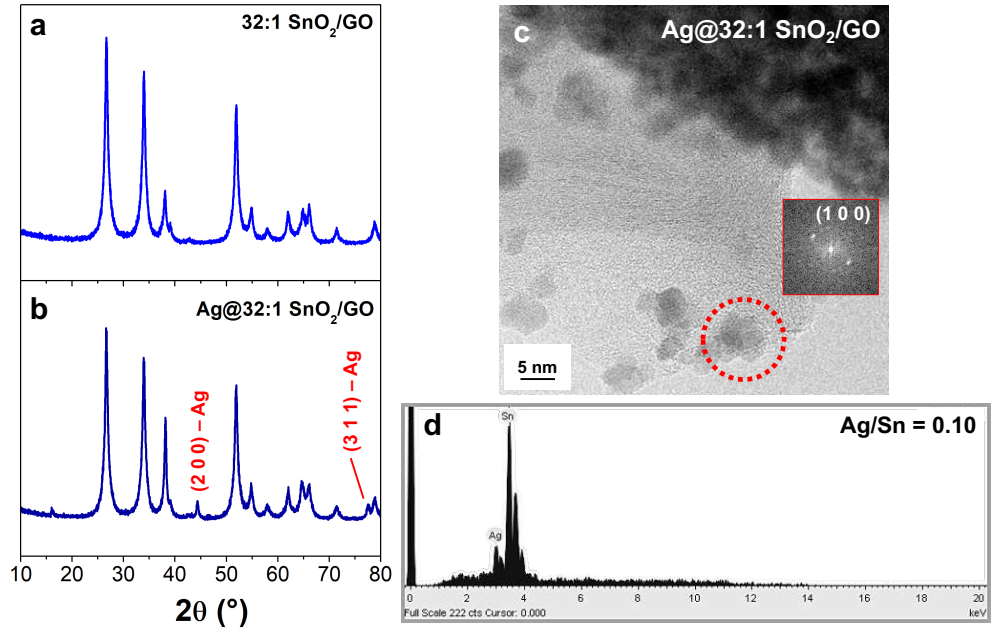

Figure 7.1. *Comparison of X-ray lines relative to (a) 32:1 SnO_2/GO and (b) Ag@32:1 SnO_2/GO, with 10 %wt of metallic silver decorating the SnO_2/GO matrix. (c) Relative TEM image with SAED map, ascribable to silver element since its main diffraction peak (1 0 0) has been observed. (d) Ag@32:1 SnO_2/GO EDX elemental map, from which Ag/Sn atomic ratio of about 0.10 corroborates the effective presence of silver at 10%.*

Indeed, as widely stated in Chapter 2, metal nanoparticles could enhance the selective sensing performances, thanks to their catalytic effect. Concerning the synthetic route, we optimize a procedure in which silver nitrate is reduced by ascorbic acid in presence of sodium citrate, polyvinylpyrrolidone (the last two used as dispersing agents) and our composite MOS-GO material, thus resulting in its decoration by Ag spherical nanoparticles with dimensions of around 5 nm (see TEM image in Figure 7.1c). With respect to the literature data, herein, the novel step is the composites doping with different decoration degrees (in Fig. 7.1, 10 %wt of silver with respect to 32:1 SnO_2/GO matrix). Surely, the as-prepared compounds will be then tested towards different VOCs and the most performing ones will be used in a real complex environment, as the human breath.

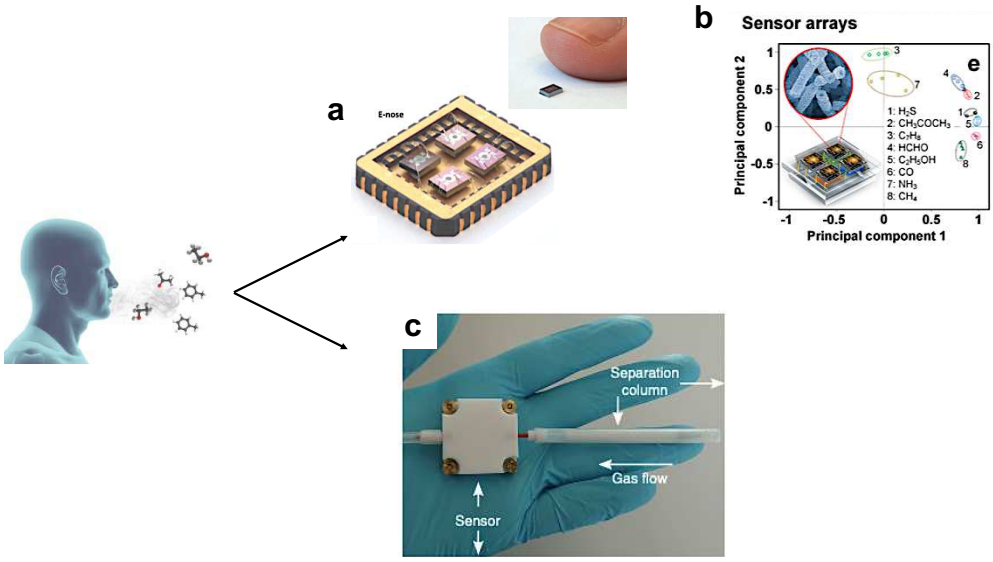

Figure 7.2. *Overview on the nanomaterial-based sensors used to treat a real complex matrix, as the human breath. (a) Sensors array and (b) further signals elaboration by Principal Component Analysis (PCA). Reproduced with permission*[1]*, Copyright 2019, American Chemical Society. (c) Photo of a handheld methanol detector, consisting of a microsensor (in Teflon housing) connected to a separation column (Tenax TA particles in Teflon tube). Reproduced with permission*[2]*, Copyright 2019, Nature Research Journal (open access). Specifically, these two approaches could help in enhancing the VOCs selectivity.*

Specifically, according to the most recent studies[1–3], two main approaches can be adopted to treat a complex system: the first one consists in using an array of sensors, each one composed by a different chemoresistive material, in which the recorded signal is elaborated by the Principal Component Analysis (PCA) technique (Fig. 7.2a,b). The second approach, instead, requires the use of a separation column, usually based on alumina or zeolite compounds, that

entraps the majority of the interfering species as CO_2 or water vapor, thus allowing only the VOCs of interest to reach the chemoresistor (Fig. 7.2c).

Besides, if the final goal is to engineer a point-of-care device, another aspect to touch on concerns the electrodes flexibility. Indeed, in the whole PhD project, glass or alumina rigid substrates were used.

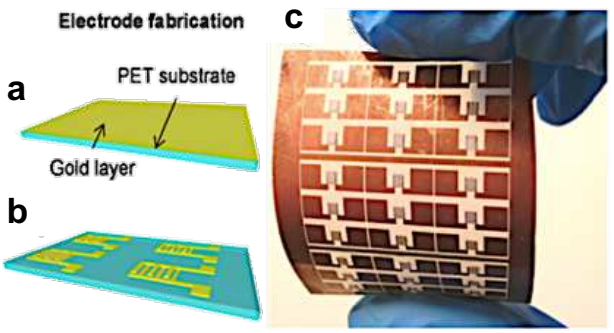

Figure 7.3. *Example of PET-flexible IDE. (a) Deposition of gold layer on PET substrate; (b) laser ablation of the gold layer; (c) picture of 3 × 3 cm sensor matrices fabricated on PET substrate.*

However, recent advancements in the field of printed electronics show increased potential for the substitution of rigid materials by flexible ones (Figure 7.3), since the latter could reduce the cost of sensors and offer good mechanical flexibility. Moreover, as concerns the metallic pattern of IDEs, low-cost printing technologies (such as ink-jet or screen-printing) are forecast to dominate the printed electronics era, since they allow high-volume production. Otherwise, laser technology is gaining interest as another alternative micropatterning technique, due to both its high precision and the possibility to use it in open air without clean room facilities. For flexible IDEs, commercially available polymeric compounds can be used, as polyethylene terephthalate (PET) or Kapton® tape (*i.e* polyimide film developed and sold by DuPont Company). Certainly, depending on the final sensor operating temperature, the most suitable and compatible polymer will be chosen, according to its physico-chemical properties.

Hence, in the near future, all the aspects described in this section will be taken into account and pursued, since they represent the main milestones that follow the PhD research work presented here.

References

[1] A. T. Güntner, S. Abegg, K. Königstein, P. A. Gerber, A. Schmidt-Trucksäss, S. E. Pratsinis, *ACS Sensors* **2019**, *4*, 268.

[2] J. van den Broek, S. Abegg, S. E. Pratsinis, A. T. Güntner, *Nat. Commun.* **2019**, *10*, 4220.

[3] D. Hashoul, H. Haick, *Eur. Respir. Rev.* **2019**, *28*, 190011.

Appendix

A.1. Materials and Methods

A.1.1. Chemicals and syntheses set-up

All the chemicals were of reagent-grade purity and were used without further purification; doubly distilled water passed through a Milli-Q apparatus was utilized. All the reagents used were purchased from Sigma-Aldrich, unless otherwise stated.

Synthesis of graphene oxide Graphene Oxide (GO) was prepared by adopting a modified Hummers method[1,2]. Concentrated H_2SO_4 (ACS reagent 95–98%, 50 mL) was added to graphite (1 g; namely G with particle size < 20 μm; or GF, flake-like one) and $NaNO_3$ (1 g), and the suspension was cooled down to 0 °C in an ice bath. $KMnO_4$ (6 g) was slowly added to keep the reaction temperature below 10 °C. The solution was stirred for 4 h. Then, 100 mL of MilliQ water was introduced dropwise, keeping the suspension in the ice bath due to the highly exothermic reaction. The mixture was stirred for other 2 h at 70–80 °C and, finally, 200 mL of MilliQ water (at 60 °C) followed by 20 mL of H_2O_2 (at 7.5, 15.0 or 30.0 %wt, previously titrated), by Sigma-Aldrich (Sigma1 and Sigma2, *i.e.* two different batches) and Carlo Erba (CE), were slowly added. The brownish slurry was left to decant overnight at room temperature. Then, it was centrifuged several times at 8000 rpm. The remaining solid material was finally washed through a dialysis method by using Spectra/Pore® molecular porous membrane tubing, until the pH became neutral. Further, the precipitate was dried in oven at 60 °C.

As reported in Chapter 3, GO samples were labelled according to the type and concentration of the adopted hydrogen peroxide reagent, as follows: **GO_x_y**, where x is S1, S2 or CE for Sigma1, Sigma2 and Carlo Erba respectively; whereas y stands for the H_2O_2 concentration (7.5, 15.0 or 30.0 %wt). Moreover, the GO prepared by using flake-like graphite was labelled as GOF.

Synthesis of ZnO-GO materials[3] The appropriate amount of $Zn(NO_3)_2$ was dissolved in 3.0 mg mL^{-1} of GO aqueous suspension (GO from 30 %wt H_2O_2, Sigma1) to have starting salt precursor-to-GO weight ratios of 4:1. 8:1, 16:1 and 32:1. The mixture was stirred (at 300 rpm) for 15 min at 50 °C and then 60 mL of a stoichiometric aqueous ammonium hydroxide solution (25% v/v) was slowly added. After the addition, the pH passed from 3 to 10 and the mixture was continuously stirred for other 5 h. The resultant product was centrifuged (at 8000 rpm) several times with MilliQ water, until the pH became neutral. Finally, it was dried in oven at 60 °C. A final calcination step under oxygen flux (6 h, 9 NL h^{-1}) followed to form a whitish

precipitate. Samples were labelled as: **X:Y ZnO/GO**, where X:Y is the zinc salt precursor-to-GO weight ratio.
Concerning the pure ZnO material, the same synthetic route was adopted without the initial addition of the GO suspension.

Synthesis of SnO_2-GO materials For the synthesis of the tin dioxide/GO composite materials, the appropriate amount of $SnCl_4 \times 5H_2O$ was dissolved in 3.0 mg mL^{-1} of an aqueous GO suspension (GO from 30.0 %wt H_2O_2, Sigma1) to have starting salt precursor-to-GO weight ratios equal to 4:1, 8:1, 16:1 and 32:1. The mixture was stirred (at 300 rpm) for 3 h at 50 °C and, then, 30 mL of stoichiometric urea aqueous solution was added dropwise. The mixture was continuously stirred for other 3 h. Subsequently, the resultant product was centrifuged (at 8000 rpm) several times with MilliQ water, until the pH became neutral. Then, it was dried in oven at 60 °C. A final calcination step at 400 °C, under oxygen flux (6 h, 9 NL h^{-1}) followed to form a greyish or whitish precipitate (according to the different coverage degree of the graphene oxide surface). Samples were labelled as: **X:Y SnO_2/GO**, where X:Y is the tin salt precursor-to-GO weight ratio.
For the sake of comparison, pure SnO_2 has been prepared through the same synthetic route.

Synthesis of SnO_2-TiO_2-GO materials For the synthesis of the tin dioxide-titanium dioxide/GO composite materials, the appropriate amount of $SnCl_4 \times 5H_2O$ was dissolved in 3.0 mg mL^{-1} of a 2-propanol-based GO suspension (GO from 30.0 %wt H_2O_2, Sigma1) to have Sn+Ti salt precursors-to-GO weight ratios equal to 32:1. The mixture was stirred (at 300 rpm) for 1.5 h at 50 °C and, then, the suitable amount of $Ti(OCH(CH_3)_2)_4$ (titanium tetraisopropoxide, TTIP) was added to the previous mixture. The system was left under stirring for another 1.5 h. Subsequently, 2 M NaOH was put dropwise into the flask in a stoichiometric amount (considering both tin and titanium salt precursors moles). The mixture was continuously stirred for other 3 h. Then, the resultant product was centrifuged (at 8000 rpm) several times with MilliQ water, until the pH became neutral. Afterwards, it was dried in oven at 60 °C. A final calcination step at 400 °C, under oxygen flux (6 h, 9 NL h^{-1}) followed to form a whitish precipitate. Notably, the chemical composition of the system was varied over a full range from 100 mol% of SnO_2 (namely, **32:1 SnO_2/GO**) to 100 mol% of TiO_2 (namely, **32:1 TiO_2/GO**). These oxide-based composites were labelled as: **32:1 Sn_xTi_{1-x}/GO**, where x represents the Sn/(Sn+Ti) molar ratios (*i.e.* 0.21, 0.35, 0.44, 0.55 and 0.71).
For the sake of comparison, pure TiO_2 was prepared through the same synthetic route.

Synthesis of WO_3 materials Pristine tungsten trioxide was synthesized following different preparation routes (such as hydrothermal, sol-gel, flame spray pyrolysis and sputtering ones), aiming at increasing the active surface area and porosity of the powders.

i. *Hydrothermal route*: the appropriate amount of $Na_2WO_4 \times 2H_2O$ was dissolved in 50 mL of MilliQ water to have a final concentration of 0.2 M. Afterwards, 10 mL of HCl (37%) were added dropwise to the previous solution, under continuous stirring, resulting in the formation of a yellowish precipitate. Then, the suspension was kept at 200 rpm and at 30 °C for 3 h. Subsequently, around 0.90 g of oxalic acid ($H_2C_2O_4$, stoichiometric with the tungsten precursor) were added into the reaction system, maintaining the system stirred for other 10 min. The product was washed several times with MilliQ water till the complete neutrality and, then, with ethanol solvent. The precipitate was dried in oven at 60 °C. A final calcination step at 400 °C, under oxygen flux (5 h, 9 NL h^{-1}), was performed.

   In order to improve the surface area of the aforementioned powder, the same synthetic route was adopted, with the substitution of the structure-directing agent (*i.e.* oxalic acid)[4] with two different tensides: Pluronic® F127 and Pluronic® P123 (both by BASF Corporation). The former is a non-ionic surfactant ($HO(C_2H_4O)_a(C_3H_6O)_b(C_2H_4O)_aH$, where *a* is 101 and *b* is 56) with an average molecular weight of 12.6 kDa[5]. It forms spherical micelles, having a diameter of 25 nm, at concentrations higher than 950-1000 ppm (25 °C, critical micelle concentration (CMC))[5] and, from thermogravimetric analysis, it completely burns out at 400 °C[5]. Instead, the second surfactant is composed by PEG-PPG-PEG (*i.e.* $HO(CH_2CH_2O)_a(CH_2CH(CH_3)O)_b(CH_2CH_2O)_aH$, where *a* is 20 and *b* is 70) chains[6–8]. It has an average molecular weight of about 5800 Da, a decomposition temperature in the range 400-500°C, and CMC value of about 1-2 ppm (at 25 °C)[6–8]. These tensides were used by adopting a constant surfactant-to-tungsten precursor molar ratio of 0.006, *i.e.* much higher than the corresponding CMCs[8], thus resulting in micelles configuration during the reaction process. In a typical procedure, they are added in the reaction flask, containing 50 mL of MilliQ water, before $Na_2WO_4 \times 2H_2O$. Then, the synthetic route is analogous to the above-mentioned one (reported for oxalic acid). In this case, the washing step followed the drying process, since a more gelatinous-like precipitate was formed, due to the tenside presence. These samples, deriving from the tungsten salt precursor, were labelled as: **WWS_Z**, where the first W stands for tungsten trioxide, the second W for wet synthetic route, S for the adopted salt (*i.e.*

$Na_2WO_4 \times 2H_2O$), and Z can be OX (oxalic acid), F127 (Pluronic® F127) or P123 (Pluronic® P123), depending on the used templating agent.

ii. *Sol-gel route*: in a typical synthesis, oxalic acid, Pluronic® F127 or Pluronic® P123 (2.0 g) were dispersed in a mixture of ethanol (25 mL) and MilliQ water (20 mL). Under vigorous stirring (at 80 °C), ca. 5.0 g of H_2WO_4 (templating agent/tungsten precursor weight ratio equal to 0.4) were added into the previous ethanol/aqueous solution. The system was kept under stirring at 200 rpm for 3 h. The resultant sol solution was dried in oven at 60 °C, then calcined at 400 °C under oxygen flux (5 h, 9 NL h^{-1}) to remove the organic compounds. Finally, the powder was washed several times with ethanol and MilliQ water to eliminate the residual block copolymers. Afterwards, the as-synthesized powder was dried in oven at 60 °C. Also, in the present case, samples were labelled as: **WWA_Z**, where the first W stands for tungsten trioxide, the second one for wet synthetic route, A for acid (H_2WO_4) and Z can be OX (oxalic acid), F127 (Pluronic® F127) and P123 (Pluronic® P123).

iii. *Flame Spray Pyrolysis (FSP)*: a flame spray pyrolysis setup (shown in Figure A.1) was used for the synthesis and direct deposition of the WO_3 nanopowder.

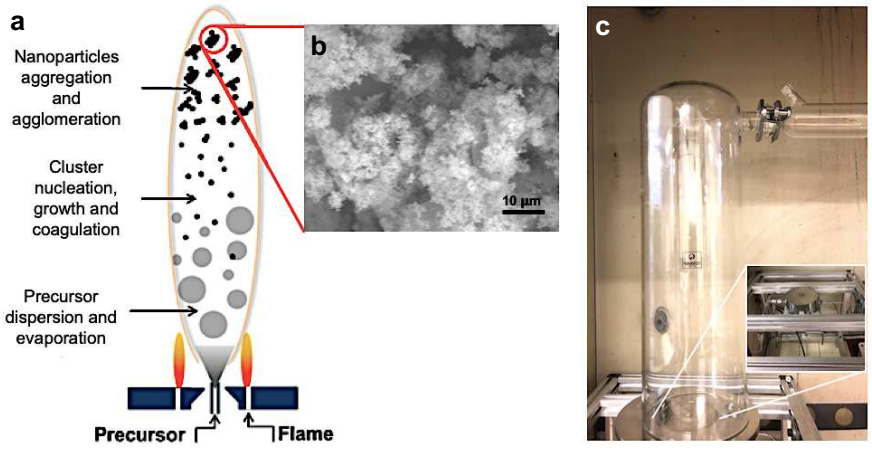

Figure A.1. *(a) Schematic representation of the one-step rapid nanofabrication of highly porous WO_3 nanopowder, by scalable flame spray synthesis; b) top view SEM image the as-synthesized powder; c) flame spray pyrolysis system used in this work.*

A glass cup was used for powders preparation and cleaned with multiple ethanol/drying cycles before aerosol deposition. A tungsten salt precursor, *i.e.* ammonium metatungstate hydrate (purity 99.99%), was dissolved in reagent-grade

dimethylformamide to produce a 0.2 M solution. This precursor solution worked as a seed for the FPS, and the clean glass substrate was placed at a Height Above Burner (HAB) of about 50 cm. The precursor solution was supplied at a constant rate of 4 mL min^{-1} through a syringe pump and dispersed into a fine spray with 5 L min^{-1} oxygen at a constant pressure drop of 3 atm. The spray was ignited by supporting premixed hydrogen/oxygen flames (H_2 = 1 L min^{-1}, O_2 = 2 L min^{-1}). Sample was labelled as **WF**, accordingly.

iv. *Magnetron sputtering*: for sputtered films, the metal oxide coating was directly deposited on the interdigitated electrodes.

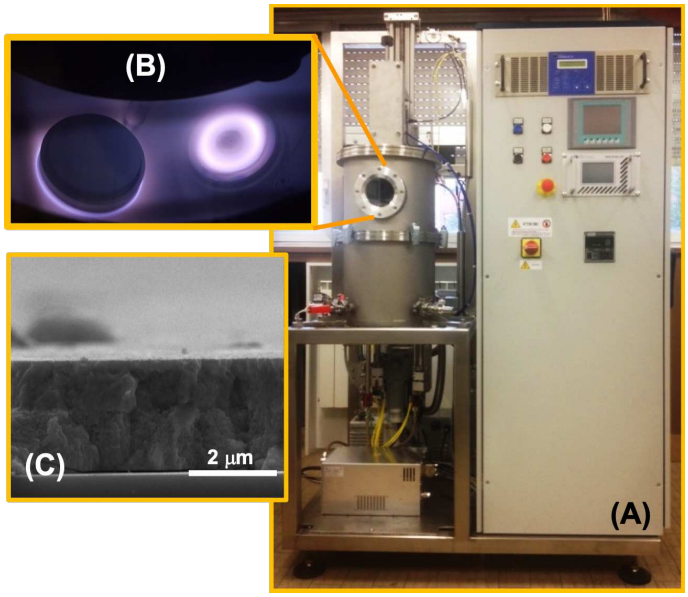

Figure A.2. *(A) Reactive magnetron sputtering system available at the SmartMatLab centre at UNIMI and used for the preparation of WO_3-covered IDE; (B) the two sputtering sources inside the vacuum chamber; (c) a WO_3 coating deposited on a silicon wafer by reactive DC-Magnetron sputtering, showing the film thickness (around 2.2 μm).*

As displayed in Figure A.2A, the sputtering system, used herein, is equipped with two cathodes (Fig. A.2B) that can be powered by both Radio Frequency (RF) and/or pulsed Direct Current (p-DC) sources. The sputter can operate in reactive mode, *i.e.* the vacuum chamber can be fed with argon gas mixed with O_2, N_2, CH_4, *etc.* during the deposition process. This sputter set-up is, also, equipped with a microbalance that allows to control the deposition rate and the final film thickness (example in Fig.

A.2C), and with a rotating and heating sample holder that increase the coating homogeneity and crystallinity.

In the present PhD project, metallic tungsten target was adopted and both pulsed reactive DC- and RF-sputtering technique were adopted. Table A.1 reports all the experimental variables adopted for the deposition of 1000 nm WO_3 film (sample labelled as **WS_1000**).

Pulsed Reactive DC-Magnetron Sputtering experimental set-up	
Samples height (cm)	10
p_{O2} (Pa)	0.4
p_{Ar} (Pa)	1.6
$p_{tot.}$ (Pa)	2.0
Power (W)	100
Frequency (kHz)	100
Sample holder rotation rate (rpm)	5
$T_{sample\ holder}$ (°C)	240
Off time (μs)	5

Table A.1. *Experimental conditions adopted for the deposition of a 1000 nm WO_3 monolayer.*

Besides, in order to either improve the film porosity or the efficiency of the photoactive materials, a multiple-layer strategy can be adopted, as already stated by Chiarello *et al*.[9]. In this case, RF-sputtering set-up was used as reported in Table A.2.

RF-Magnetron Sputtering experimental set-up	
Samples height (cm)	10
p_{O2} (Pa)	0.4
$p_{tot.\ I\ layer}$ (Pa)	1.5
$p_{tot.\ II\ layer}$ (Pa)	3.0
Power (W)	150
Sample holder rotation rate (rpm)	5
$T_{sample\ holder}$ (°C)	240
Off time (μs)	5

Table A.2. *Experimental conditions adopted for the deposition of 500+500 nm WO_3 bilayer.*

This sample was labelled as **WS_500+500**.

A.1.2. Thin films deposition and thickness evaluation

The hot-spray method (Figure A.3) was adopted for the deposition of the powders (except the WO_3 by sputtering) onto InterDigitated Electrodes (IDEs), thanks to the achievement of very highly porous layers (> 90%; see the following and Chapters 4, 5) by means of this technique.

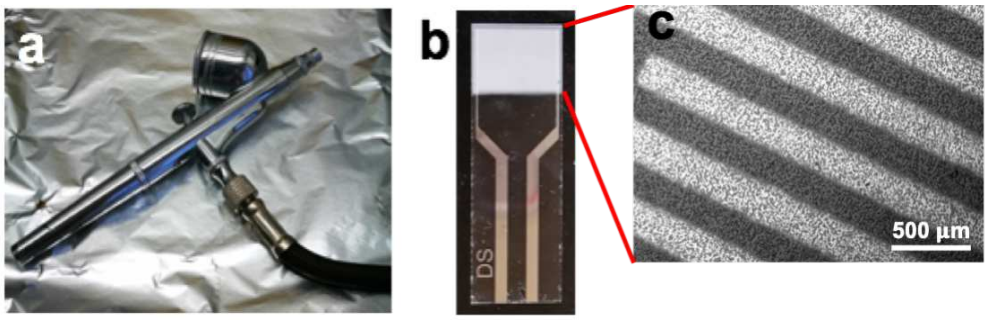

Figure A.3. *(a) Air-brush used to deposit the as-prepared composite materials; (b) glass substrate Pt-IDE with a representative hybrid material (whitish part is the one deposited by spraying technique); (c) SEM image showing the IDE Pt lines homogeneously covered by powder nanoparticles.*

ZnO-GO and SnO_2-GO powders were deposited on glass substrates topped with interdigitated Pt electrodes (IDEs) by hot-spray method (work performed at the Australian National University, ANU). The IDEs were made of glass on which interdigitated Pt lines with 5 µm in width and space have been deposited (G-IDEAU5, DropSens, Oviedo, Spain)[10]. Conversely, SnO_2-TiO_2-GO and WO_3 compounds were deposited on ceramic substrates topped with Au electrodes (work carried out at UNIMI). These IDEs were made of alumina on which interdigitated Au lines with 200 µm in width and space have been deposited (DropSens, Oviedo, Spain). To remove any contamination from the electrodes, all substrates were sintered at 300 °C for 12 h and washed by several washing (ethanol)/drying cycles before deposition. Then, 4.0 mL of 2.5 mg mL^{-1} ethanol powders suspensions were sprayed by keeping constant the air-brush pressure (0.8 bar), the temperature of the heating plate (230-250 °C) and the deposition height (around 8 cm). A final calcination step at 350 °C for 1 h was performed to guarantee a good powders film adhesion on IDEs.

As regards the film thickness evaluation, cross-sectional SEM images (see Figure A.4, as a representative case) were taken by means of Zeiss Ultraplus (a filed-emission scanning electron microscopy, FESEM; at the Centre of Advanced Microscopy (CAM), ANU) at 3 kV; and of SEM Hitachi TM-1000 microscope at UNIMI). For all the synthesized powders, the obtained thickness was in the range between 2 and 5 µm.

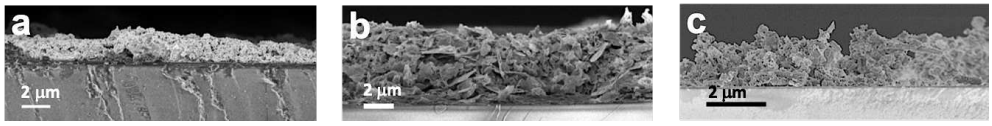

Figure A.4. *Representative cross-sectional images of (a) pure ZnO, (b) 4:1 ZnO/GO and (c) 32:1 ZnO/GO films, deposited on IDEs. All the as-obtained films have a thickness in the range 2–5 μm.*

The porosity of nanoparticle networks of the prepared films was estimated from the optical density and SEM visible thickness as suggested by Bo *et al.*[10], by adopting the absorption coefficients relative to ZnO (2.24×10^7 m^{-1} at 370 nm)[11], SnO_2 (3.08×10^7 m^{-1} at 312 nm)[12] or WO_3 (2.80×10^6 m^{-1} at 380 nm)[13], accordingly.

A.1.3. Instrumentations

The *BET surface area* values, determined by a multipoint BET method, were acquired by Tristar II, Micromeritics. Before each analysis, samples were pretreated at 150 °C for 4 h under a nitrogen flux. Desorption isotherms were used to determine the total pore volume using the Barrett-Joyner-Halenda (BJH) method.

For pure GO, ZnO-GO and SnO_2-GO, *X-Ray Powder Diffraction* (XRPD) analyses were performed on a Philips PW 3710 Bragg-Brentano goniometer equipped with a scintillation counter, 1° divergence slit, 0.2 mm receiving slit and 0.04° soller slit systems. We employed graphite-monochromated Cu Kα radiation (Cu $K\alpha_1$ λ = 1.54056 Å, $K\alpha_2$ λ = 1.54433 Å) at 40 kV × 40 mA nominal x-rays power. Diffraction patterns were collected between 5° and 80° with a step size of 0.02° and a total counting time of about 1 h. A microcrystalline Si-powdered sample was used as a reference to correct for instrumental line broadening effects. Instead, in the case of SnO_2-TiO_2-GO and WO_3 samples, a high-resolution Panalytical X'pert Pro, equipped with a Bragg-Brentano goniometer was used. A graphite-monochromated Cu Kα radiation (Cu $K\alpha_1$ λ = 1.54056 Å, $K\alpha_2$ λ = 1.54433 Å) was employed, and diffraction patterns were collected between 5 and 75° with a step size of 0.033° and a total counting time of about 10 min. The Rietveld method implemented in the Quanto program was applied throughout to provide quantitative estimates of the crystallite domain size, by means of the Debye-Scherrer equation. Experimental profiles were modeled with pseudo-Voigt functions, using Chebyshev interpolation for the background determination.

ATR-FTIR analyses were recorded by Nicolet 380 Spectrophotometer-Thermo Electron Corporation, between 4000 – 400 cm^{-1}, with a total scan of 64.

For pure GO, ZnO-GO and SnO_2-GO samples, *Raman spectra* were taken on a Renishaw InVia micro-Raman Spectrometer. A 50 mW, 532 nm diode laser was used for excitation. The

spectrometer was equipped with a Nikon 50× objective lens (WD = 17 mm, NA = 0.45), which produced a focal spot of 1 μm^2 and a total power of 0.71 mW from the objective. All spectra were processed to remove cosmic rays using the inbuilt software package Wire 4.2. Raman spectra of graphite and graphene oxide samples have been deconvoluted in eight and five modes, respectively, by using the Lorentzian function and the intensity ratios between D and G bands have been calculated according to Atchudan *et al.*[14]. Conversely, for SnO_2-TiO_2-GO solid solutions, Raman spectra were recorded on a Bruker Vertex 70 spectrometer, equipped with the RAM II accessory and a Ge detector, by exciting with a Nd:YAG laser (1064 nm), having a resolution of 4 cm^{-1}.

To evaluate powders optical band gaps by Kubelka-Munk elaboration, *Diffuse Reflectance Spectra* (DRS) were measured on a UV/Vis spectrophotometer Shimadzu UV-2600 equipped with an integrating sphere; a "total white" $BaSO_4$ was used as reference.

The morphology and elemental composition were investigated by using: (a) Zeiss Ultraplus (*field-emission scanning electron microscopy*, FESEM) at 3 kV coupled with an *Energy Dispersive X-ray spectrophotometer* (EDX) for the elemental analysis; (b) SEM Hitachi TM-1000 microscope, coupled with Hitachi ED3000 spectrophotometer for the EDX analyses.

Transmission Electron Microscopy (TEM) analyses were performed on: (a) Hitachi H7100FA at 100 kV; and (b) Jeol TEM 3010 instrument equipped with LaB_6 filament (operating at 300 kV). The TEM grids were prepared dropping the dispersed suspension of nanoparticles in ethanol onto a holey-carbon supported copper grid and drying it in air at room temperature overnight.

Thermogravimetric analyses (TGA) were carried out by means of Metter Toledo Star and System TGA/DSC 3+ under air atmosphere (5 °C min^{-1} from 30 to 800°C; available at the SmartMatLab centre at UNIMI).

For pure GO, ZnO-GO and SnO_2-GO materials, *X-ray Photoemission Spectroscopy* (XPS) data were collected in a Thermofisher Kratos Axis Supra photoelectron spectrometer at the Central Analytical Research Facility of the Queensland University of Technology (Brisbane, Australia). The apparatus is equipped with a monochromated Al k_α source (1486.7 eV), and the spectra were calibrated with respect to their Fermi level. Survey spectra were acquired at pass energy 160, high resolution spectra at pass energy 20. On the other hand, for SnO_2-TiO_2-GO samples, X-Ray Photoelectron Spectroscopy (XPS) were obtained using a Mprobe apparatus (Surface Science Instruments). The source was the monochromatic Al K_α radiation (1486.6eV); a spot size of 200 × 750 mm and a pass energy of 25 eV were used. The 1s level of hydrocarbon-contaminant carbon was taken as the internal reference at 284.6 eV. The accuracy of the

reported binding energies (B.E.) can be estimated to be around 0.2 eV and the resolution is equal to 0.74 eV.

The evaluation of the acidic groups present on the graphene oxide surface was obtained by *potentiometric titration*[15]. Particularly, 300 mg of GO were suspended into 25 cm^3 of 0.1 M NaOH and let it stabilize for 24 hours. The suspension was then centrifuged to remove as much solid as possible. The obtained browinish solution was diluted 1:10 with MilliQ water. Subsequently, the suitable amount of KCl was added to 25 cm^3 of the previous solution in order to have a concentration of 0.1 M, and it was titrated by 0.01 M HCl.

Cyclic Voltammetry (CV) analyses were carried out on Glassy Carbon (GC) working electrode, modified by drop casting (20 µL) of 0.5 mg mL^{-1} dimethylformamide powders suspensions. The electrochemical measurements were performed in a conventional three-electrode cell using a platinum foil as the counter electrode and a Saturated Calomel Electrode (SCE) as the reference one (E = 0.244 V vs SHE). A phosphate buffered saline solution (PBS) 0.1 M, at fixed pH 7.4, was utilized as the supporting electrolyte. Tests have been performed by adding $[Ru(NH_3)_6]Cl_3$ probe to have a final concentration in PBS equal to 3 mM (otherwise stated). The choice of hexaaminеruthenium(III) chloride was due to its widely reported surface insensitivity, *i.e.* no chemical interaction or catalytic mechanism (adsorption step) with the electrode surface[16,17]. Indeed, the so-called outer-sphere redox mediators are not influenced by both the surface oxygen/carbon ratio and the presence of surface impurities or adsorbates. In this case the electrode merely serves as a source of electrons and, as such, outer-sphere systems are sensitive primarily to the electronic structure the electrode material[16,17]. The CVs were recorded at room temperature by using an Autolab PGStat30 (Ecochemie, The Netherlands) potentiostat/galvanostat controlled by NOVA 2.0 software for data acquisition. Usually, a step potential of 0.005 V and a scan rate of 0.1 V s^{-1} were adopted (otherwise stated). For the materials capacitance determination, CVs were recorded by varying the scan rates (from 10 to 750 mV s^{-1}) and the intensity of the current, at a fixed potential in the capacitive region (potential at which no reaction occurs), were plotted against the scan rate. The capacitance was calculated according to the Ohm's law:

(A.1.3.a) $$\frac{dq}{dt} = C\frac{dV}{dt}$$

where $\frac{dV}{dt}$ is the scan rate and $\frac{dq}{dt}$ is the intensity of the current, calculated as $\frac{i_a - i_c}{2}$ (i_a and i_c are the anodic and cathodic current, respectively). Conversely, in order to investigate the interfacial electron transfer properties of the synthesized materials, a positively charged probe (*i.e.* hexamine ruthenium (III) chloride, $[Ru(NH_3)_6]Cl_3$; 3 mM) was adopted. Also herein, CVs

were recorded at different scan rates (between 10 and 750 mV s^{-1}) and, subsequently, elaborated according to the Randles-Sevčík equation:

(A.1.3.b) $$i_{peak} = 2.69 \cdot 10^5 \cdot n^{1.5} \cdot cA \cdot D^{0.5} \cdot v^{0.5}$$

where n stands for the electron exchanged during the reaction (usually 1), c (mol cm^{-3}) is the probe bulk concentration (3 mM in the present case), A (cm^2) stands for electrode area, D (cm^2 s^{-1}) for diffusion coefficient and v (V s^{-1}) for the scan rate. Herein, only the current of the cathodic peak (i_c) was considered.

Electrochemical Impedance Spectroscopy (EIS) experiments were carried out at -0.15 V (*i.e.* the potential at which the $[Ru(NH_3)_6]Cl_3$ probe is oxidized), with a range of frequencies between 65,000 and 0.1 Hz and an amplitude of 10 mV, using an Autolab PGSTAT30 (Ecochemie, The Netherlands) potentiostat/galvanostat equipped with an FRA module and controlled by GPES and FRA softwares. Impedance data were then processed with Z-View 3.1 software.

A.1.4. Gas sensing measurements

For gas sensing of ethanol, acetone and ethylbenzene with ZnO-GO and SnO_2-GO materials (work performed at ANU, Figures A.5a,b), O_2 (BOC Ltd) and N_2 (BOC Ltd) were controlled by mass flow controller (Bronkhorst), with a total gas flow rate of 0.5 L min^{-1}. The target gases (10 ppm in N_2, Coregas) were diluted to 1 ppm and lower concentrations by using the simulated air (0.1 L min^{-1} O_2 + 0.4 L min^{-1} N_2, BOC Ltd) before purging into the chamber, keeping constant the total flow rate of 0.5 L min^{-1}. The temperature of the hotplate in the gas sensing chamber (Linkam) was controlled by a temperature controller and, when UV light was exploited, the samples were illuminated through a quartz window by a solar simulator (NewSpec, LCS-100; effective power density of 2–20 μW cm^{-2} in the range 290–370 nm) with an FGUV5-UV – Ø25 mm UG5 Colored Glass Filter (AR Coated: 290–370 nm, Thorlabs Inc). Indeed, the operating temperature was varied between 25 and 350 °C (exploiting the UV irradiations for T lower than 350 °C). For the gas sensing measurements, two gold probes were separately placed on top of the powders covered IDEs, and the dynamic response was recorded by an electrochemical workstation (CHI 660E, USA) by applying a bias of +1.0 V.

An analogous sensing set-up was adopted for the sensing of acetone and toluene with the other materials (work carried out at UNIMI, Figure A.5c). Also, in this case, a total gas flow rate of 0.5 L min^{-1} was adopted. The target gases (500 ppm in N_2, Coregas) were diluted to 1 ppm and lower concentrations by using the simulated air (0.1 L min^{-1} O_2 + 0.4 L min^{-1} N_2, BOC Ltd) before purging into the chamber, keeping constant the total flow rate of 0.5 L min^{-1}. The current/resistance variation was recorded by using an Autolab PGStat30 (Ecochemie, The

Netherlands) potentiostat/galvanostat controlled by NOVA 2.0 software. The light used herein is a Jesosil HG 500 W UV irradiation source (λ = 280–370 nm, effective power density of 57.5 mW cm^{-2}).

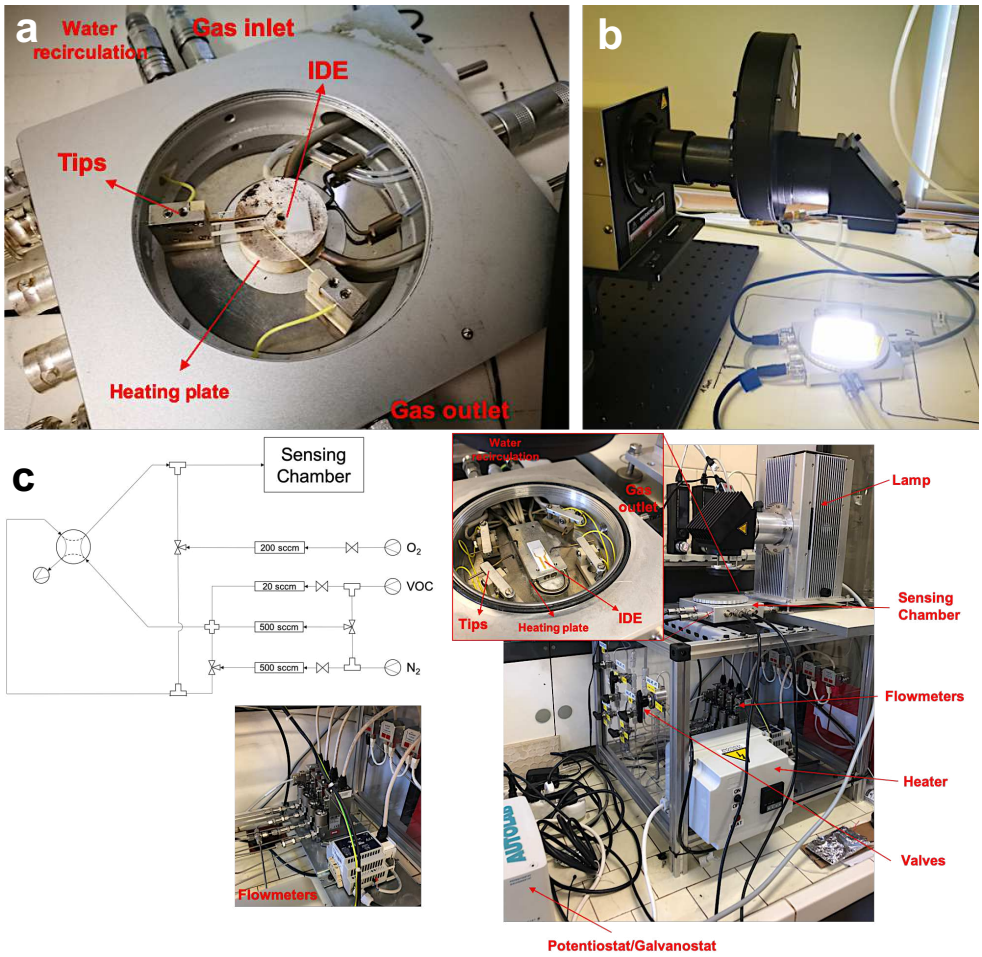

Figure A.5. *(a,b) Sensing chamber and light-assisted measurements set-up used during the abroad period at ANU; (c) sensing set-up alongside with a corresponding schematic representation (inset: magnification of the inside part of the sensing chamber).*

The sensor response is reported as: (R_{air} / $R_{analyte}$) – 1, where R_{air} is the film resistance in air and $R_{analyte}$ is the film resistance at a given concentration of the target gas[18]. The sensor response time is the time needed to reach the 90% of the sensor response, while the recovery time is the time necessary to recover the 90% of the response[19]. The sensing tests were

repeated ten times to verify the stability of the as-prepared sensors. In all cases, no performance loss was observed.

As concern the powders photodetector properties, photo- and dark-currents were measured at 25 °C with an LCS-100 Series Small Area Solar Simulator (Newport Co.). The electrode active surfaces were equal to 0.4 cm^{-2} and the irradiation power for ZnO was 19.2 $\mu W \cdot cm^{-2}$ (at 370 nm, *i.e.* the ZnO maximum absorption peak of the UV/Vis spectrum) and for SnO_2 was 1.5 $\mu W\ cm^{-2}$ (at 312 nm). The responsivity and detectivity were, then, calculated according to the equations reported elsewhere[10].

A.1.5. *In situ* tests at the European Synchrotron Radiation Facility

For data collection at the ESRF synchrotron facilities in Grenoble, acetone sensing with WO_3 powder (namely WWS_OX) was deeply investigated *in situ* by depositing it, through the aforementioned hot-spraying method, onto Pt-IDEs reported in Figure A.6.

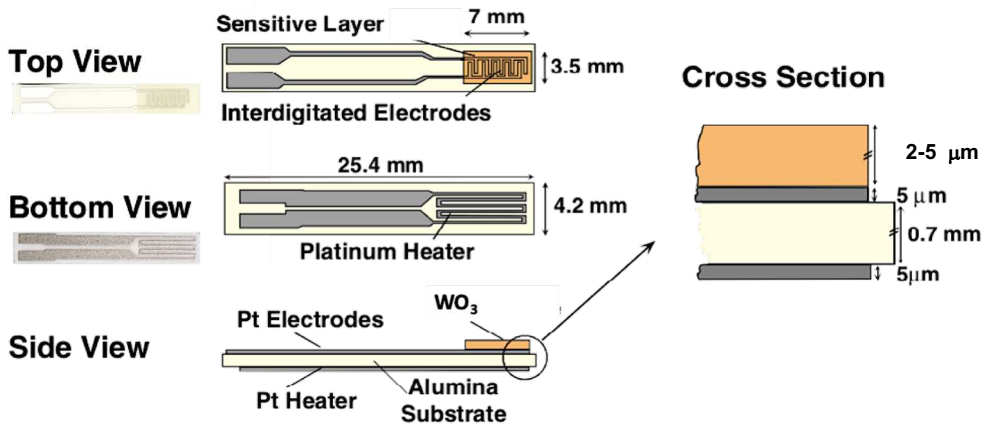

Figure A.6. *Layout of the planar alumina substrate with Pt electrodes (top view) and Pt heater (bottom view), used at ESFR. The WO_3 layer was air-brushed on top of the interdigitated electrodes (side view). The heater on the back keeps the sensor at a constant temperature. Adapted with permission*[20]*, Copyright 2003, IOP Publishing Ltd (open access).*

The adopted Pt-IDEs were the same already reported in Barsan *et al.*[20] work: the platinum electrodes were fabricated by screen-printing (EKRA Microtronic II screen-printer) the paste onto CeramTec Rubalit® 708S Alumina (96%) substrate. The sensing set-up, instead, can be clearly resumed in the schematic representation of Figure A.7. Also in this case, the sensing chamber was equipped with a quartz window to assure the x-rays could reach the sample.

The main challenge in spectroscopic analyses is the discernment of the signal variation originated by the materials surface, involved in the adsorption/desorption mechanisms, and the bulk. The exploitation of high energy x-rays, like in the X-ray Absorption Spectroscopy (XAS), is characterized by large penetration depth of such radiations, giving information of the local coordination and the oxidation states. Nevertheless, changes in the materials surface do not lead to observable modifications in the XAS spectra. Hence, to improve the sensitivity of this technique, the combination of the time-resolved XAS analyses with Modulated Excitation Spectroscopy (MES) has proved to be a valuable tool. A phase Sensitive Detection (PSD) function is then exploited by MES to gain better signal-to-noise ratio and to hide all those parts of the spectra unaffected by the periodic stimulation, *e.g.* the bulk of nanoparticles.

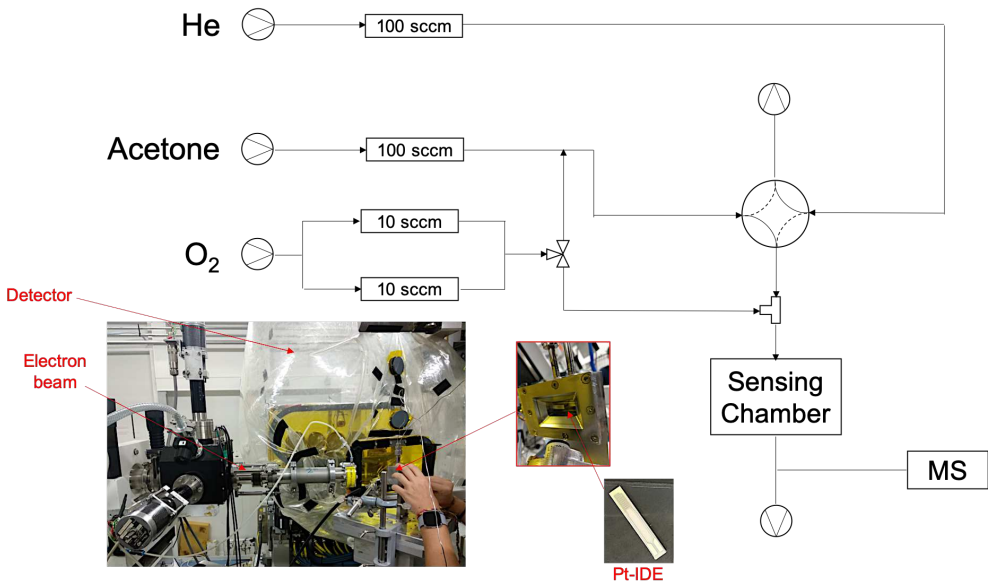

Figure A.7. *Schematic representation of the sensing set-up used at the ESFR, alongside with photos of the ID26 line used and the chamber with the Pt-IDE. In order to analyze the reaction products, a mass spectrometry apparatus was also linked after the sensing chamber.*

Specifically, in a MES experiment, the system is subject to an external stimulus in a time window ($T/2$). Then, the stimulus is removed for another time window ($T/2$), concluding a cycle of period T. During this period, N spectra are recorded, each one requiring an acquisition time τ, with $N\tau = T$. Thus, M cycles were performed in total. Assuming that acetone adsorption-desorption is a completely reversible process, each spectrum in a given cycle can be averaged with the corresponding one in the other cycles, significantly reducing the signal noise. Hence, N new spectra are obtained, each one being the average of the M raw spectra. Moreover, given the acquisition time τ and the total number of spectra N in each cycle, a series of instants

$t_i = n_i \cdot \tau$ (with n_i = 0, 1, 2, …, N) can be determined. Therefore, for each energy value E, the corresponding intensity value in the averaged spectra can be monitored at each instant t_i, constructing the associated time-resolved spectrum $I(t; E)$. For instance, if 1000 points are sampled in the spectra, 1000 time-resolved spectra will be obtained. Subsequently, each time-resolved spectrum gets transposed into a phase-resolved spectrum, by applying a transform called PSD (Phase Sensitive Detection, see Eq. A.1.5.a).

(A.1.5.a) $$\tilde{I}(\varphi^{PSD}; E) = \frac{2\pi}{T}\int_0^T I(t; E)\, sin\left(\omega t + \varphi^{PSD}\right)dt$$

where φ^{PSD} is the phase angle and $\omega = (2\pi/T)$ is the frequency associated to the experimental cycle. This step represents the core of the MES approach. The $\tilde{I}(E; \varphi^{PSD})$ graphs represent the so-called "demodulated spectra" and they are mathematically the equivalent of difference spectra, showing an amplification of all the contributions to the intensity that undergo variations during the external stimulation. As such, all the constant contributions are then cancelled. Furthermore, among all the available φ^{PSD} values, one produces the $\tilde{I}(E; \varphi^{PSD})$ graph with the maximum amplitude; whereas, all the others are simply multiplied by an attenuation factor[21].

Now, the experimental data may differ significantly from an ideal case. Indeed, the demodulated spectra are exact difference spectra only if the time-resolved spectra are perfect square waves. Otherwise, in any portion of the spectra in which $I(t; E)$ is not constant, $\tilde{I}(\varphi^{PSD}; E)$ also depends on time t and its interpretation becomes difficult. However, if the system reaches stationary conditions in a fast-enough time, compared to the duration of a whole cycle (*i.e.* it shows a fast response), these contributions are small and the time-resolved spectra can be approximated to square waves. Therefore, the demodulated spectra can be considered to be the difference between the spectra of the system before and after the stimulation. Hence, the main advantage of this technique is the applicability to *in situ* experiments, while traditional difference approaches ($\Delta\mu$−spectroscopies) require static measurements and a reference system.

In this work, XANES measurements were performed on WWS_OX-IDE in two different situations: *i*) acetone sensing (2000 ppm, to guarantee a quite high concentration of acetone in the sensing chamber) in the presence of only helium (as inert gas); *ii*) acetone sensing in the presence of helium and oxygen gases, as carrier species. In both cases, when acetone was not purged into the chamber, helium and oxygen fluxes were always used. All the tests were carried out at 300 °C, without light. Thus, by adopting these configurations, the possible effect of oxygen on the sensing mechanism may be observed. Moreover, concerning the experimental acquisition of XANES spectra, the L_3-edge (10.2 keV, *i.e.* excitation of $2p_{3/2}$ core

electrons) of tungsten was chosen due to the features of the beamline adopted (ID26). For every experiment, 24 cycles were recorded, each one consisting in N = 30 spectra (15 with acetone and 15 without the analyte molecules) acquired in τ = 10 s. Thus, a complete cycle lasted T = 300 s. Since the IDE and the sensing cell did block the transmitted rays, spectra were acquired in reflectance mode. During the XANES acquisition, the current variation in the system was monitored by means of an Autolab PGStat30 (Ecochemie, The Netherlands) potentiostat/galvanostat, controlled by NOVA 2.0 software. At the same time, as displayed in the schematic representation of Figure A.7, a mass spectrometry apparatus (MS, by Hiden Analytical) was utilized to continuously monitor either the gases purged into the camber or the species possibly produced by the sensing phenomenon.

As concern the obtained XANES signals, a complex elaboration was performed according to Chiarello *et al.* works[21,22], as schematically reported in Figure A.8. Indeed, our aim was the evaluation of the semiconductor surface modification subsequently to the acetone interaction with the material. Notably, we expect a possible variation of the t_{2g} (peak on the left in XANES spectrum)-e_g (peak on the right) energy gap when the oxygen/analyte molecules are adsorbed and sensed by the tungsten trioxide.

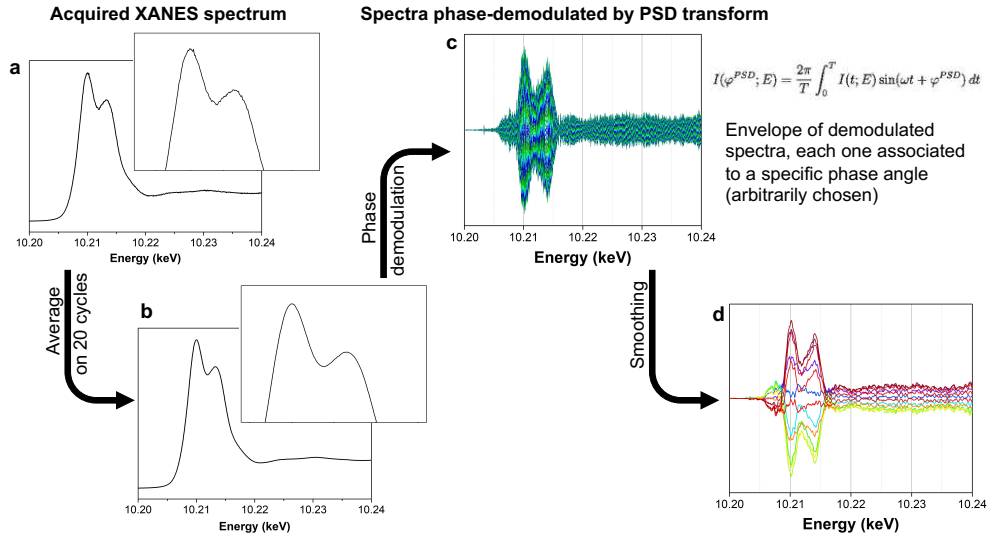

Figure A.8. *XANES spectra elaboration necessary to highlight the possible changes connected to the interaction of acetone molecules with WO_3 material surface. (a,b) Calculation of average spectrum to eliminate the possible signals noise (the first 4 cycles were discarded to ensure the steady state conditions were achieved). (c) Spectrum demodulation by Phase Sensitive Detection (PSD), in which $0 < t < T$ (T = 300 s). PSD is a function that transforms a set of time-resolved data I(t) into a new set of phase-resolved data $I(\varphi^{PSD})$, with $0° < \varphi^{PSD} < 360°$ (φ^{PSD} is the demodulation phase angle). (d) Smoothing of the as-obtained demodulated spectra.*

Specifically, on each spectra pack, an average spectrum was calculated (Figs. A.8a,b). Then, a phase demodulation was computed by applying the Phase Sensitive Detection (PSD, see equation in Figure A.8c, using a homemade MATLAB routine)[21] to increase the signal-to-noise ratio and to remove those parts of the spectra that are not affected by the external stimulation, significantly improving the active species response. The first four modulation periods were always discarded to ensure that the steady state conditions were achieved. This approach becomes particularly important to unravel structural information, especially in the present case, where the possible modifications are limited to the material surface. Once obtained the demodulated spectra, a final smoothing step followed.

As shown in Figure A.9, a typical XANES profile is approximately the sum between five gaussian curves and an arctangent or sigmoidal representing the background. The five gaussian (Fig. A.9b) can be reconducted to tungsten density of states projected on the five 5d orbitals. The latter are subdivided in two broad bands, whose maxima are separated by a ca 3.4 eV gap: the lower energy one is mostly localized on W t_{2g} orbitals, whereas the other has a strong e_g character. Notably, their relative heights mimic the 3:2 ratio between t_{2g} and e_g orbital populations.

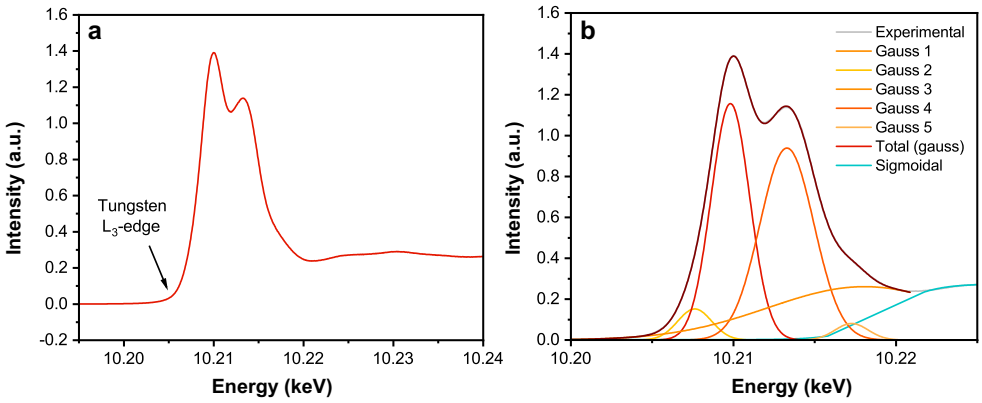

Figure A.9. *(a) Example of a raw XANES spectra obtain during the experiment, (b) same spectrum fitted with gaussian and sigmoidal curves.*

Hence, the presence of a characteristic shape (*e.g.* presence of peaks or sinusoidal curve) of the aforementioned demodulated spectra could be a symptom of the possible surface modification after molecules adsorption, seen as a rearrangement in the energy level distribution of tungsten surface atoms.

A.1.6. Computational set-up

The computational part was carried out in collaboration with the group of Dr. Ceresoli Davide, Dr. Trioni Mario Italo, Dr. Fausto Cargnoni and Dr. Soave Raffaella of the Institute of Molecular Science and Technologies – CNR Research Centres (ISTM–CNR, Milan). Notably, a CINECA Iscra C project, entitled "Modeling of the electronic properties of WO_3-based nanosensors upon gas adsorption", was obtained. The aim of this theoretical approach was to reproduce the oxide surface which, computationally wise, results in a rather complex system containing a large number of atoms. The *ab initio* calculations were performed using density functional theory (DFT)[23], implemented in the code SIESTA (Spanish Initiative for Electronic Simulation with Thousands of Atoms)[24], choosing PBE[25] as the exchange-correlation functional. The pseudopotentials for W and O atoms are norm-conservative and based on a Troullier-Martins parametrization[26]. The tungsten pseudopotential includes scalar relativistic corrections and it is based on the [Xe]$6s^1 5d^5$ configuration, although the commonly reported one for isolated W is [Xe]$6s^2 5d^4$. Our choice is justified by the fact that, following orbital population analysis, it is found that [Xe]$6s^1 5d^5$ configuration better represents tungsten valence state inside the WO_3 lattice. Specifically, in the input pseudopotentials generation, the used cutoff radii were the ones provided by Rivero *et al.*[27] for tungsten, and the default ones for oxygen (Table A.3).

Oxygen		Tungsten	
Orbital	**Cutoff radius (Å)**	**Orbital**	**Cutoff radius (Å)**
2s	1.47	6s	2.81
2p	1.47	6p	2.88
3d	1.47	5d	2.36
4f	1.47	5f	2.33

Table A.3. *List of the atomic orbitals cutoff radii in oxygen and tungsten pseudopotentials.*

The SIESTA code calculates charge densities and energies on a finite grid in the real space, whose fineness increases with the value of the specified mesh cutoff parameter. Calculations performed on a finer grid are less susceptible to the so-called eggbox effect, which causes unwanted (due to the periodicity of the system) oscillations in energy depending on the position of the grid origin. Similarly, when determining properties in the reciprocal space such as the band structure or the density of states, the code needs a finite grid of k-points. In both cases, a finer grid produces more accurate results. Since convergence on either energy cutoff or number of k-points mostly depends on the pseudopotentials, in order to speed up the calculations, we decided to perform our convergence tests over the small ReO_3-like cubic

system, whose elementary cell contains only four atoms. Figure A.10 shows the results of these tests. Therefore, we believe that the best compromise between computational cost and accuracy was the combination of a 450 Ry mesh cutoff with a 11 × 11 × 11 k-point grid. Moreover, since all the three cell axes of our experimental monoclinic WO_3 system (this polymorph was chosen as the most stable one at the calcination temperature, adopted in the synthetic route; see Chapter 5) are approximately double with respect to the lattice constant of this ReO_3-cubic system (3.86 Å), the reciprocal cell axes are approximately halved. Hence, in calculations performed over the actual bulk phase, a 6 × 6 × 6 k-point grid was used. Notably, the specified mesh cutoff parameter is, in most cases, slightly different from the actual value, used by the code. This is due to the fact that SIESTA performs calculations over a finite grid of points. Therefore, the effective mesh cutoff is the nearest value on the grid to the specified one.

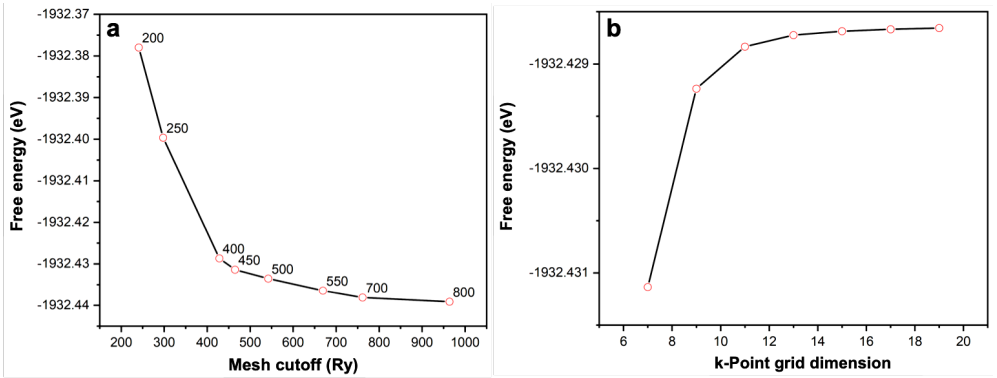

Figure A.10. *(a) Free energy convergence test with respect to the mesh cutoff parameter. Labels indicate the specified values, while the red circles correspond to the effective ones. (b) Free energy convergence test with respect to the number of k-points. On the x axis is reported the number of k-points on each side of the grid (e.g. 7 corresponds to a 7 × 7 × 7 grid).*

Concerning the basis set, we adopted a custom double-ζ (DZ) one with polarization functions, parametrized according to the studies made by Lambert-Mauriat *et al.*[28] (for the oxygen cutoff radii) and Rivero *et al.*[27] (for the tungsten one). Our final choice was the result of a comparison among three different basis sets: *i*) the custom DZP optimized for both W and O, *ii*) the custom DZP optimized only for O, and *iii*) the default DZP. After performing a variable-cell optimization of WO_3 bulk structure with each one, we compared several parameters with the experimental ones (Tables A.4A and B): cell axes and angles, band gap, ratio between the longest cell axis and the shortest ones, sequence of bond lengths along the three axes and basis enthalpy (H; according to the SIESTA manual, this value is obtained by adding to the total energy a term of the form $p_{basis}V_{orbs}$, where p_{basis} is a fictitious basis pressure

and V_{orbs} is the volume of the system orbitals). Furthermore, in order to exclude any dependence of basis enthalpy on the cell volume, this parameter was evaluated for a single point calculation on the experimental cell. We finally decided for the basis set optimized for both O and W, because it reproduces at best the β angle, the bond length sequences along the cell axes, and the ratios between the *c* axis (the longest one) and the other two. Notably, it was associated to the lowest basis enthalpy. Regarding the band gap, all basis sets significantly underestimate the correct value. This behavior is typical of pure exchange-correlation functionals and can be improved by using hybrid functionals, as explained by Di Valentin *et al.*[29], which are not implemented in SIESTA.

A	*a* (Å)	*b* (Å)	*c* (Å)	*β* (Å)	*V* (Å³)	*c*/*a*	*c*/*b*	Basis H (eV)	E_g (eV)
Experimental	7.3271	7.5644	7.7274	90.49	428.3	1.055	1.022	–	2.60
Default DZP	7.3211	7.3805	7.8320	91.65	423.0	1.070	1.061	-15448.6	1.70
Oxygen-modified DZP	7.4275	7.7202	7.9542	90.44	456.1	1.071	1.030	-15451.3	1.34
Oxygen and tungsten-modified DZP	7.4565	7.6837	7.9033	90.46	452.8	1.060	1.029	-15454.0	1.10

B	Bond seq. (*a* axis) (Å)	Bond seq. (*b* axis) (Å)	Bond seq. (*c* axis) (Å)
Experimental	1.94 – 1.86 – 1.91	1.81 – 2.05 – 1.81	1.72 – 2.19 – 1.71
Default DZP	1.87 – 1.97 – 1.92	2.05 – 1.84 – 2.05	1.77 – 2.25 – 1.77
Oxygen-modified DZP	1.92 – 1.93 – 1.92	1.80 – 2.13 – 1.80	1.78 – 2.24 – 1.78
Oxygen and tungsten-modified DZP	1.92 – 1.93 – 1.92	1.82 – 2.09 – 1.82	1.79 – 2.20 – 1.79

Table A.4. *(A) Comparison between structural and energetic parameters obtained on WO_3 bulk phase with standard and custom DZP basis sets with respect to the experimental ones. H is the basis enthalpy. (B) Comparison between the bond sequences along the three cell axes of the experimental cell and the ones calculated with custom and default basis sets.*

However, since the present study does not involve absorption phenomena between the valence band and the conduction band, the calculated band gap was not adopted in the following steps.

Once built the WO_3 surface, we optimized the structures of the other species involved in the sensing mechanism, namely acetone, molecular oxygen and atomic oxygen. Since they all contain oxygen, we selected for it the same custom basis set used for WO_3. Basis sets for C and H contained in acetone, instead, are the default ones. We also kept the same 450 Ry mesh cutoff.

A.2. Results

A.2.1. Chapter 4 – Zinc oxide-based materials

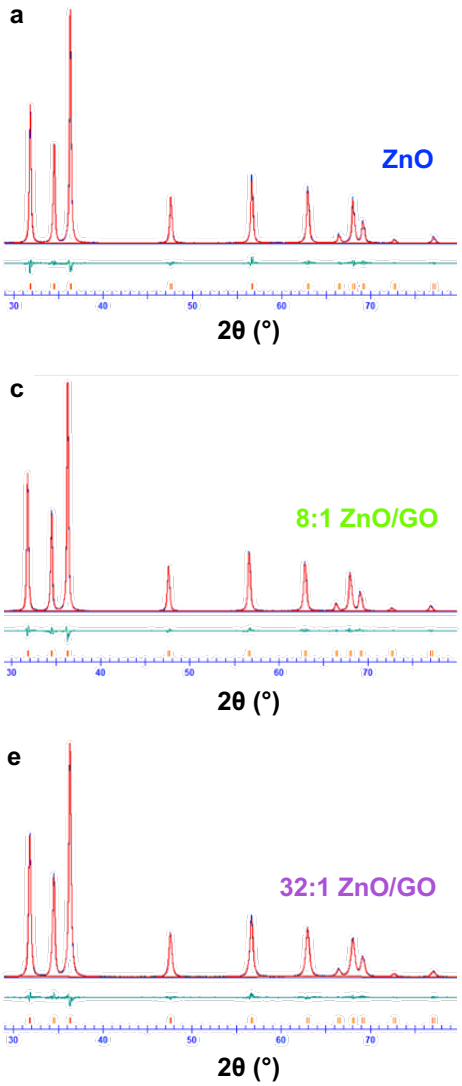

Sample	a = b (Å)	c (Å)	α = β (°)	γ (°)
ZnO	3.247 ± 0.004	5.201 ± 0.007	90	120
4:1 ZnO/GO	3.249 ± 0.005	5.204 ± 0.009	90	120
8:1 ZnO/GO	3.249 ± 0.004	5.202 ± 0.005	90	120
16:1 ZnO/GO	3.248 ± 0.004	5.204 ± 0.007	90	120
32:1 ZnO/GO	3.247 ± 0.004	5.201 ± 0.007	90	120

Figure A.11. *Experimental XRPD patterns (blue line), alongside with the relative fitted spectra by Rietveld refinement (red line) and difference spectra (green line) of (a) pure ZnO, (b) 4:1, (c) 8:1, (d) 16:1 and (e) 32:1 ZnO/GO. The corresponding cell parameters are reported in the Table.*

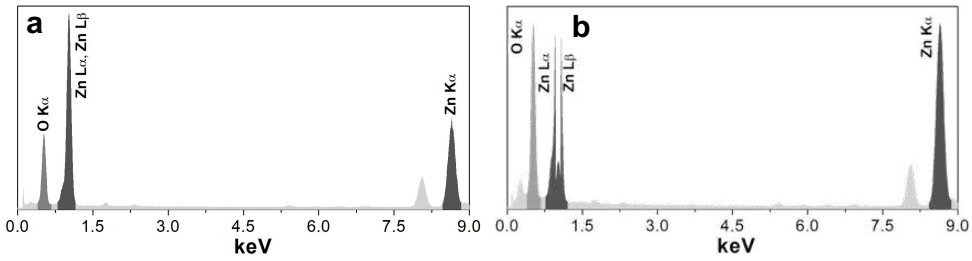

Figure A.12. *EDX spectra of (a) 4:1 ZnO/GO and (b) 32:1 ZnO/GO samples.*

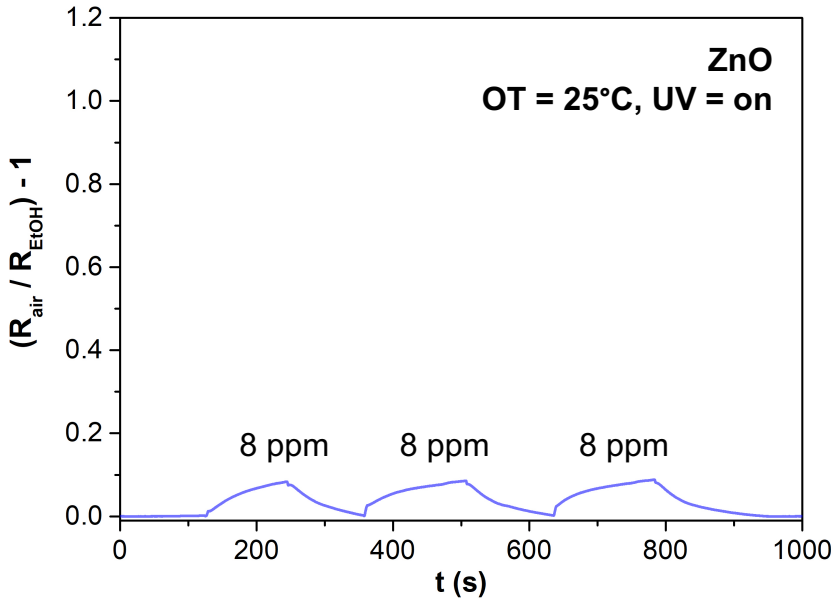

Figure A.13. *Pure ZnO sensor response when exposed to 8 ppm of ethanol, in simulated air (20% O_2 – 80% N_2), at RT and under UV light.*

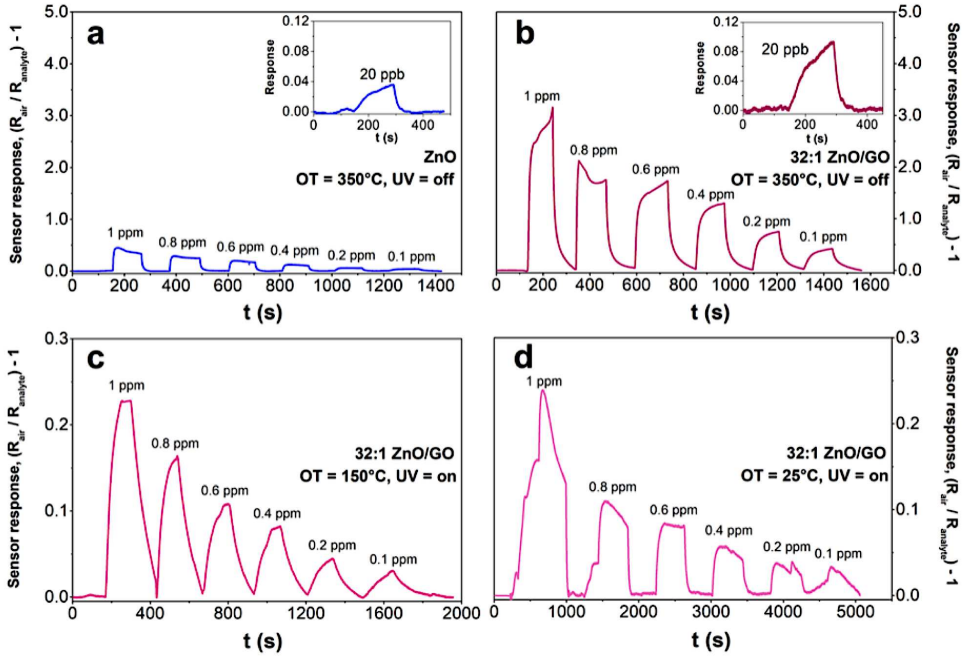

Figure A.14. *(a) Pure ZnO and (b–d) hybrid 32:1 ZnO/GO sensors response when exposed to different acetone concentrations (1 ppm to 20 ppb) in simulated air (20% O_2 – 80% N_2). OT = Operating Temperature.*

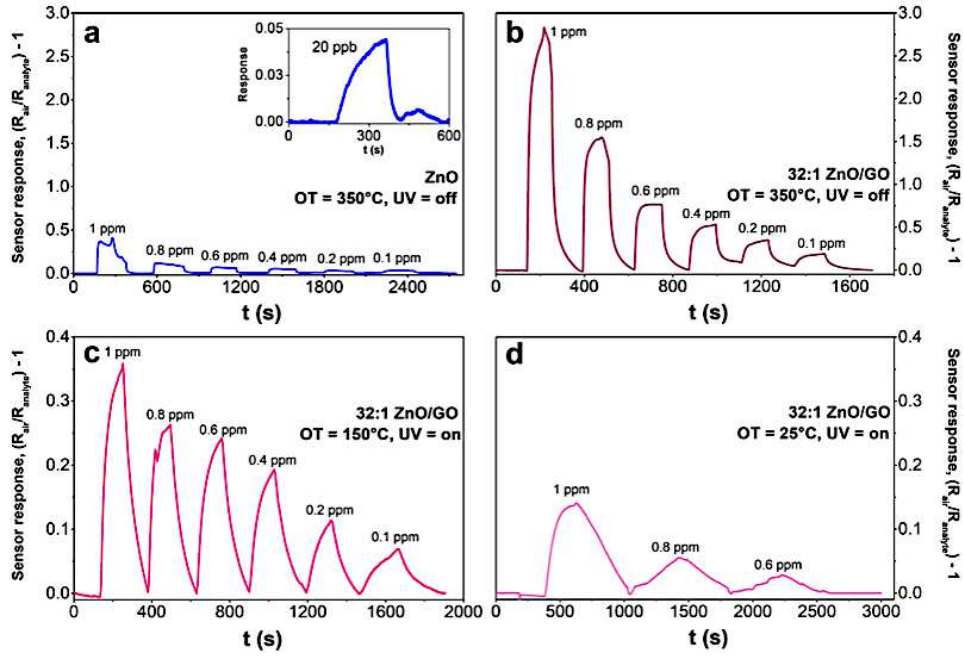

Figure A.15. *(a) Pure ZnO and (b–d) hybrid 32:1 ZnO/GO sensors response when exposed to different ethylbenzene concentrations (1 ppm to 20 ppb) in simulated air (20% O_2 – 80% N_2). OT = Operating Temperature.*

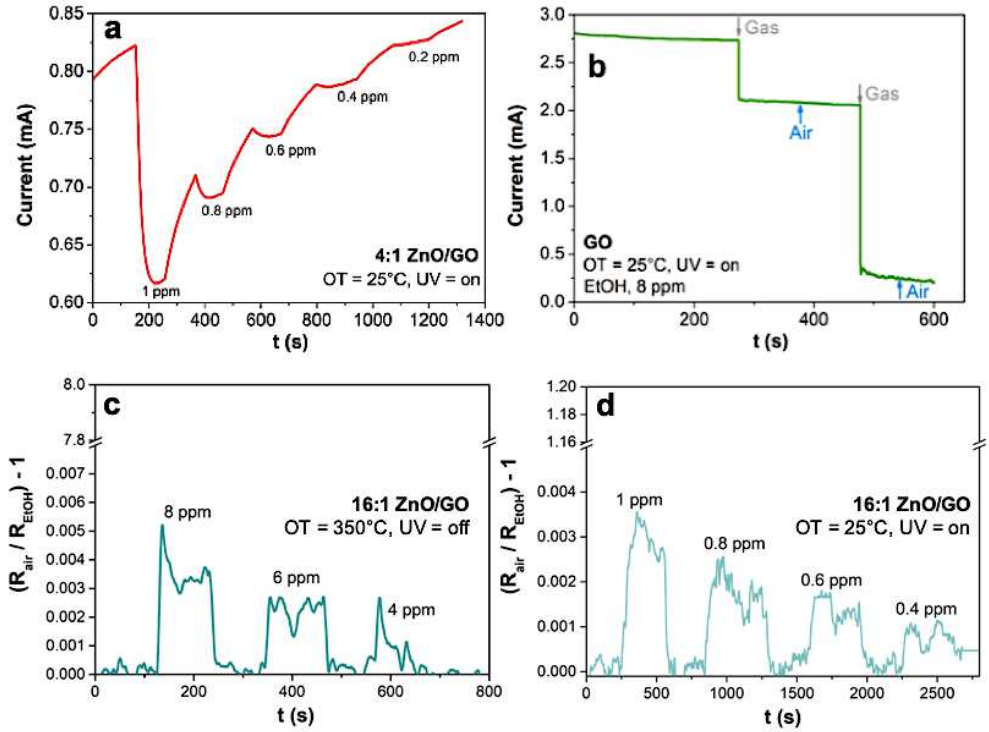

Figure A.16. *(a) Hybrid 4:1 ZnO/GO, (b) pure GO, (c,d) hybrid 16:1 ZnO/GO sensors responses when exposed to different ethanol concentrations, in simulated air (20% O_2 – 80% N_2) at (a,b,d) room temperature (under UV light) and (c) 350°C.*

A.2.2. Chapter 4 – Tin dioxide-based materials

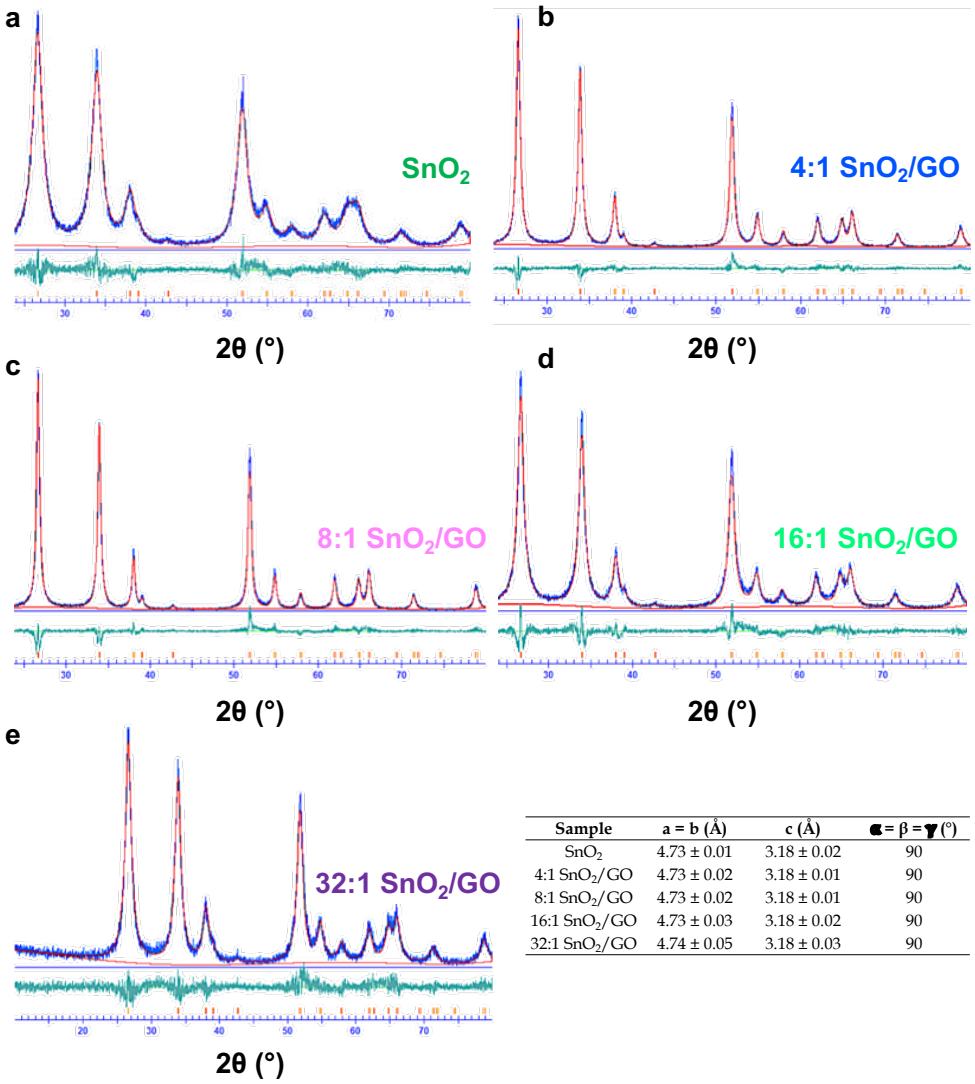

Sample	a = b (Å)	c (Å)	α = β = γ (°)
SnO_2	4.73 ± 0.01	3.18 ± 0.02	90
4:1 SnO_2/GO	4.73 ± 0.02	3.18 ± 0.01	90
8:1 SnO_2/GO	4.73 ± 0.02	3.18 ± 0.01	90
16:1 SnO_2/GO	4.73 ± 0.03	3.18 ± 0.02	90
32:1 SnO_2/GO	4.74 ± 0.05	3.18 ± 0.03	90

Figure A.17. *Experimental XRPD patterns (blue line), alongside with the relative fitted spectra by Rietveld refinement (red line) and difference spectra (green line) of (a) pure ZnO, (b) 4:1, (c) 8:1, (d) 16:1 and (e) 32:1 ZnO/GO. The corresponding cell parameters are reported in the Table.*

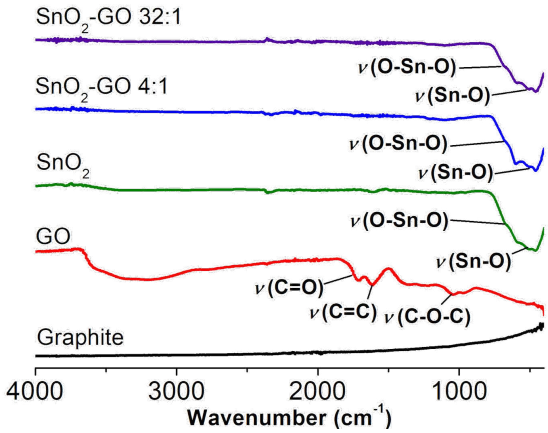

Figure A.18. *Comparison of FTIR spectra relative to graphite, pure GO, pristine SnO_2 and the two hybrids 4:1 and 32:1 SnO_2/GO samples.*

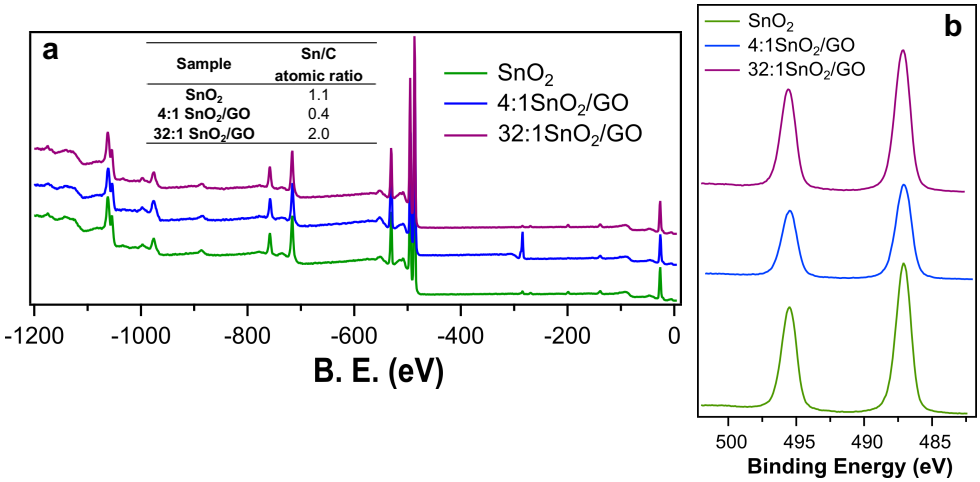

Figure A.19. *XP (a) surveys and (b) Sn 3d region relative to pure SnO_2, 4:1 and 32:1 SnO_2/GO samples (as representative ones). Inset: experimental Sn/C atomic ratios for pure and hybrid samples (in the case of pristine SnO_2, carbon is an adventitious species always present in XPS measurements).*

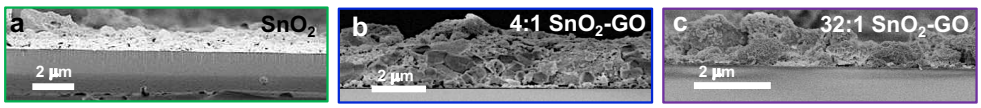

Figure A.20. *Representative FESEM images of (a) pure SnO_2, (b) 4:1 SnO_2/GO and (c) 32:1 SnO_2/GO, showing the relative films thickness.*

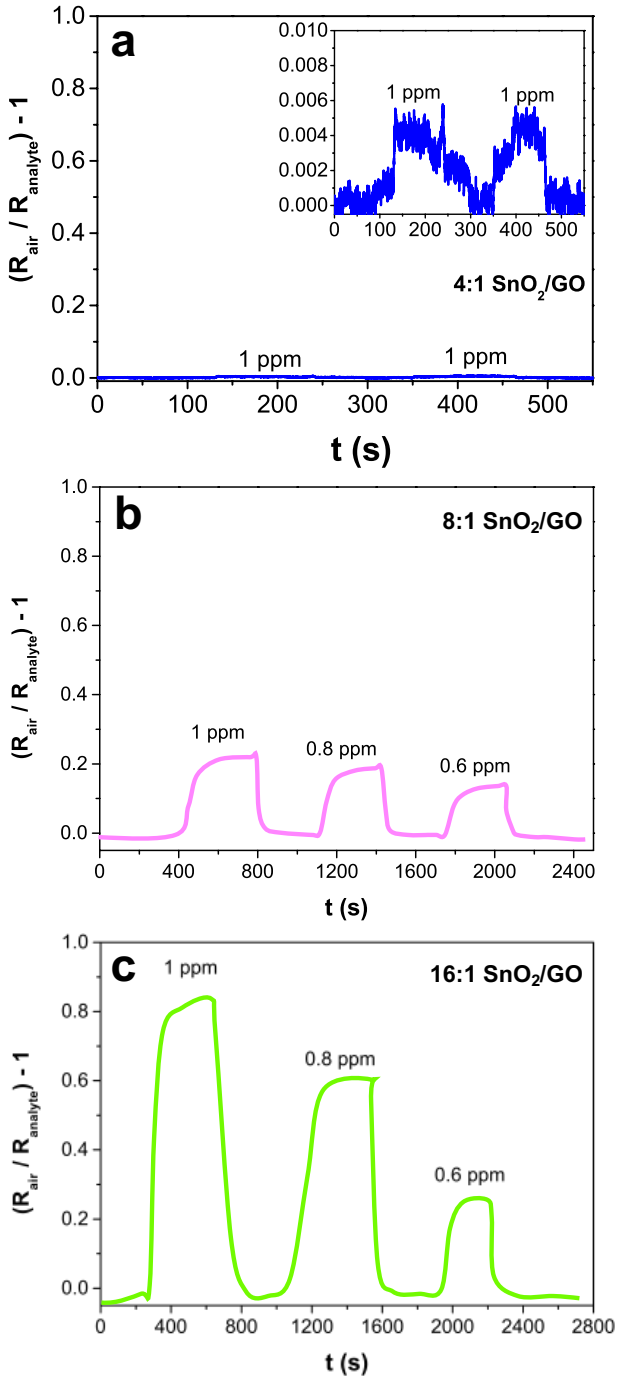

Figure A.21. *Room temperature ethanol sensor responses obtained by hybrid (a) 4:1, (b) 8:1 and (c) 16:1 SnO_2/GO. All the tests were carried out in simulated air (80% N_2 – 20% O_2) at 25°C, under UV light. Adapted with permission*[30]*, Copyright 2019, Elsevier.*

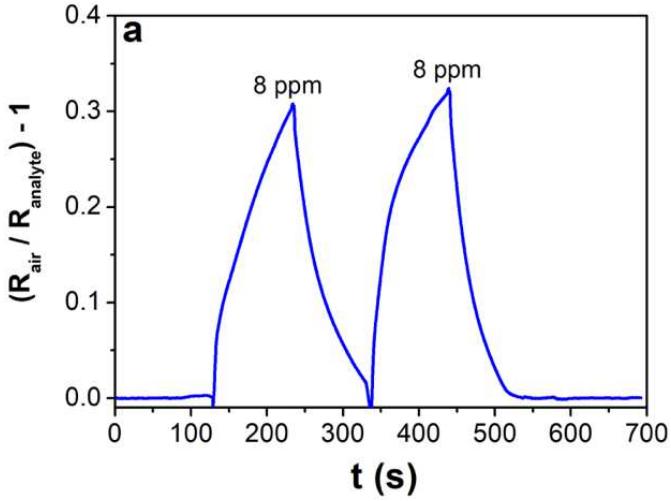

Figure A.22. *Ethanol sensor responses obtained by pure SnO_2, at 150 °C, UV light-aided. All the tests were carried out in simulated air (80% N_2 – 20% O_2).*

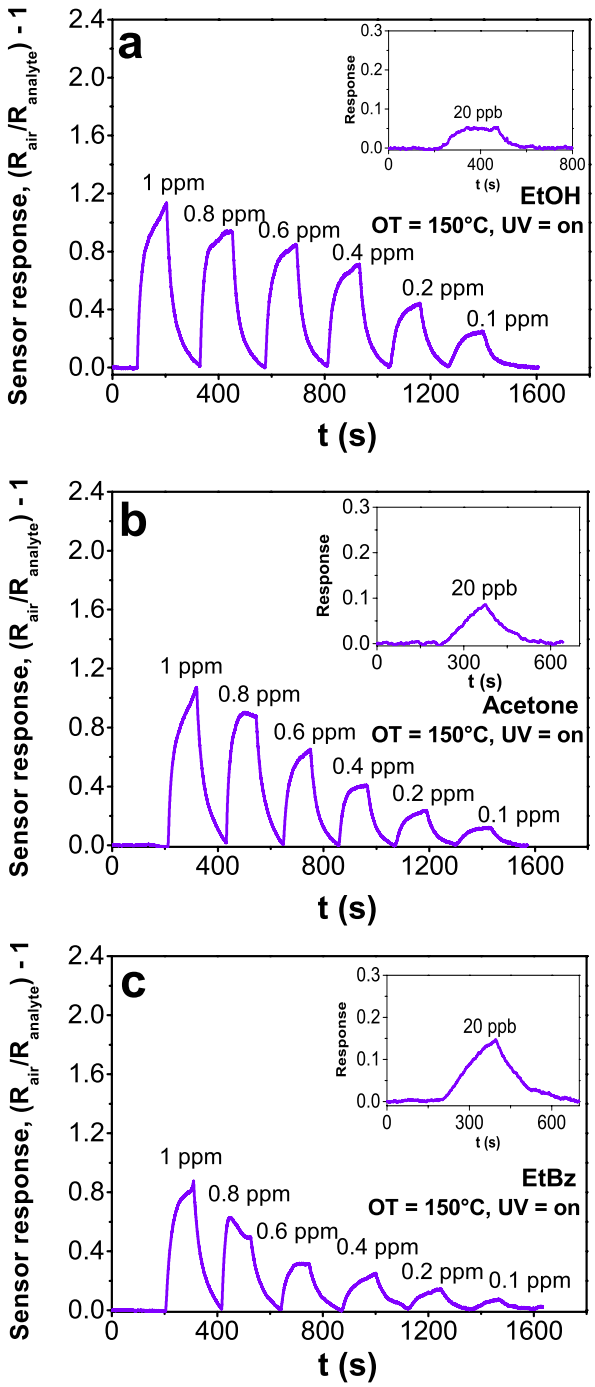

Figure A.23. *Hybrid 32:1 SnO_2/GO sensors response when exposed to different concentrations of (a) ethanol, (b) acetone and (c) ethylbenzene, in simulated air (20% O_2 – 80% N_2). OT = 150°C, UV-light assisted measurements.*

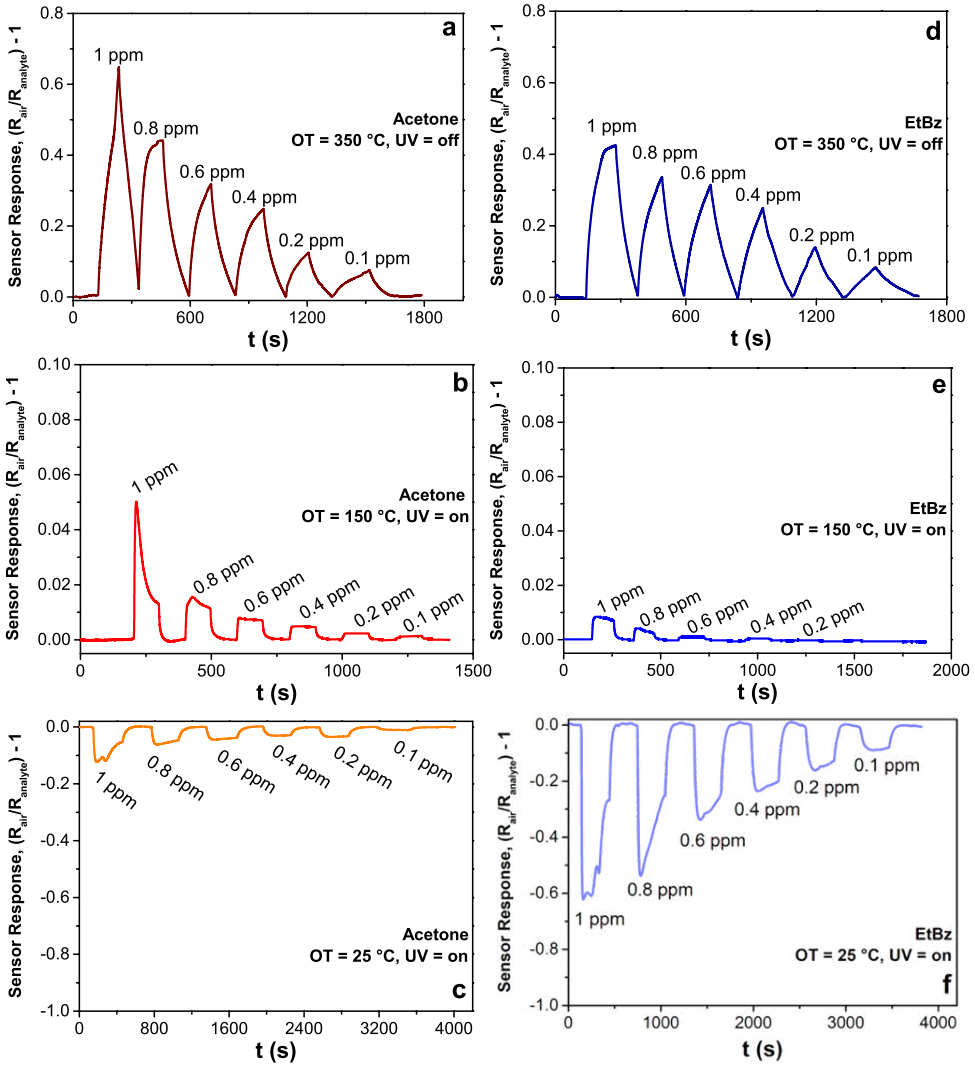

Figure A.24. *(a–c) Acetone and (d–f) ethylbenzene sensing by 4:1 SnO_2/GO sample at 350 °C without UV light, 150 °C and room temperature under UV irradiation. All the measurements were carried out in simulated air (20% O_2 – 80% N_2). OT = Operating Temperature.*

A.2.3. Chapter 4 – Composite Sn/Ti mixed oxides-based materials

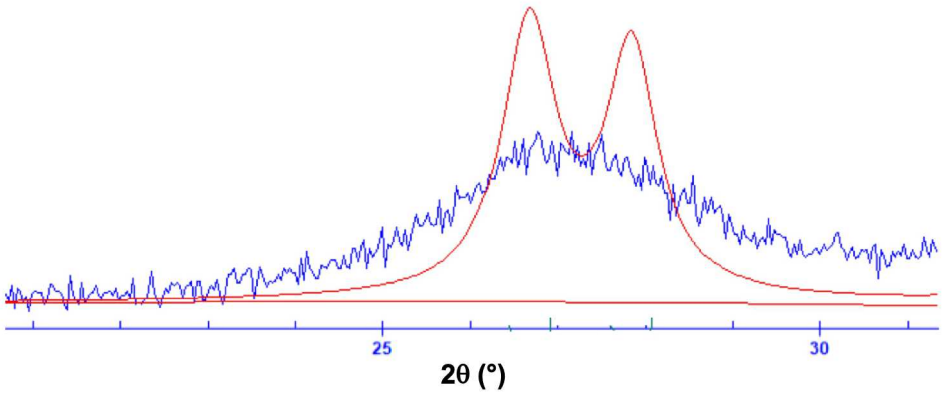

Figure A.25. *Representative composite SnO_2-TiO_2 sample (blue line) fitted by both SnO_2 cassiterite (main peak at 2θ of 26.6°, red line) and TiO_2 rutile (main peak at 2θ of 27.4°, red line). It is clearly observable that the as-synthesized samples are solid solution composed by either the two phases.*

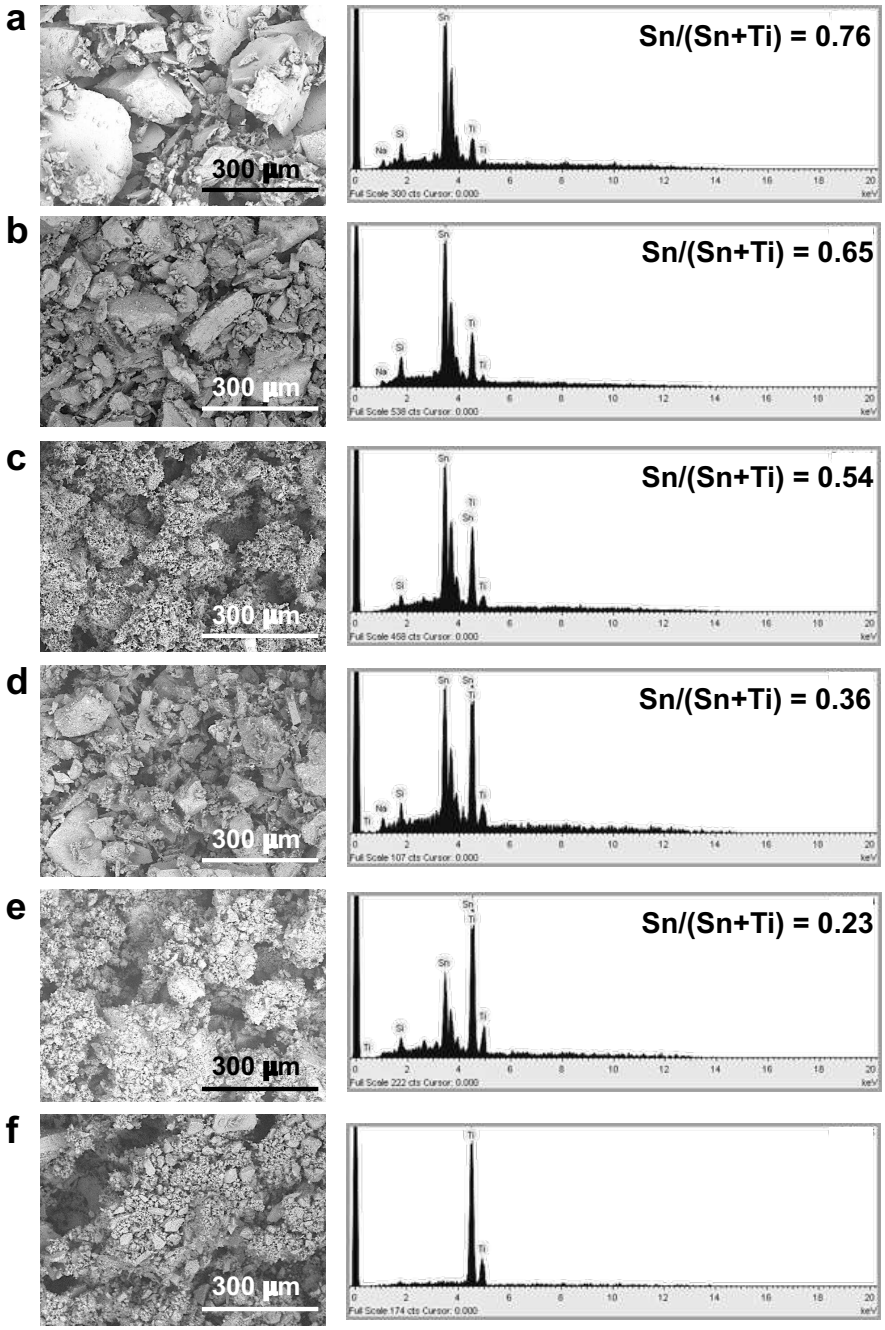

Figure A.26. *SEM images alongside with the relative EDX spectra of (a) 32:1* $Sn_{0.71}Ti_{0.29}$ */GO, (b) 32:1* $Sn_{0.55}Ti_{0.45}$*/GO, (c) 32:1* $Sn_{0.44}Ti_{0.56}$*/GO, (d) 32:1* $Sn_{0.35}Ti_{0.65}$*/GO, (e) 32:1* $Sn_{0.21}Ti_{0.79}$*/GO, (f) 32:1* TiO_2*/GO. The molar ratios Sn/(Sn+Ti) by EDX analysis have been reported, accordingly.*

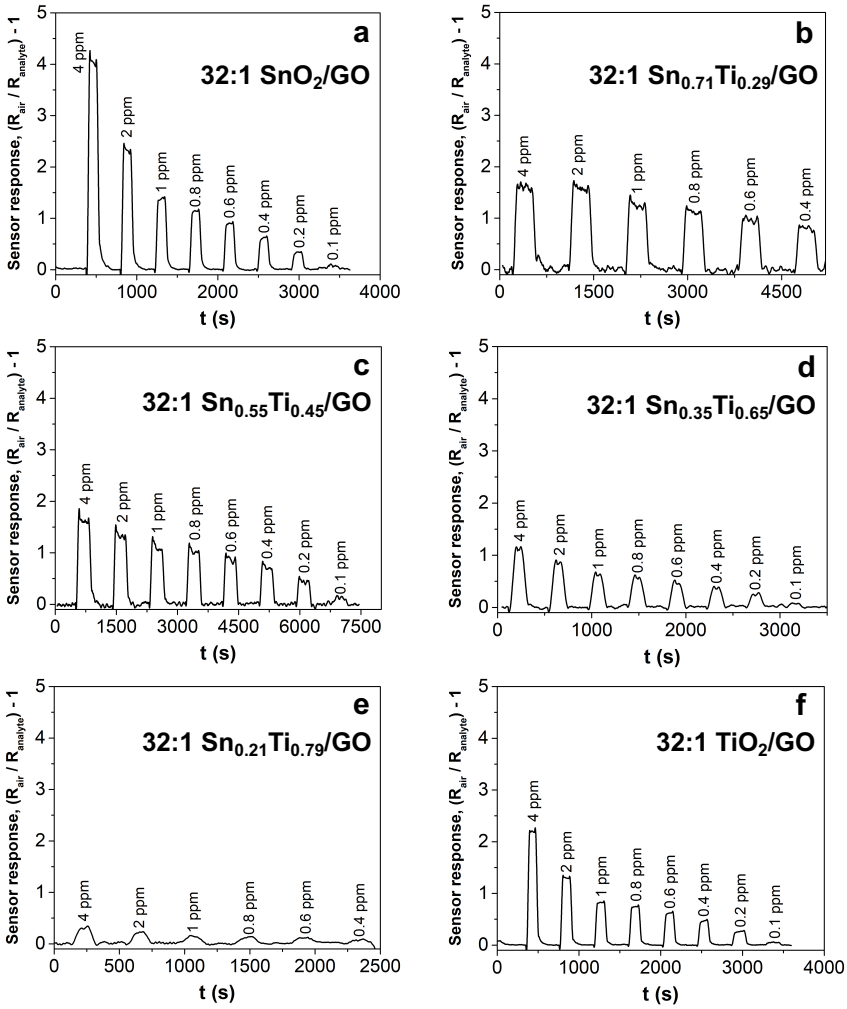

Sensor	t_{res} (s)	t_{rec} (s)
32:1 SnO_2/GO	20	30
32:1 $Sn_{0.71}Ti_{0.29}$/GO	50	55
32:1 $Sn_{0.55}Ti_{0.45}$/GO	36	65
32:1 $Sn_{0.44}Ti_{0.56}$/GO	–	–
32:1 $Sn_{0.35}Ti_{0.65}$/GO	55	60
32:1 $Sn_{0.21}Ti_{0.79}$/GO	100	50
32:1 TiO_2/GO	25	30

Figure A.27. *Toluene sensing by (a) 32:1 SnO_2/GO, (b–e) mixed oxides (with the exception of 32:1 $Sn_{0.44}Ti_{0.56}$/GO, since it did not show any signal), and (f) 32:1 TiO_2/GO compounds. The corresponding response and recovery times (towards 1 ppm of toluene molecules) have been reported in the Table, accordingly. Tests were performed at 350 °C, without UV light, in simulated air (20% O_2 – 80% N_2).*

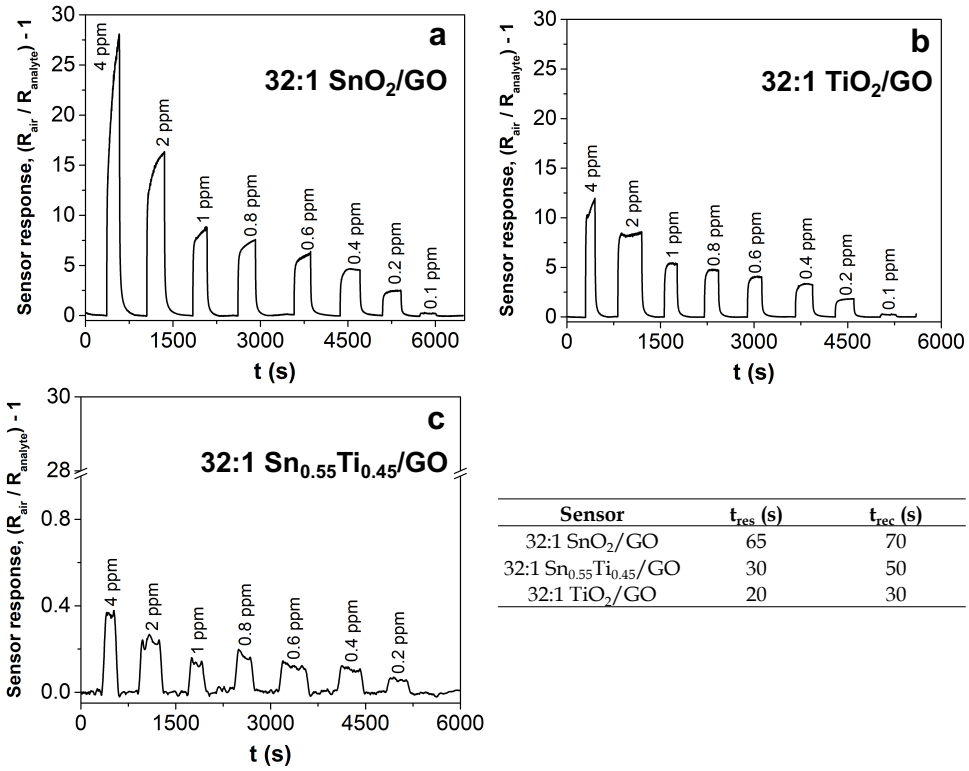

Sensor	t_{res} (s)	t_{rec} (s)
32:1 SnO_2/GO	65	70
32:1 $Sn_{0.55}Ti_{0.45}$/GO	30	50
32:1 TiO_2/GO	20	30

Figure A.28. *Acetone sensing by (a) 32:1 SnO_2/GO, (b) 32:1 TiO_2/GO and (c) 32:1 $Sn_{0.55}Ti_{0.45}$/GO mixed oxide, at 350 °C, without UV light, in simulated air (20% O_2 – 80% N_2). The corresponding response and recovery times (towards 1 ppm of the analyte molecules) have been reported in the Table, accordingly.*

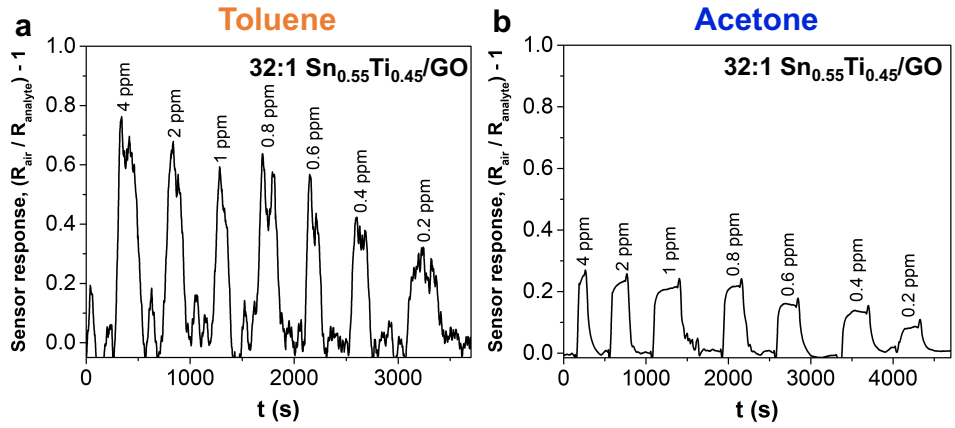

Figure A.29. *(a) Toluene and (b) acetone sensing by 32:1 $Sn_{0.55}Ti_{0.45}$/GO mixed oxide, at 250 °C with UV light. All the measurements were carried out in simulated air (20% O_2 – 80% N_2). OT = Operating Temperature.*

A.2.4. Chapter 5 – Tungsten trioxide

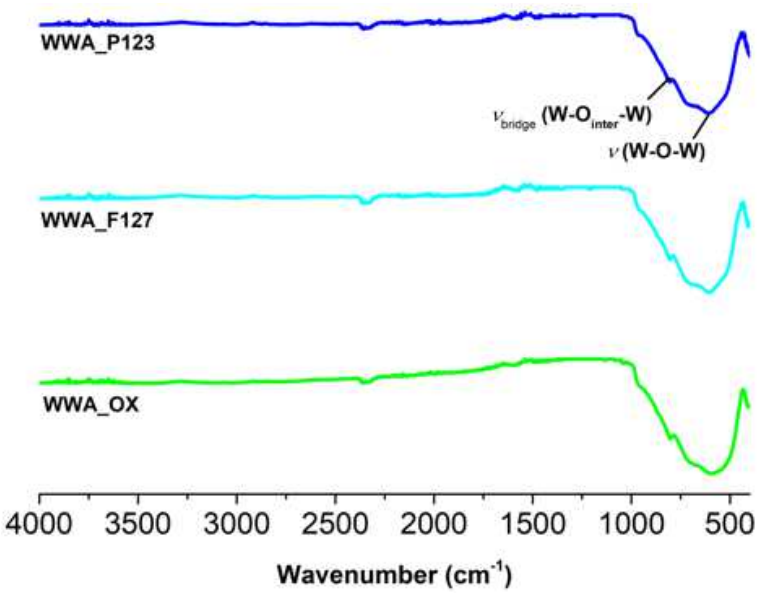

Figure A.30. *Comparison of FTIR spectra relative to WWA-series samples (as representative case). The main stretching modes*[31] *have been highlighted, accordingly.*

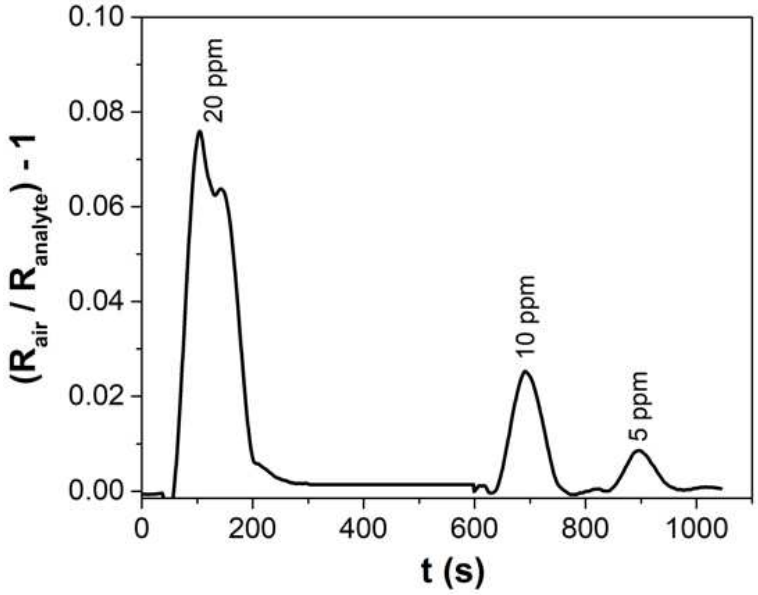

Figure A.31. *WWS_P123 toluene response obtained at 300 °C, without UV light, in simulated air (20% O_2 – 80% N_2).*

References

[1] C. Botas, P. Álvarez, P. Blanco, M. Granda, C. Blanco, R. Santamaría, L. J. Romasanta, R. Verdejo, M. A. López-Manchado, R. Menéndez, *Carbon N. Y.* **2013**, *65*, 156.

[2] J. Chen, B. Yao, C. Li, G. Shi, *Carbon N. Y.* **2013**, *64*, 225.

[3] E. Pargoletti, U. H. Hossain, I. Di Bernardo, H. Chen, T. Tran-Phu, J. Lipton-Duffin, G. Cappelletti, A. Tricoli, *Nanoscale* **2019**.

[4] L. Li, J. Zhao, Y. Wang, Y. Li, D. Ma, Y. Zhao, S. Hou, X. Hao, *J. Solid State Chem.* **2011**, *184*, 1661.

[5] BASF, Technical Data Sheet of Pluronic F127 **2007**.

[6] S.-Y. Chen, S. Cheng, W.-T. Chuang, J.-J. Lee, Y.-P. Chiang, C.-Y. Tang, C.-Y. Lin, In *Scientific Bases for the Preparation of Heterogeneous Catalysts*; Gaigneaux, E. M.; Devillers, M.; Vos, D. E. De; Hermans, S.; Jacobs, P. A.; Martens, J. A.; Ruiz, P., Eds., *Studies in Surface Science and Catalysis*, Elsevier, **2006**, *162*, pp. 369–376.

[7] U. Ashraf, O. A. Chat, M. Maswal, S. Jabeen, A. A. Dar, *RSC Adv.* **2015**, *5*, 83608.

[8] L. M. U. Dutra, M. E. N. P. Ribeiro, I. M. Cavalcante, D. H. A. de Brito, L. D. M. Semião, R. F. da Silva, P. B. A. Fechine, S. G. Yeates, N. M. P. S. Ricardo, *Polímeros* **2015**, *25*, 433.

[9] G. L. Chiarello, M. Bernareggi, M. Pedroni, M. Magni, S. M. Pietralunga, A. Tagliaferri, E. Vassallo, E. Selli, *J. Mater. Chem. A* **2017**, *5*, 12977.

[10] R. Bo, N. Nasiri, H. Chen, D. Caputo, L. Fu, A. Tricoli, *ACS Appl. Mater. Interfaces* **2017**, *9*, 2606.

[11] F. Dejene, A. Ali, H. Swart, R. Botha, K. Roro, L. Coetsee, M. Biggs, *Open Phys.* **2011**, *9*, 1321.

[12] D. Lakhdari, O. Belgherbi, L. Lamiri, M. Hamissi, .

[13] J. Velevska, N. Stojanov, M. Pecovska-Gjorgjevich, M. Najdoski, *J. Electrochem. Sci. Eng.* **2017**, *27*.

[14] R. Atchudan, T. N. J. I. Edison, S. Perumal, M. Shanmugam, Y. R. Lee, *J. Photochem. Photobiol. A Chem.* **2017**, *337*, 100.

[15] S. Hanelt, G. Orts-Gil, J. F. Friedrich, A. Meyer-Plath, *Carbon N. Y.* **2011**, *49*, 2978.

[16] D. A. C. Brownson, D. K. Kampouris, C. E. Banks, *Chem. Soc. Rev.* **2012**, *41*, 6944.

[17] M. M. Lounasvuori, M. Rosillo-Lopez, C. G. Salzmann, D. J. Caruana, K. B. Holt, *Faraday Discuss.* **2014**, *172*, 293.

[18] M. Righettoni, A. Tricoli, S. E. Pratsinis, *Chem. Mater.* **2010**, *22*, 3152.

[19] M. Righettoni, A. Tricoli, S. Gass, A. Schmid, A. Amann, S. E. Pratsinis, *Anal. Chim. Acta* **2012**, *738*, 69.

[20] N. Barsan, U. Weimar, *J. Phys. Condens. Matter* **2003**, *15*, R813.

[21] G. L. Chiarello, D. Ferri, *Phys. Chem. Chem. Phys.* **2015**, *17*, 10579.

[22] G. L. Chiarello, In *Experimental methods and instrumentation for chemical engineers*; **2017**, pp. 366–376.

[23] W. Kohn, L. J. Sham, *Phys. Rev.* **1965**, *140*, A1133.

[24] J. M. Soler, E. Artacho, J. D. Gale, A. Garcia, J. Junquera, P. Ordejón, D. Sánchez-Portal, *J. Phys. Condens. Matter* **2002**, *14*, 2745.

[25] J. P. Perdew, K. Burke, M. Ernzerhof, *Phys. Rev. Lett.* **1996**, *77*, 3865.

[26] N. Troullier, J. L. Martins, *Phys. Rev. B* **1991**, *43*, 1993.

[27] P. Rivero, V. M. Garcia-Suárez, D. Pereñiguez, K. Utt, Y. Yang, L. Bellaiche, K. Park, J. Ferrer, S. Barraza-Lopez, *Comput. Mater. Sci.* **2015**, *98*, 372.

[28] C. Lambert-Mauriat, V. Oison, *J. Phys. Condens. Matter* **2006**, *18*, 7361.

[29] F. Wang, C. Di Valentin, G. Pacchioni, *J. Phys. Chem. C* **2011**, *115*, 8345.

[30] E. Pargoletti, A. Tricoli, V. Pifferi, S. Orsini, M. Longhi, V. Guglielmi, G. Cerrato, L. Falciola, M. Derudi, G. Cappelletti, *Appl. Surf. Sci.* **2019**.

[31] P. Periasamy, T. Krishnakumar, M. Sathish, M. Chavali, P. F. Siril, V. P. Devarajan, *J. Mater. Sci. Mater. Electron.* **2018**, *29*, 6157.

Glossary

ACVD	*Atmospheric chemical vapor deposition*
ALD	*Atomic layer deposition*
BET	*Brunauer Emmett Teller*
BSSE	*Basis Set Superpositioned Error*
CB	*Conduction band*
CCVD	*Combustion assisted chemical vapor deposition*
CMC	*Critical micelle concentration*
CNTs	*Carbon nanotubes*
CPE	*Constant phase element*
CV	*Cyclic voltammetry*
CVD	*Chemical vapor deposition*
δ	*Debye length*
D	*Effective crystalline domain size*
DC sputtering	*Direct current sputtering*
DFT	*Density functional theory*
DOS	*Density of states*
d_p or D	*Grain particles size*
DZP	*Double-ζ polarization*
E_F	*Fermi level*
E_g	*Band gap*
EIS	*Electrochemical Impedance Spectroscopy*
EtBz	*Ethylbenzene*
EtOH	*Ethanol*
EVP	*Evaporation*
EXAFS	*Extended x-ray absorption fine structure*
FESEM	*Field-emission scanning electron microscopy*
FSP	*Flame spray pyrolysis*
FTIR	*Fourier-transformed infrared spectroscopy*
GCE	*Glassy carbon electrode*
GO	*Graphene oxide*
HWLP	*Hot wall aerosol reactor and low-pressure impactor*
IDE	*Interdigitated electrode*
LOD	*Limit of detection*
MBE	*Molecular beam epitaxy*
ME-XAS	*Modulated excitation X-ray absorption spectroscopy*

MOS	*Metal oxide semiconductor*
NPs	*Nanoparticles*
OMCVD	*Organometallic chemical vapor deposition*
OT	*Operating temperature*
PCA	*Principal Component Analysis*
PDOS	*Projected density of states*
PECVD	*Plasma enhanced chemical vapor deposition*
PG	*Pristine graphene*
PLD	*Pulsed layer deposition*
PSD	*Phase sensitive detection*
PTR-MS	*Proton transfer reaction mass spectrometry*
PVD	*Physical vapor deposition*
QDs	*Quantum dots*
RF sputtering	*Radio frequency sputtering*
rGO	*Reduced graphene oxide*
RGTO	*Rheotaxial growth and thermal oxidation*
RH	*Relative humidity*
RT	*Room temperature*
SAED	*Selected area electron diffraction*
S_{BET}	*Active surface area*
SCBD	*Supersonic cluster beam deposition*
SCE	*Saturated calomel electrode*
SEM	*Scanning electron microscopy*
SIESTA	*Spanish Initiative for Electronic Simulation with Thousands of Atoms*
SP	*Spray pyrolysis*
SV	*Surface-to-volume*
T	*ME-XAS stimulation period*
TGA	*Thermogravimetric analysis*
VAFS	*Vapor-fed aerosol flame synthesis*
VB	*Valence band*
VLS	*Vapor liquid solid*
VOA	*Volatile organic amine*
VOC	*Volatile organic compound*
$V_{tot.\ pores}$	*Total pores volume*

XANES	*X-ray absorption near edge structure*
XRPD	*X-ray powder diffraction*
φ^{PSD}	*ME-XAS Demodulated phase angle*
ω	*ME-XAS stimulation frequency*

List of papers, conference contributions, attended schools and seminars

The research activity of the present PhD Thesis has led to the following publications:

- **E. Pargoletti***, A. Tricoli, V. Pifferi, S. Orsini, M. Longhi, V. Guglielmi, G. Cerrato, L. Falciola, M. Derudi and G. Cappelletti, "An electrochemical outlook upon the gaseous ethanol sensing by graphene oxide-SnO_2 hybrid materials", *Applied Surface Science*, 483 (**2019**) 1081-1089, doi: 10.1016/j.apsusc.2019.04.046.

- **E. Pargoletti**, U. H. Hossain, I. Di Bernardo, H. Chen, T. Tran-Phu, J. Lipton-Duffin, G. Cappelletti* and A. Tricoli*, "Room-Temperature Photodetectors and VOCs sensors based on Graphene Oxide – ZnO Nano-Heterojunctions", *Nanoscale*, 11 (**2019**), 22932-22945, doi: 10.1039/C9NR08901B.

- **E. Pargoletti**, U. H. Hossain, I. Di Bernardo, H. Chen, T. Tran-Phu, G. L. Chiarello, J. Lipton-Duffin, A. Tricoli* and G. Cappelletti*, "Graphene Oxide – SnO_2 Nano-Heterojunctions for the Selective and Sensitive Light-Assisted Room-Temperature Sensing of Volatile Compounds", *in preparation*.

Other publications:

- A. Minguzzi, G. Longoni, G. Cappelletti*, **E. Pargoletti**, C. Di Bari, C. Locatelli, M. Marelli, S. Rondinini and A. Vertova, "The influence of carbonaceous matrices and electrocatalytic MnO_2 nanopowders on Lithium-Air Battery performances", *Nanomaterials*, 6 (**2016**) 10, doi: 10.3390/nano6010010.

- **E. Pargoletti**, G. Cappelletti*, A. Minguzzi, S. Rondinini, M. Leoni, M. Marelli and A. Vertova, "High-performance of bare and Ti-doped α-MnO_2 nanoparticles in catalyzing the Oxygen Reduction Reaction", *Journal of Power Sources*, 325 (**2016**) 116-128, doi: 10.1016/j.jpowsour.2016.06.020.

- S. Mostoni, V. Pifferi, L. Falciola, D. Meroni, **E. Pargoletti**, E. Davoli and G. Cappelletti*, "Tailored routes for home-made Bi-doped ZnO nanoparticles. Photocatalytic performances towards *o*-toluidine, a toxic water pollutant", *Journal of Photochemistry and Photobiology A: Chemistry*, 332 (**2017**) 534–545, doi: 10.1016/j.jphotochem.2016.10.003.

* Corresponding author

- **E. Pargoletti**, S. Mostoni, G. Rassu, V. Pifferi, D. Meroni, L. Falciola, E. Davoli, M. Marelli and G. Cappelletti*, "Zn- vs Bi-based oxides for *o*-toluidine photocatalytic treatment under solar light", *Environmental Science and Pollution Research*, (**2017**) 1–10, doi: 10.1007/s11356-017-8430-x.

- L. Rimoldi*, **E. Pargoletti***, D. Meroni*, E. Falletta, G. Cerrato, F. Turco and G. Cappelletti, "Concurrent role of metal (Sn, Zn) and N species in enhancing the photocatalytic activity of TiO_2 under solar light", *Catalysis Today*, 313 (**2018**) 40–46, doi: 10.1016/j.cattod.2017.12.017.

- S. Orsini, **E. Pargoletti***, A. Vertova, A. Minguzzi, C. Locatelli, S. Rondinini and G. Cappelletti, "*Ad hoc* tailored electrocatalytic MnO_2 nanorods for the oxygen reduction in aqueous and organic media", *Journal of Electroanalytical Chemistry*, 808 (**2018**) 439–445, doi: 10.1016/j.jelechem.2017.05.035.

- V. Sabatini*, H. Farina, A. Montarsolo, **E. Pargoletti**, M. A. Ortenzi and G. Cappelletti, "Fluorinated Polyacrylic Resins for the Protection of Cultural Heritages: the effect of Fluorine on Hydrophobic Properties and Photo-Chemical Stability", *Chemistry Letters*, 47 (**2018**) 280–283, doi: 10.1246/cl.171020.

- A. Olietti, **E. Pargoletti**, A. Diona and G. Cappelletti*, "A novel optimized mold release Oil-in-Water emulsion for polyurethane foams production", *Journal of Molecular Liquids*, 261 (**2018**) 199-207, doi.org/10.1016/j.molliq.2018.03.122.

- M. Longhi*, C. Cova, **E. Pargoletti**, M. Coduri, S. Santangelo, S. Patanè, N. Ditaranto, N. Cioffi, A. Facibeni and M. Scavini, "Synergistic Effects of Active Sites' Nature and Hydrophilicity on the Oxygen Reduction Reaction Activity of Pt-Free Catalysts", *Nanomaterials*, 8 (**2018**) 643, doi:10.3390/nano8090643.

- M. Stucchi*, D. C. Boffito, **E. Pargoletti**, G. Cerrato, C. L. Bianchi and G. Cappelletti, "Nano-MnO_2 decoration of TiO_2 microparticles to promote gaseous ethanol visible photoremoval, *Nanomaterials*, 8 (**2018**) 686, doi: 10.3390/nano8090686.

* Corresponding author

- L. Rimoldi, D. Meroni*, **E. Pargoletti**, I. Biraghi, G. Cappelletti and S. Ardizzone, "Role of the growth step on the structural, optical and surface features of TiO_2/SnO_2 composites", *R. Soc. open sci.*, 6 (**2018**) 181662, doi: 10.1098/rsos.181662.

- **E. Pargoletti***, V. Pifferi, L. Falciola, G. Facchinetti, A. Re Depaolini, E. Davoli, M. Marelli and G. Cappelletti, "A detailed investigation of MnO_2 nanorods to be grown onto activated carbon. High efficiency towards aqueous methyl orange adsorption/degradation", *Applied Surface Science*, 472 (**2019**) 118–126, doi: 10.1016/j.apsusc.2018.03.170.

- V. Sabatini*, **E. Pargoletti**, M. Longoni, H. Farina, M. A. Ortenzi, G. Cappelletti*, "Stearyl methacrylate co-polymers: Towards new polymer coatings for mortars protection", *Applied Surface Science*, 488 (**2019**) 213–220, doi: 10.1016/j.apsusc.2019.05.097.

- V. Sabatini*, **E. Pargoletti**, V. Comite, M. A. Ortenzi, P. Fermo, D. Gulotta and G. Cappelletti, "Towards Novel Fluorinated Methacrylic Coatings for Cultural Heritage: A Combined Polymers and Surfaces Chemistry Study", *Polymers*, 11 (**2019**), 1190, doi:10.3390/polym11071190.

- **E. Pargoletti**, L. Motta, V. Comite, P. Fermo and G. Cappelletti*, "The hydrophobicity modulation of glass and marble materials by different Si-based coatings", *Progress in organic coatings*, 136 (**2019**) 105260, doi: 10.1016/j.porgcoat.2019.105260.

* Corresponding author

The research activity of the present PhD Thesis has been presented as poster or oral contributions in the following scientific conferences:

- **E. Pargoletti***, A. Tricoli, S. Orsini, M. Longhi, V. Guglielmi, G. Cerrato and G. Cappelletti, "Detection of VOCs Traces by Graphene Oxide-Metal Oxide Gas Sensors"
  Oral - ISE 2018–69th Annual Meeting of the International Society of Electrochemistry (Bologna, 2–7 September **2018**).

- **E. Pargoletti***, A. Tricoli, S. Orsini, V. Pifferi, M. Longhi, V. Guglielmi, L. Falciola and G. Cappelletti, "Graphene Oxide-Based Hybrids for Chemiresistive VOCs Sensors"
  Oral - AEM 2018–Advanced Energy Materials (Guildford, 10–12 September **2018**).

- **E. Pargoletti***, A. Tricoli, M. Longhi, V. Guglielmi and G. Cappelletti, "Low Temperature Composite Sensors for Environmental and Medical Applications"
  Oral - ISE 2019–70th Annual Meeting of the International Society of Electrochemistry (Durban, 4–9 August **2019**).

- **E. Pargoletti**, A. Tricoli, G. L. Chiarello and G. Cappelletti*, "Low temperature/UV-assisted composites as gas sensors for medical applications"
  Oral - SP7–7th International Conference on Semiconductor photochemistry SP7 (Milan, 11–14 September **2019**).

- **E. Pargoletti***, A. Tricoli, M. I. Trioni, M. Longhi, G. L. Chiarello and G. Cappelletti, "Graphene oxide – metal oxides nano-heterojunctions for low temperature sensing: an experimental and theoretical approach"
  Poster - SP7–7th International Conference on Semiconductor photochemistry SP7 (Milan, 11–14 September **2019**).

Other oral contributions:

- **E. Pargoletti***, G. Facchinetti, V. Pifferi, L. Falciola, G. Cappelletti, "Tailored MnO_2 Nanorods as Highly Efficient Materials for Methyl Orange Adsorption/Degradation"

* The author presented the work personally

ANM2017 – 9th International Conference on Advanced Nanomaterials (Aveiro, 19–21 July **2017**).

- M. Stucchi, **E. Pargoletti*,** G. Cappelletti, D.C. Boffito, C.L. Bianchi and G. Cerrato, "A comparative study on adsorption and photocatalytic degradation of VOCs by Mn-Oxides modified TiO_2 micro-particles"
  EUROPACAT – A bridge to the future (Florence, 27–31 August **2017**).

- **E. Pargoletti***, G. Cappelletti, A. Vertova and V. Pifferi, "Bare and titanium-doped manganese dioxide nanoparticles. Their pivotal role in energetic and sensoristic applications"
  Master thesis "Bio-Logic SAS" award - SCI2017–XXVI Congresso Nazionale della Società Chimica Italiana (Paestum, 10–14 September **2017**).

- M. Longhi, C. Cova, **E. Pargoletti**, M. Coduri, S. Santangelo, S. Patanè, N. Ditaranto, N. Cioffi, A. Facibeni and M. Scavini, "Surface characterization of non-noble metals embedded in n-doped carbon catalysts: the importance of hydrophilicity on oxygen reduction reaction activity"
  XXVII Congresso della Divisione di Chimica Analitica (Bologna, 16–20 September **2018**).

- V. Sabatini, **E. Pargoletti**, G. Longhi, P. Fermo, V. Comite, H. Farina, M. A. Ortenzi and G. Cappelletti, "Fluorine-Modified Polyacrylic Coatings for Cultural Heritage Protection"
  3rd Milan Polymer Days MIPOL2019 (Milan, 11–13 March **2019**).

- M. Longhi, C. Cova, **E. Pargoletti**, M. Coduri, S. Santangelo, S. Patanè, N. Ditaranto, N. Cioffi, A. Facibeni, M. Scavini, "Synergistic Effects of Active Sites Nature and Hydrophilicity on Oxygen Reduction Reaction Activity of Pt-Free Catalysts"
  WEEM 2019 – International Workshop of Electroactive Materials (Borovets, Bulgaria, 16–21 June **2019**).

- V. Sabatini, **E. Pargoletti**, H. Farina, M. A. Ortenzi and G. Cappelletti, "Stone materials and polymer coatings: new perspectives for the protection of the cultural heritages"
  EPF 2019–European Polymer Congress (Crete, 9–14 June **2019**).

* The author presented the work personally

- M. Longhi, C. Cova, **E. Pargoletti**, M. Coduri, S. Santangelo, S. Patanè, N. Ditaranto, N. Cioffi, A. Facibeni, and M. Scavini, "Synergistic Effects of Active Sites Nature and Hydrophilicity on Oxygen Reduction Reaction Activity of Pt-Free Catalysts"
  GEI 2019–Giornate dell'Elettrochimica Italiana (Padua, 8–12 September **2019**).

Other poster contributions:

- L. Rimoldi, **E. Pargoletti**, D. Meroni, E. Falletta, G. Cerrato, F. Turco and G. Cappelletti, "How Sn and Zn species affect both the physicochemical properties and the photocatalytic power of N-doped nano titania"
  EAAOP–5th European Conference on Environmental Applications of Advanced Oxidation Processes (Prague, 25–29 June **2017**).

- C. M. Cova, **E. Pargoletti**, N. Ditaranto, N. Cioffi, S. Santangelo, S. Patanè, M. Scavini and M. Longhi, "ORR activity of mesoporous N-modified carbon doped with non-noble metals. Effects of metal"
  68th Annual ISE Meeting–Electrochemistry without borders (Providence, 27 August–1 September **2017**).

- **E. Pargoletti***, V. Comite, P. Fermo and G. Cappelletti, "Marble hydrophobicity tuned by Si-based coatings"
  Workshop Le scienze e i beni culturali: innovazione e multidisciplinarietà (Milan, 26 February **2019**).

- V. Sabatini, **E. Pargoletti**, H. Farina, M. A. Ortenzi and G. Cappelletti, "Stone materials and polymer coatings: new perspectives for the protection of the cultural heritages"
  Workshop Le scienze e i beni culturali: innovazione e multidisciplinarietà (Milan, 26 February **2019**).

* The author presented the work personally

During the PhD period, the following schools and seminars were attended:

- "Scuola di Chemiometria" – Applications in the industrial and environmental fields, Università degli Studi di Genova – Dipartimento di Farmacia (**2016**).

- Workshop "La Chimica delle Formulazioni nell'Industria e nelle Università" by Federchimica, Auditorium Mapei, Milan (18th May **2017**).

- "Prima Scuola Nazionale sui Sensori Chimici" – Sensors Group of the Italian Chemical Society, Università degli Studi di Napoli Federico II – Dipartimento di Scienze Chimiche (24–26 May **2017**).

- SmartMatLab Workshop at Dipartimento di Chimica, Università degli Studi di Milano (15th November **2017**).

- Seminar about synthesis and characterization of carbon-based materials to be applied for drug-delivery applications, by Prof. Pistone and Prof. Iannazzo from Università di Messina (at the Australian National University, 17th January **2018**).

- Seminar about hydride materials for energy storage and catalysis, by Prof. Kondo-Francois Aguey-Zinsou from University of New South Wales (at the Australian National University, 14th March **2018**).

- Seminar entitled "X-ray absorption spectroscopy – an ideal analytical tool for understanding heterogeneous catalysts at work", by Prof. Jan-Dierk Grunwaldt from Institut für Tecnische Chemie und Polymerchemie Karlsruher Institut für Technologie (KIT) (at Università degli Studi di Milano, 16th April **2019**).